Downloaded from orbit.dtu.dk on: Dec 18, 2017

Technical University of Denmark

Reduction Methods for Real-time Simulations in Hybrid Testing

Andersen, Sebastian; Poulsen, Peter Noe; Stang, Henrik

Publication date:
2016

Document Version
Publisher's PDF, also known as Version of record

Link back to DTU Orbit

Citation (APA):
Andersen, S., Poulsen, P. N., & Stang, H. (2016). Reduction Methods for Real-time Simulations in Hybrid Testing. (B Y G D T U. Rapport; No. R-343).

DTU Library
Technical Information Center of Denmark

General rights
Copyright and moral rights for the publications made accessible in the public portal are retained by the authors and/or other copyright owners and it is a condition of accessing publications that users recognise and abide by the legal requirements associated with these rights.

- Users may download and print one copy of any publication from the public portal for the purpose of private study or research.
- You may not further distribute the material or use it for any profit-making activity or commercial gain
- You may freely distribute the URL identifying the publication in the public portal

If you believe that this document breaches copyright please contact us providing details, and we will remove access to the work immediately and investigate your claim.

Reduction Methods for Real-time Simulations in Hybrid Testing

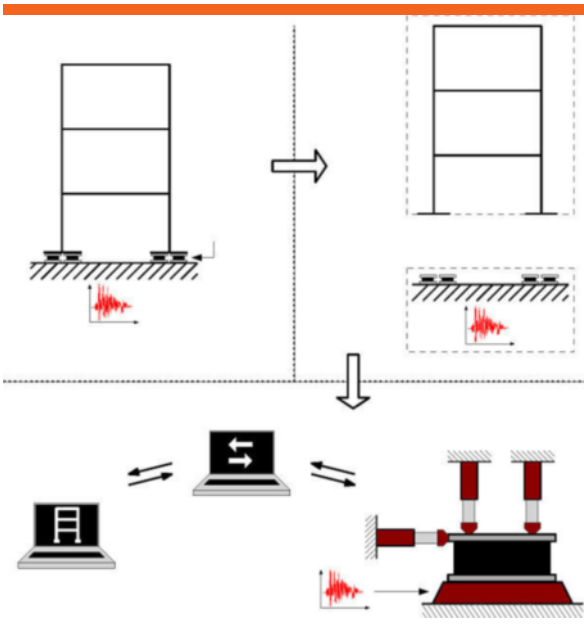

Sebastian Andersen

PhD Thesis

Department of Civil Engineering
2016

DTU Civil Engineering, Report - R-343
September, 2016

DTU Civil Engineering
Department of Civil Engineering

Reduction Methods for Real-time Simulations in Hybrid Testing

Sebastian Andersen

Ph.D. Thesis

Department of Civil Engineering
Technical University of Denmark

2016

Supervisors:

Associated Professor Peter Noe Poulsen, DTU Byg
Professor Henrik Stang, DTU Byg

Assesment Committee:

Reduction Methods for Real-time Simulations in Hybrid Testing

Copyright © 2016 by Sebastian Andersen

Printed by DTU-Tryk
Department of Civil Engineering
Technical University of Denmark
ISBN: 9788778774347
ISSN: 1601-2917

Preface

This thesis is submitted as a partial fulfilment of the requirement for the Danish PhD degree. The presented work has been carried out at the Department of Civil Engineering, Technical University of Denmark (DTU) between March 2013 and February 2016 under supervision of Associate Professor Peter Noe Poulsen and Professor Henrik Stang. The PhD project has been financed partly by the Graduate School and partly by Danish Centre for Composite Structures And Materials for Wind Turbines.

The thesis consist of 7 chapters and 4 appended papers. The chapters give a description of the background and the motivation for the research and conclude the major findings. Also a presentation of the work conducted is given here. In the four appended the delivered research contributions are considered in detail.

Kongens Lyngby, the 29th February, 2016

Sebastian Andersen

Acknowledgements

I would like to thank my supervisors Associate Professor Peter Noe Poulsen and Professor Henrik Stang both from the Department of Civil Engineering, DTU. They helped me through the research study with plenty of good advices and useful discussions.

Furthermore I would also like to thank Associate Professor Emeritus Leif Otto Nielsen, Associate Professor John Forbes Olesen and Associate Professor Jens Henrik Nielsen for always taking the time to discuss various scientific problems faced during the study.

Otto Mønsteds Fond is acknowledged for supporting the participation in the EURODYN 9th international conference on structural dynamics.

A thank is also given to my office colleagues Jan Winkler, Rocco Custer, Anna Emilie Thybo, Joan Rolsgaard, Jesper Sørensen, Asmus Skar and Morten Herfelt. Thank you for your support in both scientific as well as nonscientific contexts and for providing a good atmosphere in the office.

Finally, thank you to all the people in the section for Structural Engineering, Department of Civil Engineering, DTU, for being supportive and helpful.

Abstract

Hybrid testing constitutes a cost-effective experimental full scale testing method. The method was introduced in the 1960's by Japanese researchers, as an alternative to conventional full scale testing and small scale material testing, such as shake table tests. The principle of the method is to divide a structure into a physical substructure and a numerical substructure, and couple these in a test. If the test is conducted in real-time it is referred to as *real time* hybrid testing.

The hybrid testing concept has developed significantly since its introduction in the 1960', both with respect to the size and the complexity of the physical and numerical substructures. However, due to a rapid increase in the computational time, a further increase in the size and complexity of the numerical substructures is challenged. In this thesis a number of elements that can help to improve the size and complexity of kinematic nonlinear numerical substructures are presented, with special emphasis on the use of basis reduction methods. Three elements that can help to improve the accuracy are presented and illustrated.

In kinematic nonlinear systems, various deformation modes are coupled through a nonlinear strain measure. If these coupling-activated modes are not represented in the basis reduction, a significant increase in the structural stiffness can appear, which can ruin the numerical accuracy. One way to represent the coupling-activated modes is by use of so-called modal derivatives. Equations to evaluate these exist. However, due to singularities these can only by solved approximately. A modified and a novel set of system of equations of motion governing the modal derivatives are, therefore, derived. From these a set of improved modal derivatives are found. By use of an example it is, furthermore, illustrated that the modal derivatives determined from the novel system represent the exact modal derivatives.

One of the most time consuming tasks in the numerical time integration

is the evaluation of the internal restoring forces. Due to its nonlinear format, a time consuming element-by-element assembling is used. It is shown, that by adopting an existing mathematical reformulation technique, the costly element-by-element assembling is replaced by a significantly more efficient global assembling in a reduced co-ordinate system.

By use of the novel modal derivatives an efficient basis formulation is arranged, combining linear modes with modal derivatives. The basis is based on a Taylor series, and is, therefore, referred to as a Taylor basis. The basis predicts a relation between the linear normal modes and the modal derivatives. Utilizing this basis formulation, the modal derivatives are included without introducing further unknowns into the system. The basis formulation is shown to exhibit high precision and to reduce the computational cost significantly. Furthermore, the basis formulation exhibits a significant higher stability, than standard nonlinear algorithms.

A real-time hybrid test is performed on a glass fibre reinforced polymer composite box girder. The test serves as a pilot test for prospective real-time tests on a wind turbine blade. The Taylor basis is implemented in the test, used to perform the numerical simulations. Despite of a number of introduced errors in the real-time hybrid testing loop, the test confirms the high stability and efficiency of the Taylor basis.

Resumé

Hybrid tests udgør en omkostningseffektiv eksperimentel fuldskala testmetode. Metoden blev introduceret in 1960'erne af Japanske forskere, som et alternativ til konventionelle fuldskala tests og materiale tests foretaget i mindre skalaer, såsom test udført på et rystebord. Princippet bag metoden består i at opdele konstruktion i en fysisk subkonstruktion og en numerisk subkonstruktion, som kobles i en test. Hvis testen udføres i realtid, kaldes det for en realtids hybrid test.

Hybrid test princippet har oplevet en markant udvikling siden det blev indført i 1960'erne, både med hensyn til størrelsen og kompleksiteten af de fysiske og de numeriske subkonstruktioner. Grundet en hurtigt stigende beregningstid, er en yderligere forøgelse i størrelsen og kompleksiteten af de numeriske subkonstruktioner udfordret. I denne afhandling præsenteres en række elementer der kan hjælpe til at øge størrelsen og kompleksiteten af de numeriske subkonstruktioner, med vægt på brugen af basis reduktionsmetoder. Tre elementer der kan forbedre nøjagtigheden præsenteres og illustreres.

I kinematisk ikke-lineære systemer kobles diverse deformation modes gennem et ikke-lineært tøjningsmål. Hvis disse koblings-aktiverede modes ikke er repræsenteret i basis reduktionen, så kan stivheden af konstruktionen øges markant, og derved ødelægge den numeriske nøjagtighed. En måde hvorpå disse koblingsaktiverede modes kan repræsenteres, er ved hjælp af såkaldte modale afledte. Der findes ligninger til at bestemme disse, men de kan kun løses approksimativt. Et modificeret samt et nyt system af ligninger der styrer de modale afledte udledes derfor. Ud fra disse kan der beregnes forbedrede modal afledte. Ud fra et eksempel, vises det at de modale afledte bestemt ud fra det nye ligningssystem, repræsenterer de eksakte modale afledede.

En af de mest tidskrævende opgaver i den numeriske tidsintegration er evalueringen af de indre knudkræfter. Grundet dets ikke-lineære format, er en tidskrævende evaluering benyttet, hvor hvert elementbidrag evalueres et ad

gangen. Det vises, at ved at adoptere en eksisterende matematisk omformulerings teknik, så kan den tidskrævende evaluering erstattes af en markant mere effektiv global evaluering i et reduceret koordinatsystem.

Ved benyttelse de nye modale afledte opstilles en effektiv basis, der kombinerer lineære modes med modale afledte. Basisen er baseret på en Taylor serie, og kaldes derfor for en Taylor basis. Basisn forudsiger en relation mellem de lineære modes koordinater og de modale afledtes koordinater. Ved at benytte denne basisformulering, kan de modale afledte blive inkluderet uden at øge antallet af ubekendte i systemet. Denne basisformulering udviser en høj nøjagtighed og reducerer de beregningsmæssige omkostninger markant. Derudover udviser basisformuleringen en signifikant forøget stabilitet, sammenlignet med standard algoritmer benyttet til ikke-lineære problemer.

En realtids hybrid test udføres på en glasfiberarmeret kompositbjælke. Testen benyttes som en pilottest for fremtidige realtids test på vindmøllevinger. Taylor basisn implementeres i testen og benyttes til at foretage de numeriske simuleringer. På trods af en række fejl introduceret i realtids hybrid test loopet, bekræfter testen stabiliteten og effektiviteten af Taylor basisen.

Contents

1 Introduction **1**
1.1 Concept of Hybrid Testing 3
1.2 Numerical Challenges in RTHT 6
1.2.1 Computational Time - Example 7
1.3 Hybrid Testing at DTU 10
1.4 Objective and Structure of the Thesis 12

2 History of Hybrid Testing **15**
2.1 Introduction of Hybrid Testing 15
2.2 Real-time Hybrid Testing 16

3 Existing Time Integration **25**
3.1 Time Integration 25
3.2 Time Integration in Hybrid Testing 28
3.2.1 Implicit Integration Schemes 29
3.2.2 Explicit Integration Schemes 36
3.3 Concluding Remarks 38

4 Existing and New Basis Reduction Methods **39**
4.1 Basis Projection 41
4.1.1 Nonlinear Cantilever - Example 42
4.1.2 Basis Vectors 46
4.2 Improved Basis Reduction 50
4.2.1 Global Assembling of the Internal Restoring Forces . . 52
4.2.2 Modified Governing System of Equations 53
4.2.3 The Taylor Basis 62
4.2.4 Concluding Remarks 72

5 Application of Reduction Methods in Hybrid Testing **75**
5.1 Basis Reduction in Hybrid Testing 75
5.2 Real-time Hybrid Test 76

5.2.1 Test Structure and Hybrid Setup 76
5.2.2 Numerical Modelling 79
5.2.3 Reference Structures 80
5.2.4 Test Results 81
5.2.5 Potential Numerical Improvements 82
5.3 Evaluation of Basis Vectors 85
5.4 Concluding Remarks 86

6 Future Research Subjects **89**

7 Conclusion **91**

Bibliography **95**

Errata **100**

I Appendix **103**

A Kinematic Nonlinear Beam Example **105**

II Appended Papers **107**

Paper I
"Reduction Method for Real-Time Simulations in Hybrid Testing",
S. Andersen & P.N. Poulsen.
Proceedings of the 9th International Conference on Structural Dynamics
EURODYN 2014, Porto, Portugal 109

Paper II
"Reduction Method for Kinematic Nonlinear Real-time Simulations",
S. Andersen & P. N. Poulsen.
Submitted: *International Journal for Numerical Methods in Engineering, 2015* 119

Paper III
"Nonlinear Real-time Simulations Using a Taylor Basis",
S. Andersen & P. N. Poulsen.
Submitted: *International Journal for Numerical Methods in Engineering, 2016* 149

Paper IV
"Single-component Multi-rate Real-Time Hybrid Simulation Pilot Test on a Composite Structure",
J. P. Waldbjoern, S. Andersen, J. H. Hoegh, J. W. Schmidt & C. Berggreen.
To be submitted: *Strain, 2016* 177

Chapter 1

Introduction

Hybrid testing, also referred to as hybrid simulation, on-line testing and hardware in the loop simulation, is a cost-effective experimental technique introduced in the 1960's, used to investigate the response of complex structural engineering problems under dynamic response. The principle of the technique is to divide the problem into a physical substructure and a virtual substructure and couple these in a test. The physical substructure typically represents a part of the problem of particular interest with a behavior too complex to be modelled. Therefore, this part requires to be tested in a physical test setup. The virtual substructure, on the other hand, represents a part of the structure with known behavior and is modelled as a computer model, typically by use of finite element method (FEM). In this case the virtual substructure is also referred to as the numerical substructure. During the hybrid simulation the substructures run in parallel and communicate and exchange information through a control system.

The point of introducing hybrid testing was to have an alternative to conventional full scale testing and small scale material testing, such as shake table tests. Full scale testing is important, as this is the only test where exact knowledge of structural behavior is provided. However, for large and complex structures this can be an expensive and time consuming solution. The shake table tests, on the other hand, do not require much space, and can lower the cost compared to the full scale testing significantly. However, in shake table tests scaling problems are an issue. Especially nonlinear behavior can be difficult to handle in small scale models. In hybrid testing such scaling problems are automatically avoided, as this is considered a full scale test. Moreover, by use of the substructure technique, only the structural components of specific interest need to be tested in an actual physical test setup. This can reduce the size of the required physical surroundings significantly, and thereby also the cost and time of the experiment.

Initially hybrid tests were performed under the assumption that the physical substructures exhibited no rate dependent behavior, and only the numerical substructure contained dynamic effects, such as viscosity and inertia. This assumption allowed the tests to be performed on an extended time scale. In this regard the technique is also referred to as pseudo-dynamic testing. As rate dependent devices, such as e.g. dampers, started to become a more integrated part of the infrastructure, the interest for testing rate dependent devices in hybrid testing started to grow. Effort to improve technology and replace the extended time scale by a true time scale was increased. This succeeded in the beginning of the 1990s where the first real-time test was reported. In this context the method is referred to as *real-time* hybrid testing (RTHT).

Since then the field of real-time hybrid testing has expanded tremendously, and still is. Today RTHT is e.g. used for testing of dampers, nonlinear reinforced concrete and frame structures, soil-structure interactions, offshore platforms and the concept has also been adopted in the aerospace and vehicle industry. The concept of hybrid testing is, however, still a field under development, with many challenges to be solved, before it can be fully integrated as a standard tool for engineering practice. One problem is related to the capacity of the numerical engine. As the concept improves, the requirement for improving the complexity and size of the numerical substructures grows simultaneously. However, computational speed limits the capacity, and only models with limited complexity can be included in real-time experiments today.

At the Technical University of Denmark (DTU), it is a declared ambition, within a short period of years, to be able to perform state of the art research when it comes to the development of methods and models in the analysis of composite materials and lightweight structures, such as e.g. wind turbine blades and airplanes. A key to fulfil the ambition is by use of hybrid testing. Therefore, DTU has decided to invest in facilities and equipment used to perform RTHT. Today, no such facilities exist. The present PhD project can be seen as a part of the RTHT implementation project at DTU.

The present chapter serves as a general introduction to the hybrid testing concept and to give the reader an overview of the some of the challenges in the field of RTHT. Furthermore the chapter will explain the context and objective of the given PhD project in more detail. A detailed list of references is not given in the present chapter, but will be introduced in the following chapters covering, among other things, the historic development and detailed theory behind RTHT.

1.1 Concept of Hybrid Testing

In the following the principle of hybrid simulation is explained in more detail. For the purpose an imaginary example, with a frame structure exposed to a ground acceleration, $\ddot{a}$, is considered, see Figure 1.1. The potential damage to the structure is minimized by installing a number of dampers, at the ground level, in order to dissipate the energy. To ensure that the dampers work as intended these are tested in a hybrid test.

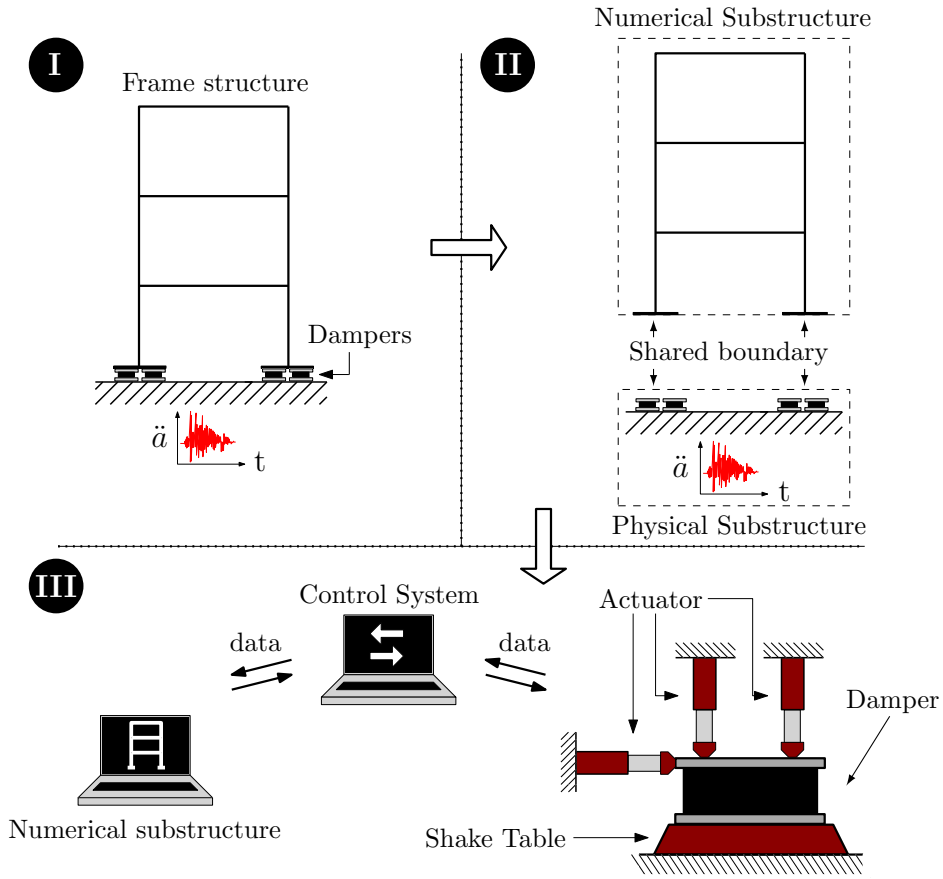

Figure 1.1: (I) Damped structure exposed to ground acceleration (II) is divided into substructures and (III) organized in a hybrid testing setup.

The substructuring technique is used to divide the structure in a numerical and physical substructure. The dampers usually display complex behavior, and these are therefore chosen to constitute the physical substructure, i.e. the structural part to be tested in a physical framework. The frame structure, on the other hand, displays known behavior, and its response can be modelled numerically, using FEM. Thus, this part of the structure constitutes the numerical substructure. A hybrid test setup is then organized,

by installing a set of actuators on each of the dampers at the contact surface between the numerical and physical substructures. In the present this is referred to here as the shared boundary. Three actuators are installed on the shared boundary each damper to be able to introduce translations in the horizontal and vertical directions combined with rotations. Furthermore, the ground acceleration is imposed by a shake table at the bottom. For the actuators and the numerical substructure to communicate, a control system is arranged.

The RTHT is then ready to be initiated. In Figure 1.2 is visualized the closed hybrid testing loop, with the coupling between boxes indicated by the arrows.

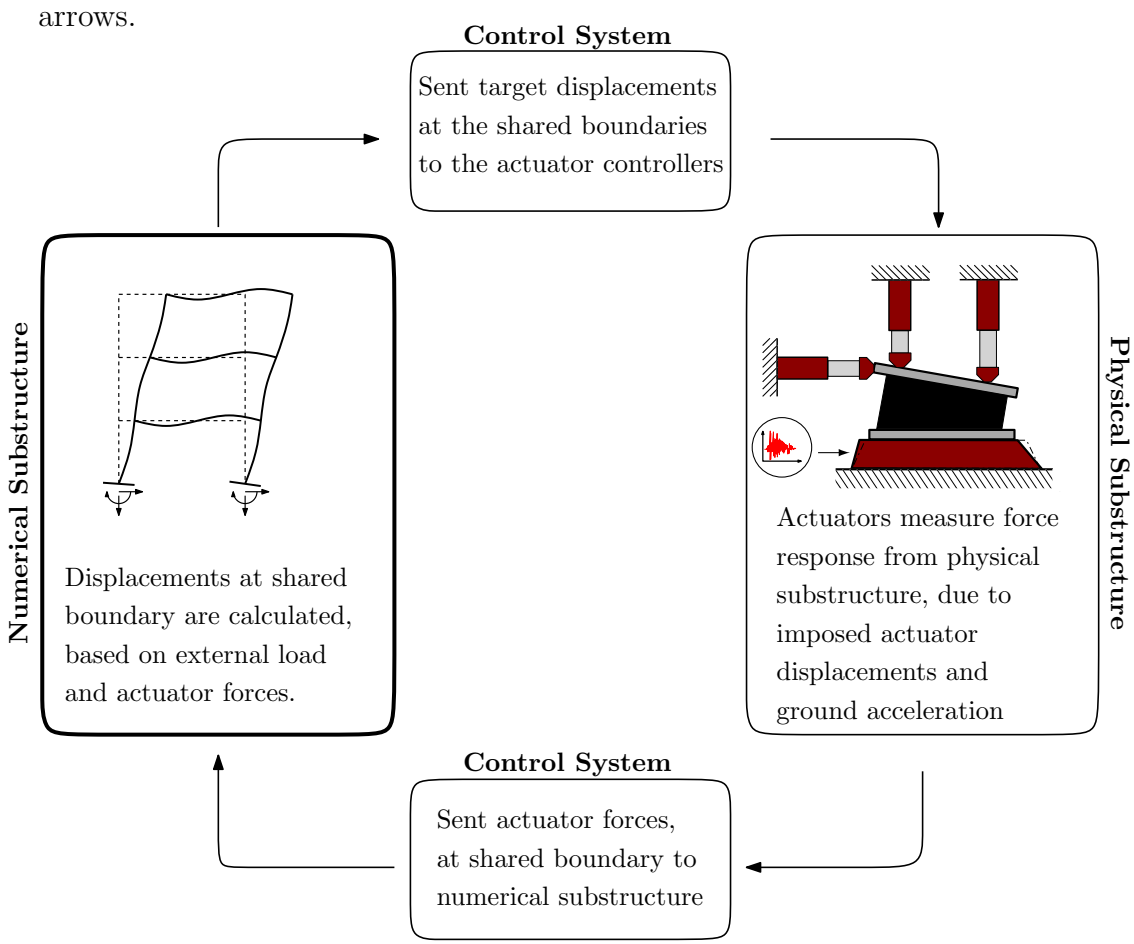

Figure 1.2: Hybrid testing loop.

The test is started by exposing the dampers to the ground acceleration, $\ddot{a}$. The actuators then measure the force response at the shared boundary through a load cell. The measured actuator forces are sent to the numerical substructure through the control system, and the response of the numerical

model is determined by use of a time integration scheme. The response displacements are also referred to as the target displacements. The rotations and translational displacements at the shared boundary of the numerical substructure are then sent back through the control system to a digital servo-controller, that controls the actuator motion. The displacements are then imposed onto the dampers by the actuators and the loop is ended. This loop is repeated until the test is finished.

In order to keep up with real time, each loop in Figure 1.2 has to be ended within single time step, Δt, corresponding to the time steps taken by the numerical model in each integration step. Typically the time steps applied in a real-time test are in the order of Δt=1-10 ms, see e.g. Chen et al. (2012). This is a strict requirement, which requires fast responding actuators and associated control system, an efficient computational model, and a fast interchange of data, to succeed.

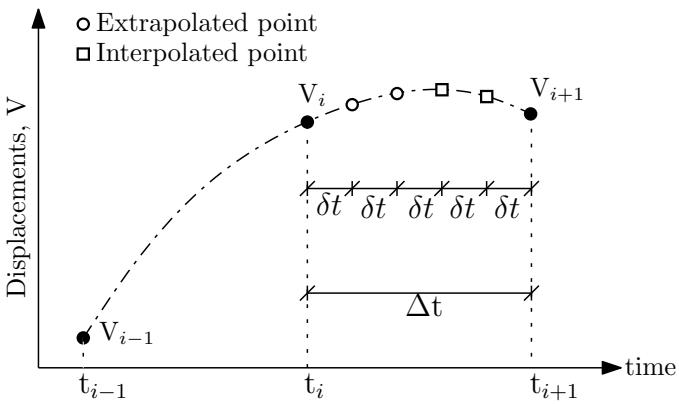

Figure 1.3: Displacements, V, evaluated by extrapolation and interpolation, are sent to the digital controller with time intervals δt.

To ensure that the actuators move continuously with a smooth velocity, the target displacements calculated in the numerical model have to be sent at the sampling frequency of the digital controller. To meet this demand each time interval, Δt, is divided into a number of sub steps, δt, see Figure 1.3. The displacements, V, at each sub step can be found from, respectively, extrapolation and interpolation between the numerically evaluated displacements, V_i and V_{i+1}, at the specific times t_i and t_{i+1}, see e.g. Nakashima and Masaoka (1999). The numerical calculation of the displacement V_{i+1} requires the actuators forces measured at time, t_i. Therefore, the displacements V_{i+1} will not be available from time t_i, and the initial displacements sent to the digital controller are evaluated through extrapolation of previous displacements. When the displacement V_{i+1} is calculated, the interpolation

can start. In Figure 1.3, the displacement V_{i+1} is known beyond the time t $= t_i + 2\delta t$.

As will be described in more detail in the end of the chapter, the main focus of the present work is on the numerical engine, enhanced by bold in Figure 1.2, with special emphasis on the computational time and cost. Therefore, further details of the various components in the hybrid simulation loop related to communication and the physical test, are not described in more depth in the present. For details of included hardware and communication software, the reader is referred to e.g. Waldbjoern et al. (2016).

1.2 Numerical Challenges in RTHT

The application of RTHT is rapidly growing, and the complexity and size of both the numerical and physical substructures increase. However, if this development should continue, many challenges need to be solved. In Marazzi et al. (2011) are listed some of the most obvious challenges which can limit the potential expansion of real time hybrid testing. The list is based on the outcome of the so called EFAST project from 2010, initiated by the European commission. Among the things related specifically to the numerical substructures, are mentioned:

- Increasing computation time for increased complexity
- Accuracy and efficiency of integration algorithms

Since the first real-time simulation was reported in the early 1990s, the numerical substructures have increased in both size and complexity. Initially small linear systems were considered. Rapidly, the complexity was increased by adoption of nonlinearities, and an increase in the degrees of freedom (DOFs) in the FEM models. However, when nonlinearities are included in the numerical simulations, the computational time is rapidly increased with the number of DOFs. To the best of the present authors knowledge, the capacity today, is about 500 DOFs, considering a material nonlinear frame structure with assumed bilinear constitutive behavior, cf. Chae et al. (2013). For this a specialized software was developed.

It is important to stress that the number of DOFs is not necessarily a direct measure for the complexity or accuracy of a numerical model. If highly advanced elements are used, few elements can be sufficient in some cases. On the other hand, if simple constitutive relations are applied, many DOFs can be needed to model even small size structures in a sufficient manner. So the amount of DOFs do not directly indicate the level of complexity and accuracy, but it can serve as a good indicator.

As will be accounted for in the following chapter, frame structures appear to comprise the most used type of numerical substructures applied in RTHT. When considering the global response of frame structures, with nonlinear constitutive relations as in Chae et al. (2013), then 500 DOFs can typically be considered to be a fairly large amount of DOFs for modest size structures. However, for three dimensional structures modelled with continuum elements, including nonlinear constitutive relations, the capacity of 500 DOFs can rapidly be exhausted, even for modest size structures. Thus, if such numerical substructures should be adopted in RTHT, more accurate and efficient time integration techniques and methods are required.

In the following an example illustrating the rapidly increasing computational time in kinematic nonlinear analysis, as a function of the number of DOFs, is given. Furthermore the reason for the rapid time increase is identified. The time integration techniques applied in the example are described in detail in chapter 3.

1.2.1 Computational Time - Example

A kinematic nonlinear beam exposed to a harmonic load, F(t), with excitation frequency, ω_e, is considered, see Figure 1.4. The beam is of length l, has a density ρ, a bending stiffness EI, and a relative damping ratio ζ. In Table 1.1 the parameter values are presented, selected such, that the first bending mode of the beam is $\omega_1 = 1$ rad/s. The beam is rigid supported at the left end and prevented from horizontal displacements at the right end.

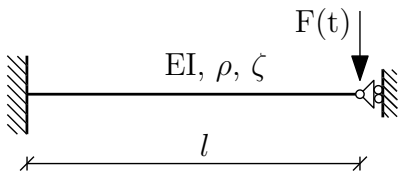

Figure 1.4: Kinematic nonlinear beam

Using FEM to analyse the beam, the governing equations of motion on discretized form, with assumed linear damping, are formulated as:

$$\mathbf{M}\ddot{\mathbf{V}} + \mathbf{C}\dot{\mathbf{V}} + \mathbf{g}(\mathbf{V}) = \mathbf{F}(t) \tag{1.1}$$

$\mathbf{M}$ and $\mathbf{C}$ are the mass and damping matrices, $\mathbf{g}(\mathbf{V})$ represents the internal restoring forces, $\mathbf{F}(t)$ is the external load dependent on time, $\mathbf{V}$ represents the displacement field and d()/dt = $\dot{()}$. For nonlinear systems the restoring forces are a nonlinear function of $\mathbf{V}$, whereas for linear systems it is given as the linear product $\mathbf{g}(\mathbf{V}) = \mathbf{K}\mathbf{V}$, where $\mathbf{K}$ is a constant stiffness matrix.

Table 1.1: Beam parameters.

Parameter	Unit	Magnitude
l	m	1
EI	Nm^2	$6.44 \cdot 10^4$
ρ	kg/m^3	7800
ζ	%	2
F_{max}	kN	644
ω_e	rad/s	1

Plane Euler-Bernoulli beam elements are used to model the beam. These are described in detail in Andersen and Poulsen (2015). In appendix A is presented a full analysis of the beam. Here, only the computational simulation time, t_{sim}, is considered. In Figure 1.5b is presented the relative simulation time spend on simulating three periods of the first bending modes in the range 14 DOFs to 59 DOFs. The relative time is defined as:

$$r = t_{sim}/t_0 \tag{1.2}$$

with t_0 representing a reference time. In the given case t_0 is chosen as the simulation time with 14 DOFs. The reference time, t_0, was 37 times larger in the nonlinear case compared to the linear case.

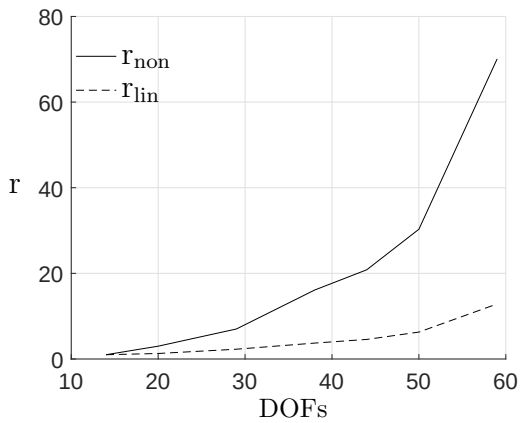

Figure 1.5: Simulation times, r, as a function of the number of DOFs.

Two curves are plotted in Figure 1.5 for comparison; the relative time based on the kinematic nonlinear beam, r_{non}, and a relative time, based on a linear version of the considered beam, r_{lin}. Both curves are found by use of the central difference method (CDM), which is en explicit time integration scheme. The relative simulation times are seen to be a nonlinear function of the DOFs. The r_{non} curve increases from a relative time of 1 to approximately

70, over the DOF range considered. The r_{lin} curve increases significantly less, going from a ratio of 1 to approximately 12. The increase in the simulation times are partly attributed to the fact that more equations have to be solved for an increasing number of DOFs. Furthermore, the simulation time was increased because the time steps had to be decreased for an increasing number of DOFs. Increasing the DOFs, higher frequencies are introduced, which calls for smaller time step magnitudes to keep stability. The same time step magnitudes were applied in the linear and nonlinear analysis.

The reason for the significant higher relative increase in the nonlinear analysis is due to the evaluation of the internal restoring forces, $\mathbf{g}(\mathbf{V})$. Due to the nonlinear formulation, these have to be evaluated element by element, after each time step, which is very time consuming. In Table 1.2 a prozentual division of the computational times are presented, when using the CDM and the implicit Newmark method with assumed average acceleration, to analyse the beam. The time is split in the element assembling (EA) time, covering the evaluation of $\mathbf{g}(\mathbf{V})$ and the tangent stiffness matrix $\mathbf{K}_T$, and the remaining tasks denoted 'Others', covering e.g. evaluation of residuals, prediction steps and solving the equations. The tangent stiffness matrix $\mathbf{K}_T$ is used for iterations in the implicit schemes, and also has to be assembled element-by-element after each time step.

Table 1.2: Relative computational times.

	14 DOFs		59 DOFs	
Integration Scehmes	EA	Others	EA	Others
CDM (Nonlinear)	**91** %	9 %	**94**%	6%
Newmark (Nonlinear)	**90** %	10 %	**96**%	4%
CDM (Linear)	**20** %	80 %	**28** %	72 %
Newmark (Linear)	**15** %	85 %	**13** %	87 %

From Table 1.2 it is obvious that the EA tasks constitute far most of the computational time in the nonlinear analysis, whereas it constitutes slightly less in the linear analysis. Furthermore, increasing the number of DOFs is seen to increase the relative EA task in the nonlinear integration. This development implies, that if the computational time should be reduced in kinematic nonlinear analysis, the element assembling task is a key component to consider.

Furthermore, in the given kinematic nonlinear analysis, 29 DOFs was the real-time limit with a time step magnitude of Δt=1 ms. This real-time DOF capacity will be used as a reference point in the given work.

1.3 Hybrid Testing at DTU

At DTU the ambition is to become experts in the development of methods and models for the analysis and design of composite materials and lightweight structures, such as wind turbines, bridge sections and airplanes. Today, design of large scale composite structures is performed by wind turbine and aerospace industries. However, a frequent amount of failures still appear in e.g. wind turbine blades, due to an incomplete understanding of the very complex composite behavior. A way to improve testing and gain more knowledge in the field of composite materials and lightweight structures, is by use of hybrid simulation.

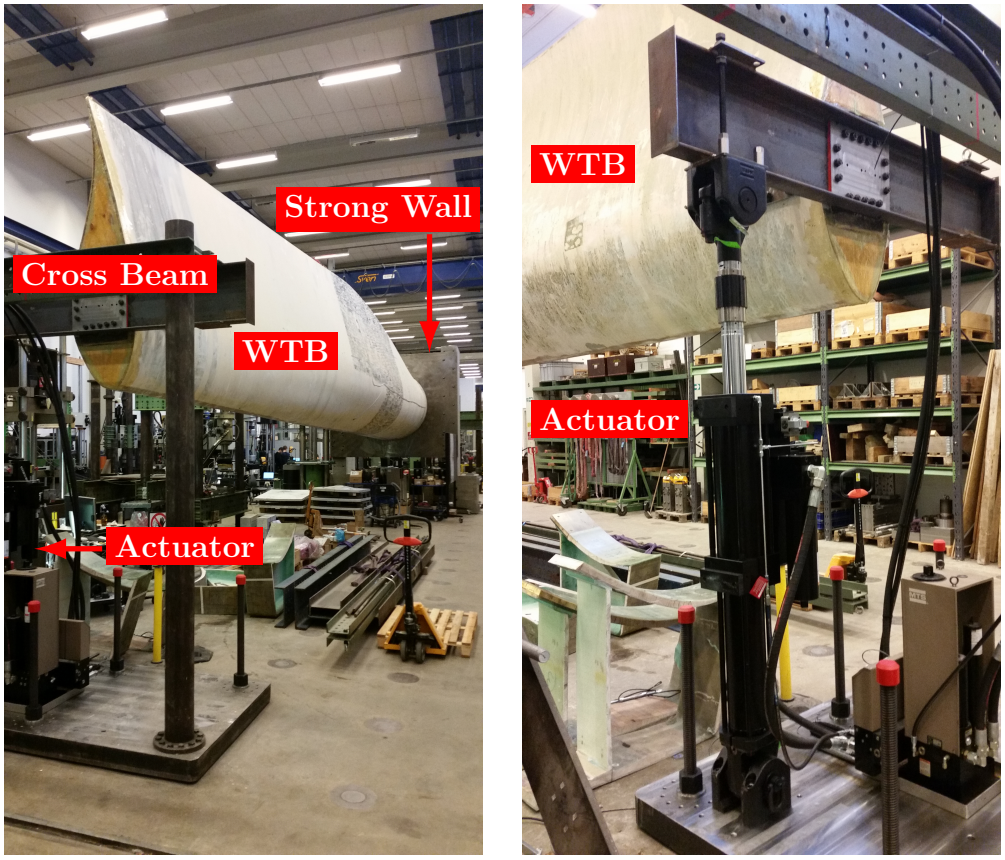

Figure 1.6: Wind Turbine Blade installed at a beam support by a 250 kN actuator, DTU Civil Engineering, January 2016, DTU Byg.

In 2012 DTU applied the Villum Fond for 10 million euro, with the proposal to establish a center for mechanical testing and materials. The application was made through a collaboration between three DTU departments;

The Department of Civil Engineering, Department of Mechanical Engineering and Department of Wind Energy. The purpose of establishing the center is to support the need for multi-scale experimental research in Danish as well as in international engineering, covering micron scale to large scale, with the latter including hybrid testing.

In 2014 the money were granted from the Villum Fond, and DTU has started the project. Out of the full grant, approximately 3 million euro are ear marked to establish the hybrid testing facilities, where most of the money are intended to be invested in so called strong floors and strong walls, used for organizing the physical test setup, and furhtermore actuators, hydraulic supply systems and advanced measuring systems. Part of equipment has been bought and is in its implementing phase. In Figure 1.6 is shown a 15 m long section of a SSP wind turbine blade, with a normal full length spanning 34 m. The blade root is installed on a so called strong wall, and a cross beam with single actuator is installed at the other end. The actuator is one of the investments made by use of the funding, and has a load capacity of 250 kN. In Figure 1.7 a close up on the WTB root on the strong wall is shown from two different angles.

Figure 1.7: Installation of Wind Turbine Blade Root on Strong Wall, January 2016, DTU Byg.

In connection with the hybrid testing investment plans at DTU, Danish Centre for Composite Structures and Materials for Wind Turbines (DCCSM) has started a project at DTU with focus on implementing wind turbine testing in RTHT. The purpose of the project is to test wind turbine blades and study e.g. the global response including the impact of local phenomena such as interlaminar buckling and fracture, with complex load application. Local effects such as interlaminar buckling and fracture can be difficult to model and, therefore, hybrid testing is an ideal tool for such tests.

1.4 Objective and Structure of the Thesis

The present PhD project constitutes one out of a number of PhD projects on DTU, started on the initiative of DCCSM. The overall objective for DCCSM is to implement the required facilities at DTU Civil Engineering Test Facilities, to be able to perform RTHT on wind turbine blades. Each of the PhD projects contribute to different areas of the hybrid testing facility implementation, such as; improving sensor technology used to measure and detect data from the physical substructure such as response and local failure mechanisms, improvement of actuator displacements, and an extension of present available software programs to handle real-time hybrid simulations. Focus of the present PhD project is on the numerical substructures.

As previously discussed, todays computational speed allows nonlinear numerical substructures of dimension 500 DOFs to be included in real-time hybrid tests, when using specialized software for the purpose. For frame structure like models this can in many cases be sufficient, but if e.g. complex three dimensional structures should be included, such as in e.g. wind turbine modeling, the available capacity can rapidly be exhausted. A demand for improving the complexity of numerical substructures therefore exist. The object of the present PhD project is related to the numerical capacity, and is stated as:

Objective of PhD project:
To improve the accuracy of kinematic nonlinear numerical models, in real-time simulations, by use of mathematical models and methods.

To improve the accuracy, special emphasis has been on projection based reduction methods, which is a mathematical way to sort out some of the less important content of large numerical models. If a reasonable basis is chosen, this is a very efficient tool to obtain accurate simulations with a significant reduction in computational time. Said in another way, basis reduction can be a clever way to utilize the available computational capacity, if the right basis is applied. As will be accounted for in chapter 2 only little emphasis has been given to the use of basis reduction in hybrid testing context so far.

Furthermore, kinematic nonlinearities are taken as the focus area. In composite materials both material and kinematic nonlinearities are important. However, in RTHT litterature, kinematic nonlinearities have been paid significantly less attention, than material nonlinearities. Thus, emphasis was chosen to be on the kinematic nonlinearities.

It is important to stress, that it is not within the scope of the present

project to increase the accuracy by improving the given hardware or by organizing specialized software with adoption of special programming languages or programming strategies. Focus is on improving the accuracy with the given computational capacity as a reference point. To have a comparable reference to evaluate the contribution of the present work, the real-time capacity of 29 DOFs reported in the example in section 1.2.1, is used.

The present dissertation presents the work conducted over the three years PhD period, and consist of 7 chapters followed by four appended papers. The appended papers present the essential results of the work with detailed analysis and discussion hereof. The preceding chapters serve as a introduction and background to hybrid testing. Furthermore, the chapters present and sum up on the methods applied and developed and the results achieved in the PhD study. In more detail:

In **Chapter 2** a brief historical survey of hybrid testing is given. A view on the development of hybrid testing since its introduction in the 1960s is considered, with special emphasis on the development of the numerical capacity, after the introduction of real-time tests in the 1990s.

In **Chapter 3** time integration in hybrid testing context is considered. Some of the most obvious challenges in the real-time time integration are discussed, and different existing time integration schemes and methods are presented.

In **Chapter 4** the concept of projection based reduction methods are presented, and a discussion of the most important modes to include in the basis, when considered kinematic nonlinear systems, is given. Furthermore three elements, which can help to improve the accuracy of real-time simulations, are presented. The three elements constitute the major research contributions of the present PhD study.

In **Chapter 5** the use of reduction methods in hybrid testing is discussed. Furthermore, a real-time hybrid test performed at DTU Byg, December 2015, is presented. The results are discussed, and potential improvements to the test are suggested.

In **Chapter 6** potential future research activities in the field of hybrid testing, with reference to the presented research elements, are briefly discussed.

In **Chapter 7** the findings of the numerical work are summarized and the work is concluded.

Chapter 2

History of Hybrid Testing

In the present chapter a brief historic survey of hybrid testing is presented, with focus on some of the significant steps made towards what is known as today's conventional real-time hybrid testing. Furthermore, the development of the size and complexity, of the numerical substructures, is considered.

Historic reviews of the hybrid testing are given in e.g. Saouma and Sivaselvan (2008) and Carrion and Spencer Jr. (2007). These have been used, among others, as support in the present PhD study to get an overview of the historic development.

2.1 Introduction of Hybrid Testing

The concept of hybrid simulation was initially introduced by Japanese researchers in the 1960s, cf. **Hakuno et al. (1969)**. A single dof (SDOF) structure, loaded by an electromagnetic actuator, was considered under seismic loading, and the belonging equation of motion (EOM) was solved by use of an analog computer. With the introduction of the hybrid testing concept, a potential future alternative to the use of shake table testing of seismic loaded structures, was introduced.

In the 1970s **Takanashi et al. (1975)** improved the accuracy of hybrid simulation by replacing the analog computer with a digital computer. Furthermore, the actuator loads were introduced on an extended time scale, using a so called ramp and hold method, characterized by shifting between imposing a load increment and taking a hold. Today, this type of load application is considered as the conventional pseudo-dynamic (PsD) testing approach.

Since the work of Hakuno et al. (1969) and Takanashi et al. (1975) the field of hybrid testing has developed significantly. Up untill the 1990s the

majority of the development within the field of hybrid testing was performed mainly in Japan and the United States. In Takanashi and Nakashima (1987), Mahin et al. (1989), and Shing et al. (1996) a summary of some the the work performed in these countries, is given. In the beginning of the 1990s hybrid testing started to receive a growing interest in other parts of the world, such as Europe and Asia, see e.g. Donea et al. (1996) and Chang (1998).

Various branches of the conventional pseudo-dynamic testing have developed since its introduction in order to improve the test method. A step in the direction of the later introduced real-time PsD testing was introduced with the so called continuous pseudo-dynamic testing by **Takanashi and Ohi (1983)**. The ramp and hold method, applied for the actuator loading, was replaced by a continues applied loading. In the given work a dynamic actuator was used for the purpose and tested on a SDOF beam structure supported by two columns. The initial idea for introducing a continues loading, was to remove the potential effect from force relaxation of the considered structure during the hold periods of the actuator. With the introduction of the continues pseudo-dynamic testing the possibility to perform fast hybrid simulations was introduced. However, due to computational speed limitations, only experiments on a time scale larger than one could be executed at this point.

Another significant contribution to the field came with the introduction of the substructure technique in PsD testing in the 1980s by **Dermitzakis and Mahin (1985)**. The substructure technique made it possible to test only the structural part displaying complex behavior in a physical configuration, whereas the structural parts displaying well known behavior, could be modelled numerically. Since its introduction, the substructure technique has been extensively applied, and it is considered to be a more or less implicit part of the hybrid testing concept today. In Bursi and Wagg (2008) a more in depth description on the development and the use of the substructure technique is given in pseudo-dynamic context as well as in real-time context.

2.2 Real-time Hybrid Testing

In the beginning of the 1990s an important milestone in the history of hybrid testing was reached. **Nakashima et al. (1992)** reported the first system capable of performing a pseudo-dynamic test in real time using a digital computer. In the given case a building, installed on top of rubber bearings and a viscous damper, was considered. The substructure technique was applied, and the superstructure, including the rubber bearings, was taken as the numerical substructure, and the viscous damper as the physical substructure

loaded by a dynamic actuator. The key elements to succeed with performing a real-time experiment, were improved displacement and velocity control of the actuators, and the use of staggered time integration. The actuator displacement and velocity were improved by installing a digital servo-mechanism between the computer and the actuator servo-controller, which frequently checked and corrected, if necessary, the actuator movement. Furthermore, time integration based on the even ad odd time states were applied, using the central difference method. In this way the data needed to predict the displacement at time t_{n+1} was already available from the time t_{n-1} and could be determined before the time t_n. Thus, the actuators did not have to hold for a predictor displacement to be determined at the end of each time step, and could instead sustain a continues movement. However, due to limited computational speed, large time steps of magnitude Δt=20 ms had to be applied, and only a numerical SDOF substructure was considered.

Since the first reported real-time simulation reported by Nakashima et al. (1992) an extensive amount of work in the field has been made and many real-time tests have been reported. However, in the strive for improving and expand the size and complexity of the structural systems considered in real-time hybrid testing, many new challenges have been met. Especially issues in the domain of control and communication have received extensively attention.

One such field is time delays. These are an inevitable issue in real-time testing, and has to be properly compensated to obtained accurate experimental results. **Horiuchi et al. (1996)** considered the effect of actuator time lag, i.e. the delay by which the displacement imposed by the actuator on the shared boundary. It was demonstrated, for a linear SDOF system, that actuator lag corresponds to introducing negative damping into the system.

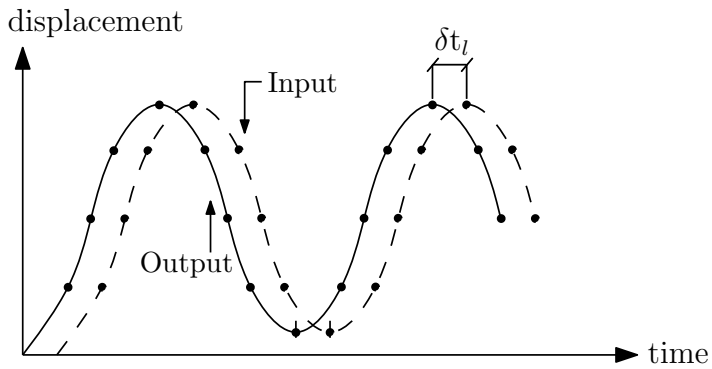

Figure 2.1: Actuator input displacement field compensated by shifting it a time step, δt_l, ahead of the actual calculated displacement field.

To compensate for the time lag it was suggested to predict the actuator input displacements a time step ahead, corresponding to the actuator time lag, δt_l, see Figure 2.1. In this way the correct actuator output displacements would be imposed onto the structure. For the input prediction, a polynomial based on n previous calculated values was applied. The effect was promising, and extrapolation has been widely since, see e.g. Darby et al. (2002), Wu et al. (2006b) and Chae et al. (2013).

Another challenge in expanding the real-time testing, lies in the limitation of the numerical capacity. Since the first real-time test, the numerical models have increased in both size and complexity. However, as opposed to the communication and control domain, the numerical aspects have received less attention.

In Figure 2.2 the development of the amount of DOFs applied in RTHT, based on a selection of work ranging from the introduction of RTHT in 1992 up until today, is sketched. The development is seen to be increasing, starting with a linear SDOF numerical substructure in 1992 to nonlinear numerical substructures containing more than 500 DOFs today. However, a demand for being able to increase the DOF capacity, and thereby increase the complexity, still exist.

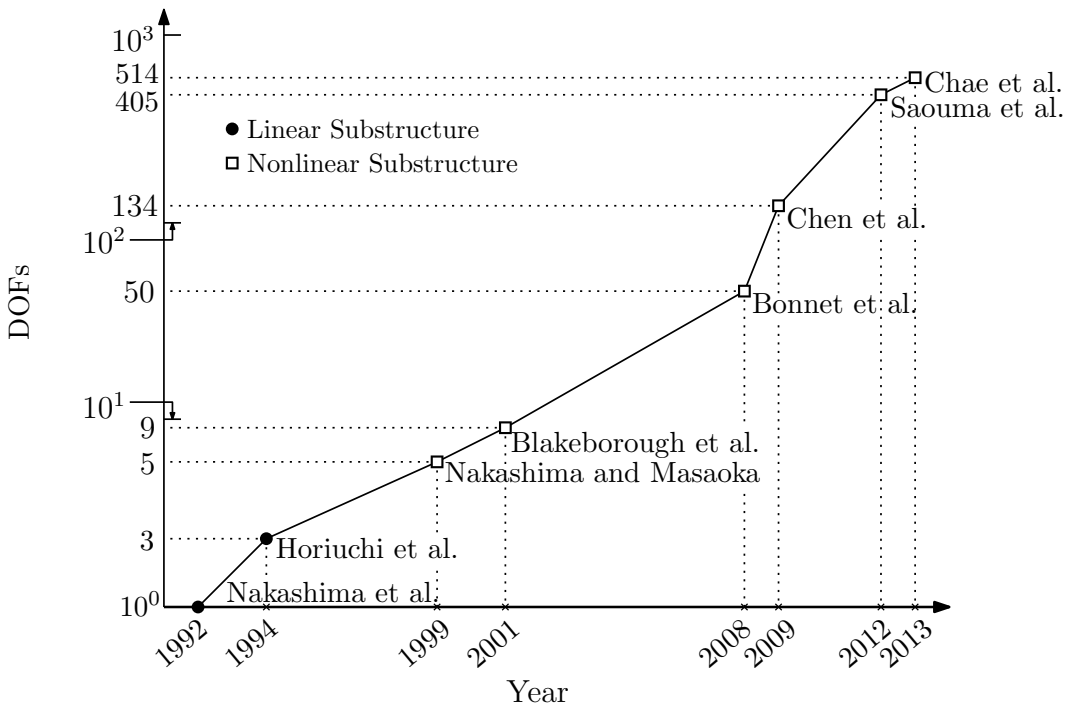

Figure 2.2: Development of the real-time DOF capacity in numerical substructures since the introduction of real-time simulation, plotted on a logarithmic scale.

The initial attempts made to improve the numerical capacity focused on improving the applied technology. **Horiuchi et al. (1994)** introduced a new real-time system including parallel programming and a new programming language, all to improve the computational speed. Significant increase in speed was reported, with one iteration cycle executed in 0.5 ms. With the new system, real-time simulations with linear numerical substructures, containing up to three DOFs, were successfully conducted.

Nakashima and Masaoka (1999) came up with an improved edition of the system applied in Nakashima et al. (1992), characterized by adoption of the C language to improve the flexibility of the programming and the use of digital signal processors, both to improve the computational speed and capacity. Furthermore extrapolation, interpolation and compensation techniques for various time delays were included to obtain accurate displacements and velocities. To test the real-time capabilities of the improved system, a multi-storey building, with four rubber bearings installed at the bottom, was considered. The multi-storey building was modelled numerically, with each floor represented by a lumped mass, connected to the neighbor floors by shear springs. The rubber bearings formed the physical test setup with one DOF in the common interface between the substructures, represented through a single actuator. It was found that in case the numerical substructure was represented by a linear model, the system could handle 12 DOFs in real time. To test the capability in a nonlinear context, the constitutive relations of the springs were assumed to be described by a bilinear curve, formulated as a sum of multiple bilinear curves to increase the computational demand. With a time step of 10 ms and ten sub steps, the system was able to run a 5 DOF nonlinear substructure with the constitutive relations described by a total sum of 150 bilinear relationships.

In the beginning of the new millennium **Darby et al. (2001)** and **Blakeborough et al. (2001)** suggested the use of basis reduction to improve the numerical capacity. The benefit of using a basis reduction is, that for linear systems, choosing a linearly independent basis, the EOM are decoupled. Furthermore the higher frequency modes, which do not represent physics well, can be removed, and at the same time improve the stability of the system.

Darby et al. (2001) used the approach to purely linear numerical substructures, whereas Blakeborough et al. (2001) extended to concept to consider material nonlinear substructures. For the nonlinear structural analysis a Ritz basis, consisting of linear modes and plastic deformation vectors, was applied. The plastic deformation vectors were determined from a nonlinear static analysis of the structure considered, where a load was continuously increased in order to raise the number of yield points. The deformation patterns at the various yield stages were subtracted from each other and

represented a set of plastic vectors. However, high natural frequencies were associated with the plastic vectors. To be able to keep a small time step, and avoid instability, the frequencies were artificially decreased. The basis was verified by running a numerical test on a cantilever beam with an additional support at the 'free' end. Furthermore, a real-time hybrid simulation of a simple portal frame with material nonlinearities, modeled with bi-linear constitutive relations, was analysed. The frame was exposed to the El-Centro earthquake record, and was executed by using a time step of 25 ms. The numerical part of the simple frame was initially modelled with 50 DOFs. A basis consisting of nine modes, with three linear modes and six plastic modes, was used for the analysis. The results were not verified against other models or measurements, but it was concluded that the method was encouraging, but needed additional work to be improved.

One of the major focuses for improving the numerical accuracy, speed and complexity has been on investigating and improving various time integration techniques and methods. The ideal integration algorithm for hybrid testing would be an algorithm with unconditional stability, high precision and the ability to perform a fast execution. The idea of possessing such a scheme has motivated a number of researchers to put an effort in developing explicit like algorithms with unconditional stability. In **Chang (2002)** an explicit scheme, referred to as the Newmark-Chang algorithm, was organized by introducing two weighting parameters, $\boldsymbol{\beta}_1$ and $\boldsymbol{\beta}_2$ in the predictor displacement equation of the explicit Newmark scheme, see (2.1).

$$\mathbf{V}_{i+1} = \mathbf{V}_i + \boldsymbol{\beta}_1 \Delta t \dot{\mathbf{V}}_i + \boldsymbol{\beta}_2 \Delta t^2 \ddot{\mathbf{V}}_i \tag{2.1}$$

The weighting parameters were based on the initial stiffness of the system, and remained constant throughout the time integration. With the chosen parameters, the properties of the scheme were shown to be identical with those in the constant average acceleration method, i.e. with unconditional stability, good precision and a low error propagation. Later, in **Chang (2010)** a further analysis of the algorithm properties of the scheme were examined in a nonlinear context. Here it was shown that only in case of softening behavior, i.e. for at decreasing tangent stiffness, unconditional stability is achieved, while for stiffness hardening structures, the algorithm is conditionally stable.

Nakashima et al. (1990) suggested to use the so-called operator-splitting method (OSM). The method builds on the key assumption, that the nonlinear restoring force of a system can be split in a nonlinear part and a linear part, respectively. The nonlinear part is the restoring forces based on the predictor displacements, $\mathbf{V}^*$, and the linear part is a corrector term given as a stiffness, $\mathbf{K}$, times the difference between the predictor displacements and

the corrector displacements, $\mathbf{V}$, see (2.2).

$$\mathbf{g} \approx \mathbf{g}(\mathbf{V}^*) + \mathbf{K}(\mathbf{V} - \mathbf{V}^*) \tag{2.2}$$

By introducing the assumption in (2.2) in an implicit scheme, iterations can be avoided. In Nakashima et al. (1990) the OSM was introduced into α-modified Newmark scheme, introduced by Hilber et al. (1977). The method showed to be unconditionally stable for softening-behaving structures.

In **Wu et al. (2006a)** it was argued that the OSM was implicit in case of nonlinear damping. To make the OSM explicit in both displacement and velocity in case of nonlinear damping, a predictor velocity was introduced together with a damping force increment proportional to the difference between the predictor velocity and the target velocity, see (2.3).

$$\mathbf{g} \approx \mathbf{g}(\mathbf{V}^*) + \mathbf{K}(\mathbf{V} - \mathbf{V}^*) + \mathbf{C}(\dot{\mathbf{V}} - \dot{\mathbf{V}}^*) \tag{2.3}$$

In **Bonnet et al. (2008)** the OSM, the Newmark-Chang algorithm, and four other widely used integration schemes, were compared and evaluated in a nonlinear real-time hybrid simulation context, with focus on, among other things; stability, accuracy and computational efficiency. Two of the integration schemes considered were explicit, and represented the explicit Newmark method and the Newmark-Chang method. Furthermore, the constant average acceleration method and the α-modified version were implemented in full implicit form. The last two schemes considered, were the OSM incorporated in the average acceleration method and the α-method.

To test the various integration methods in a real-time context, a series of masses connected by material nonlinear springs, characterized by strain-hardening ratio of 0.5, were considered. The physical substructure represented a single mass exposed to a sinusoidal load, imposed by an hydraulic actuator. Furthermore, the numerical and physical substructures were connected through a single DOF.

To be able to apply the two fully implicit schemes for nonlinear systems, a so-called sub-step feedback strategy was introduced, where the nonlinear forces were written as a sum of a linear contribution plus an additional nonlinear increment. The increment was divided in sub-steps, and required a frequent feedback from the physical substructure. However, due to the sub-step feedback approach, the implicit schemes required the highest computational demand, and showed the poorest results, DOF wise. It was only possible to run a nonlinear substructure including 20 DOFs.

The remaining four schemes however, were capable of simulating a 50 DOF system with time steps in the range 5 - 25 ms. The explicit Newmark scheme exhibited the highest precision and stability, and was concluded to

be the preferred scheme. The Newmark-Chang, the OSM and the α-OSM also showed high precision and stability, but the former was a little more efficient. Furthermore, the α-OSM was recommended in case high frequency content should be removed.

In **Chen and Ricles (2008)**, **Chen et al. (2009)** and **Chen et al. (2012)** yet another integration algorithm, denoted the CR algorithm, was presented and tested in a real-time hybrid simulation context. The CR algorithm is an explicit scheme in both displacement and velocity. By using a target displacement and target velocity with weighting parameters chosen by use of a pole mapping technique from discrete control theory, the algorithm was made unconditional stable for linear analysis. Furthermore the CR algorithm was reported to have the same accuracy, in terms of equivalent damping and period elongation, as the constant average acceleration method. To examine its real-time potential in nonlinear cases, a three-storey frame with an elastomeric damper installed at the bottom floor was considered. The frame was assumed to exhibit a material non-linear behavior, characterized by the Bouc-Wen model, and was modelled by membrane, beam and truss elements. The damper was taken as the physical substructure coupled by 3 DOFs to the numerical frame structure. A successful real-time hybrid simulation with stable and accurate results was executed with a time step in the order of 10 ms. In the given case the capacity was reported to be 134 DOFs. Furthermore the algorithm was shown to be unconditionally stable in the case of softening behavior, but conditional stable for hardening behavior.

In recent years the increase in the DOF capacity is mainly attributed to an increasing available computational speed and more flexible software with improved programming strategies. In **Saouma et al. (2012)** a specialized software, called Mercury, was developed with main emphasis on improving the real-time capacity in or to be able to consider highly nonlinear reinforced concrete members. The simulation software was developed in both a MATLAB version and a C++ version, with the latter used for real-time applications. Two dimensional beam flexibility elements and stiffness based beam elements were included in the implementation. Different constitutive models were implemented for the steel and concrete. Classic isotropic and kinematic hardening models were applied for the steel, and modified Kent-Park models were used for the concrete. To model reinforced concrete an innovative anisotrpic damage based element was applied. Furthemore, to improve the evaluation of the restoring forces, which is one of the heaviest task as discussed in chapter 1, a multi-threading of the code was organized, which greatly improved the speed. The code was capable of simulating a 405 DOF steel reinforced concrete frame connected by 3 DOFs in the shared boundary to a physical substructure made up by a reinforced concrete col-

umn. For the purpose, an implicit time integration strategy introduced by Shing et al. (2004) using a fixed numbers iterations was adopted. In the given case ten iterations and a time step of 10 ms were used.

In **Chae et al. (2013)** another specialized software, called HybridFEM, was used by to test an actuator compensation scheme in a real-time context. A three story steel frame with a viscous damper installed at the third floor was considered for the real-time validation. The damper was taken as the physical substructure and the remaining frame structure as the numerical substructure. The explicit CR algorithm by Chen and Ricles (2008) was applied using a time step of magnitude 10/1024 s, with ten sub steps. The numerical substructure was modelled by so called distributed plasticity displacement-based beam-column fiber elements with five fiber sections along each element. The fibers were assumed to have a bilinear stress-strain relationship, with a strain-hardening ratio set to 0.01. Furthemore, nonlinear panel zone elements were applied to model joints and a single column was modelled wtih kinematic nonlinear elements. The test was successfully performed with a total of 150 elements representing 514 DOFs, which constitutes the highest amount of DOFs applied in a nonlinear substructure today.

Chapter 3

Existing Time Integration

The present chapter focus on time integration in numerical simulations. First the general principles behind time integration are presented, with the Newmark method as point of reference. For this, the work of Krenk (2009), Cook et al. (1974) and Chopra (1995) has been used as inspiration. Next the use of time integration in a hybrid testing context is considered. The the pros and cons of using implicit and explicit integrations schemes are discussed, and a number of examples on methods implemented for real-time hybrid testing experiments are presented. The chapter is ended with some concluding remarks, arguing for the choice of time integration methods used in the present PhD study.

3.1 Time Integration

The global EOM, on temporally discretized form at the specific time t_i, are considered:

$$\mathbf{M}\ddot{\mathbf{V}}_i + \mathbf{q}\left(\mathbf{V}_i, \dot{\mathbf{V}}_i\right) = \mathbf{F}(t_i) \tag{3.1}$$

$\mathbf{V}$ is the displacement vector, $\mathbf{M}$ represents the mass matrix, $\mathbf{F}$ is the external load vector, $\mathbf{q}(\mathbf{V}_i, \dot{\mathbf{V}}_i)$ represents the internal force vector of the system and $\dot{()} = d()/dt$.

Numerical time integration of the EOM is applied when the dynamic problems become large or complex. The aim of the integration is to determine the state of the system at the specific time $\mathrm{t}_{i+1} = \mathrm{t}_i + \Delta t$ by use of the state at the previous times t_i, t_{i-1}, ..., and the loading over the interval Δt, see Figure 3.1. In some integration methods, also the state at the time t_{i+1} can be included in an iterative approach. The standard methods applied in time integration are the so called collocation-type methods, where the equations

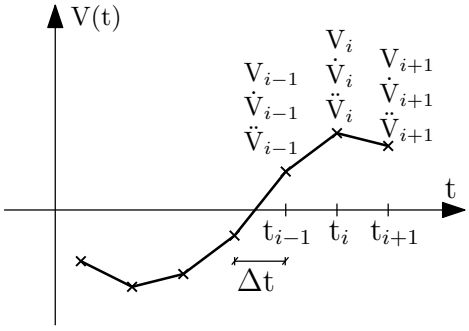

Figure 3.1: Displacement history.

of motion in (3.1) is fulfilled at selected points in time, cf. Krenk (2009). As the displacements, velocities and accelerations comprise three unknowns, three set of equations are required to evaluate these. In addition to the EOM, a suitable relationship between the displacements, velocities and acceleration are assumed. These are typically given a set of Taylor approximations.

One of the most applied time integration schemes, is the Newmark method, cf. Newmark (1959). Here the displacements, velocities and accelerations are at the specific times t_i and t_{i+1} are related by the expressions:

$$\mathbf{V}_{i+1} = \mathbf{V}^*_{i+1} + \Delta t^2 \beta \ddot{\mathbf{V}}_{i+1} \tag{3.2}$$

$$\dot{\mathbf{V}}_{i+1} = \dot{\mathbf{V}}^*_{i+1} + \Delta t \gamma \ddot{\mathbf{V}}_{i+1} \tag{3.3}$$

where $()^*$ denote the predictor terms, which are defined as

$$\mathbf{V}^*_{i+1} = \mathbf{V}_i + \Delta t \dot{\mathbf{V}}_i + \Delta t^2 (\frac{1}{2} - \beta) \ddot{\mathbf{V}}_i \tag{3.4}$$

$$\dot{\mathbf{V}}^*_{i+1} = \dot{\mathbf{V}}_i + (1-\gamma) \Delta t \ddot{\mathbf{V}}_i \tag{3.5}$$

with the weighting parameters β and γ.

When thinking of time integration methods, these are often divided in two categories; explicit and implicit schemes. Implicit schemes usually require iterations in nonlinear context, whereas explicit schemes do not. This allows explicit schemes to proceed faster from one state in time to the next. However, the time step magnitude is usually required to be much smaller in explicit schemes, in order to remain the stability and accuracy of the algorithm. Based on the choice of parameter values of β and γ, the Newmark method offers both implicit and explicit versions.

In case a linear system is considered, the internal force vector in (3.1) is given as:

$$\mathbf{q}(\mathbf{V}_i, \dot{\mathbf{V}}_i) = \mathbf{C}\dot{\mathbf{V}}_i + \mathbf{K}\mathbf{V}_i \tag{3.6}$$

where $\mathbf{C}$ and $\mathbf{K}$ are constant damping and stiffness matrices.

With (3.6) the approximate displacements in (3.2)-(3.3) can be introduced into the EOM in (3.1) at time t_{i+1}, and a linear expression in $\ddot{\mathbf{V}}_{i+1}$ is found. Evaluating $\ddot{\mathbf{V}}_{i+1}$, the displacements and velocities can be determined by use of (3.2)-(3.3), and one can proceed on to the next time step.

In case, the internal force vector is a nonlinear function on the displacements and velocities, an iterative solution on the residual, $\mathbf{r}_{i+1}$, is required. The residual is defined as:

$$\mathbf{r}_{i+1} = \mathbf{F}(t_{i+1}) - \mathbf{M}\ddot{\mathbf{x}}_{i+1} - \mathbf{q}(\mathbf{x}_{i+1}, \dot{\mathbf{x}}_{i+1}) \tag{3.7}$$

In Newton iteration the linearized increment, $\delta\mathbf{r}_i$, of the residual is considered

$$\mathbf{r}_{i+1} + \delta\mathbf{r}_{i+1} + ... = \mathbf{0} \tag{3.8}$$

with the dots indicating the higher order increments. These higher order terms are not needed, as only linear equations can be solved anyway.

The linearized increment in the residual, can be expressed as an increment in the displacements, $\delta\mathbf{V}_i$, velocities, $\delta\dot{\mathbf{V}}_i$, and accelerations, $\delta\ddot{\mathbf{V}}_i$, as

$$\delta\mathbf{r}_i = \left(\frac{\partial\mathbf{r}_i}{\partial\mathbf{V}_i}\delta\mathbf{V}_i + \frac{\partial\mathbf{r}}{\partial\dot{\mathbf{V}}_i}\delta\dot{\mathbf{V}}_i + \frac{\partial\mathbf{r}}{\partial\ddot{\mathbf{V}}_i}\delta\ddot{\mathbf{V}}_i\right) \tag{3.9}$$

From (3.2) and (3.3) the displacement, velocity and acceleration increments in (3.9) are related by the expressions:

$$\delta\mathbf{V}_i = \Delta t^2\beta\delta\ddot{\mathbf{V}}_i \tag{3.10}$$

$$\delta\dot{\mathbf{V}}_i = \Delta t\gamma\delta\ddot{\mathbf{V}}_i \tag{3.11}$$

Introducing the expression (3.9)-(3.11) into (3.8) a linear form for evaluation of the displacements increment is found

$$\mathbf{K}^*\delta\mathbf{V} = \mathbf{r} \tag{3.12}$$

where $\mathbf{K}^*$ is denoted the modified tangent stiffness matrix, formulated as

$$\mathbf{K}^* = \mathbf{K}_T(\mathbf{V}) + \frac{\gamma}{\beta\Delta t}\mathbf{C} + \frac{1}{\beta\Delta t^2}\mathbf{M} \tag{3.13}$$

with $\mathbf{K}_T(\mathbf{V})$ representing the tangent stiffness matrix, which is a nonlinear function of $\mathbf{V}$. Evaluating the incremental displacement $\delta\mathbf{V}$ from (3.12), the state of the system can be updated by use of (3.10)-(3.11)

$$\mathbf{V}_{i+1} = \mathbf{V}_{i+1} + \delta\mathbf{V}_{i+1} \tag{3.14}$$

$$\dot{\mathbf{V}}_{i+1} = \dot{\mathbf{V}}_{i+1} + \frac{\gamma}{\beta\Delta t}\delta\mathbf{V}_{i+1} \tag{3.15}$$

$$\ddot{\mathbf{V}}_{i+1} = \ddot{\mathbf{V}}_{i+1} + \frac{1}{\beta\Delta t^2}\delta\mathbf{V}_{i+1} \tag{3.16}$$

By use of (3.7), (3.12) and (3.14) - (3.16) an iterative process can be carried out, until the residual in (3.7) is below a chosen tolerance.

In the following the pros and cons of using implicit and explicit schemes, in relation to hybrid testing, are discussed. Furthermore, a more in depth description of some of the time integration methods and approaches adopted in RTHT, are presented. All of these build on the Newmark method presented here.

3.2 Time Integration in Hybrid Testing

Time integration constitutes a vital element in hybrid testing with stability, accuracy and computational speed as the key points for obtaining success. Accuracy and stability are desirable properties for obvious reasons. However, in case real-time testing is desired, computational speed is just as important as the former two mentioned key points. As discussed in relation with the RTHT loop in Figure 1.2, the actual simulation time, $\Delta \mathrm{t}_a$, spent on simulation each time step, has to be less than the length of the simulated time step, Δt. Thus, a real-time criteria is:

$$\Delta t_a < \Delta t \tag{3.17}$$

If not the real-time requirement in (3.17) is fulfilled, errors are introduced into the hybrid test, and strategies to make up for the these are then needed. However, in case path-dependent structures are tested, it might not be possible to attain the desired state after errors are introduced, and the test has to be restarted.

In hybrid testing the structure is partitioned in a physical part and a numerical part, as discussed previously in reference to Figure 1.1. If distinguishing between the two contributions in the equation of motion in (3.1), and assuming that the numerical substructure contains linear damping, this can be written on the form:

$$\mathbf{M}_n \ddot{\mathbf{V}}_i + \mathbf{C}_n \dot{\mathbf{V}}_i + \mathbf{g}_n(\mathbf{V}_i) + \mathbf{R}_{p,i} = \mathbf{F}_i \tag{3.18}$$

with the subscripts n and p referring to the numerical and physical contributions, respectively. The vector $\mathbf{R}_{p,i}$ includes the inertia, damping and restoring forces of the physical substructure. It is measured by the actuators and given as a direct input to the EOM during the hybrid loop, as described in relation to Figure 1.2.

In the following, $\mathbf{R}_{p,i}$ is referred to as the actuator forces. Furthermore, for simplicity the subscripts n and p in (3.18) are neglected in the following,

and the internal restoring forces of the numerical substructure at the time t_i, are denoted $\mathbf{g}_n(\mathbf{V}_i) = \mathbf{g}_i$.

To solve the EOM in (3.18) various types of integration schemes have been used in RTHT. The, most preferred integration schemes are the Newmark method, the CDM and the OSM. The CDM is an explicit scheme, whereas the Newmark method offers both implicit and explicit versions, depending on the integration parameters chosen. The OSM is characterized as a noniterative, linearly implicit and nonlinear explicit method.

In table 3.1 are listed some of the most obvious pros and cons related to implicit and explicit schemes in a RTHT application. In the following these are discussed and examples on integration schemes applied are presented.

Table 3.1: Pros and Cons in Time Integration Schemes for RTHT.

	Implicit Schemes	**Explicit Schemes**
Pros	• Higher stability and accuracy than explicit schemes	• Knowledge of physical substructure is not required • Simple and computational efficient
Cons	• Number of required iterations are unknown • Require information about physical substructure for iteration	• Lower stability and accuracy than implicit schemes

3.2.1 Implicit Integration Schemes

As listed in Table 3.1, the typical advantage of implicit schemes compared to explicit schemes, are that they are more stable and provide a higher accuracy in terms of the displacement output. This typically allows larger time steps to be applied, compared with explicit methods. Furthermore, some implicit schemes offer unconditional stability for linear analysis. In nonlinear analysis, however, the unconditional stability property vanish, or is, at most, only present for softening type behavior, considering collocation-type methods.

The high precision and stability of implicit schemes are desirable properties, especially as large times can be required, in order to fulfill the real-time criteria in (3.17). However, in RTHT context many challenges also arise with the use of implicit schemes. One issue is in case of nonlinear systems, where iterations are introduced. This complicates the process, as the number of

iterations are typically unknown prior to the simulations. Furthermore, iterations require a frequent exchange of data between the substructures, which in Bonnet et al. (2008) was shown to be potentially very computational expensive. Also properties, such at the stiffness, of the physical substructure, are often required in the iteration process. These can be difficult to measure during a test.

Furthermore, the conventional iteration process is not possible in RTHT. By this is meant, that it is not possible to impose a predicted displacement at the following time step, Δt ahead in time, onto the physical substructure, evaluate the residual and correct this with a displacement increment found in a subsequent iteration. The displacement imposed onto the physical substructure a time step, Δt, ahead should be the converged displacement, and not a predicted displacement. Thus, the iterations have to be performed in parallel while imposing the displacements onto the physical substructure. For this additional strategies have to be adopted in the iteration processes.

Thus, the use of implicit schemes in RTHT context faces a number of challenges. However, different schemes and approaches have been adopted to work out these in the best way. In the following three examples on different implicit integration schemes and strategies applied in real-time context are given, with focus on solving the challenges discussed above.

Implicit Method With Fixed Number of Iterations

Shing et al. (2004) and Jung and Shing (2007) suggested a nonlinear solution approach, combining a Newton-type iteration with sub-increments imposed onto the physical substructure through interpolation. A key points of the method, is that a fixed number of iterations are adopted in each time step, to ensure that the iterations can be finished within the real-time requirement.

The approach is sketched in Figure 3.2 for a one dimensional case, where the actuator displacement has reached the value V_i at time t_i and the displacement V_{i+1}, a time step Δt later, should be evaluated next. The interval, Δt, is divided in n equal time steps, δt, corresponding to the number of fixed iterations applied, with k denoting the iteration step, k ϵ [1;n]. In each iteration step an estimate for the displacement at time t_{i+1}, is made, referred to as V_{i+1}^k. After evaluation of this, a polynomial through the displacement points V_{i-1}, V_i and V_{i+1}^k, is then used to interpolate the displacement, $\tilde{V}_{i+1}^k$, at the following sub-step. The interpolated displacement is sent to the actuators, where the actuator force $\tilde{R}_{i+1}^k$ is measured at sub step k, and is sent to the numerical substructure, where it is used in the following iteration step.

The point of the iteration steps is to update the displacement V_{i+1}^k. For this the residual, $\tilde{r}_{i+1}^k$, at the imposed displacements, $\tilde{V}_{i+1}^k$, is used. Intro-

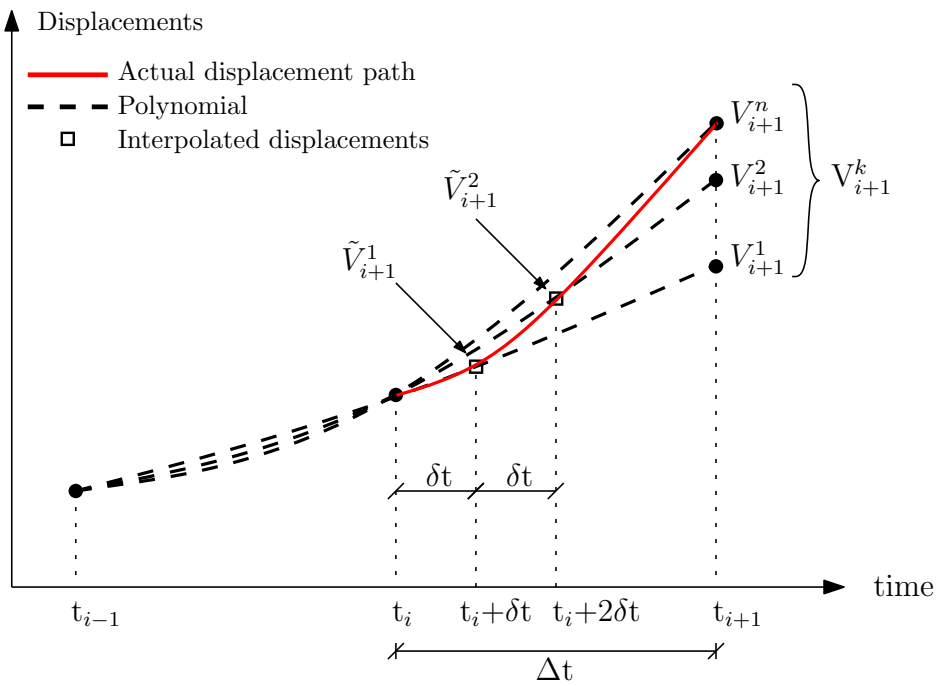

Figure 3.2: Implicit Integration Method by Shing et al.

ducing the approximate displacements and velocities in (3.2)-(3.3) into the EOM in (3.18) together with the forces $\tilde{R}^k_{i+1}$ and $\tilde{g}^k_{i+1}$, the residual can be evaluated as:

$$\tilde{r}^k_{i+1} = F_{i+1} + \bar{M}(V^*_{i+1} - \tilde{V}^k_{i+1}) - C\dot{V}^*_{i+1} - \tilde{g}^k_{i+1} - \tilde{R}^k_{i+1} \tag{3.19}$$

with

$$\bar{M} = \left(\frac{M + \Delta t \gamma C}{\Delta t^2 \beta}\right) \tag{3.20}$$

$$V^*_{i+1} = V^k_{i+1} \tag{3.21}$$

$$\dot{V}^*_{i+1} = \dot{V}^k_{i+1} \tag{3.22}$$

Knowing the residual, $\tilde{r}^k_{i+1}$, the incremental displacement, δV, can then be evaluated from (3.12). During the test it can however be difficult to measure the properties of physical substructure required to evaluate the modified stiffness matrix in (3.12). Instead, Shing et al. (2004) and Jung and Shing (2007) suggested to use the initial measured mass, damping and stiffness properties of the substructures, in the nonlinear iteration process. Using this approximation, the modified tangent stiffness matrix in (3.13) can then be

formulated as:

$$\mathbf{K}^* = (\mathbf{K}_{n,0} + \mathbf{K}_{p,0}) + \frac{\gamma}{\beta \Delta t}(\mathbf{C}_n + \mathbf{C}_p) + \frac{1}{\beta \Delta t^2}(\mathbf{M}_n + \mathbf{M}_p) \tag{3.23}$$

with the subindex p and n referring to the physical and numerical substructures. The exact values for the physical substructure are not required in the iteration process. Using approximate values can however slow down the iteration process. When using the initial properties in the iteration Shing et al. (1991) and Shing and Vannan (1991) suggested to use a stiffness slightly higher than the actual stiffness, as this improved the stability of the algorithm.

After having evaluated the displacement increment, δV, by use of (3.12) with residual in (3.19) and the modified stiffness in (3.23), the predicted displacement at time t_{i+1} can be updated to be

$$V_{i+1}^{k+1} = \tilde{V}_{i+1}^{k} + \delta V \tag{3.24}$$

It is important to stress, that displacement $\tilde{V}_{i+1}^{k}$ in (3.19) should be the displacement actual imposed by the actuators, in order to ensure consistency between the numerical calculations and the actual experiment. The final displacement, $\tilde{V}_{i+1}^{n}$, imposed by the actuators onto the physical substructure, is taken as the converged displacement, V_{i+1}^{n}.

Shing et al. (2004) and Jung and Shing (2007) pointed out, that it is uncertain how big the residuals will be, when a specific amount of iterations are applied. It is however expected that these will be larger than in conventional iteration. In the given case, though, ten iterations were reported to be enough for even highly nonlinear systems. Another issue is, that if many iterations are adopted, the frequent amount of feedback between the substructures potentially can be problematic, as illustrated in Bonnet et al. (2008) where the frequent feedback limited the DOF capacity of implicit schemes compared to explicit schemes.

Despite of these uncertainties, the scheme has demonstrated to be fully applicable in real-time context. In Jung and Shing (2007) the method was reported to be successfully included in a nonlinear real-time test considering a steel braced frame with kinematic as well as geometric nonlinearities, including a 35 DOF numerical substructure. As previously mentioned in Chapter 2, the method was also recently applied by Saouma et al. (2012), to run a 405 DOF nonlinear substructure in a RTHT.

Combined Implicit or Explicit Method

In Mosqueda and Ahmadizadeh (2007) a so-called combined implicit or explicit method was presented. A key point in the method is, that polynomial expressions, based on previous measurements, are used to express the actuator forces, $\mathbf{R}_{i+1}$, in the iteration process. Furthermore, the displacement corrections found during the iteration process are not compensated for until the following time step. This was done in order to avoid unrecoverable damage due to potential iterative displacement reversals.

The principle of the method is shown in Figure 3.3, where the displacement, V, at the shared boundary is sketched as a function of time. Two curves are shown; an implicit solution curve, and the actual actuator displacement curve. The latter is based on the predictor displacements of the implicit solution curve, determined by use of the fully explicit Newmark scheme ($\beta = \gamma = 0$), cf. (3.4) - (3.5):

$$\mathbf{V}^*_{i+1} = \mathbf{V}_i + \Delta t \dot{\mathbf{V}}_i + \frac{1}{2}\Delta t^2 \ddot{\mathbf{V}}_i \tag{3.25}$$

$$\dot{\mathbf{V}}^*_{i+1} = \dot{\mathbf{V}}_i + \Delta t \ddot{\mathbf{V}}_i \tag{3.26}$$

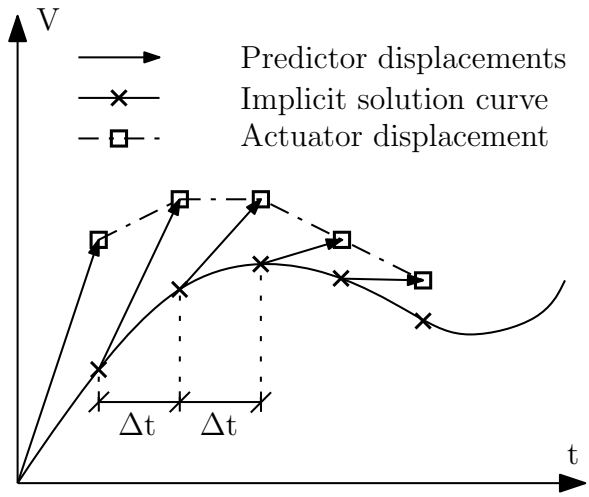

Figure 3.3: Combined implicit or explicit method.

During the time interval, Δt, where the actuators impose the predictor displacements and velocoties in (3.25) and (3.26), a Newton-type iteration is running in parallel. However, to avoid iterating on the physical substructure and to minimize the communication between the substructures, the actuator force, R_{i+1}, is approximated. For this the most recently measured actuator

forces and displacements are used to oragnize two second order polynomials, see (3.27)-(3.28), with t denoting the time, and a_i, b_i and c_i representing the polynomial coefficients, i ϵ [1;2].

$$V(t) = a_1 t^2 + b_1 t + c_1 \tag{3.27}$$

$$R(t) = a_2 t^2 + b_2 t + c_2 \tag{3.28}$$

During an iteration, the polynomial in (3.27) is used to determine the time, where displacement in iteration step k, V_{i+1}^k, appears. Entering the corresponding time into (3.28) the actuator force, R_{i+1}^k, can be evaluated. By adopting this strategy, the iteration task can be separated from the physical substructure, and iterations can then proceed until convergence is fulfilled. Hence, no actuator feedback is required in the iteration process with the present method.

As stated previously, the corrections to the predictor displacement found in the iteration process, are not enforced along with the iterations. Instead they are implicit compensated for in the following time step by the prediction step of the implicit solution curve. However, as sketched in Figure 3.3, the approach entails that the actuator displacements will deviate from the equilibrium curve, but that the implicit solution curve is intended to keep it close the the actual response. Furthermore, in case equilibrium is not achieved during the time step, the initial prediction displacements in (3.25), are taken as the equilibrium state. The method then converts to an explicit method.

In Mosqueda and Ahmadizadeh (2007) the integration strategy was tested on a frame structure exposed to an earthquake, with one column taken as the physical substructure. In a linear test the method was compared with the central difference method, and it was demonstrated that the presented algorithm is much more stable when the time step magnitudes were increased, due to its implicit character. The algorithm was also successfully tested in a case where the physical substructure exhibited material nonlinear behavior.

The authors pointed out a number of weaknesses of the method. In case of displacement reversals, the polynomial prediction in (3.27) will perhaps not be able to represent the displacments, and complex numbers will then appear. Furthermore, the approximation for the actuator force is based solely on displacements, i.e. the effects of velocity and acceleration are neglected. Thus, the approach is mainly applicable for displacement-dependent structures, and not for highly rate dependent structures, such as e.g. dampers. Thus, improvements are required. Furthermore, it was not demonstrated if the method worked well with adoption of nonlinear numerical substructures. Only linear substructures were included.

Operator Splitting Method

Nakashima et al. (1990) introduced the Operator-splitting method (OSM) in pseudo-dynamic testing. The algorithm was initially suggested by Hughes et al. (1979). A key point of the method is that the restoring force is split into an approximated linear and nonlinear part, cf. (2.2). With this assumption the actuator forces and the restoring forces of the numerical substructures are approximated as

$$\mathbf{g}_{i+1} = \mathbf{g}^*_{i+1} + \mathbf{K}_{n,0}(\mathbf{V}_{i+1} - \mathbf{V}^*_{i+1}) \tag{3.29}$$

$$\mathbf{R}_{i+1} = \mathbf{R}^*_{i+1} + \mathbf{K}_{p,0}(\mathbf{V}_{i+1} - \mathbf{V}^*_{i+1}) \tag{3.30}$$

where $\mathbf{K}_{n,0}$ and $\mathbf{K}_{p,0}$ are stifnesses close to the initial elastic stifnesses of the numerical and physical substructures, respectively. Furthermore $\mathbf{g}^*_{i+1}$ and $\mathbf{R}^*_{i+1}$ represent the restoring force of the numerical and physical substructures, evaluated at the predictor displacements. The assumption for the actuator forces in (3.30) in the one dimensional case, is sketched in Figure 4.1.

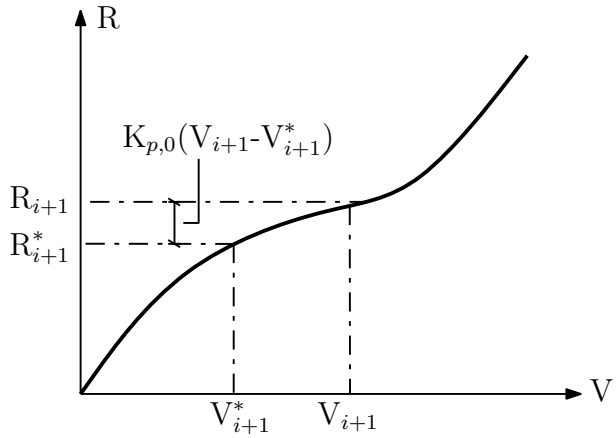

Figure 3.4: Approximate actuator force in the OSM.

With the approximations in (3.29) and (3.30) the EOM in (3.18) can be written on the form;

$$\mathbf{M}\ddot{\mathbf{V}}_{i+1} + \mathbf{C}\dot{\mathbf{V}}_{i+1} + \mathbf{g}^*_{i+1} + \mathbf{R}^*_{i+1} + (\mathbf{K}_{n,0} + \mathbf{K}_{p,0})(\mathbf{V}_{i+1} - \mathbf{V}^*_{i+1}) = \mathbf{F}_i \tag{3.31}$$

Introducing the predictor and corrector terms in (3.2)-(3.5) into (3.31) an expression linear in $\ddot{\mathbf{V}}_{i+1}$ is given. By evaluation $\ddot{\mathbf{V}}_{i+1}$ the displacements and velocities at the specific time t_{i+1} can be found, and the displacements and velocities used for the following time step can be evaluated from (3.2)-(3.3). In this way iterations are avoided.

It should be stressed, that the corrector displacement, $\mathbf{V}_{i+1}$, is never imposed onto the substructure, but is used to compensate for the error of the predictor displacement, $\mathbf{V}^*_{i+1}$, in the following step. This is similar to the procedure used in the combined implicit or explicit method by Mosqueda and Ahmadizadeh (2007).

The introduced assumption in (3.30) is only valid in case displacement related nonlinearities exist in the physical substructure. As discussed in chapter 2, Wu et al. (2006a) extended the method to the case where the structural response would also be a nonlinear function of the velocity. This was done by introducing a similar corrector term for the nonlinear damping. With this the approximation for the actuator forces in (3.30) were extended to

$$\mathbf{R}_{i+1} = \mathbf{R}^*_{i+1} + \mathbf{K}_{p,0}(\mathbf{V}_{i+1} - \mathbf{V}^*_{i+1}) + \mathbf{C}_{p,0}(\dot{\mathbf{V}}_{i+1} - \dot{\mathbf{V}}^*_{i+1}) \tag{3.32}$$

where $\mathbf{C}_{p,0}$ is a prescribed damping matrix related to the physical substructure.

The Operator splitting method is theoretically an implicit scheme, but uses explicit predictor displacement to impose onto the structure. This makes it very simple and straight forward to use. It is second order accurate and has shown unconditional stability for linear systems and for nonlinear systems with softening behavior. It can also be combined with the α-method to introduce damping into the system. As concluded in Bonnet et al. (2008), the scheme is however a little less efficient than the explicit Newmark scheme, and the Newmark-Chang scheme.

3.2.2 Explicit Integration Schemes

Next, explicit time integration in hybrid testing is considered. The characteristics of an explicit scheme is that the evaluation of $\mathbf{V}_{i+1}$ does not require an iterative solution on any system of equations at time t_{i+1}, but instead can be evaluated directly from the results at the previous time-steps. An example on a scheme which is explicit in the displacement, is the explicit Newmark scheme, using the parameters $\beta = 0$. The displacement vector in (3.2) is then approximated as

$$\mathbf{V}_{i+1} = \mathbf{V}_i + \Delta t \dot{\mathbf{V}}_i + \Delta t^2 \frac{1}{2} \ddot{\mathbf{V}}_i \tag{3.33}$$

Explicit schemes tend to be more appealing in a RTHS context as the actuator forces, and the stiffness, mass and damping properties of the physical substructure are not required in an iterative process. Explicit schemes are

typically also simple to implement, and can be very time efficient as listed in Table 3.1. However, when using explicit schemes, more strict requirements exist with respect to the stability and precision. The stability limit for the time step magnitude is typically inverse proportional with the highest frequency of the system, i.e. when high frequency content is present, the applied time steps have to be small. Typically the time steps in explicit schemes will be significantly smaller compared to if implicit schemes are used. However, the efficiency can compensate for this.

The Central Difference Method

The CDM is as previously mentioned, a popular applied explicit scheme in hybrid testing, due to its simplicity and efficiency. In real-time context the scheme has been applied e.g. by Nakashima et al. (1992), Nakashima and Masaoka (1999), Darby et al. (1999) and Carrion and Spencer Jr. (2007). In the CDM the velocities and the accelerations are approximated as

$$\dot{\mathbf{V}}_i = \frac{\mathbf{V}_{i+1} - \mathbf{V}_{i-1}}{2\Delta t} \tag{3.34}$$

$$\ddot{\mathbf{V}}_i = \frac{\mathbf{V}_{i+1} - 2\mathbf{V}_i + \mathbf{V}_{i-1}}{\Delta t^2} \tag{3.35}$$

Inserting the approximations in (3.34) and (3.35) into the EOM in (3.18) evaluated at time t_i, the displacement, $\mathbf{V}_{i+1}$, at the following specific time, t_{i+1}, can be evaluated as

$$\mathbf{V}_{i+1} = \left(\frac{1}{\Delta t^2}\mathbf{M} + \frac{1}{2\Delta t}\mathbf{C}\right)^{-1} (\mathbf{F}_i - \mathbf{g}(\mathbf{V_i}) - \mathbf{R}_i + \mathbf{b}\mathbf{V}_i - \mathbf{a}\mathbf{V}_{i-1}) \tag{3.36}$$

where the coefficients a and b are:

$$\mathbf{a} = \frac{1}{\Delta t^2}\mathbf{M} - \frac{1}{2\Delta t}\mathbf{C} \tag{3.37}$$

$$\mathbf{b} = \frac{2}{\Delta t^2}\mathbf{M} \tag{3.38}$$

As seen from (3.36) the displacements at the specific time t_{i-1} are required. In the first step the value for $\mathbf{V}_{-1}$ can be evaluated by use of (3.34) and (3.35) as:

$$\mathbf{V}_{-1} = \mathbf{V}_0 - \Delta t\dot{\mathbf{V}}_0 + \frac{\Delta t^2}{2}\ddot{\mathbf{V}}_0 \tag{3.39}$$

The stability requirement of the CDM in the linear domain is inversely proportional to the highest frequency, cf. Cook et al. (1974):

$$\Delta t \leq \frac{2}{\omega} \tag{3.40}$$

where ω has the unit rad/s. In nonlinear context the stability requirement, (3.40), is however no longer valid. Thus, in nonlinear analysis a suitable time step magnitude has to be evaluated in another way, for example through a number of test simulations.

A main disadvantage of the CDM is that that it is only explicit in the displacement, which makes it implicit for nonlinear rate-dependent structures. However, the scheme also possesses many good qualities, such as; its is second order accurate, it exhibits no numerical energy dissipation, it is simple and last but not least, it is very efficient. These quantities are most likely the reasons why the scheme has been so popular in hybrid testing application.

3.3 Concluding Remarks

In the present chapter, the pros and cons of using implicit and explicit time integration methods in real-time hybrid testing, have been discussed. Furthermore a number of examples on different integration schemes and techniques used in applied test cases, have been presented.

In the present PhD study the central difference method has been used as the preferred time integration method. The reason for choosing this scheme is first of all because it is very simple and efficient. Furthermore, an explicit scheme was chosen in order to put aside the iteration issues discussed above, and focus purely on the numerical substructures.

Chapter 4

Existing and New Basis Reduction Methods

The present chapter focus on the use of projection based reduction methods, also referred to as basis reduction, with special emphasis on its application in kinematic nonlinear structures. Generally reduction methods are used to reduce the dimension of large discretized numerical models with the aim of decreasing the computational time, and simultanesouly maintain a high solution accuracy.

The principle of basis reduction is to define a subspace represented by a reduced basis, where the nonlinear EOM are projected onto. Ideally a basis that spans a low-dimensional subspace, and at the same time can span the solution, **V**, to the EOM, is chosen.

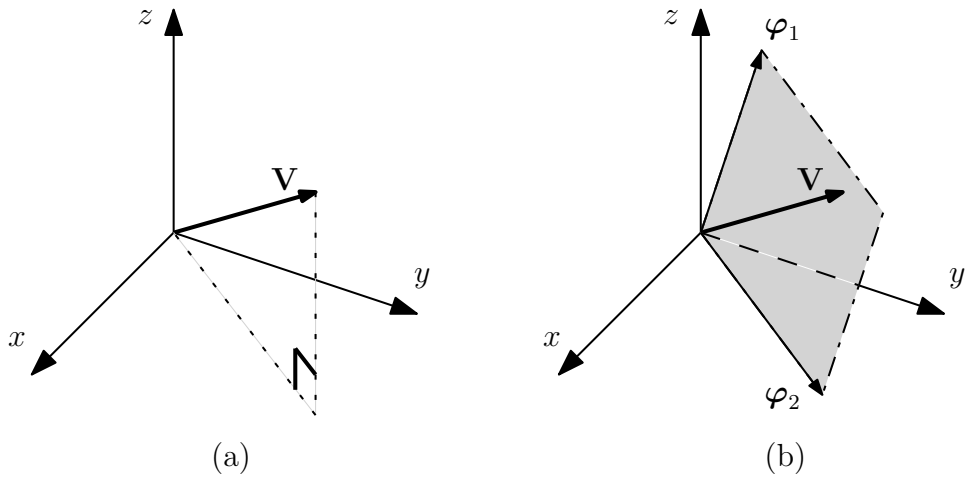

Figure 4.1: (a) Solution vector **V** in (x,y,z) space and (b) basis vectors $\boldsymbol{\varphi}_1$ and $\boldsymbol{\varphi}_2$ spanning a plane, that contains **V**.

In Figure 4.1 the principle is illustrated, with a solution vector $\mathbf{V}$ spanned in a three-dimensional (x,y,z) co-ordinate system. Instead of solving the EOM described in the three-dimensional space, it can be projected onto a reduced basis consisting of the two basis vectors, $\boldsymbol{\varphi}_1$ and $\boldsymbol{\varphi}_2$, spanning a plane in which the full solution vector, $\mathbf{V}$, is also located. By this the EOM is reduced by one dimension, meaning that less equations have to be solved, but with a retained solution accuracy.

The concept of basis reduction is well known from linear analysis, but has also found its use in nonlinear analysis, see e.g. Horri and Kawahara (1969) and Nickell (1976). In linear structural analysis basis reduction can be used to decouple the equations of motion, and thereby improve the efficiency of the simulations, see e.g. Chopra (1995). In nonlinear analysis this property also exist, but requires the basis to be updated in between each time step. This is a costly procedure, and is not well suited for real-time simulations. Furthermore, the selection of basis vectors for nonlinear systems is more complex than for linear systems. In linear systems the basis vectors orthogonal to the loading are typically not of importance, and can be disregarded. However, in kinematic nonlinear analysis, different deformation modes are coupled through a nonlinear strain measure, which can cause the basis vectors orthogonal to the loading to be activated. If the coupling activated modes are omitted from the basis, locking can become a consequence, potentially ruining the accuracy of the response.

Another potential benefit of basis reduction, is that it provides an efficient way of removing some of the high frequency content of the discrete FEM models. Removing the high frequency content, the stability of the system is increased, and larger time steps can be applied in the time integration. This can help to improve the efficiency of the simulations.

In the present chapter, the general principles behind basis reduction are given, and some of the most applied basis vectors are presented. These encounter the Linear Normal Modes, Ritz vectors and Modal Derivatives. To illustrate the importance of choosing a basis that can represent the nonlinear effects of the system, an example is given. After the general introduction, three elements that can improve the accuracy in a real-time context are presented. These consist of the adoption of a efficient global evaluation of the internal restoring forces, an improvement of the modal derivatives, and the use of a so-called Taylor basis. The elements constitute the major contributions of the present PhD study.

It should be stressed, that in the present chapter, purely numerical systems are considered. The coupling of physical substructures with numerical substructures including basis reduction, is discussed in the following chapter.

4.1 Basis Projection

The starting point of basis reduction is the EOM on discretized form

$$\mathbf{M}\ddot{\mathbf{V}} + \mathbf{C}\dot{\mathbf{V}} + \mathbf{g}(\mathbf{V}) = \mathbf{F}(t) \tag{4.1}$$

where the mass and damping matrices are of dimension n×n and the remaining components are vectors of dimension n×1. A basis is then chosen, consisting of N basis vectors, $\boldsymbol{\varphi}_i$, of dimension n×1, and their belonging reduced co-ordinates, s_i, i ϵ [1;N]. The basis vectors are organized as columns in a basis matrix, $\mathbf{\Phi}$, of dimension n×N and the reduced co-ordinates are organized in a vector $\mathbf{s}$ of dimension N×1. The displacement field, $\mathbf{V}$, can then be approximated as:

$$\mathbf{V} \approx \sum_{i=1}^{N} \boldsymbol{\varphi}_i s_i = \mathbf{\Phi}\mathbf{s} \tag{4.2}$$

In the following the basis formulation in (4.2) is referred to as the linear basis formulation, because of the linear relation between the basis vectors and the reduced co-ordinates. The EOM in (4.1) are projected onto the reduced basis in (4.2) to obtain the reduced system of equations, yielding the formulation:

$$\mathbf{m}\ddot{\mathbf{s}} + \mathbf{c}\dot{\mathbf{s}} + \tilde{\mathbf{g}}(\mathbf{s}) = \mathbf{f}(t) \tag{4.3}$$

with the projected matrices and vectors defined as:

$$\mathbf{m} = \mathbf{\Phi}^T\mathbf{M}\mathbf{\Phi} \tag{4.4}$$

$$\mathbf{c} = \mathbf{\Phi}^T\mathbf{C}\mathbf{\Phi} \tag{4.5}$$

$$\tilde{\mathbf{g}}(\mathbf{s}) = \mathbf{\Phi}^T\mathbf{g}(\mathbf{\Phi}\mathbf{s}) \tag{4.6}$$

$$\mathbf{f}(t) = \mathbf{\Phi}^T\mathbf{F}(t) \tag{4.7}$$

The mass and damping matrices in (4.4) and (4.5) are of dimension N×N and the internal restoring forces and the load vector in (4.6) and (4.7) are of dimension N×1. Typically N $\ll$ n, and the projected EOM in (4.3) can potentially be solved significantly faster than the initial system in (4.1). However, due to the nonlinear character of the internal restoring forces, these have to be assembled element-by-element before they can be projected as done in (4.6). The assembling was previously illustrated to be a costly procedure, cf. section 1.2.1. In section 4.2.1 a reformulation technique of the restoring forces in (4.6) is discussed, which can ease the computational burden significantly.

To obtain an accurate solution when solving the system of equations in (4.3), it is of major importance that the chosen basis in (4.2) can span the

response with a high accuracy. For linear systems, typically the basis vectors, $\boldsymbol{\varphi}_i$, with frequencies in the domain of the load excitation frequency and with a relatively high load, $\mathrm{f}_i = \left|\boldsymbol{\varphi}_i^T \mathbf{F}\right|$, are significant to the response. These basis vectors are also important in nonlinear systems. However, in kinematic nonlinear systems, the nonlinear strain measures couple various deformations modes. This can cause modes orthogonal to the loading to be excited as well. In the following an example is given to illustrate the importance of representing the coupling activated deformation modes in the applied basis. The example is taken from the work in Andersen and Poulsen (2014).

4.1.1 Nonlinear Cantilever - Example

A nonlinear cantilever beam of length l, exposed to an external harmonic load F(t), with an excitation frequency, ω_e, and an amplitude, $\mathrm{F}_{\max}$, is considered, see Figure 4.4a. The beam has a bending stiffness EI, a density ρ, a damping ratio ζ, a poisson's ratio ν, and a cross section of height h and width b. The beam parameters are given in table 4.1. Furthermore, the displacement in a point (x,y,z) is described by the vector $\mathbf{u}(x, y, z) = [u_x \ u_y \ u_z]^T$, with the normal center in (x,y)=($\frac{1}{2}$,$\frac{1}{2}$) m.

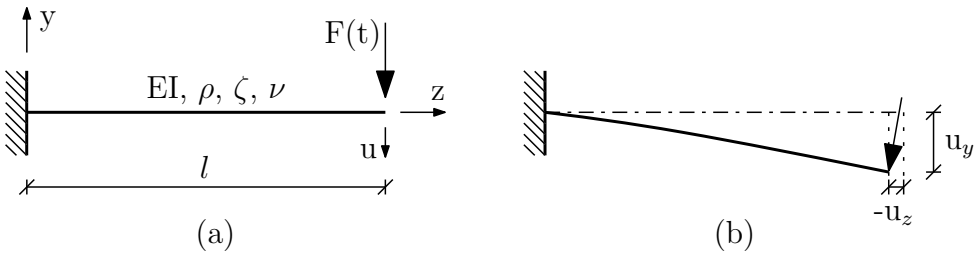

Figure 4.2: (a) Cantilever exposed to harmonic load in the (y,z)-plane. (b) Sketch of deformed state.

The beam is modelled by use of 10-nodal isoparametric tetrahederal continuum elements with three translational DOFs in each node. For details about the element and the mesh, see Andersen and Poulsen (2014). Green strains are assumed, and the strain measure along the beam length, ε, is constituted by first and second order terms in the displacement field, see e.g. Krenk (2009):

$$\varepsilon(x, y, z) = \frac{\partial u_z}{\partial z} + \frac{1}{2}\left[\left(\frac{\partial u_x}{\partial z}\right)^2 + \left(\frac{\partial u_y}{\partial z}\right)^2 + \left(\frac{\partial u_z}{\partial z}\right)^2\right] \tag{4.8}$$

The strain measure in (4.8) introduces a coupling between deformations in

Table 4.1: Cantilever parameters.

Parameter	Unit	Magnitude
l	m	4
h	m	1
b	m	1
EI	Nm^2	$17.5 \cdot 10^9$
ρ	kg/m^3	7800
ν	-	0.3
ζ	%	0
F_{max}	GN	2
ω_e	rad/s	4π

the x-, y- and z-direction, respectively. In linear analysis the higher order terms in (4.8) vanish, and the coupling disappears.

If, for simplicity, it is assumed that the normal force along the beam axis in the deformed state is negligible, then the strain, ε, will be zero. Furthermore, if it is assumed that $u_x = 0$ and $(\partial u_z/\partial z)^2 \ll (\partial u_y/\partial z)^2$, then (4.8) can be approximated as:

$$\frac{\partial u_z}{\partial z} + \frac{1}{2}\left(\frac{\partial u_y}{\partial z}\right)^2 = 0 \tag{4.9}$$

By integrating over the beam length, a deformation in the y-direction is seen to introduce a negative axial deformation due to the coupling:

$$u_z(z) = -\frac{1}{2}\int_0^z \left(\frac{\partial u_y}{\partial z}\right)^2 dz \tag{4.10}$$

To illustrate the importance of representing the axial deformation in (4.10) due to bending, the dynamic response of the cantilever in Figure 4.4a is analysed by use of basis reduction. Part of the basis consists of so-called Linear Normal Modes (LNMs), $\boldsymbol{\varphi}_i$. These are described in more detail in section (4.1.2). Furthermore a set of higher order terms are included. These are organized by solving the linear and kinematic nonlinear systems in (4.11) and (4.12) and subtracting the solutions from each other, cf. (4.13). The parameter α is a scalar, that is scaled so that the maximum deviation in a discrete point between $\mathbf{V}_{\text{non}}$ and $\mathbf{V}_{\text{lin}}$ is 1%, with $\mathbf{V}_{\text{lin}}$ taken as reference.

$$\mathbf{K}_T(\mathbf{0})\mathbf{V}_{\text{lin}} = \alpha\mathbf{M}\boldsymbol{\varphi}_i \tag{4.11}$$

$$\mathbf{K}_T(\mathbf{V})\mathbf{V}_{\text{non}} = \alpha\mathbf{M}\boldsymbol{\varphi}_i \tag{4.12}$$

$$\boldsymbol{\varphi}_i^h = \mathbf{V}_{\text{non}} - \mathbf{V}_{\text{lin}} \tag{4.13}$$

Three different basis combinations are considered, referred to as reduced basis formulation (RBF) 1 to 3, listed in Table 4.2. In the RBF1 case the four first LNMs are included, in the RBF2 case the first LNM and its higher order mode is included, and in the RBF3 case LNMs number 1 and 4 and their higher order modes are included. The LNMs number 1 and 4 are bending modes in the loading plane, LNM 2 is a bending mode in the (x,y)-plane, and LNM 3 is a twisting mode with the z-axis as rotation axis. None of the LNMs included deformation in the z-direction.

Table 4.2: Mode combination in cantilever analysis.

Case	Linear modes, $\boldsymbol{\varphi}_i$	Higher order modes, $\boldsymbol{\varphi}_i^h$
RBF1	1-4	-
RBF2	1	1
RBF3	1, 4	1, 4

The LNMs number 1 and 4 are plotted in the top of Figure 4.3 in the (y,z)-plane. For simplicity only the deformation along the line (x,y) = $(0, \frac{1}{2})$ m of the cantilever is considered. The corresponding higher order modes are

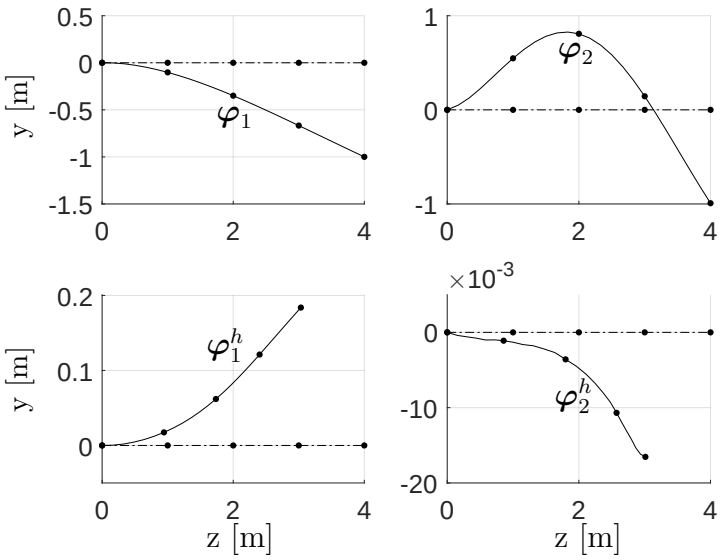

Figure 4.3: Basis vectors, marked by solid lines, used for analysis of Cantilever - plotted in the (y,z)-plane.

also plotted in the bottom of Figure 4.3. In contrast to the linear modes, that are based on a linear system, the higher order modes are seen to contain deformations in the z-direction, introduced due to the coupling effects.

In Figure 4.4 the transverse deformation, -u$_y$, in the point (x,y,z) = ($\frac{1}{2}$,$\frac{1}{2}$,4) m is plotted over a time interval of 0.25 s, which corresponds to half a load period. Four solution curves are presented; a solution based on the implicit Newmark algorithm (NA) of the full model and three solution curves based on the three RBF listed in table 4.2, evaluated by use of the CDM. The NA solution is taken as the 'exact' solution.

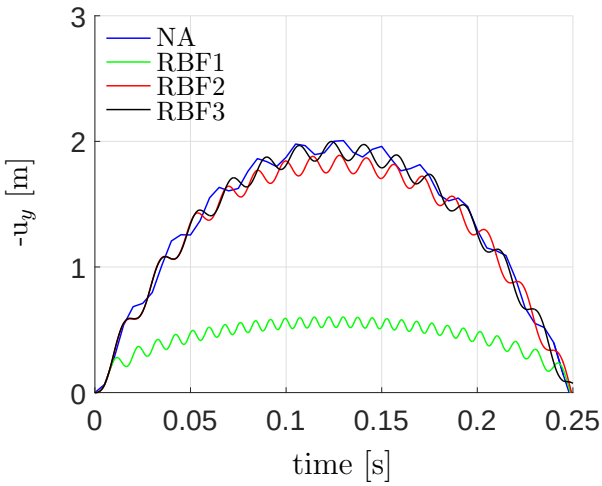

Figure 4.4: Cantilever endpoint deformation.

From Figure 4.4 the global NA response is seen to be in phase with the excitation frequency, ω_e. Furthermore local oscillations in the order of 50 Hz are present. This is caused by the influence of the first bending mode of the system, $\boldsymbol{\varphi}_1$, which has a frequency of that magnitude.

The RBF1 solution is seen to deviate from the NA response, with a significantly smaller amplitude and a higher local frequency. Thus, the given basis seems to increase the stiffness of the system. This is because the LNMs do not allow any horizontal deformation. The increase in stiffness can be loosened by including the higher order modes. This is verified by the RBF2 and RBF3 solution curves. Solely by including a single higher order mode, $\boldsymbol{\varphi}_1^h$, significant improvement in the response is seen. Including the second higher order mode, $\boldsymbol{\varphi}_2^h$, in the basis, the response is improved further. Increasing the number of modes, the solution will converge at some point. This is however not shown in the given case considered.

From the example it is obvious that it is of high importance to include the coupling activated deformations in the basis.

4.1.2 Basis Vectors

Many different bases exist, each with many variants and refinements. In Lülf et al. (2013) an extensive review on some of the most popular applied bases in kinematic nonlinear dynamic context were presented and compared. The methods used to evaluate the bases were divided in so called *post priori methods* and *a priori methods*, with the characteristics:

- *post priori methods*: Require information from actual full order solution to generate bases.
- *a priori methods*: Do not require information from the full order solution to generate bases.

Among the post priori methods are e.g. the Proper Orthogonal Decomposition (POD) method and the smooth orthogonal decomposition, whereas among priori methods can be mentioned the Modal decomposition and the Ritz method. For details about the various methods, see Lülf et al. (2013).

As stated above, the post priori methods require information on the full order solution, e.g. found from a simulation of a numerical model or from physical experiments, in the evaluation of the basis vectors. The a priori methods, on the other hand, do not require any information on the solution prior to the evaluation. In a hybrid testing context the response is not available prior to the analysis, and therefore only bases based on a priori methods are considered in the given study. In Lülf et al. (2013) the LNMs and the Ritz vectors were stated as the preferred a priori basis, based on a number of nonlinear tests considering both local and global kinematic nonlinear systems exposed to different loading types. The LNMs and the Ritz vectors also represent the two types of basis vectors applied in RTHT context by the present author and other researchers. Therefore, the Ritz vectors, and LNMs are elaborated in the following. Furthermore, the so-called modal derivatives are considered. These represent the higher order effects of the displacement field, discussed in more detail in the following. The modal derivatives have also been extensively used in the present PhD study.

Modal Decomposition & Linear Normal Modes

Modal decomposition, also referred to as modal superposition, is one of the most commonly applied projection based reduction methods. The basis is constituted by a number of modal vectors, $\boldsymbol{\varphi}_i$, which describe the free vibration modes of the undamped structure, referred to as LNMs or mode-shape vectors. Each LNM has an associated natural frequency, ω_i.

The classic LNMs and the associated natural frequencies are given as the corresponding eigenvectors and the eigenvalues to the linearized eigenvalue problem in (4.14), see e.g. Chopra (1995):

$$\left(\mathbf{K}_T - \omega_i^2 \mathbf{M}\right) \boldsymbol{\varphi}_i = \mathbf{0} \tag{4.14}$$

For linear systems, the mode-shape vectors are mass and stiffness orthogonal;

$$\boldsymbol{\varphi}_i^T \mathbf{M} \boldsymbol{\varphi}_j = \mathbf{0} \quad , \quad \boldsymbol{\varphi}_i^T \mathbf{K}_T \boldsymbol{\varphi}_j = \mathbf{0} \quad , \quad i \neq j \tag{4.15}$$

The orthogonality conditions in (4.15) can be used to decouple the EOM, which helps to improve the efficiency of the time integration. This was e.g. utilized in Darby et al. (2001) in a RTHT context, where modal decomposition was applied. However, for nonlinear systems, the orthogonality conditions in (4.15) are only preserved if the modes are updated between each time step. This is however an expensive task, and it is not beneficial in a real-time context.

The mode superposition has also been applied by Wu et al. (2006a) to perform a RTHT analysis of an off shore platform to consider the performance of a damper installed to prevent vibrations induced by i.a. earthquake loading. In the given case a simplified model of the platform was analysed using three LNMs. Also part of the basis vectors in the Ritz basis applied in Blakeborough et al. (2001) consisted of LNMs.

The first application of modal superposition in kinematic nonlinear systems is dated back to Horri and Kawahara (1969) and later Nickell (1976). To the best of the authors knowledge, modal decomposition has not yet been used for kinematic nonlinear substructures in RTHT context.

The Ritz Method

Ritz vectors is another widely used basis vector, that was initially suggested to be used as basis vectors by Wilson et al. (1982). In contrast to the LNMs, where the vectors represent the free vibration modes of the system, the Ritz vectors, $\boldsymbol{\psi}_i$, are based on the load distribution of the system.

To evaluate the classic Ritz vectors a harmonic loaded system is considered. Introducing a harmonic solution, the EOM can be written on the form, cf. Kapania and Byun (1993):

$$\mathbf{K}_T \boldsymbol{\psi} = \mathbf{F}_A + \omega^2 \mathbf{M} \boldsymbol{\psi} \tag{4.16}$$

where $\mathbf{F}_A$ is the load amplitude. The first Ritz vector, $\boldsymbol{\psi}_1$, is based on the static problem in (4.16), and is normalized with respect to the mass, cf.

(4.17) and (4.18).

$$\tilde{\boldsymbol{\psi}}_1 = \mathbf{K}_T^{-1}\mathbf{F}_A \tag{4.17}$$

$$\boldsymbol{\psi}_1 = \frac{\tilde{\boldsymbol{\psi}}_1}{\left(\tilde{\boldsymbol{\psi}}_1^T\mathbf{M}\tilde{\boldsymbol{\psi}}_1\right)^{1/2}} \tag{4.18}$$

To compensate for the inertia forces neglected in the evaluation of $\boldsymbol{\psi}_1$, the following Ritz vectors are based on an equivalent static system with a force given as the mass times the previous Ritz vector, cf. (4.19). After the evaluation of each vector the Gram-Schmidt method is used to make it orthogonal to the previous generated vectors, and it is then normalized with respect to the mass, cf. (4.19)-(4.22).

$$\mathbf{K}_T\boldsymbol{\psi}_{i+1}^* = \mathbf{M}\boldsymbol{\psi}_i \quad , \quad i \geq 1 \tag{4.19}$$

$$\tilde{\boldsymbol{\psi}}_{i+1} = \boldsymbol{\psi}_{i+1}^* - \sum_{j=1}^{i-1} c_j\boldsymbol{\psi}_j \tag{4.20}$$

$$c_j = \boldsymbol{\psi}_j^T\mathbf{M}\boldsymbol{\psi}_{i+1}^* \tag{4.21}$$

$$\boldsymbol{\psi}_{i+1} = \frac{\tilde{\boldsymbol{\psi}}_{i+1}}{\left(\tilde{\boldsymbol{\psi}}_{i+1}^T\mathbf{M}\tilde{\boldsymbol{\psi}}_{i+1}\right)^{1/2}} \tag{4.22}$$

In order to account for material nonlinearities, the Ritz vectors applied in Blakeborough et al. (2001) to perform real-time hybrid tests, deviate from the classic Ritz vectors. As previously explained in chapter 2, each vector was taken as the increment in the deformation pattern between various yield stages found from a nonlinear static analysis, and made orthogonal to the other basis vectors.

In the example in section 4.1.1, the expressions in (4.11) and (4.12) used to evaluate the higher order modes were also inspired by (4.19). However, the formula in (4.12) was replaced by a kinematic nonlinear system.

Modal Derivatives

Idelsohn and Cardona (1984, 1985a) introduced at set of higher order basis vectors, $\partial\boldsymbol{\varphi}_i/\partial s_j$, to the LNMs, referred to as modal derivatives. The displacement field, $\mathbf{V}$, can be expanded into a Taylor series around the reference points s_{i0}, with s_i referring to the reduced co-ordinates. In (4.23) a second order expansion is presented:

$$\mathbf{V} = \mathbf{V}_0 + \sum_{j=1}^{N}\frac{\partial\mathbf{V}_0}{\partial s_j}(s_j - s_{j0}) + \frac{1}{2}\sum_{j=1}^{N}\sum_{k=1}^{N}\frac{\partial^2\mathbf{V}_0}{\partial s_j\partial s_k}(s_j - s_{j0})(s_k - s_{k0}) \tag{4.23}$$

By introducing the basis in (4.2) into (4.23), the LNMs, $\boldsymbol{\varphi}_i$, are seen to represent only the first order displacement terms, whereas the modal derivatives, $\partial\boldsymbol{\varphi}_i/\partial s_j$, also contribute to the second order terms, cf. (4.24) and (4.25). Thus, the Taylor series indicate, that modal derivatives will contribute with important information in nonlinear analysis.

$$\frac{\partial \mathbf{V}}{\partial s_j} = \frac{\partial}{\partial s_j}\left(\sum_{i=1}^{N} \boldsymbol{\varphi}_i s_i\right) = \sum_{i=1}^{N} \frac{\partial \boldsymbol{\varphi}_i}{\partial s_j} s_i + \boldsymbol{\varphi}_j \tag{4.24}$$

$$\frac{\partial^2 \mathbf{V}}{\partial s_j \partial s_k} = \sum_{i=1}^{N} \frac{\partial^2 \boldsymbol{\varphi}_i}{\partial s_j \partial s_k} s_i + \frac{\partial \boldsymbol{\varphi}_k}{\partial s_j} + \frac{\partial \boldsymbol{\varphi}_j}{\partial s_k} \tag{4.25}$$

To determine the modal derivatives, a governing system of equations were found in Idelsohn and Cardona (1984, 1985a) by differentiating the linearized eigenvalue problem in (4.14). This yielded the system of equations:

$$\left(\mathbf{K}_T(\mathbf{V}) - \omega_i^2 \mathbf{M}\right) \frac{\partial \boldsymbol{\varphi}_i}{\partial s_j} = \left(\frac{\partial \omega_i^2}{\partial s_j}\mathbf{M} - \frac{\partial \mathbf{K}_T(\mathbf{V})}{\partial s_j}\right) \boldsymbol{\varphi}_i \tag{4.26}$$

The matrix on the left hand side of (4.26) is seen to be identical with the eigenvalue problem in (4.14), which by definition is singular for the given natural frequencies, ω_i. Thus, it is not possible to evaluate the modal derivative from (4.26) in its initial form.

Different ways to handle the singularity issue have been proposed. In Idelsohn and Cardona (1984, 1985a) one suggestion was to set one of the elements in $\partial\boldsymbol{\varphi}_i/\partial s_j$ to a fixed number and only solve for the remaining elements. Another suggestion was to neglect the inertia terms of (4.26), yielding the static formulation:

$$\mathbf{K}_T(\mathbf{V}) \frac{\partial \boldsymbol{\varphi}_i}{\partial s_j} = -\frac{\partial \mathbf{K}_T(\mathbf{V})}{\partial s_j} \tag{4.27}$$

In Slaats et al. (1993) a numerical approach to determine the modal derivates was suggested, cf. (4.28).

$$\frac{\partial \boldsymbol{\varphi}_i}{\partial s_j} \approx \frac{\boldsymbol{\varphi}_i\left(\mathbf{V}_0 + \boldsymbol{\varphi}_j \delta s_j\right) - \boldsymbol{\varphi}_i(\mathbf{V}_0)}{\delta s_j} \tag{4.28}$$

Here $\boldsymbol{\varphi}_i(\mathbf{V}_0 + \boldsymbol{\varphi}_j \delta s_j)$ and $\boldsymbol{\varphi}_i(\mathbf{V}_0)$ were the eigenvectors to the eigenvalue problem in (4.14) based on the tangent stiffness matrices $\mathbf{K}_T(\mathbf{V}_0 + \boldsymbol{\varphi}_j \delta s_j)$ and $\mathbf{K}_T(\mathbf{V}_0)$. Furthermore δs_j represented a small increment. The magnitude of this should also be sufficiently small to ensure precision, but at the same time it should be sufficiently large to avoid round-off errors.

Despite the approximate evaluations of the modal derivatives in (4.27) and (4.28), the higher order terms were stated to include valuable information in nonlinear analysis performed in Idelsohn and Cardona (1984, 1985a) and in Slaats et al. (1993). The modal derivatives have also been applied in combination with the use of Ritz vectors, see e.g. Idelsohn and Cardona (1985b) and Chang and Engblom (1991).

In the present PhD study the modal derivatives have constituted a vital tool. Not only do the modal derivatives include valuable information to nonlinear systems, but the Taylor series in (4.23) also allows the modal derivatives to be included with a minimum of computational expense. This is discussed in more details in the following section. To the best of the authors knowledge, modal derivatives have not yet been applied in a RTHT context.

4.2 Improved Basis Reduction

In the present section three elements contributing to an improved accuracy in real-time simulations are presented. The elements constitute the tools applied and developed in the present PhD study, and consist of:

- An efficient global formulation of the internal restoring forces
- Two modified system of equations governing the modal derivatives
- An efficient basis formulation, based on a Taylor series

The first element listed considers the use of an existing mathematical reformulation of the projected internal restoring forces in (4.6). The formulation can replace the standard element-by-element assembling with a significantly faster global assembling. The second element consists of two sets of improved system of equations governing the modal derivatives, organized by the present author. One is found by proposing a geometric restriction on the modal derivatives in (4.26) in order to remove the singularity. The other consists in the derivation of a novel set of governing systems of equations. The final element consist in using the modal derivatives, to arrange a new efficient basis formulation, based on a Taylor series. This is referred to as a Taylor basis.

As will be demonstrated in the following sections, the three elements help to improve the accuracy in two ways. First of all a set of improved modal derivatives can be determined from the modified system of equations. These improve the accuracy of the coupling activated deformations. Furthermore,

the elements contributing to an improved efficiency, makes it possible to increase number of basis vectors (DOFs), that can be used to span the solution in the real-time simulations.

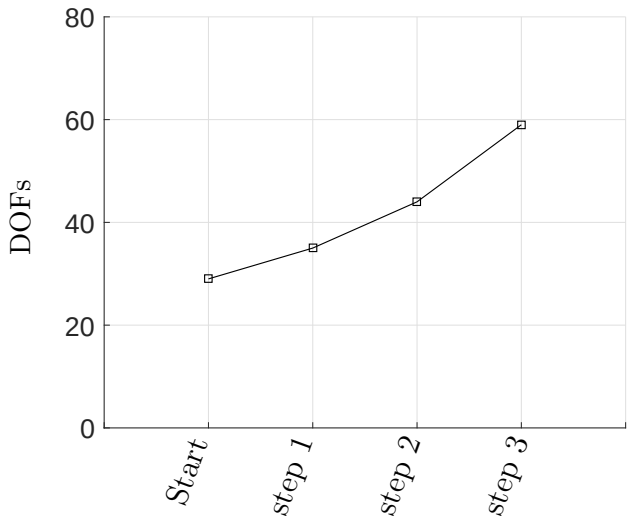

Figure 4.5: Development of real-time DOF capacity for a time step $\Delta t=10^{-3}$ s during the present PhD study.

In Figure 4.5 is plotted the real-time DOF capacity development experienced in the present PhD study, achieved by implementing the three elements. The presented DOF capacity is based on a time step magnitude $\Delta t = 10^{-3}$ s, and takes its starting point at 29 DOFs, found in the example in section 1.2.1. A three step development has followed increasing the real-time DOF capacity to 35, 44 and 59 DOFs, respectively. In round numbers this corresponds to an increase of, respectively, 20%, 50% and 100%, with the 29 DOFs as reference. The first two steps referred to in Figure 4.5 are a consequence of the efficient global formulation of the restoring forces, whereas the third step is achieved by a combining the global formulation with the efficient Taylor basis. The steps are described in more detail in the following along with the three elements.

It should be stressed, that the increase in the real-time DOF capacity in Figure 4.5 is a result based on the authors FEM programmes and computational power. Thus, a similar increase in real-time DOF capacity is not necessarily achieved when implemented on other computers. However, the increase in Figure 4.5 strongly indicates, that the mentioned elements can improve the real-time DOF capacity in the general case.

In the following, each of the above listed elements are considered, starting with the mathematical reformulation of the internal restoring forces.

4.2.1 Global Assembling of the Internal Restoring Forces

To ease the computational costly element-by-element assembling of the internal restoring forces in (4.6), an efficient global assembling in the reduced co-ordinates can be organized. This is done by use of a simple mathematical reformulation technique, initially introduced by Nash (1977).

In kinematic nonlinear systems, the internal restoring forces are typically given on a cubic form in the displacements, cf. Andersen and Poulsen (2015, 2016):

$$\begin{aligned}\mathbf{g}(\mathbf{V}) &= (\mathbf{K}_0 + \mathbf{K}_1(\mathbf{V}) + \mathbf{K}_2(\mathbf{V},\mathbf{V}))\,\mathbf{V} \\ &= \mathbf{K}_S(\mathbf{V},\mathbf{V})\mathbf{V}\end{aligned} \tag{4.29}$$

with $\mathbf{K}_0$ representing the constant linear stiffness matrix and $\mathbf{K}_1(\mathbf{V})$ and $\mathbf{K}_2(\mathbf{V},\mathbf{V})$ representing two stiffness matrices linear and quadratic dependent on the displacement field, respectively. The sum of these three stiffness matrices represent the secant stiffness matrix, $\mathbf{K}_S(\mathbf{V},\mathbf{V})$. With the cubic format in (4.29), the projected internal forces in (4.6) can by mathematical reformulations be written on the form

$$\mathbf{\Phi}^T\mathbf{g}(\mathbf{\Phi}s) = \left(\tilde{\mathbf{K}}_0 + \sum_{i=1}^{N}\tilde{\mathbf{K}}_{1,i}s_i + \sum_{i=1}^{N}\sum_{j=1}^{i}\tilde{\mathbf{K}}_{2,ij}s_is_j\right)\mathbf{s} \tag{4.30}$$

with $\tilde{\mathbf{K}}_0$, $\tilde{\mathbf{K}}_{1,i}$, and $\tilde{\mathbf{K}}_{2,ij}$ being constant coefficient matrices. These are defined as:

$$\tilde{\mathbf{K}}_0 = \mathbf{\Phi}^T\mathbf{K}_0\mathbf{\Phi} \tag{4.31}$$

$$\tilde{\mathbf{K}}_{1,i} = \mathbf{\Phi}^T\mathbf{K}_1(\boldsymbol{\varphi}_i)\mathbf{\Phi} \tag{4.32}$$

$$\tilde{\mathbf{K}}_{2,ij} = \mathbf{\Phi}^T(\mathbf{K}_2(\boldsymbol{\varphi}_i,\boldsymbol{\varphi}_j) + (1-\delta_{ij})\mathbf{K}_2(\boldsymbol{\varphi}_j,\boldsymbol{\varphi}_i))\mathbf{\Phi} \tag{4.33}$$

with the Kronecker delta, δ_{ij}. Introducing the vector $\mathbf{s}$ in (4.30) on the form in (4.34)-(4.35):

$$\mathbf{s} = \sum_{i=1}^{N}\mathbf{I}_is_i \tag{4.34}$$

$$\mathbf{I}_i = \begin{bmatrix}\delta_{1i} & \delta_{2i} & \dots & \delta_{Ni}\end{bmatrix}^T \tag{4.35}$$

the formulation in (4.30) can be written as a sum of constant equivalent force vector coefficients:

$$\mathbf{\Phi}^T\mathbf{g}(\mathbf{\Phi}s) = \sum_{i=1}^{N}\tilde{\mathbf{q}}_{1,i}s_i + \sum_{i=1}^{N}\sum_{j=1}^{i}\tilde{\mathbf{q}}_{2,ij}s_is_j + \sum_{i=1}^{N}\sum_{j=1}^{i}\sum_{k=1}^{j}\tilde{\mathbf{q}}_{3,ijk}s_is_js_k \tag{4.36}$$

The equivalent force vectors in (4.36) are of dimension N×1 and are all constant. Furthermore, they are defined as, cf. Andersen and Poulsen (2015):

$$\tilde{\mathbf{q}}_{1,i} = \tilde{\mathbf{K}}_0 \mathbf{I}_i \tag{4.37}$$

$$\tilde{\mathbf{q}}_{2,ij} = \tilde{\mathbf{K}}_{1,i} \mathbf{I}_j + (1-\delta_{ij}) \tilde{\mathbf{K}}_{1,j} \mathbf{I}_i \tag{4.38}$$

$$\begin{aligned} \tilde{\mathbf{q}}_{3,ijk} = & \mathbf{q}_{ijk} + (\mathbf{q}_{jki} + \mathbf{q}_{kij})(1-\delta_{ij}\delta_{jk}) + \\ & (\mathbf{q}_{ikj} + \mathbf{q}_{kji} + \mathbf{q}_{jik})(1-\delta_{ij})(1-\delta_{jk}) \end{aligned} \tag{4.39}$$

$$\mathbf{q}_{ijk} = \mathbf{\Phi}^T \mathbf{K}_2(\boldsymbol{\varphi}_i, \boldsymbol{\varphi}_j) \mathbf{\Phi} \mathbf{I}_k \tag{4.40}$$

The benefit of using the global formulations in (4.29) and (4.36) to evaluate the projected restoring forces, is that the constant matrix and vector coefficients can be organized prior to the simulations. This is computationally more efficient than the usual element-by-element assembling approach.

The reformulation technique has been applied by different researchers, with a variety of ways to determine the matrix and vector coefficients in (4.30) and (4.36). Some manipulate the FEM equations as indicated by the procedure above, see e.g. Barbic and James (2005) and Shi and Mei (1996). Others determine the coefficients based on a number of nonlinear static solutions, cf. Mcewan et al. (2001), Muravyov and Rizzi (2003) and Brake and Segalman (2010), or by use of experimental data, cf. Spottswood and Allemang (2006).

In Andersen and Poulsen (2014) the real-time potential of the formulation in (4.30) was investigated in combination with the higher order modes introduced in the example in 4.1.1. For the time step magnitude of Δt=10^{-3} s it was found that a real-time simulation with 35 DOFs was possible. This refers to the step 1 in Figure 4.5. Furthermore, the real-time potential of the formulation in (4.36) was investigated in Andersen and Poulsen (2015, 2016). Here it was found that the formulation allowed a real-time capacity of 44 DOFs. This is referred to as step 2 in Figure 4.5. The real-time capacity analysis is presented in section 4.2.3. As previously stated, the real-time DOF capacity increase is based on the present authors computational capacity. However, the achieved real-time DOF increase indicates that the global restoring force formulation is very beneficial.

4.2.2 Modified Governing System of Equations

Next two modified system of equations governing the modal derivatives are presented. According to the Taylor series in (4.23)-(4.25) the modal derivatives are important to include in basis reduction, in order to represent the higher order effects. To avoid using approximate modal derivatives, a modified and a novel set of governing system of equations were derived in Andersen

and Poulsen (2015). One was based on the systems of equations in (4.26) where the singularity was removed by introducing a geometric restriction. The other was a novel system of equations derived by introducing the Taylor series into the free and undamped kinematic nonlinear EOM. These systems are presented in the following.

Geometric Restriction on Modal Derivatives

In Andersen and Poulsen (2015) the singularity of (4.26) was removed by introducing a geometric restriction on the modal derivatives. The solution to (4.26) consist in a homogeneous and a particular solution:

$$\left\{\frac{\partial \boldsymbol{\varphi}_i}{\partial s_j}\right\} = \left\{\frac{\partial \boldsymbol{\varphi}_i}{\partial s_j}\right\}_{Part} + \left\{\frac{\partial \boldsymbol{\varphi}_i}{\partial s_j}\right\}_{Hom} \tag{4.41}$$

The homogeneous solution must be identical to the solution of the eigenvalue problem in (4.14), i.e.

$$\left\{\frac{\partial \boldsymbol{\varphi}_i}{\partial s_j}\right\}_{Hom} = \beta \boldsymbol{\varphi}_i \tag{4.42}$$

with β being a scalar free of choice. It Andersen and Poulsen (2015) it was assumed that the particular and homogenous solutions were orthogonal. Otherwise, part of the information in the two solution parts would be redundant. A geometric restriction was therefore given as:

$$\left\{\frac{\partial \boldsymbol{\varphi}_i}{\partial s_j}\right\}_{Part}^T \left\{\frac{\partial \boldsymbol{\varphi}_i}{\partial s_j}\right\}_{Hom} = \mathbf{0} \tag{4.43}$$

If the governing system of equations in (4.26) are considered to be derived from a minimization condition with the modal derivative as the variable parameter, the Lagrange multiplier method can be applied to introduce the geometric restriction, cf. Belytschko et al. (2000). This yields the following nonsingular systems of equations:

$$\begin{bmatrix} (\mathbf{K}_T(\mathbf{V}) - \omega_i^2 \mathbf{M}) & \boldsymbol{\varphi}_i \\ \boldsymbol{\varphi}_i^T & 0 \end{bmatrix} \begin{Bmatrix} \left\{\frac{\partial \boldsymbol{\varphi}_i}{\partial s_j}\right\}_{Part} \\ \lambda \end{Bmatrix} = \begin{Bmatrix} \left(\frac{\partial \omega_i^2}{\partial s_j}\mathbf{M} - \frac{\partial \mathbf{K}_T(\mathbf{V})}{\partial s_j}\right)\boldsymbol{\varphi}_i \\ 0 \end{Bmatrix} \tag{4.44}$$

with λ being the Lagrange multiplier, which is an additional unknown introduced. In the following the particular modal derivatives determined from (4.44) by inverting the matrix on the left hand side, are referred to as the improved modal derivatives.

Novel Governing System of Equations

Next the derivation of a novel system of equations governing the modal derivatives is presented. Only the main steps are presented in the following. For full details the reader is referred to Andersen and Poulsen (2015).

The starting point of the derivation are the free and undamped discretized kinematic nonlinear equations of motion:

$$\mathbf{M}\ddot{\mathbf{V}} + \mathbf{g}(\mathbf{V}) = \mathbf{0} \tag{4.45}$$

The next step consist in introducing the Taylor series in (4.23) together with (4.24) and (4.25) into the equations in (4.45). When doing so, it is furthermore assumed that the solution to the reduced co-ordinates, s_j, are given as an amplitude, A_j, times a complex exponential function dependent the time, t, and the frequency, $\omega_j(s_k)$:

$$s_j = A_j e^{i\omega_j(s_k)t} \tag{4.46}$$

$$\omega_j(s_k) = \omega_{j0} + \sum_{l=1}^{N} \frac{\partial \omega_{j0}}{\partial s_l}(s_l - s_{l0}) + ... \tag{4.47}$$

The amplitude in (4.46) is assumed to be constant as the free and undamped vibrations are considered, whereas the frequency is assumed to be dependent on the deformation due to the kinematic nonlinear nature of the system. The frequency is formulated as a Taylor series with the subindex 0 referring to the reference point, cf. (4.47). With the introduced assumptions in (4.46)-(4.47), the introduction of the Taylor series in (4.23) into the free and undamped EOM in (4.45) leads to a vector polynomial on the form:

$$\mathbf{A} + \sum_{j=1}^{N} \mathbf{B}_j s_j + \sum_{j=1}^{N}\sum_{k=1}^{N} \mathbf{C}_{jk} s_j s_k + ... = \mathbf{0} \tag{4.48}$$

where $\mathbf{A}$, $\mathbf{B}_j$ and $\mathbf{C}_{jk}$ are vector coefficients and the dots represent higher order terms. As the reduced co-ordinates, s_j, can take on any value, each of the vector coefficients in (4.48) have to be zero to fulfill (4.48). Setting $\mathbf{A}$ equal to zero the EOM are found, setting $\mathbf{B}_j$ equal to zero the eigenvalue problem in (4.14) is found, and setting $\mathbf{C}_{jk}$ equal to zero the system of equations governing the modal derivatives is found.

In Andersen and Poulsen (2015) a kinematic nonlinear Euler-Bernouilli beam element was used in the derivations of the three vector coefficients in (4.48). This lead to the following system of equations governing the modal

derivatives:

$$\left[\mathbf{K}_T(\mathbf{0}) - (\omega_{j0} + \omega_{k0})^2\mathbf{M}\right]\frac{1}{2}\left(\frac{\partial\boldsymbol{\varphi}_k}{\partial s_j} + \frac{\partial\boldsymbol{\varphi}_j}{\partial s_k}\right) = \left[2\frac{\partial\omega_{k0}}{\partial s_j}(\omega_{k0} - \omega_{j0})\mathbf{M} - \frac{\partial\mathbf{K}_S(\mathbf{0})}{\partial s_k}\right]\boldsymbol{\varphi}_j \quad (4.49)$$

The equations in (4.49) were considered for the special case with zero initial deformation, i.e. for s_i=0, as the system of equations would otherwise be implicit dependent on the modal derivatives.

The novel system of equations in (4.49) are seen to govern a sum of two modal derivatives with switched indeces, appearing on the left hand side. These are multiplied by a matrix containing the tangent stiffness subtracted by the mass matrix multiplied by a squared sum of the linear natural frequencies, ω_{j0} and ω_{k0}. On the right hand side the secant stiffness matrix on differentiated form is subtracted from the mass matrix times a frequency coefficient, and multiplied onto the LNM number j. The frequency coefficient is given as two times the difference between two linear frequencies, and a differentiated natural frequency. Furthermore, the left hand side is seen to be symmetric with respect to the indeces j and k. Thus, the same should be valid with respect to the right hand side. Setting the right hand side it equal to itself, but with switched indeces, the following relation can be found for the frequency coefficients, cf. Andersen and Poulsen (2016):

$$2\frac{\partial\omega_{k0}}{\partial s_j}(\omega_{k0} - \omega_{j0}) = \frac{\boldsymbol{\varphi}_j^T}{\boldsymbol{\varphi}_j^T\mathbf{M}\boldsymbol{\varphi}_j}\left(\frac{\partial\mathbf{K}_S(\mathbf{0})}{\partial s_k}\boldsymbol{\varphi}_j - \frac{\partial\mathbf{K}_S(\mathbf{0})}{\partial s_j}\boldsymbol{\varphi}_k\right) \quad (4.50)$$

In the following the modal derivatives evaluated from (4.49) are denoted the novel modal derivatives.

Nonlinear Cable Analysis

In Andersen and Poulsen (2015) the novel modal derivatives and the improved modal derivatives were used to analyse the dynamic response of a highly nonlinear simple supported steel cable, see Figure 4.6.

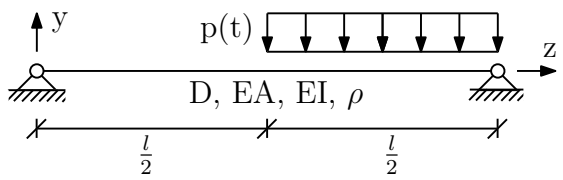

Figure 4.6: Simple supported cable.

The cable was of length l, had a diameter D, a bending stiffness EI, an axial stiffness EA, and a density ρ. Furthermore, the cable was simple supported in both ends and loaded by a harmonic line load p(t):

$$\mathrm{p}(t) = \mathrm{F}_1 sin(\omega_1 t) + \mathrm{F}_2 sin(\omega_2 t) \tag{4.51}$$

ω_1 and ω_2 represented the frequencies of the first and second bending modes, and F_1 and F_2 represented two load amplitudes. The applied parameters are listed in Table 4.3.

Table 4.3: Cable and load parameters.

Parameter	Unit	Formula	Magnitude
l	m	-	20
E	GPa	-	210
D	m	-	$50{\cdot}10^{-3}$
A	m^2	$\pi(D/2)^2$	$2{\cdot}10^{-3}$
I	m^4	$\pi\frac{D^4}{64}$	$3.07{\cdot}10^{-7}$
F_1	N/m	-	-1
F_2	N/m	-	-3
ω_1	rad/s	-	1.60
ω_2	rad/s	-	6.40
ρ	$\mathrm{kg/m}^3$	-	7800

To model the response of the numerical substructure, a plane Euler-Bernoulli element with a nonlinear strain measure was applied. The element had two nodes with three DOFs in each node; two translations, u_{ix} and u_{iy}, and one ration, θ_i, i ϵ [1;2]. The element is sketched in Figure 4.7, with l denoting the element length. The transverse displacements and horizontal displacements were approximated by second and first order shape functions, respectively. A detailed description of the element is given in Andersen and Poulsen (2015).

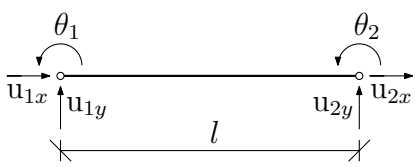

Figure 4.7: Plane Euler-Bernoulli beam element.

The nonlinear strain strain measure, ε, was taken as the Lagrange strain measure, cf. (4.52), with u denoting the axial deformation of a beam fiber

and w the transverse deformation.

$$\varepsilon = \frac{\partial u}{\partial x} + \frac{1}{2}\left(\frac{\partial w}{\partial x}\right)^2 \tag{4.52}$$

With the given element, the model required a discretization with 21 elements, corresponding to 59 free DOFs, for the displacements to converge. In Figure 4.8a a ten seconds response of the transverse deformation in the cable midpoint is plotted, with a close up in Figure 4.8b. All of the curves were simulated by use of the CDM. The solid curve (NC) represents the converged

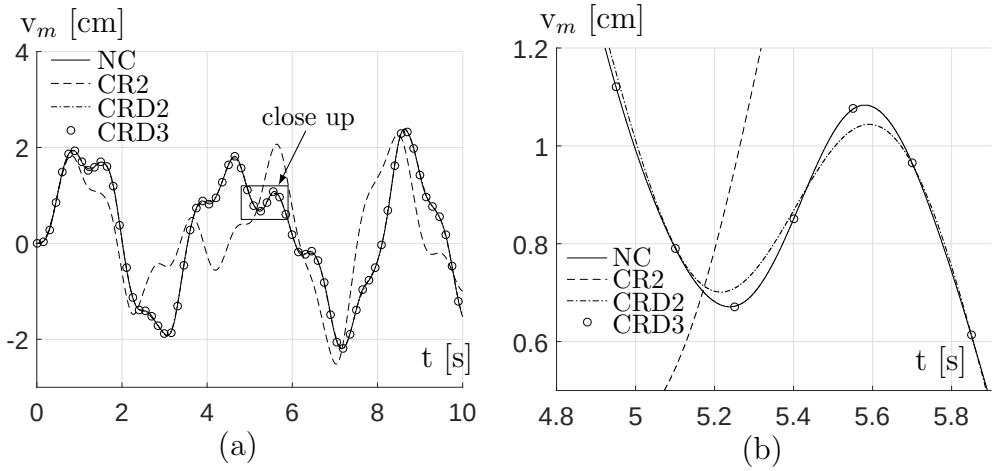

Figure 4.8: Transverse deformation of cable midpoint based on nonlinear central difference method (NC) and three reduced bases with modal derivatives (CRD) and without modal derivatives (CR) considering (a) a 10 seconds interval and (b) a close up.

solution of the 59 DOF model. The remaining three curves were found by use of basis projection. The dashed curve (CR2) represented a reduced basis with the first two LNMs of the cable, the dash-dotted curve (CRD2) included the first two LNMs and three modal derivatives, and the final curve (CRD3) contained three LNMs and six modal derivatives. The included modal derivatives were organized on the form in (4.53), with N representing the number of LNMs. This form was used to be able to directly compare the novel modal derivatives and the modified modal derivatives determined from (4.49) and (4.44), respectively. To ease notation the applied modal derivatives in (4.53) are referred to as $\partial\boldsymbol{\varphi}_{ij}$.

$$\partial\boldsymbol{\varphi}_{ij} = \frac{\partial\boldsymbol{\varphi}_i}{\partial s_j} + (1-\delta_{ij})\frac{\partial\boldsymbol{\varphi}_j}{\partial s_i} \quad , \quad \mathrm{i,\ j}\ \epsilon\ [1;\mathrm{N}]\ \wedge\ \mathrm{j} \leq \mathrm{i} \tag{4.53}$$

From Figure 4.8a the CR2 curve is seen to diverge significantly from the converged solution. However, by considering the CR2D curve, the response is seen to improve significantly by including the associated modal derivatives. Furthermore, from the close up in Figure 4.8b it is verified that a more or less converged solution required a basis containing three LNMs and the associated modal derivatives. The projection based simulation CRD3 reduced the computational time by more than 100 times compared to the full 59 DOF simulation. This time reduction was attributed the small basis size and the implementation of the restoring force formulation in (4.36).

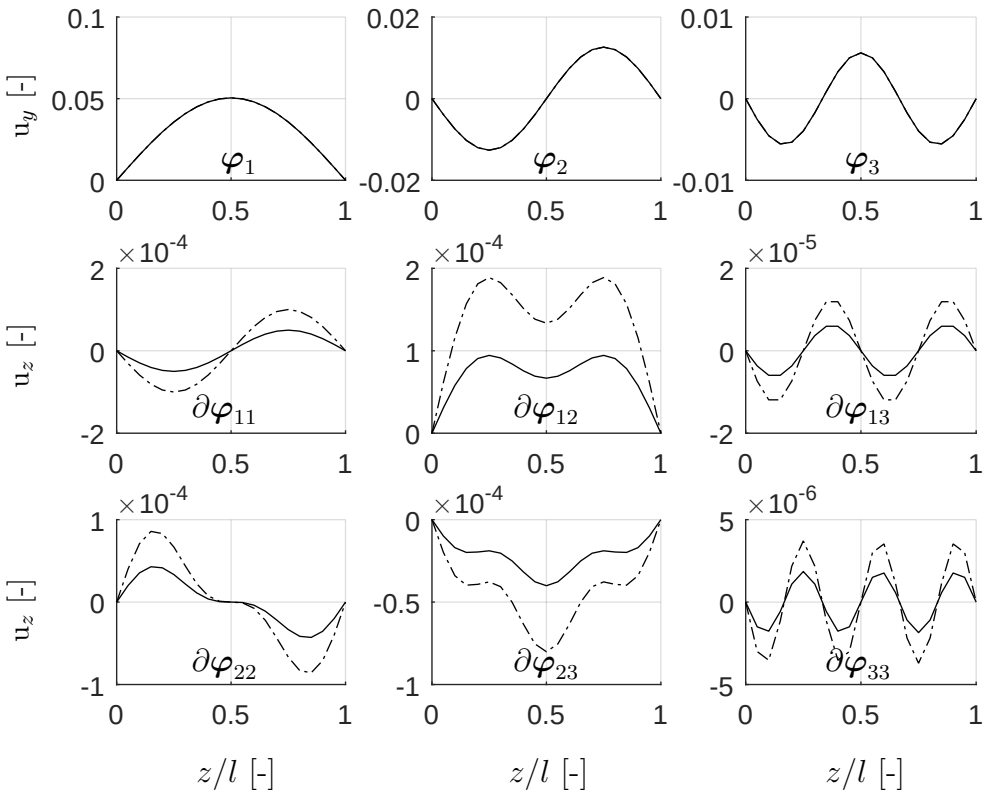

Figure 4.9: Linear basis vectors and modal derivatives used for analysis of nonlinear steel cable.

The results of the reduced basis formulations in Figure 4.8 were found by use of the novel modal derivatives. However, identical results were achieved when replacing the novel modal derivatives with the modified modal. The basis vectors used in the converged solution are plotted in Figure (4.9). In the top of the figure the first three LNMs, $\boldsymbol{\varphi}_i$, are shown. These contained only deformation transverse to the beam in the (y,z)-plane. The remaining

plots represent the modal derivatives, which all represented deformations in the beam length. The solid lines represent the novel modal derivatives and the dashed-dotted curves the modified modal derivatives, all in unscaled size. The shape of the modal derivatives are seen to be alike, but the amplitude of the modified modal derivatives are approximately twice the amplitude of the novel modal derivatives. Compared to the magnitude of the LNMs, the modal derivatives are seen to be very small. Moreover, a general trend of the modal derivatives is, that the number of local minima and maxima are higher than in their respective LNM.

Based on the fact that the novel modal derivatives and the modified modal derivatives yielded identical result, it could not be concluded if the one derivative was more exact than the other. A further analysis of the difference between the modal derivatives was therefore performed. This is discussed in the following.

Relation Between The Reduced Co-ordinates

A further evaluation of the modal derivatives was performed in Andersen and Poulsen (2015). Considering the Taylor series in (4.23) for s_{i0}=0 with (4.24) and (4.25) inserted, this can be written as:

$$\mathbf{V}(\mathbf{s}) = \sum_{i=1}^{N} \boldsymbol{\varphi}_i s_i + \sum_{i=1}^{N} \sum_{j=i}^{N} \left(\frac{\partial \boldsymbol{\varphi}_i}{\partial s_j} + \frac{\partial \boldsymbol{\varphi}_j}{\partial s_j} \right) s_i s_j \tag{4.54}$$

From (4.54) the co-ordinates of the modal derivatives are predicted to be given as a product of the LNM co-ordinates. In the analysis of the cable in Figure 4.6 the reduced bases were organized on the form in (4.55) - (4.57):

$$\mathbf{V} = \mathbf{\Phi}\mathbf{s} \tag{4.55}$$

$$\mathbf{\Phi} = \begin{bmatrix} \boldsymbol{\varphi}_1 & \boldsymbol{\varphi}_2 & \boldsymbol{\varphi}_3 & \partial\boldsymbol{\varphi}_{11} & \partial\boldsymbol{\varphi}_{12} & \partial\boldsymbol{\varphi}_{13} & \partial\boldsymbol{\varphi}_{23} & \partial\boldsymbol{\varphi}_{33} \end{bmatrix} \tag{4.56}$$

$$\mathbf{s} = \begin{bmatrix} s_1 & s_2 & s_3 & s_4 & s_5 & s_6 & s_7 & s_8 \end{bmatrix}^T \tag{4.57}$$

The co-ordinates s_1 to s_3 represent the co-ordinates of the LNMs, and s_4 to s_8 represent the co-ordinates of the modal derivatives.

In Andersen and Poulsen (2015) it was found that the modal derivative $\partial\boldsymbol{\varphi}_2/\partial s_2$ was given as the linear relation in (4.58). Thus, the mode $\partial\boldsymbol{\varphi}_2/\partial s_2$ was not included in the basis in (4.55).

$$\frac{\partial \boldsymbol{\varphi}_2}{\partial s_2} = -\frac{3}{8}\left(\frac{\partial \boldsymbol{\varphi}_1}{\partial s_3} + \frac{\partial \boldsymbol{\varphi}_3}{\partial s_1} \right) - \frac{1}{4}\frac{\partial \boldsymbol{\varphi}_1}{\partial s_1} \tag{4.58}$$

By introducing the relation in (4.58) into the Taylor series in (4.54), and comparing the Taylor series with the basis in (4.55), the relations between the reduced co-ordinates in (4.59)-(4.63) were identified.

$$s_4 = s_1^2 - \frac{1}{4}s_2^2 \tag{4.59}$$

$$s_5 = s_1 s_2 \tag{4.60}$$

$$s_6 = s_1 s_3 - \frac{3}{8}s_2^2 \tag{4.61}$$

$$s_7 = s_2 s_3 \tag{4.62}$$

$$s_8 = s_3^2 \tag{4.63}$$

In Figure 4.10 the relation in (4.59), based on the results from the cable analysis, is plotted. Figure 4.10a represents the case using the novel modal derivatives and Figure 4.10b represents the case using the modified modal derivatives. The plots show, that the co-ordinates of the novel modal derivatives fulfill the Taylor prediction, whereas the co-ordinates of the modified modal derivatives do not. In the case with the modified modal derivatives, the shape of the two relations plotted are similar, but a magnitude of about two separates them. The same observations were made by plotting the remaining relations in (4.60)-(4.63).

Based on these observation, the novel governing system of equations in (4.49) were concluded to be exact. In Andersen and Poulsen (2015) it was furthermore argued that the reason why the modified modal derivatives did not fulfill the Taylor series, was that the original governing system of equations in (4.26) were based on a linearized problem.

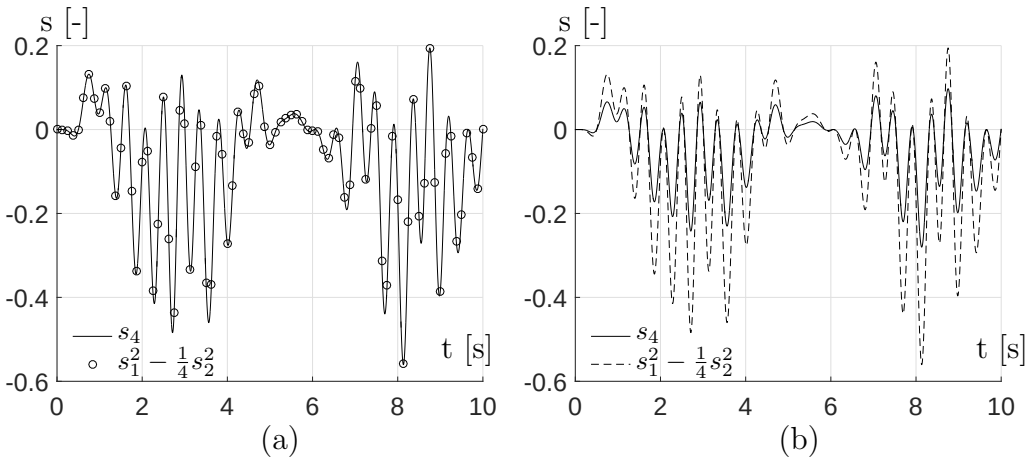

Figure 4.10: Plot of the co-ordinates s_4 and $s_1^2 - \frac{1}{4}s_2^2$ based on (a) the novel modal derivatives and (b) the modified modal derivatives.

4.2.3 The Taylor Basis

Next an efficient basis formulation introduced in Andersen and Poulsen (2016) is presented. The basis is based on the Taylor series in (4.54) and is referred to as a Taylor Basis. By utilizing the symmetry of the higher order terms in (4.54) this can be written as:

$$\begin{aligned}\mathbf{V}(\mathbf{s}) &= \sum_{i=1}^{N} \boldsymbol{\varphi}_i s_i + \sum_{i=1}^{N} \sum_{j=i}^{i} \left(\frac{\partial \boldsymbol{\varphi}_i}{\partial s_j} + (1-\delta_{ij}) \frac{\partial \boldsymbol{\varphi}_j}{\partial s_j} \right) s_i s_j \\ &= \boldsymbol{\Phi}_T \mathbf{s}_T \end{aligned} \tag{4.64}$$

where $\boldsymbol{\Phi}_T$ represents a Taylor basis matrix and $\mathbf{s}_T$ the reduced Taylor coordinates. These are organized as:

$$\boldsymbol{\Phi}_T = \left[\boldsymbol{\varphi}_1, \quad \boldsymbol{\varphi}_2, \quad ..., \quad \boldsymbol{\varphi}_N, \quad \tfrac{\partial \boldsymbol{\varphi}_1}{\partial s_1}, \quad \left(\tfrac{\partial \boldsymbol{\varphi}_1}{\partial s_2} + \tfrac{\partial \boldsymbol{\varphi}_2}{\partial s_1} \right), \quad ..., \quad \tfrac{\partial \boldsymbol{\varphi}_N}{\partial s_N} \right] \tag{4.65}$$

$$\mathbf{s}_T = \left[s_1, \quad s_2, \quad ..., \quad s_N, \quad s_1^2, \quad s_2 s_1, \quad ..., \quad s_N^2 \right]^T \tag{4.66}$$

By using the basis formulation, $\mathbf{V} = \boldsymbol{\Phi}_T \mathbf{s}_T$, the N LNMs and their $\frac{1}{2}$(N+N^2) associated modal derivatives evaluated by use of (4.49), can be included in a system with only N unknowns. In the following it will be illustrated, that this is an efficient way to include the modal derivatives.

In Brake and Segalman (2010) a similar formulation to the one proposed in (4.64) was suggested, considering the special case of Von Kármán plates. In the present case the displacement field was also approximated by a second order Taylor series, with the out of plane displacement assumed to represent the linear deformations and the membrane displacements to represent the second order displacements. However, the higher order displacement fields were approximated from a number of nonlinear static deformation cases using finite difference approximations.

In Andersen and Poulsen (2016) the higher order displacement fields were directly evaluated from the governing system of equations in (4.49). This approach appears to be more straight forward, and in this way the inertia effects are also accounted for. Furthermore, in Andersen and Poulsen (2016) the basis formulation was combined with the global formulation of the internal restoring forces, and an in depth analysis of the efficiency, accuracy and stability of the combination was investigated.

Taylor Projection and Transformation

When projecting the EOM onto a Taylor basis, an additional transformation is required before the equations can be solved, due to the quadratic co-

ordinates in (4.66). Projecting the EOM onto a Taylor basis yields:

$$\hat{\mathbf{m}}\ddot{\mathbf{s}}_T + \hat{\mathbf{c}}\dot{\mathbf{s}}_T + \mathbf{g}(\mathbf{s}_T) = \hat{\mathbf{f}}(t) \tag{4.67}$$

with the projected stiffness, mass, force and damping terms defined as;

$$\hat{\mathbf{m}} = (\mathbf{\Phi}_T)^T\mathbf{M}(\mathbf{\Phi}_T) \tag{4.68}$$

$$\hat{\mathbf{c}} = (\mathbf{\Phi}_T)^T\mathbf{C}(\mathbf{\Phi}_T) \tag{4.69}$$

$$\hat{\mathbf{g}}(\mathbf{s}_T) = (\mathbf{\Phi}_T)^T\mathbf{g}(\mathbf{\Phi}_T\mathbf{s}_T) \tag{4.70}$$

$$\hat{\mathbf{f}} = (\mathbf{\Phi}_T)^T\mathbf{F}(t) \tag{4.71}$$

The projected system of equations (4.67) is a nonlinear expression in the unknown co-ordinates (s_i,$\dot{s}_i$,$\ddot{s}_i$). However, in order to solve the system, it has to be linear in the unknown co-ordinates. Thus, a transformation from the ($\mathbf{s}_T$,$\dot{\mathbf{s}}_T$,$\ddot{\mathbf{s}}_T$) co-ordinates to the ($\mathbf{s}$,$\dot{\mathbf{s}}$,$\ddot{\mathbf{s}}$) co-ordinates is required. In Andersen and Poulsen (2016), it was shown, that by introduction of two transformation matrices denoted $\mathbf{U}(\mathbf{s})$ and $\mathbf{P}(\dot{\mathbf{s}})$, the transformed EOM can be written on the form:

$$\bar{\mathbf{m}}\ddot{\mathbf{s}} + \bar{\mathbf{c}}(\mathbf{s},\dot{\mathbf{s}})\dot{\mathbf{s}} + \bar{\mathbf{g}}(\mathbf{s}) = \bar{\mathbf{f}}(\mathbf{s},t) \tag{4.72}$$

with the mass, damping and force vectors defined as

$$\bar{\mathbf{m}} = \mathbf{U}(\mathbf{s})^T\hat{\mathbf{m}}\mathbf{U}(\mathbf{s})^T \tag{4.73}$$

$$\bar{\mathbf{c}}(\mathbf{s},\dot{\mathbf{s}}) = \mathbf{U}(\mathbf{s})^T\left[2\hat{\mathbf{m}}\mathbf{P}(\dot{\mathbf{s}}) + \hat{\mathbf{c}}\mathbf{U}(\mathbf{s})\right] \tag{4.74}$$

$$\bar{\mathbf{g}} = \mathbf{U}(\mathbf{s})^T\hat{\mathbf{g}}(\mathbf{\Phi}_T\mathbf{s}_T) \tag{4.75}$$

$$\bar{\mathbf{f}} = \mathbf{U}(\mathbf{s})^T\hat{\mathbf{f}}(t) \tag{4.76}$$

As the transformation matrices $\mathbf{U}(\mathbf{s})$ and $\mathbf{P}(\dot{\mathbf{s}})$ are dependent on the variables ($\mathbf{s}$,$\dot{\mathbf{s}}$), these have to be evaluated in between each time step in the time integration.

Furthermore, in Andersen and Poulsen (2016) the projected internal restoring forces in (4.70) were written on a global form in the reduced co-ordinates, by use of the method introduced in section (4.2.1). Due to the second order co-ordinates in $\mathbf{s}_T$, the global restoring force assembling became a sixth order polynomial on the form:

$$\begin{aligned}(\mathbf{\Phi}_T)^T\mathbf{g}(\mathbf{\Phi}_T\mathbf{s}_T) = &\sum_{i=1}^{N}\hat{\mathbf{q}}_{1,i}s_i + \sum_{i=1}^{N}\sum_{j=1}^{i}\hat{\mathbf{q}}_{2,ij}s_is_j + ...+ \\ &\sum_{i=1}^{N}\sum_{j=1}^{i}\sum_{k=1}^{j}\sum_{l=1}^{k}\sum_{m=1}^{l}\sum_{n=1}^{m}\tilde{\mathbf{q}}_{6,ijklmn}s_is_js_ks_ls_ms_n\end{aligned} \tag{4.77}$$

The mathematical definitions of the vectors coefficients in (4.77), and the matrices $\mathbf{U}(\mathbf{s})$ and $\mathbf{P}(\dot{\mathbf{s}})$ are given in Andersen and Poulsen (2016).

Frame Analysis

To investigate the precision, efficiency, and stability of the Taylor basis formulation in (4.64) with the sixth order formulation of the internal restoring forces, cf. (4.77), a highly nonlinear frame was considered in Andersen and Poulsen (2016). The geometry of the frame is sketched in Figure 4.11.

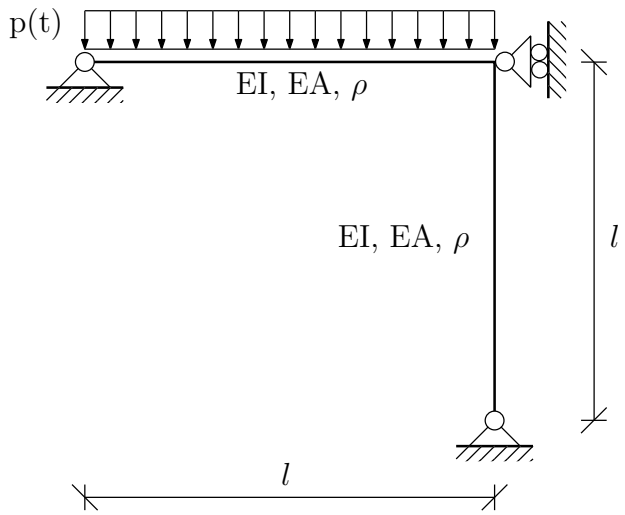

Figure 4.11: Simple frame.

It consisted of a horizontal beam and a vertical beam both with a bending stiffness EI, an axial stiffness EA and a density, ρ. Furthermore the frame was simple supported. To enhance the kinematic nonlinear effects, the frame corner was restricted from horizontal displacements. To excite the frame the horizontal beam part was loaded by a harmonic line load p(t) given by the formula:

$$\mathrm{p}(t) = \mathrm{A} \cdot sin(\omega t) \tag{4.78}$$

with A denoting the load amplitude and ω the excitation frequency. The latter was set equal to the frequency of the first bending mode of the frame. In Table 4.4 the frame and load parameters are presented.

In addition to comparing the precision and efficiency of the Taylor basis with a full FEM model of the frame, it was also compared with the standard linear basis formulation, cf. (4.2). The modal derivatives were also included in the linear basis formulation, but with independent reduced co-ordinates as in the cable analysis, cf. (4.55)-(4.57). In the following the simulations performed with the Taylor basis and the linear basis formulations are referred to as the Taylor reduced basis formulation (TRBF) and the linear reduced basis formulation (LRBF).

Table 4.4: Frame and load parameters.

Parameter	Unit	Formula	Magnitude
l	m	-	10
E	GPa	-	210
D	m	-	0.05
A	m^2	$\frac{\pi}{4}D^2$	$2{\cdot}10^{-3}$
I	m^4	$\frac{\pi}{64}D^4$	$3.07{\cdot}10^{-7}$
F	N/m	-	-3
ω	rad/s		6.40
ρ	kg/m^3	-	7800

The Frame was modelled by use of the kinematic nonlinear plane Euler-Bernoulli element used for the cable analysis in section 4.2.2. When simulating the response of the frame, a model with 40 elements, corresponding to 118 free DOFs, were required for the displacements to converge. By use of the TRBF, a converged response was achieved by including a basis with six LNMs and their twenty-one associated modal derivatives. The same was valid for the LRBF. All of the simulations were performed by use of the CDM.

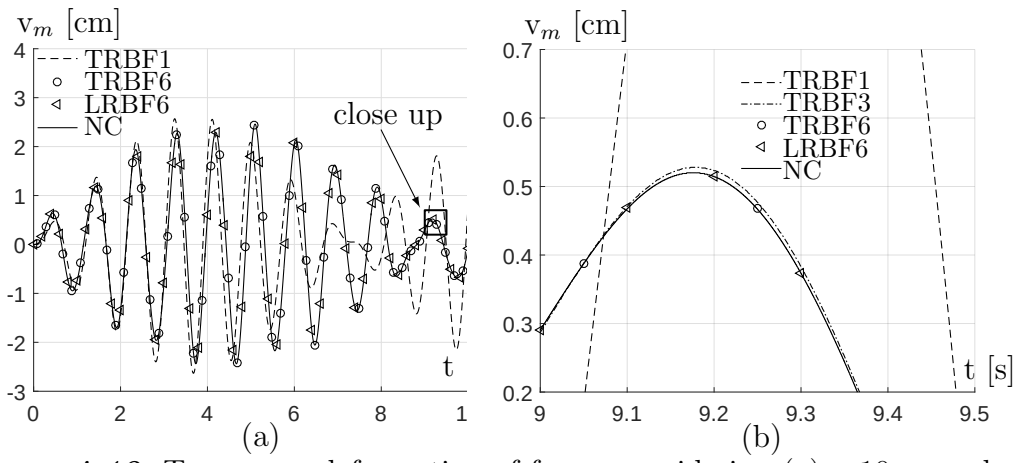

Figure 4.12: Transverse deformation of frame considering (a) a 10 second interval and (b) a close up.

In Figure 4.12 the center displacement of the frame beam, perpendicular to the length direction, is plotted. The NC curve represents the full FEM model, with 118 DOFs. Furthermore, three TRBF responses are plotted, with respectively one, three and six LNMs, marked by the number at the end of the figure legend. Also the LRBF with six LNMs is shown. From

Figure 4.12 the TRBF1 is seen to diverge significantly from the converged solution. To obtain a more or less converged solution with the TRBF, six LNMs were required, as stated previously. Identical results were found by use of the LRBF with six LNMs. Based on these observations, the LRBF and the TRBF were seen to exhibit equal precision.

It was found that the TRBF was approximately eight-hundred times faster than the full 108 DOFs model solution, and twenty times faster than the LRBF, in the converged case. The significant time reduction achieved by using the TRBF was attributed to the efficient global assembling of the internal restoring forces, the small basis applied and the use of a relatively large time step magnitude. In order to maintain the stability and accuracy of the simulations, the 108 DOF model required a time step of $\Delta t=4.5\cdot10^{-5}$ s. Using the LRBF the time step could be increased to $\Delta t=10^{-4}$ s. Increasing the two time step magnitudes further, instability occurred. However, when using the TRBF a time step of magnitude of $\Delta t=10^{-3}$ s was sufficient, both to ensure accuracy and stability. Actually, the time step could be increased even further, but this would introduce visible errors in the displacements. These observations indicated that a significant improved stability is obtained by using the TRBF compared to a standard basis formulation, as the LRBF. The stability of the TRBF is considered in more detail at the end of the present chapter.

Linear Dependent Modal Derivatives

In the analysis of the frame, it was found, that for seven or more LNMs, some of the associated modal derivatives became linear dependent on each other. For seven LNMs, two linear dependent modal derivatives existed. This amount increased concurrently with the size of the Taylor basis, and for twelve LNMs, the number had increased to twenty-eight. However, it seems, that if the size and complexity of the structures are increased, then the number of LNMs can be increased before before linear dependent modal derivatives are introduced. In the cable example in section 4.2.2 the first linear dependent modal derivative was introduced for three LNMs. The frame example increased slightly in complexity, with two elements connected in a nonzero angle and with non-symmetric supports. In the given case the first linear dependent modes were for seven LNMs, as stated above.

In conventional basis reduction methods, the linear dependent basis vectors have to be removed from the basis, in order to avoid singularities. However, when removing a linear dependent mode, this has no influence on the simulated response. The remaining basis vectors will just 'fill in' for the 'missing' contribution of the removed linear dependent modes. This was il-

lustrated in the cable example in section 4.2.2, where the linear dependent modal derivative, given by the relation in (4.58), was removed from the basis. To 'fill in' for the 'missing' contribution of the linear dependent mode, the co-ordinates of the remaining modal derivatives were given by the relations in (4.59)-(4.63), in order to fulfill the Taylor series.

In the Taylor basis formulation the singularity is automatically removed with the transformations of the projected EOM into the ($\mathbf{s}$,$\dot{\mathbf{s}}$,$\ddot{\mathbf{s}}$) co-ordinates, cf. (4.72). It is, therefore, not necessary to remove the linear dependent modes. Furthermore, as the co-ordinates of the modal derivatives are approximated as a product of the LNMs co-ordinates, the contribution that will be 'missing' in case the linear dependent modes are removed, will not be compensated for by the remaining modal derivatives. However, when the Taylor formulation is applied, the linear dependent modes should not be included in the basis (DOF) counting. Thus, in case many linear dependent modal derivatives exist, using the Taylor basis formulation to include their contribution, can possibly be considered as an expensive way to include the modal derivatives. In such potential cases, other approaches to include the modes, can maybe be considered. In the present study, however, it has been chosen to keep the initial formulation. Alternative approaches for reorganizing the terms in case of many linear dependent modes exist, can serve as a potential future research subject.

Real-time Simulations with the Taylor Basis

A further analysis of the efficiency of the Taylor basis was made in Andersen and Poulsen (2016). For this the real-time DOF capacity was considered. For comparison, the efficiency of the linear basis formulation in (4.2) was also considered. In the following these are referred to as the Taylor reduced basis formulation (TRBF) and the linear reduced basis formulation (LRBF). For simplicity the formulations were compared for a similar time step magnitude of Δt=1 ms. Thus, the improved stability of the TRBF was not accounted for in the comparison. This is considered in a separate analysis in the following section.

Two cases were considered in the analysis. In the first case the frame in Figure (4.11), with dependent modes, was considered. However, in the given case the linear dependent modes were not included in the counting of the number of DOFs. In the second case the linear dependencies were 'removed', by changing a tolerance in the simulations. This allowed all of the basis vectors to be accounted for in the DOF counting. Thus, the second case represented an idealised case. The point of 'removing' the linear dependencies, was to be able to investigate the full potential of the TRBF in case linear

dependent modes do not exist. As discussed in the previous section, it is expected that such cases exist as the complexity of the models is increased. In this perspective the analysis is valid.

In Figure 4.13a a plot illustrating the simulation time spent on simulating a ten seconds long response of the frame in Figure 4.11 is shown. It includes a varying number of modes, N_S, representing the sum of LNMs and modal derivatives without the inclusion of the number of linear dependent modes. Furthermore, the values above the horizontal dashed line represents the simulations exceeding the real-time requirement, and the simulations below the horizontal line are the simulations within the real-time requirement. Moreover, Figure 4.13b shows the relative time ratio between the two curves in Figure 4.13a given as

$$r_t = \frac{t_{TRBF}}{t_{LRBF}} \tag{4.79}$$

Furthermore, the curve r_l represents a lower bound estimate for the relative computational time, r_t, given as the ratio between the amount of operations involved in the evaluation of the internal restoring forces in (4.36) and (4.77). For details about this, see Andersen and Poulsen (2016).

Three curves are presented. The t_{LRBF} curve represents the simulation time using the LRBF, and the t^*_{TRBF} curve and the t_{TRBF} curve represent the simulation times when using the TRBF. The t^*_{TRBF} curve represents the case where linear dependent modes exist, and the t_{TRBF} curve the case where the linear dependencies have been 'removed'. The marks a, b and c represent equivalent points of the two TRBF curves, i.e. with equally many modes. However, as the linear dependent modes are not included in the DOF counting, the t^*_{TRBF} curve this is displaced to the left in relation to the t_{TRBF} curve. Furthermore, when linear dependent modes are present, the formulation of the transformation matrices are changed a little, causing the simulation time in the points a, b and c to decrease. A more detailed description of this is given in Andersen and Poulsen (2016). As the number of modal derivatives are dictated by the formulation in (4.64), the increase of N_S from step to step is fixed. Furthermore, the results are all based on the central difference method.

From Figure 4.13a it is seen that the computational time is increasing as a nonlinear function of the number of modes, N_S. This is expected due to the nonlinear formulation of the global restoring forces, see (4.36) and (4.77). The t_{LRBF} curve is seen to increase more rapidly than the other curves. The t_{TRBF} curve and the t^*_{TRBF} curve are initially identical up to N_S=27, corresponding to six LNMs. Then the linear dependent modes are introduced, and the t^*_{TRBF} experience a more rapid increase. The two TRBF

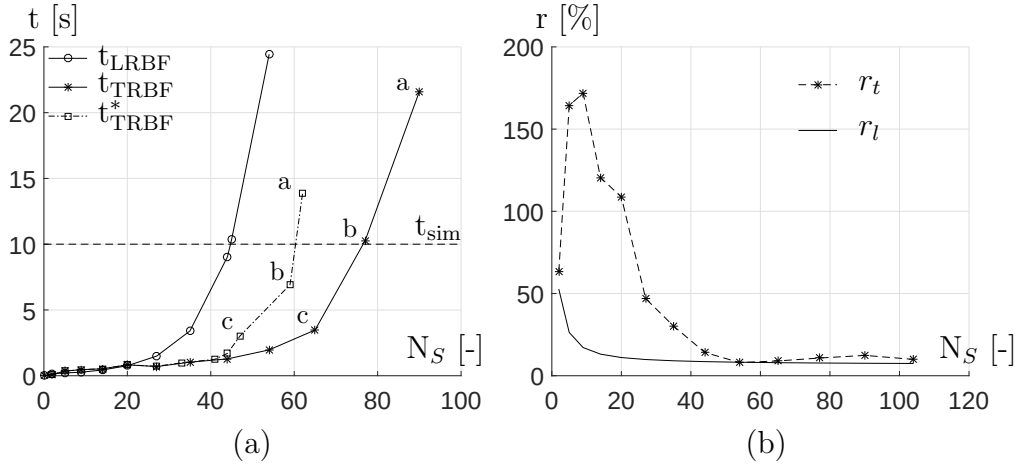

Figure 4.13: Simulation time using the Taylor basis formulation, t_{TRBF}, and the linear basis formulation, t_{LRBF}, as a function of the sum of LNMs and modal derivatives, N_s.

solution curves exceed the real-time limit going from 59 to 62 DOFs and from 65 to 77 DOFs, respectively. The LRBF exceeds the real-time limit going from 44 to 45 DOFs. Thus, a significant increase the DOF capacity is seen to be achieved by use of the TRBF. The 59 DOF real-time capacity marks the third step in Figure 4.5. This corresponds to an increase of approximately 100% in the DOF capacity, with 29 DOFs as the reference.

To get an idea of the full potential of the TRBF, the relative time ratio r_t in Figure 4.13b is considered. The ratio is seen to start at about 60% for N_S equal to two and initially increase for an increasing number of modes. It reaches a maximum value at nine DOFs of approximately 170%. Then a rapid decrease takes place for a further increase in the number of DOFs until a minima of about 7% is reached at 54 DOFs. Beyond this point the curve is seen to fluctuate a little, but it is seen to remain in the domain of one order of magnitude, which is close to the lower bound estimate, r_l.

The initial increase in r_t is attributed to operations involved in the transformations, which were dominant for small systems. For an increasing number of modes the evaluation of the restoring forces became dominant. However, due to the Taylor basis formulation, where the number of unknowns correspond to the number of LNMs only, this required significantly less operations than in the LRBF, and the ratio, r_t, is therefore significantly decreased. Thus, based on the results in Figure 4.13b the LRBF is mainly seen to more efficient for less than twenty modes. However, beyond this point the TRBF is significantly more efficient than the LRBF.

Stability of the Taylor Basis

In the following the stability of the TRBF is considered in more detail. As was reported in the analysis of the simple frame in Figure 4.11, the TRBF exhibited a significantly higher stability compared to the LRBF. This was despite the fact that the same basis vectors were included in the two formulations.

In Andersen and Poulsen (2016) the stability limit, quantified by the time step magnitudes, was analysed for a wide interval of frequencies. For this a LRBF and a TRBF, both containing one LNM and its modal derivative, were used to simulate the response of the simple frame. The basis formulations are presented in (4.80) and (4.81) with the subindexes L and T referring to the LRBF and the TRBF, respectively.

$$\mathbf{V}_L = \left[\boldsymbol{\varphi}_1, \quad \frac{\partial \boldsymbol{\varphi}_1}{\partial s_1}\right] \begin{Bmatrix} s_1 \\ s_2 \end{Bmatrix} \tag{4.80}$$

$$\mathbf{V}_T = \left[\boldsymbol{\varphi}_1, \quad \frac{\partial \boldsymbol{\varphi}_1}{\partial s_1}\right] \begin{Bmatrix} s_1 \\ s_1 s_1 \end{Bmatrix} \tag{4.81}$$

The frequencies associated with the basis vectors $\boldsymbol{\varphi}_1$ and $\partial\boldsymbol{\varphi}_1/\partial s_1$ were ω_L and ω_H, respectively. The latter was approximated by use of Rayleigh's quotient

$$\omega_H^2 = \frac{\left\{\frac{\partial \boldsymbol{\varphi}_1}{\partial s_1}\right\}^T \mathbf{K}_T \left\{\frac{\partial \boldsymbol{\varphi}_1}{\partial s_1}\right\}}{\left\{\frac{\partial \boldsymbol{\varphi}_1}{\partial s_1}\right\}^T \mathbf{M} \left\{\frac{\partial \boldsymbol{\varphi}_1}{\partial s_1}\right\}} \tag{4.82}$$

In Figure 4.14 the time step stability limits, as a function of the frequency magnitudes, are presented. Figure 4.14a shows the stability limit of the TRBF, Δt_{TRBF}, and Figure 4.14b shows the LRBF stability limit, Δt_{LRBF}. The time step magnitudes Δt_L and Δt_H refer to the time step limits evaluated by use of (3.40):

$$\Delta t_L = \frac{2}{\omega_L} \quad , \quad \Delta t_H = \frac{2}{\omega_H} \tag{4.83}$$

In order to vary the frequencies of the frame, the density, ρ, was continuously changed. The marks (*) named a, b, c etc. in the two plots in Figure 4.14, correspond to same density "state".

As illustrated in Figure 4.14a the stability of the TRBF was very close to the theoretical stability based on the LNM frequency, Δt_L. For the frequency domain considered the maximum deviation between the stability limits Δt_{TRBF} and Δt_{L} was just below 30%, with Δt_{L} taken as the reference

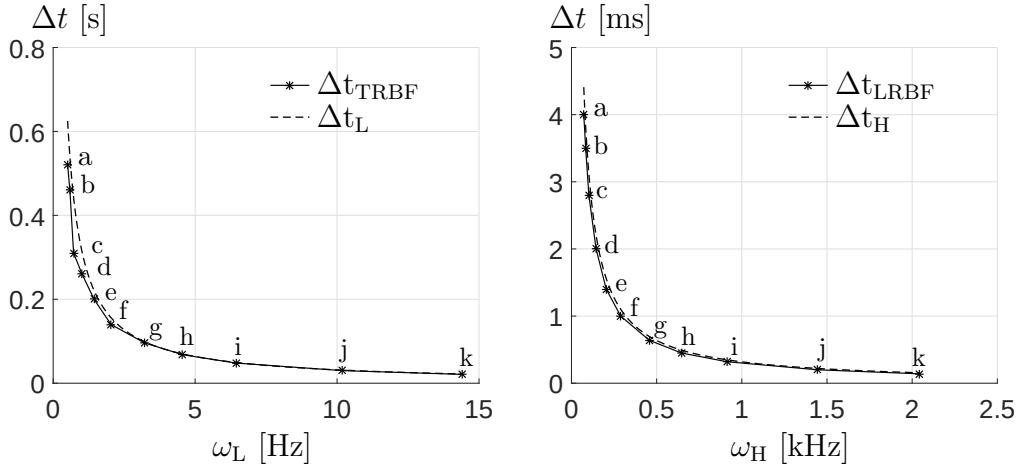

Figure 4.14: Stability curves for (left) the Taylor basis formulation and (right) the linear basis formulation.

value. This deviation appeared in the density state marked by c. In the remaining density states considered, the relative deviation was in the order of magnitude of 6-12%.

The stability of the LRBF, on the other hand, was very close to the theoretically stability limit related to the frequency of the modal derivative, Δt_H. For the given interval considered the relative deviation between Δt_{LRBF} and Δt_{H} was around 8-10%, with Δt_{H} taken as the reference value.

Based on the above presented results, the stability of the Taylor basis appears to be unaffected by the frequency of the modal derivative. Furthermore, the results indicate that a ratio between the stability limit of the TRBF and the LRBF can be approximated as:

$$\frac{\Delta t_{TRBF}}{\Delta t_{LRBF}} \approx \frac{\Delta t_L}{\Delta t_H} = \frac{\omega_H}{\omega_L} \tag{4.84}$$

As indicated by the values in Figure 4.14, the magnitude of ω_H can be significantly higher than ω_L. Thus, it appears as if the Taylor basis allows to include the high frequent content in the form of modal derivatives without their influence on the stability of the system.

In the analysis of the frame using the Taylor basis with six LNMs and the associated modal derivatives, the highest natural frequencies of the LNMs was $\omega_{\mathrm{L}}^{\max}$=67.6 rad/s. This corresponds to a stability limit of magnitude:

$$\Delta t_{\mathrm{lim}} = \frac{2}{\omega_{\mathrm{L}}^{\max}} = 30 \text{ ms} \tag{4.85}$$

In the given case instability of the TRBF occurred around a time step magnitude of Δt=28 ms, i.e. relatively close to the prediction in (4.85).

4.2.4 Concluding Remarks

In the present chapter the application of basis reduction methods in kinematic nonlinear systems has been considered. The general concepts of basis projection and various applied basis vectors were presented. Furthermore, by use of an example, it was demonstrated that it is crucial to include coupling activated deformations. Otherwise, the stiffness of the system can increase and thereby ruin the simulation results.

Three elements that can improve the accuracy of kinematic nonlinear systems have, furthermore, been presented; a global evaluation of the internal restoring forces, two improved systems of equations governing the modal derivatives and an efficient basis formulation, named a Taylor basis.

One of the heaviest task in the numerical simulations is the evaluation of the internal restoring forces. By use of an example it was illustrated, that if the standard element-by-element assembling of the internal restoring forces is replaced with a global evaluation in the reduced co-ordinates, the real-time DOF capacity can be increased with 50%, with the given computational resources as a reference point.

Furthermore, it was illustrated that the exact system of equations governing the modal derivatives can be derived by introducing a Taylor series into the free and undamped kinematic nonlinear equations of motion. The exactness was verified through an example, where the solution of the reduced co-ordinates, belonging to the modal derivatives, were shown to be identical with the prediction of a Taylor series.

By use of the modal derivatives a so-called Taylor basis was organized, including N linear normal modes and $\frac{1}{2}(\mathrm{N}+\mathrm{N}^2)$ associated modal derivatives, containing only N unknowns. This was shown to be a very efficient basis formulation. For even time step magnitudes, it was illustrated, that the Taylor basis could be up to ten times faster than a standard basis formulation. Furthermore, it was shown, that the real-time DOF capacity could be significantly increased by use of the Taylor basis. In case no linear dependent modes existed, the capacity could be increased from 29 DOFs to 65 DOFs, with a time step magnitude $\Delta t=10^{-3}$ s as reference. However, if modal derivatives existed, the efficiency was seen to decrease. For a specific frame analysis, the existence of linear dependent modes limited the real-time DOF capacity to 59 DOFs.

In addition to the high efficiency, the Taylor basis also exhibited a high stability. From an analysis it was shown, that the stability of the Taylor basis appears to be dependent on the frequencies of the LNMs, only. As the frequencies of the LNMs are, typically, significantly lower than the remaining frequencies of the system, this allows larger time steps to be applied when

using the Taylor basis compared to a standard algorithm.

Taking into account the improved stability in the evaluation of the real-time DOF capacity, this can be increased by more than the 100% found for even time step magnitudes. The improvement will, however, dependent on the structural system considered. The potential of combining the high efficiency with the high stability was illustrated in the analysis of a frame. Here the Taylor basis simulated the response 800 times faster than a full FEM model, and 20 times faster than the standard basis formulation, with equal precision.

Based on the above mentioned observations, it can be concluded that the presented elements contribute with significantly improved efficiency and stability to the numerical simulations. Contributions which can all help to improve the accuracy in real-time simulations.

Chapter 5

Application of Reduction Methods in Hybrid Testing

In the present chapter the application of reduction methods in hybrid testing is considered. To begin with, the projected EOM including the actuator forces, are considered. After this, a real-time hybrid test on a composite girder is presented. The test constituted the first real-time hybrid test in the DCCSM project and served as a pilot test for prospective real-time tests on a wind turbine blade. After the presentation of the real-time test results, the potential improvements in the numerical modelling are discussed. This is followed by another discussion on different approaches that can be used for the selection of basis vectors in hybrid testing. The chapter is concluded with some remarks on the merits of the pilot test results.

5.1 Basis Reduction in Hybrid Testing

The application of basis reduction in RTHT is in principle simple and straight forward. Given a basis $\mathbf{V} \approx \mathbf{\Phi s}$, the system of equations in (3.18) can be projected onto this, as described in chapter 4. This yields the projected equations of motion:

$$\mathbf{m}_n \ddot{\mathbf{s}}_i + \mathbf{c}_n \dot{\mathbf{s}}_i + \tilde{\mathbf{g}}_n(\mathbf{s}_i) + \mathbf{r}_{p,i} = \mathbf{f}_i \tag{5.1}$$

with the projected matrices and vectors:

$$\mathbf{m}_n = \mathbf{\Phi}^T \mathbf{M}_n \tag{5.2}$$

$$\mathbf{c}_n = \mathbf{\Phi}^T \mathbf{C}_n \tag{5.3}$$

$$\tilde{\mathbf{g}}_n(\mathbf{s}_i) = \mathbf{\Phi}^T \mathbf{g}_n(\mathbf{\Phi}\mathbf{s}_i) \tag{5.4}$$

$$\mathbf{r}_{p,i} = \mathbf{\Phi}^T \mathbf{R}_{p,i} \tag{5.5}$$

$$\mathbf{f}_i = \mathbf{\Phi}^T \mathbf{F}(t_i) \tag{5.6}$$

After each time integration step, the displacements to be imposed onto the shared boundary, $\mathbf{V}_s$, have to be transformed into the physical co-ordinates, by the relation:

$$\mathbf{V}_s = \mathbf{\Phi}_s \mathbf{s}_i \tag{5.7}$$

with the matrix, $\mathbf{\Phi}_s$, representing the specific rows in $\mathbf{\Phi}$, which relate to the DOFs at the shared boundary.

5.2 Real-time Hybrid Test

A real-time hybrid test was executed at DTU Byg, December 2015. The test constituted the first real-time hybrid test in the DCCSM project, and served as a pilot test for prospective real-time tests on the wind turbine blade shown in Figure 1.7. The test was carried out in collaboration with two other PhD students on the DCCSM project, Jacob P. Waldbjoern and Jacob H. Hoegh. The contribution from the present author consisted in delivering the FEM code, which was implemented into a RTHT loop organized by Jacob P. Waldbjoern and Jacob H. Hoegh.

A full description of the test is presented in Waldbjoern et al. (2016). In the present, an overall description of the test and the results are presented, with emphasis on the aspects and the considerations made in the numerical modelling.

5.2.1 Test Structure and Hybrid Setup

The structure selected for testing consisted of a glass fibre reinforced polymer composite box girder of a total length of 1650 mm. The geometry, loading and boundary conditions are sketched in Figure 5.1.

The girder was clamped at one end and loaded vertically by a resultant force, F(t), a distance of 47.5 mm from the free end. The physical substructure was selected as a 792 mm long part starting at the clamped support,

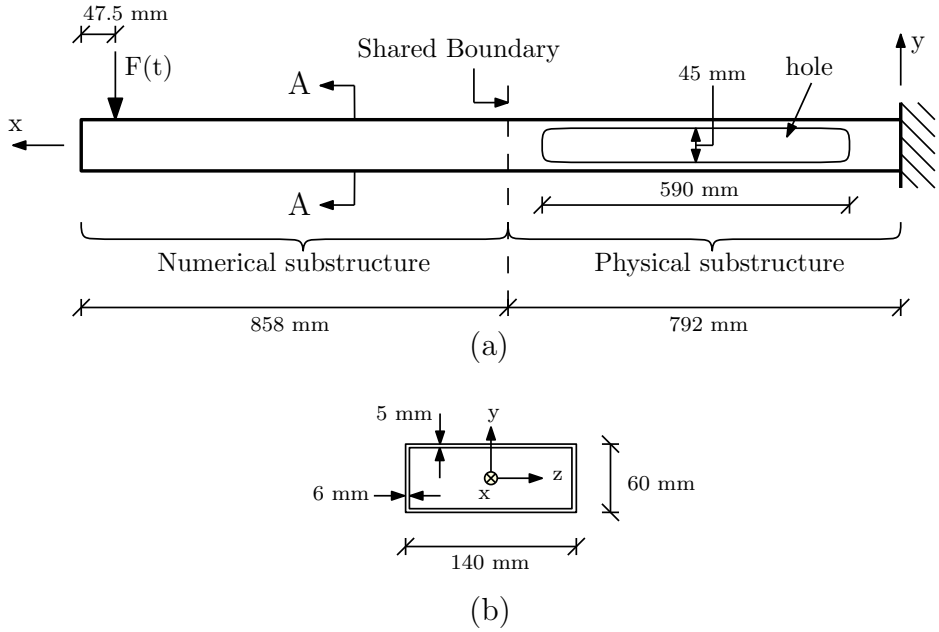

Figure 5.1: Sketch of composite beam in (a) longitudinal direction and the (b) cross section at A-A.

and the numerical part represented the remaining 858 mm of the cantilever, see Figure 5.1a. To improve the nonlinearities of the structure, two holes of length 590 mm and a height of 45 mm were cut in the sides of the physical substructure. From Figure 5.1b the thickness of the webs and flanges are seen to be respectively 5 mm and 6 mm.

To model the clamped boundary, the physical substructure was enclosed by a rectangular steel profile. The installation is seen in Figure 5.2, showing the RTHT setup. The shared boundary was considered as a discrete point with 3 DOFs in the (x,y)-plane of the composite girder; two translational DOFs, u_x and u_y, and one rotational DOF, θ. Three actuators were installed to impose the displacements of the numerical simulation onto the shared boundary, and to measure the corresponding reaction forces.

The actuators were fixed to a rectangular steel profile a distance of 108 mm from the shared boundary, denoted the load introduction zone. This was done in order to erase the effect of the steel profile on the displacements. The response of the shared boundary was monitored through real time tracking of three applied measurement points, measured through a 3D DIC system, for details see Waldbjoern et al. (2016).

Also a full scale model of the composite beam was organized. By this is meant a full physical version of the composite beam in Figure 5.1. From this the first two natural bending frequencies of the composite girder were experimentally identified to be ω_1^E=7.40 Hz and ω_2^E=47.3 Hz. From a numerical

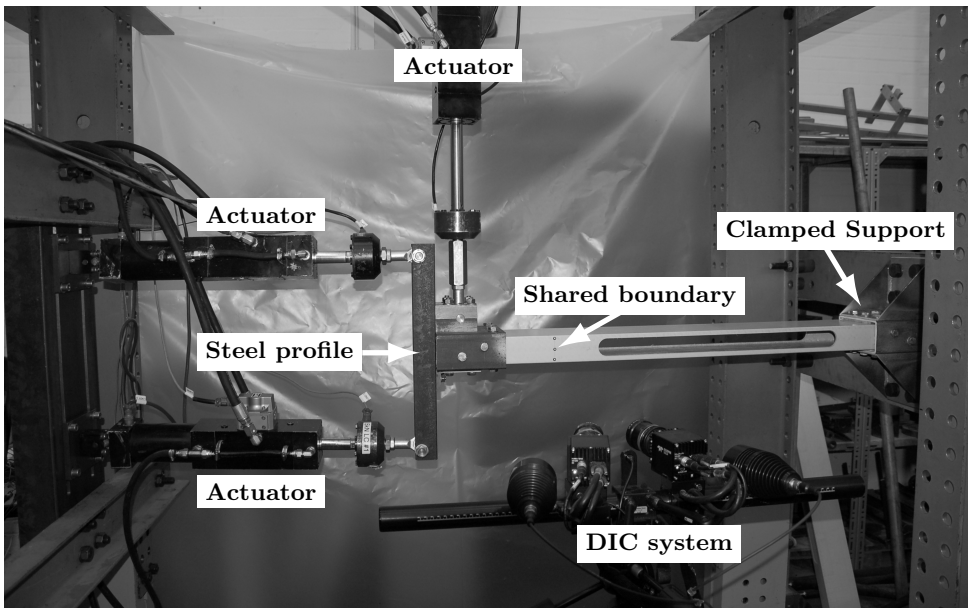

Figure 5.2: Hybrid Test Setup, December 2015, DTU Byg.

model of the composite girder modelled in the commercial FEM program ANSYS, the first natural frequency was found to be $\omega_1^A = 8.90$ Hz. The increase in the numerical frequency was attributed to the indefinitely stiff support at the clamped boundary. In Figure 5.3 the first mode identified in ANSYS, along the line (y,z) = (30,80) mm, is plotted. The mode is seen to be dominated by a shear deformation in the region with the cut-out hole.

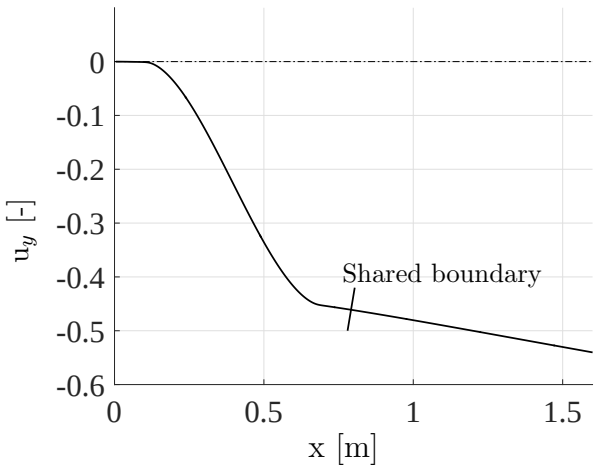

Figure 5.3: First mode shape of composite girder evaluated in ANSYS.

A number of full scale tests were performed prior to the real-time hybrid

tests, with an actuator imposing the load F(t). From these tests it was visually verified that the shear mode in Figure 5.3 was the dominating mode. This seemed reasonable, as the excitation frequencies applied in the tests covered a range from 1% to 40% of ω_1^A. The same frequencies were applied in the real-time hybrid tests.

5.2.2 Numerical Modelling

To model the response of the numerical substructure, the Euler-Bernoulli element referred to in section 4.2.2 was applied. To reduce the size of the EOM a Taylor basis was used for basis projection. To evaluate the basis vectors, a full numerical model of the composite girder was considered, modelled with the Euler-Bernoulli elements. In Figure 5.4 the first LNM, $\boldsymbol{\varphi}_1$, and its associated novel modal derivative, $\partial\boldsymbol{\varphi}_1/\partial s_1$, are plotted. The modes of the full structure are shown, but only the part of the modes, which refer to the numerical substructure were taken as the basis vectors. These parts are marked by solid lines. The LNM is seen to be a bending mode, whereas the modal derivative represent deformations in the beam length. A total of ten elements were used when evaluating the modes.

The shape of the first bending mode, $\boldsymbol{\varphi}_1$, in Figure 5.4 is seen to deviate from the shear mode shape in Figure 5.3, found in ANSYS. This is because the Euler-Bernoulli element does not include shear-flexibility. The frequency of mode one in Figure 5.4 was also significantly higher, with a magnitude of $\omega_1 = 19$ Hz. The frequency of the corresponding associated modal derivative was $\omega = 935$ Hz.

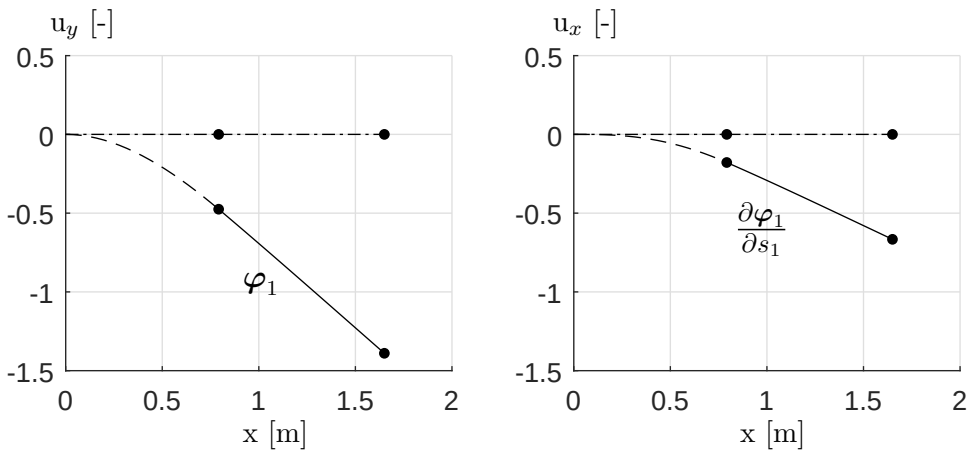

Figure 5.4: LNM number one and its associated novel modal derivative for the composite beam. The solid lines represent the mode of the numerical substructures.

During the real-time hybrid tests, it was found that the RTHT loop tasks occupied a significant part of the computational resources, leaving only a limited amount for the numerical time integration. To be able to keep up with the real-time requirement, only small models with a time step magnitude of 10 ms could be applied. This meant that only the LNM, $\boldsymbol{\varphi}_1$, together with its associated modal derivative, $\partial\boldsymbol{\varphi}_1/\partial s_1$, could be included in the reduced basis.

To make the FEM code as efficient as possible, it was implemented in the programming language C. Furthermore, the central difference method was applied for the time integration.

5.2.3 Reference Structures

To evaluate the results of the real-time hybrid test, a reference model should be applied. For this, a number full scale experiments of the composite girder were performed, as mentioned previously. However, during the real-time hybrid tests, instability issues were introduced due to, among other things, measurement noise of the actuator forces. Due to limited computational resources, it was not possible to filter out the noise. Instead the measured actuator forces, had to be reduced by 75% after each measurement, before they was sent to the numerical model. This eliminated the option of using the results from the full scale tests to compare with real-time hybrid test results.

To be able to evaluate the output of the real-time hybrid test, a numerical reference model with a force reduction of 75% at the shared boundary in each time step, was organized. For this a model with the Euler-Bernoulli element was applied. To try and compensate for the missing shear flexibility of the element, the stiffness of the elements in the physical substructural part were decreased by use of a calibration point from the full scale tests. Figure 5.5 shows a static force displacement curve for the full scale model and the numerical reference model used for comparison in the real-time hybrid tests. The displacement referred to in Figure 5.5 is at the loading point, cf. Figure 5.1. Also the calibration point used to modify the stiffness of the physical part in the numerical reference structure is shown. This is seen to be taken from the linear domain.

From Figure 5.5 the full scale and the numerical reference relations are seen to be very similar up to around a load of magnitude 100 N. Beyond this point the stiffness of the numerical reference model is seen to slightly increase, whereas the full scale model is seen to experience a softening behavior. The softening behavior was visually verified to be due to local instability of the flanges in the full scale model.

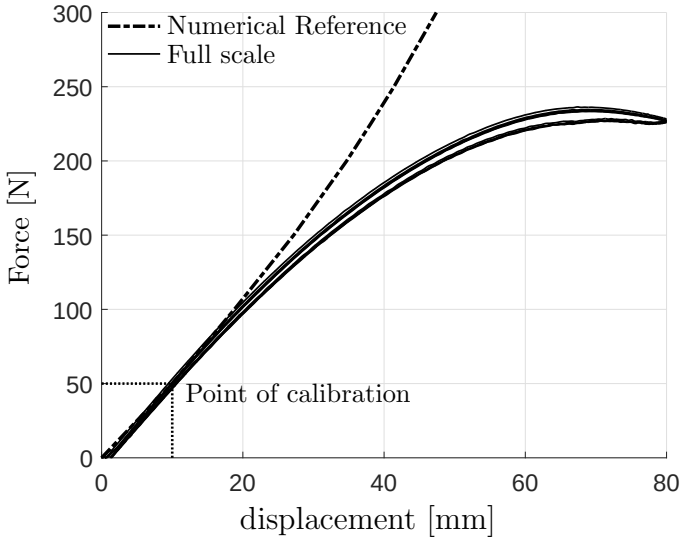

Figure 5.5: Force-displacement curve for the loading point of the composite girder.

5.2.4 Test Results

Five real-time hybrid tests were performed. The load amplitude was set to be P = 130 N in all of the tests. The excitation frequency, ω_e, on the other hand, was changed from test to test, covering a range from 1% to 40% of the first natural bending frequency, ω_1, of the composite girder. With the relatively low excitation frequencies, a more or less static response should be expected as experienced in the full scale tests. The load, F(t), was mathematically described by the formula:

$$F(t) = \frac{1}{2}P\left(1 + sin\left(\omega_e \cdot t - \frac{\pi}{2}\right)\right) \tag{5.8}$$

In Figure 5.6 - 5.8 the displacements and the rotation at the shared boundary are shown for the maximum applied excitation frequency of magnitude ω_e=2.96 Hz. The solid blue line represents the displacements measured by the DIC system from the real-time hybrid test, u_{RTHT}, the dashed line represents the numerical reference displacement, u_{num}, and the red line the maximum deviation between the former two evaluated by (5.9). The superscript *max* refers to the absolute maximum value in the full interval.

$$\text{error} = \frac{|u_{\mathrm{RTHT}} - u_{\mathrm{num}}|}{u_{\mathrm{num}}^{\mathrm{max}}} \cdot 100\% \tag{5.9}$$

From the Figure 5.6 and Figure 5.7, the translations in the real-time hybrid test and in the numerical reference are seen to be in the same order of magnitude, but with an fluctuating error ranging from 0% to approximately 40%. From Figure 5.8 the rotations of the real-time hybrid test are seen to diverge even more significantly from the numerical reference values. After the experiments, it was realized that the rotations evaluated in the numerical model, were erroneously multiplied by a factor $\pi/180$, as if converted from degrees to radians, before imposed onto the physical substructure. In the following the evaluation of the results are therefore based on the translations.

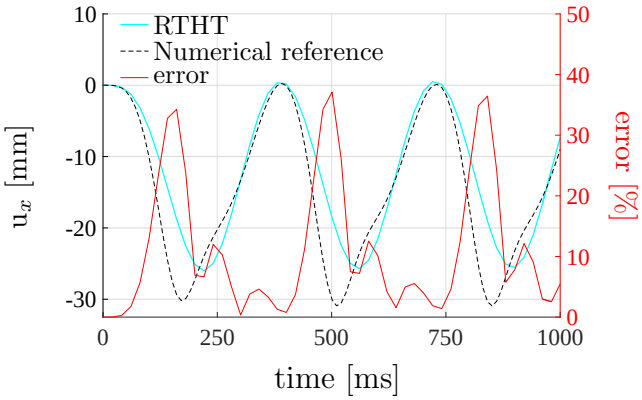

Figure 5.6: Horizontal deformation, u_x, at shared boundary.

For a load amplitude of P = 130 N it would be expected that the numerical response would be stiffer than the real-time hybrid test, cf. Figure 5.5. However, as seen in Figure 5.6 and Figure 5.7, the displacement amplitude of the numerical reference model is larger than the displacements achieved in the real-time hybrid test. Two things can explain the unexpected stiff response of the real-time hybrid test. The first reason is the erroneously reduced rotation. Preventing a rotation of the cross section will inevitably increase the stiffness. The second reason is, that only a single bending mode could be applied in the Taylor basis in the numerical model. Representing a shear mode with a bending mode will introduce discontinuities in the displacements, which are presumed to increase the stiffness. Based on these considerations, the order of magnitude of the real-time hybrid test displacements seem to be reasonable, compared with the numerical reference displacements.

5.2.5 Potential Numerical Improvements

Based on the presented real-time hybrid test results of the composite gider, it is obvious that a number of changes could improve the test. Consider-

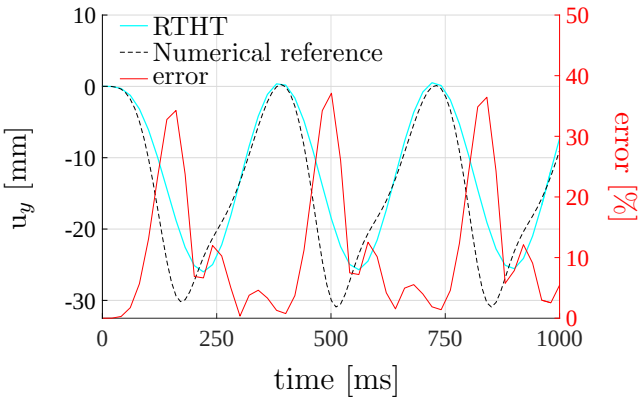

Figure 5.7: Vertical deformation, u_y, at shared boundary.

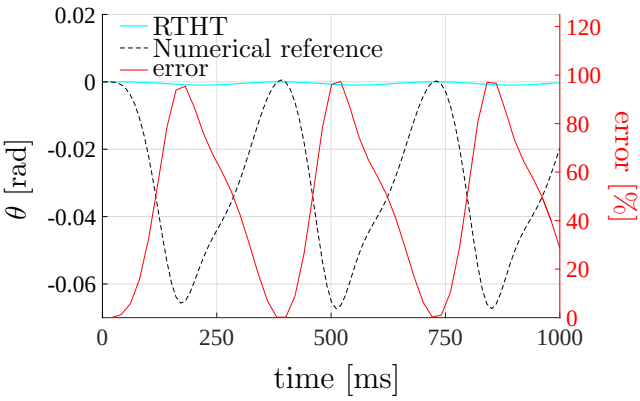

Figure 5.8: Rotation, θ, at shared boundary.

ing the numerical aspects, especially two improvements are distinctive; the approximate numerical reference model and the applied basis.

Starting with the numerical reference model, this was fitted to the displacement at the load point. Looking back, it would have made more sense to calibrate the numerical reference model with respect to the displacement at the shared boundary, as this point is used for comparison. A different point of calibration on the force-displacement curve in Figure 5.5 could also have been used, e.g. a point close to the applied load amplitude, P = 130 N. However, regardless of the choice of calibration method applied, discontinuities in the displacements at the shared boundary would have been introduced, due to the lack of shear flexibility in Euler-Bernoulli elements. Thus, such a reference model will only, at its best, be able to serve as an approximation in the evaluation. If a fully comparable numerical reference model is desired, a model containing shear flexibility should have been implemented. Due to

the need of reducing the forces of the numerical substructure by 75% in each time step, a commercial FEM programme with shear flexible elements could not be directly used.

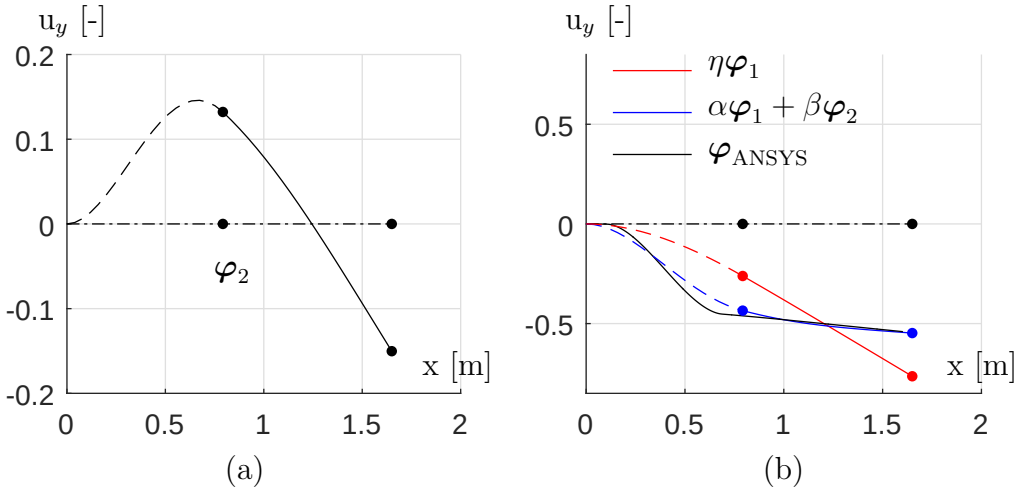

Figure 5.9: (a) LNM 2 based on Euler-Bernoulli elements and (b) the ANSYS shear mode, LNM 1 and a combination of LNM 1 and 2.

In contrast to the numerical reference model, the use of Euler-Bernoulli elements to evaluate the response of the numerical substructure, is a valid approximation. The reason for this is, that shear flexibility is not dominating in the numerical substructure part. However, the first bending mode and its associated modal derivative, were insufficient to represent the deformation of the expected shear mode. However, if the second LNM, plotted in Figure 5.9a, could have been included, a significant improvement of the response would be expected. This is illustrated in Figure 5.9b where the ANSYS shear mode, the LNM number 1 and a combination of the LNMs number 1 and 2 are shown for the chosen parameters $\alpha = 0.50$, $\beta = -1.35$ and $\eta = 0.55$. The combination of LNM 1 and 2 is seen to fit to the ANSYS shear mode significantly better in the numerical substructure domain, compared to the LNM number 1.

However, the best alternative would have been to include shear flexibility in the applied Bernoulli-Euler element. In this way the influence of the shear deformation had been included in the first mode. Furthermore, this would reduce the frequency magnitude, and thus allow for an increase of the time step magnitude.

In the following different methods to evaluate the basis vectors in hybrid testing are discussed. Here an alternative way of choosing the basis vectors is suggested.

5.3 Evaluation of Basis Vectors

When the basis vectors for numerical substructures in a hybrid test are evaluated, the boundary conditions at the shared boundary are off course important to consider. However, it is perhaps not straight forward to model these in a sufficient way, and alternative methods have to be applied.

As was done in the pilot test presented above, a model of the full structure containing both the numerical and physical substructures, can be applied in the evaluation of the basis vectors. However, if an inaccurate physical substructure is adopted in the evaluation, this will lead to deviations in mode shapes, as previously discussed, cf. Figure 5.9. A natural consequence of this is that an increase in the amount of basis vectors is required to represent the response to a sufficient degree of accuracy. Thus, this can potentially be a very inefficient approach.

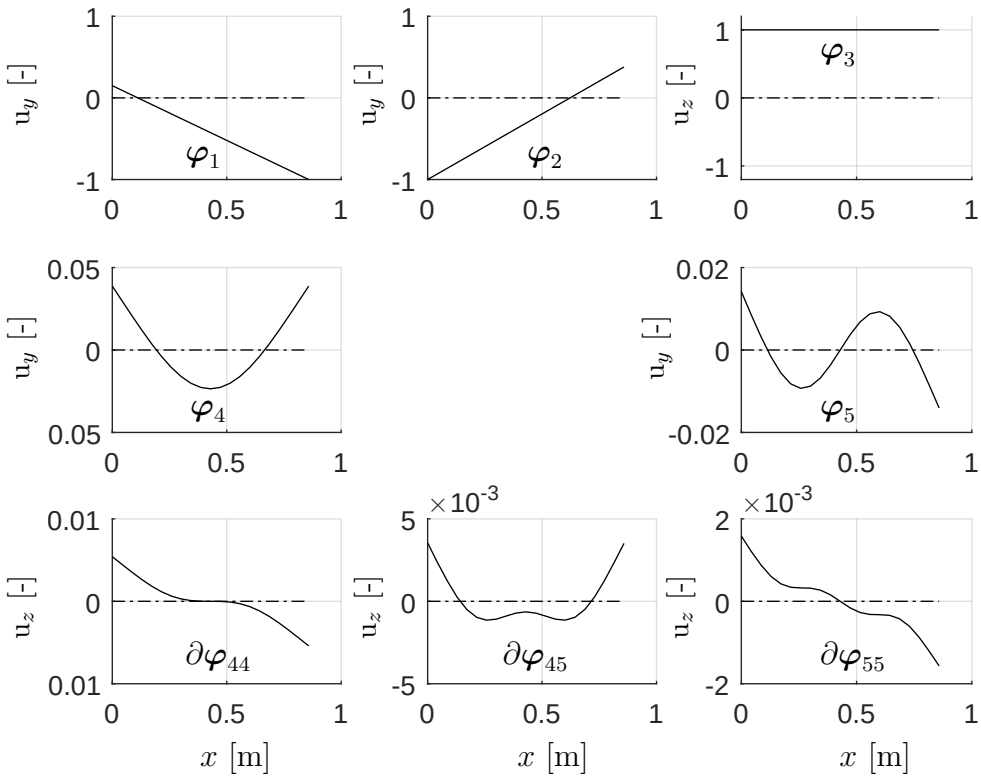

Figure 5.10: LNMs and their associated novel modal derivatives of the free beam.

Another approach, that was also considered in the pilot test, could be to consider the numerical substructure as a structural part fully disconnected

from the physical substructure. In this way the basis vectors can be evaluated, without having to consider the physical substructure.

Considering the composite beam as example, the numerical substructure would consist of a free beam. In Figure 5.10 the first five LNMs and the associated modal derivatives of the LNMs number four and five, of the free beam are shown. The first three LNMs, $\boldsymbol{\varphi}_1$, $\boldsymbol{\varphi}_2$ and $\boldsymbol{\varphi}_3$, are rigid body motions, with the former two given as a mix of rotations and translations, whereas $\boldsymbol{\varphi}_3$ is a pure horizontal translation. The linear modes $\boldsymbol{\varphi}_4$ and $\boldsymbol{\varphi}_5$, are bending modes, and their associated modal derivatives horizontal displacements. The latter are denoted by the definition in (4.53) on page 58.

The natural frequencies associated with the rigid body motions are zero, and can cause some problems with the eigenvalue solver. However, this can be fixed by shifting the eigenvalues. Adding the zero term $\alpha\mathbf{M} - \alpha\mathbf{M}$ to the linearized eigenvalue problem in (4.14), this can be formulated on the form in (5.10) with α denoting a constant free of choice. The eigenvectors remain the same, whereas a new eigenvalue, λ_i, is introduced. However, knowing λ_i, the eigenvalues, ω_i^2, can easily be found by use of (5.11).

$$\Big((\mathbf{K} + \alpha\mathbf{M}) - \lambda_i\mathbf{M}\Big)\boldsymbol{\varphi}_i = \mathbf{0} \tag{5.10}$$

$$\lambda_i = \left(\omega_i^2 + \alpha\right) \tag{5.11}$$

The frequencies of the LNMs number four and five in Figure 5.10 were of magnitude $\omega_4 = 3 \cdot 10^3$ rad/s and $\omega_5 = 8 \cdot 10^3$ rad/s, respectively. This is significantly higher than the frequencies associated with the modes applied in the pilot test. Thus, it would not have been possible to apply the basis vectors of the free beam in the pilot test, as this would have required significantly smaller time step magnitudes.

5.4 Concluding Remarks

In the present chapter the application of reduction methods in hybrid testing has been considered. The projected EOM, including the actuators forces, were considered, and a pilot test was presented. Furthermore, different methods that can be used to evaluate the basis vector for hybrid testing were discussed.

The results of the pilot test were influenced by a number of error and shortcomings in the equipment. Despite of this, the performed real-time hybrid test provided a number of important answers. One is, that an improved RTHT loop is required, if real-time hybrid tests are to be performed. Especially the computational capacity has to be improved, both to be able to filter

out the noise, but also in order to improve the size of the numerical models. But more importantly, the test confirmed the stability of the Taylor basis in an applied case. Without the stability of the Taylor basis, it would not have been possible to include the high frequent contraction mode, $\partial\boldsymbol{\varphi}_1/\partial s_1$. In this perspective, the test has been useful.

Chapter 6

Future Research Subjects

In the following chapter two potential future research topics are mentioned. The topics relate to the present work and the numerical substructures in RTHT.

Linear Dependent Modal Derivatives

One subject that could be of interest to consider, relates to the phenomena of linear dependent modal derivatives. As was illustrated in chapter 4, the efficiency of the Taylor basis formulation is decreased for an increasing number of linear dependent modal derivatives. In this regard it could be of interest to consider if the linear dependent modal derivatives could be included in a more efficient way, e.g. by moving them to the linear term of the Taylor basis formulation, without ruining the stability. Alternatively, it could be of interest to investigate the effects of removing the linear dependent modes.

Choice of Basis Vectors in Hybrid Testing

As discussed in chapter 5 different ways of selecting the basis vectors for the hybrid tests exist. It is however not obvious to the writer how the choice of basis vectors will influence on the behavior of the full structural response, e.g. how the frequencies of the coupled system will be influenced by the choice of basis vectors. This is considered to be highly relevant to investigate. Furthermore, it could be of interest to investigate if the physical substructure influence on the stability of the numerical model in a hybrid test, or if the stability is only dependent on the frequencies of the selected basis vectors.

Chapter 7

Conclusion

In the present PhD study mathematical tools and methods have been adopted and developed, in order to improve the accuracy of kinematic nonlinear numerical substructures, simulated in real time.

Special emphasis has been on projection based reduction methods, which is a mathematically way to reduce the dimension of large discretized models, with the purpose of decreasing the computational time, while simultaneously keeping a high solution accuracy. Three elements that can help to improve the accuracy of reduction methods in real-time simulation have been presented. The elements consist of:

An Efficient Global Formulation of the Internal Restoring Forces

The first element consisted in implementing an existing global formulation of the internal restoring forces. The formulation was organized by introducing a reduced basis into the discrete equations of motion and manipulate these into a sum of constant equivalent force vector coefficients times the reduced co-ordinates. By replacing the standard element-by-element assembling of the internal restoring forces with the global formulation, it was shown that the real-time DOF capacity could be increased by 50%, with the given computational resources taken as a reference point. The real-time DOF capacity increase allows for more elements to be included in the modelling, and thereby helps to improve the accuracy.

Two System of Equations Governing the Modal Derivatives

The second element consisted in the organization of two different system of equations governing the so-called modal derivatives. Modal derivatives represent the second order terms of a displacement field, and these are important

to include in nonlinear analysis. In kinematic nonlinear systems the second order terms represent coupling activated deformations. By use of an example it was illustrated, that if the coupling activated deformations are omitted from the basis projection, this can increase the stiffness of the system, and ruin the accuracy.

The first organized system of equations was based on an existing formulation found by differentiating the linearized eigenvalue problem. However, this formulation is by nature singular, and can only be solved by use of approximations. A geometric restriction on the modal derivatives was introduced to remove the singularity of the system.

The second organized system of equations comprised a novel set of equations. This was derived by introducing a Taylor series for the displacement field into the free and undamped kinematic nonlinear equations of motion.

The modal derivatives determined from the two governing system of equations were compared by using them in the analysis of a nonlinear cable. Identical results were found independent of the modes applied. However, only the modal derivatives based on the novel system of equations fulfilled the Taylor series. Thus, the novel system of equations were concluded to be exact.

An Efficient Basis Formulation Based on a Taylor Series

The third element consisted in the organisation of an efficient basis formulation. By use of the novel modal derivatives, a second order Taylor series of the displacement field was organized on a basis format with N linear modes and $\frac{1}{2}(N^2+N)$ associated modal derivatives, containing only the N unknowns of the linear modes. In this way the modal derivatives were included without increasing the number of unknowns. The formulation was named a Taylor basis and it was shown to exhibit high efficiency, accuracy and stability.

It was illustrated, that if more than 40 basis vectors are included in the basis, and an even time step magnitude is applied, the Taylor basis can be up to ten times faster than a standard basis formulation. Furthermore, when using even time step magnitudes, the Taylor basis was shown to be able to increase the real-time DOF capacity by more than 100%, compared to a simulation that makes use of the standard element-by-element assembling.

Moreover, the stability of the Taylor basis was shown to be dependent on the frequencies of the linear normal modes only. The linear frequencies are, typically, significantly lower than the frequencies of the higher order terms. Thus, with the Taylor basis significantly larger time steps can be applied compared to other algorithms. This can increase the real-time DOF capacity even further. The potential of combining the high efficiency with the improved stability was illustrated in an example of a simple harmonic

loaded frame. Here the Taylor basis was able to simulate the response 800 times faster than a full FEM model, and 20 times faster than a standard basis formulation, with equal precision.

Bibliography

S. Andersen and P. N. Poulsen. Reduction method for real-time simulations in hybrid testing. In *Proceedings of the 9th International Conference on Structural Dynamics*, Porto, Portugal, 2014.

S. Andersen and P. N. Poulsen. Reduction method for kinematic nonlinear real-time simulations. *International Journal for Numerical Methods in Engineering*, 2015.

S. Andersen and P. N. Poulsen. Nonlinear real-time simulations using a taylor basis. *International Journal for Numerical Methods in Engineering*, 2016.

Jernej Barbic and Doug James. Real-Time Subspace Integration for St . Venant-Kirchhoff Deformable Models c. *ACM Transactions on Graphics*, 24(3):982–990, 2005.

Ted Belytschko, Wing Kam Liu, and Brian Moran. *Nonlinear Finite Elements for Continua and Structures*. John Wiley & Sons, Chicester, England, first edition, 2000.

A. Blakeborough, M. S. Williams, A. O. Darby, and Williams D. M. The development of real-time substructure testing. *The royal society A: Mathematical, Physical and Engineering Sciences*, 359:1869–1891, 2001.

P. A. Bonnet, M. S. Williams, and A. Blakeborough. Evaluation of numerical time-integration schemes for real-time hybrid testing. *Earthquake Engineering and Structural Dynamics*, 37:1467–1490, 2008.

M. R. Brake and D. J. Segalman. Nonlinear Model Reduction of von Kármán Plates Under Quasi-Steady Fluid Flow. *AIAA Journal*, 48(10):2339–2347, 2010.

Oreste E. Bursi and David Wagg. *Modern Testing Techniques for Structural Systems*, volume 502. Springer, 2008.

J.E. Carrion and B.F. Spencer Jr. *Model-based strategies for real-time hybrid testing*, volume 6. Newmark Structural Engineering Laboratory Report Series, University of Illinois at Urbana-Champaign, Urbana, IL, 2007.

Y. Chae, K. Kazemibidokthi, and J. M. Ricles. Adaptive time series compensator for delay compensation of servo-hyrdaulic actuator systems for real-time hybrid simulation. 42:1697–1715, 2013.

C. Chang and J. J. Engblom. Nonlinear dynamical response of impulsively loaded structures: a reduced basis approach. *AIAA Journal*, 29:613–618, 1991.

S. Y. Chang. Explicit pseudodynamic algorithm with unconditional stability. *Journal of Engineering Mechanics*, 128(9):935–947, 2002.

S. Y. Chang. Nonlinear performance of explicit pseudodynamic algorithms. *Journal of Earthquake Engineering*, 14(2):211–230, 2010.

Shuenn-Yih Chang. A time integration pseudodynamic algorithm. *Eleventh European Conference on Earthquake Engineering, Paris, France*, pages 117–130, 1998.

Cheng Chen and James M. Ricles. Development of direct integration algorithms for structural dynamics using discrete control theory. *Journal of Engineering Mechanics*, 134(8):676–683, 2008.

Cheng Chen, James M. Ricles, Thomas M. Marullo, and Oya Mercan. Real-time hybrid testing using the unconditionally stable explicit cr integration algorithm. *Earthquake Engineering and Structural Dynamics*, 38(1):23–44, 2009.

Cheng Chen, James M. Ricles, Theodore L. Karavasilis, Yunbyeong Chae, and Richard Sause. Evaluation of a real-time hybrid simulation system for performance evaluation of structures with rate dependent devices subjected to seismic loading. *Engineering Structures*, 35:71–82, 2012.

Anil K. Chopra. *Dynamics of Structures: Theory and Application to Earthquake Engineering*, volume 1. Prentice-Hall, second edition, 1995.

Robert D. Cook, David S. Malkus, Michael E. Plesha, and Robert J. Witt. *Concepts and Applications Of Finite Element Analysis*. John Wiley & Sons, New York, USA, fourth edition, 1974.

A. P. Darby, A. Blakeborough, and M. S. Williams. Real-time substructure tests using hydraulic actuator. *Journal of Engineering Mechanics*, 10(125): 1133–1139, 1999.

A.P. Darby, A. Blakeborough, and M.S. Williams. Improved control algorithm for real-time substructure testing. *Earthquake Engineering and Structural Dynamics*, 30(3):431–448, 2001.

A.P. Darby, M.S. Williams, and A. Blakeborough. Stability and delay compensation for real-time substructure testing. *Journal of Engineering Mechanics*, 128(12):1276–1284, 2002.

S. N. Dermitzakis and S. A. Mahin. Development of substructuring techniques for on-line computer controlled seismic performance testing. Technical report, Earthquake Engineering Research Center, University of California, Berkeley *Report UCB/EERC-85/04*; 1985.

J. Donea, G. Magonette, P. Negro, P. Pegon, A. Pinto, and G. Verzeletti. Pseudodynamic capabilities of the elsa laboratory for earthquake testing of large structures. *Earthquake Spectra*, 12(1):163–180, 1996.

M. Hakuno, M. Shidawara, and T. Hara. Dynamic destructive test of a cantilever beam, controlled by an analog-computer (in japanese). *Transactions of the Japan Society of Civil Engineers*, 171:1–9, 1969.

H. M. Hilber, Hughes T. J. R., and R. L. Taylor. Improved Numerical Dissipation for Time Integration Algorithms in Structural Dynamics. *Earthquake Engineering and Structural Dynamics*, 5:282–292, 1977.

T Horiuchi et al. Development of real-time hybrid experimental system with actuator delay compensation. *9th Japanese Symposium on Earthquake Engineering (in japanese)*, 1:1531–1536, 1994.

K. Horri and M. Kawahara. A numerical analysis on the dynamic response of structures. *Proceedings of 19th Japan National Congress for Applied Mechanics*, pages 17–22, 1969.

T. J. R. Hughes, K. S. Pister, and R. L. Taylor. Implicit-explicit finite elements in nonlinear transient analysis. *Computer Methods in Applied Mechanics and Engineering*, 18(17):159–182, 1979.

Sergio R. Idelsohn and Alberto Cardona. Recent advances in reduction methods in nonlinear structural dynamics. In *Proceedings of the Second International Conference on: Recent Advances in Structural Dynamics*, volume 2, pages 475–482, University of Southampton, 1984.

Sergio R. Idelsohn and Alberto Cardona. A Reduction Method for Nonlinear Structural Dynamic Analysis. *Computer Methods in Applied Mechanics and Engineering*, 49:253–279, 1985a.

Sergio R. Idelsohn and Alberto Cardona. A load-dependent basis for reduced nonlinear structural dynamics. *Computers and Structures*, 20:203–210, 1985b.

Rae-Young Jung and P. Benson Shing. Performance of a real-time pseudodynamic test system considering nonlinear structural response. *Earthquake Engineering and Structural Dynamics*, 36(20):1785–1809, 2007.

R. k. Kapania and C. Byun. Reduction methods based on eigenvectors and ritz vectors for nonlinear transient analysis. *Computational Mechanics*, 11: 65–82, 1993.

Steen Krenk. *Non-linear Modeling and Analysis of Solids and Structures.* Cambridge University Press, New York, 2009.

Fritz Adrian Lülf, Duc-Minh Tran, and Roger Ohayon. Reduced bases for nonlinear structural dynamic systems: A comparative study. *Journal of Sound and Vibration*, 332(15):3897–3921, July 2013.

S. A. Mahin, P.S.B. Shing, C.R. Thewalt, and R.D. Hanson. Pseudodynamic test method - current status and future directions. *Journal of Structural Engineering*, 115(8):723–731, 1989.

Francesco Marazzi, Ioannis Politopoulos, and Alberto Pavese. An overview of seismic testing needs in europe: towards a new advanced experimental facility. *Bull Earthquake Engineering*, 9:623–640, 2011.

M.I. Mcewan, J.R. Wright, J.E. Cooper, and a.Y.T. Leung. a Combined Modal/Finite Element Analysis Technique for the Dynamic Response of a Non-Linear Beam To Harmonic Excitation. *Journal of Sound and Vibration*, 243(4):601–624, June 2001.

G. Mosqueda and M. Ahmadizadeh. Combined implicit or explicit integration steps for hybrid simulation. *Earthquake Engineering and Structural Dynamics*, 36:2325–2342, 2007.

Alexander A Muravyov and Stephen A Rizzi. Determination of nonlinear stiffness with application to random vibration of geometrically nonlinear structures. *Computers & Structures*, 81(15):1513–1523, 2003.

M. Nakashima and N. Masaoka. Real-time on-line test for mdof systems. *Earthquake Engineering and Structural Dynamics*, 28(4):393–420, 1999.

M. Nakashima, T. Kaminosono, and M. Ishida. Integration techniques for substructure pseudodynamic test. In *Proc. of the 4th U.S. National Conference on Earthquake Engineering.*, pages 514–524, 1990.

M. Nakashima, H. Kato, and E. Takaoka. Development of real-time pseudo dynamic testing. *Earthquake Engineering and Structural Dynamics*, 21(1): 79–92, 1992.

M. Nash. *Nonlinear structural dynamics by finite element modal synthesis.* PhD thesis, Imperial College, The University of London, 1977.

N.M. Newmark. *A method of computation for structural dynamics*, volume 1. Prentice-Hall, second edition, 1959.

R. Nickell. Nonlinear dynamics by mode superposition. *Computer Methods in Applied Mechanics and Engineering*, 7:107–129, 1976.

V. Saouma and M. Sivaselvan. *Hybrid Simulation: Theory, Implementation and application.* Taylor & Francis, 2008.

V. Saouma, Dae-Hubg Kang, and Gary Haussmann. A computational finite-element program for hybrid simulation. *Earthquake Engineering and Structural Dynamics*, 41:375–389, 2012.

Y. Shi and C. Mei. A finite element time domain modal formulation for large amplitude free vibrations of beams and plates. *Journal of Sound and Vibration*, 193(2):453–464, 1996.

P. Benson Shing, Zhong Wei, Rae-Young Jung, and Eric Stauffer. Nees fast hybrid test system at the university of colorado. In *13th World Conference on Earthquake Engineering, Vancouver, B.C., Canada*, 2004.

P.B. Shing, M. Nakashima, and O.S. Bursi. Application of pseudodynamic test method to structural research. *Earthquake Sprectra*, 12:29–56, 1996.

Pui-Shum B. Shing and Mani T. Vannan. Implicit Time Integration for Pseudodynamic Tests: Convergence and Energy Dissipation. *Earthquake Engineering and Structural Dynamics*, 20:809–819, 1991.

Pui-Shum B. Shing, Mani T. Vannan, and Edward Cater. Implicit Time Integration for Pseudodynamic Tests. *Earthquake Engineering and Structural Dynamics*, 20:551–576, 1991.

P. M. A. Slaats, J. de Jongh, and A. A. H. J. Sauren. Model Reduction Tools for Nonlinear Structural Dynamics. *Computers and Structures*, 54: 1155–1171, 1993.

S.M. Spottswood and R.J. Allemang. Identification of nonlinear parameters for reduced order models. *Journal of Sound and Vibration*, 295:226–245, August 2006.

K. Takanashi and M. Nakashima. Japanese activities on on-line testing. *Journal of Engineering Mechanics*, 113(7):1014–1032, 1987.

K. Takanashi and K. Ohi. Earthquake response analysis of steel structures by rapid computer-actuator on-line system, (1) a progress report, trial system and dynamic response of steel beams. *Bull. Earthquake Resistant Struct. Research Center (ERS)*, 16:103–109, 1983.

K. Takanashi et al. Non-linear earthquake response analysis of structures by a computer actuator on-line system (part 1 details of system) - (in japanese). *Transactions of the Architectural Institute of Japan*, 229:77–83, 1975.

J. Waldbjoern, S. Andersen, J. Hoegh, J. W. Schmidt, and C. Berggren. Single-component Multi-rate Real-Time Hybrid Simulation Pilot Test on a Composite Structure. *Strain*, 2016.

E. L. Wilson, M.-W. Yuan, and J. M. Dickens. Dynamic analysis by direct superposition of ritz vectors. *Earthquake Engineering and Structural Dynamics*, 10:813–821, 1982.

B Wu, G. Xu, Q. Wang, and Williams M.S. Operator-splitting method for real-time substructure testing. *Earthquake Engineering and Structural Dynamics*, 35(3):2325–2342, 2006a.

Bin Wu, Qianying Wang, and Jinping Ou. Stability-analysis of operator-splitting method for real-time substructure testing with actuator delay and compensation. *8th US National Conference on Earthquake Engineering*, 3: 1515–1524, 2006b.

Errata

Here the known errors in the Appended Papers are listed.

Appended Paper I

In the introduction is it stated that reference [13] introduces a basis into a set of *linear* equations of motion. This should have been a set of *material nonlinear* equations of motion.

Equation (14) should be

$$\mathbf{\Phi}_i^h = \mathbf{\Phi} - \mathbf{V}_0$$

with $\mathbf{V}_0$ referring to the solution of the linear static static problem:

$$\mathbf{K}(\mathbf{0})\mathbf{V}_0 = \alpha \mathbf{M} \mathbf{\Phi}_i$$

Part I

Appendix

Appendix A

Kinematic Nonlinear Beam Example

A kinematic nonlinear beam rigid supported at the left end and prevented against horizontal deformations at the right end, is considered, see Figure A.1.

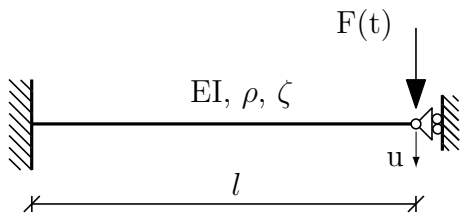

Figure A.1: Kinematic nonlinear beam.

The beam has a density ρ, a bending stiffness EI, a relative damping ratio, ζ, and is exposed to an external periodic load, F(t), with a excitation frequency, ω_e;

$$F(t) = F_{\max} \cdot sin(\omega_e t) \tag{A.1}$$

A FEM model is used to analyse its response. The EOM on discretized form, assuming linear damping, is

$$\mathbf{M}\ddot{\mathbf{x}} + \mathbf{C}\dot{\mathbf{x}} + \mathbf{g}(\mathbf{x}) = \mathbf{F}(t) \tag{A.2}$$

where $\mathbf{M}$ is the mass matrix, $\mathbf{C}$ is the damping matrix, $\mathbf{g}(\mathbf{x})$ are the internal restoring forces and $\mathbf{F}(t)$ is the external load dependent on time, $\mathbf{x}$ the displacement field and d/dt = $\dot{()}$.

In table 1.1 are listed the properties of cantilever beam applied, corresponding to the first bending mode with a frequency $\omega_1 = 1$ rad/s. The beam is modelled with plane Euler-Bernoulli elements. A full description of the element is presented in Andersen and Poulsen (2015).

In Figure A.2a the transverse deformation, u, at the load point, is plotted. The central difference method (CDM) and the Newmark implicit scheme, with assumed average acceleration, are used to evaluate the response. The linear response is plotted in Figure A.2b, using the CDM.

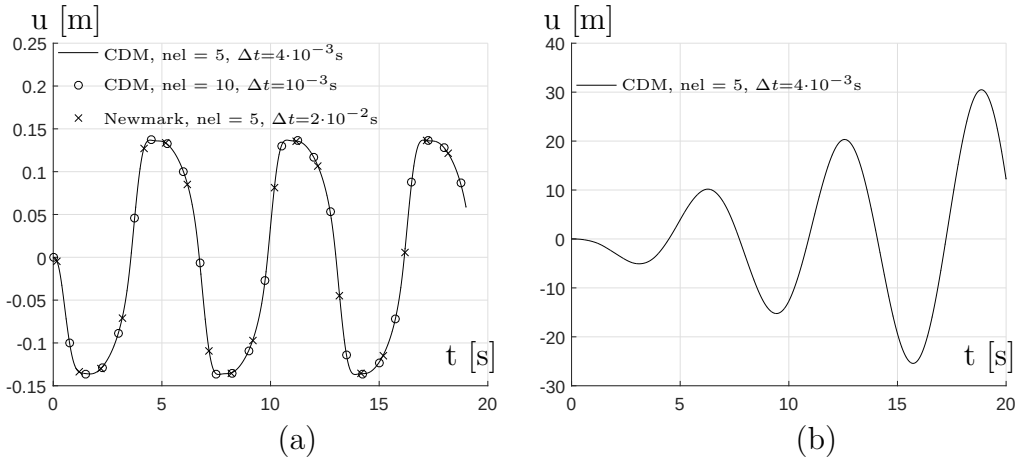

Figure A.2: Response of (a) kinematic nonlinear beam and (b) linear beam.

Three nonlinear solutions are plotted in Figure A.2a; two with five elements and one with ten elements. Furthermore, different time step magnitudes are applied in the three solutions. As all of the three nonlinear responses are identical, the solution has converged. Furthermore, by comparing the magnitude of the linear and nonlinear responses, the nonlinear effects are seen to be significant.

Part II

Appended Papers

Paper I

"Reduction Method for Real-Time Simulations in Hybrid Testing"

S. Andersen & P.N. Poulsen

Proceedings of the 9th International Conference on Structural Dynamics *EURODYN 2014, Porto, Portugal*

Reduction Method for Real-Time Simulations in Hybrid Testing

Sebastian Andersen[1], Peter Noe Poulsen[2]
[1]Department of Civil Eng., Technical University of Denmark, PhD. Student, 2800 Kgs. Lyngby, Denmark
[2] Department of Civil Eng., Technical University of Denmark, Associate Professor, 2800 Kgs. Lyngby, Denmark
email: seba@byg.dtu.dk, pnp@byg.dtu.dk

ABSTRACT: Real-time hybrid testing combines testing of physical components with numerical simulations. The concept of the method requires that the numerical simulations should be executed in real time. However, for large numerical models including nonlinear behavior a combination of computationally costly assembling of the internal forces element by element at each equilibrium point and a strict requirement for small time steps to maintain accuracy and stability often prevents real time execution. Thus, enhanced numerical capacity is required. In the present study a basis reduction method is used to reformulate kinematic nonlinear equations of motion into a sum of constant matrices each multiplied by a reduced coordinate decreasing the assembling time. Furthermore the method allows for cutting off some of the higher frequency content not representing real physics decreasing the stability requirement for the time step. However, it is important that the chosen basis can represent the nonlinearities of the system. If not locking of the system can be a consequence ruining the accuracy of the results. To demonstrate the potential of the method in a real time simulation perspective and the importance of choosing a sufficient basis a composite beam and a cantilever beam including kinematic nonlinearities and exposed to harmonic loadings are analyzed. To reduce locking modes with higher order terms are included. From the analysis it is concluded that the method exhibits encouraging potential with respect to real time execution if a sufficient basis is chosen.

KEY WORDS: Kinematic Nonlinearities, Basis reduction, Real-time simulation, Finite Element Analysis.

1 INTRODUCTION

Hybrid testing is a testing method that was developed by Japanese scientists in the 1960's, cf. [1]. If conducted in real-time in order to include dynamic effects the method is often referred to as real-time hybrid testing (RTHT).

The principle of the method is that the considered structure is partitioned into two parts; a physical substructure and an analytical substructure. The physical component is a structural part that displays complicated or unknown structural behavior and therefore has to be tested in a physical test setup. The analytical substructure on the other hand is well understood. Thus, this part does not have to be tested but can instead be modeled numerically and solved by a time integration scheme. As only the component displaying complicated behavior has to be build and tested physically a full scale test can be conducted in more modest physical frames which makes it highly economically profitable.

During the hybrid test an iterative loop is running where the response of the numerical model found from the time integration is imposed onto the physical substructure through servo-hydraulic actuators in a finite number of points. The force response from the physical component is then measured by the actuators and sent to the numerical model. Together the experimental substructure(s), the analytical substructure(s), the integration algorithm and the servo-hydraulic actuators are integrated through an IT control system to form the real-time hybrid simulation system. For further details about the principle of Hybrid testing see e.g. [2-3].

For RTHT to be successful it is required that servo-hydraulic actuators are able to impose the displacements accurately onto the physical substructure in real time, that the communication between the analytical and physical substructure has a minimum delay and that the time integration is robust, accurate and fast to ensure real time execution.

The requirement that the numerical time integration has to be executed in real time limits the size of the nonlinear numerical substructures that can be applied in RTHT. Main part of the computation time in nonlinear analysis is due to the internal nodal forces computed element by element followed by an assembling into the global set of equations before each time step. When increasing the size of the numerical models the assembling time is obviously increased as well. Simultaneously, when increasing the size and complexity of the models higher frequencies are introduced, which calls for smaller time steps in the integration schemes in order to maintain stability and accuracy. Decreasing the time steps increases the computational time further as the number of assemblings of the internal nodal forces within a given simulated time interval are increased. Thus, increasing the size and complexity of the numerical substructures increases the computational time, which work against the real time execution requirement.

Both implicit and explicit algorithms and combinations of these are considered among researchers in RTHT context, see e.g. [4-10]. In [10] a selection of implicit and explicit integration schemes is evaluated in a RTHT setup with nonlinear substructures. The study concludes that explicit schemes are preferable. These schemes are simpler and do not require equilibrium iterations, making them less time consuming than implicit algorithms. However, the downside of explicit schemes is that smaller time steps are required to maintain stability of the system compared to implicit schemes.

The study in [10] also concludes that due to the performance of the time integration schemes the capacity with respect to degrees of freedom (dof) in the discretized system is very modest if real time execution should be performed. Under the given circumstances around 50 dofs in a nonlinear context dictates the upper limit. As far as known the maximum number of dof's used in a RTHT with a nonlinear analytical substructure is 134, cf. [11]. Thus, a very interesting

and important issue related to RTHT is how to improve the computational capacity in order to be able to simulate the response of large and complex numerical substructures including nonlinear effects in real time.

One way of decreasing the computational time is by using reduced order modeling (ROM) reducing the discretized nonlinear equations of motion by projecting them onto a subspace represented by a reduced basis. This is a simple way to reduce the number of dof's and at the same time to cut off some of the higher frequency content contained in the model not representing real physics. The latter allows one to increase the time steps whereby the assembling frequency of the internal nodal forces and thereby the computation time are reduced.

In [12] the concept of ROM is described together with an overview and evaluation of the most common used bases for kinematic nonlinear structures considering robustness and accuracy. From the study it is concluded that linear normal modes are among the best performing bases under the given circumstances despite the fact that they neglects the nonlinear nature of the system.

In [13] is considered a material nonlinear structure. To model the response a reduced basis consisting of a number of Ritz vectors encapsulating the material nonlinear response is used. The Ritz-basis is derived from a combination of linear normal modes and a number of plastic deformation shapes found from a static analysis. The basis is introduced into a set of linear equation of motion whereby the costly assembling every time step is avoided. This enables the authors to model the response of a 50-dof nonlinear plastic model with three elastic and six plastic modes in real time. However, the plastic modes obtained in this way possessed high frequencies which had to be decreased artificially by including additional inertia to be able to perform real-time simulations. Furthermore, the approach is not very suitable for systems with alternately increase and decrease in stiffness which is the case for kinematic nonlinear structures.

When using ROM for nonlinear systems the time consuming assembling of the nonlinear internal nodal forces is still required in every time step before projecting them onto the reduced subspace. As an answer to this problem researchers in [14] have presented a reduced basis formulation (RBF) where the discretized equations of motion by a simple mathematical reformulation can be written as a sum of stiffness matrix terms that remain constant throughout the entire analyses each multiplied by a reduced coordinate in the projected subspace. For a subspace consisting of m modes $1+m+m^2$ constant matrix terms are arranged. This reformulation enables a much faster assembling of the nonlinear internal nodal forces compared to the usual assembling element by element.

To the best of the present authors' knowledge no study has been performed illustrating the potential of the method in [14] in a real-time perspective. Thus, in the present study the RBF is used to analyze kinematic nonlinear structures in a real-time perspective to illustrate the applicability in nonlinear real time analysis. Two examples are considered. The first example constitutes a composite beam exposed to harmonic loadings. The beam parameters are based on inspiration from a composite beam planned to be tested in a RTHT arrangement at the Technical University of Denmark (DTU) in the spring 2014, making the example relevant in that perspective.

As will be evident to the reader the analysis of the composite beam is exposed to the phenomena of locking ruining the results. The locking effect is introduced through the choice of basis consisting of purely linear modes. To reduce the effect of this, modes containing higher order terms can be included. This is illustrated in a second example considering a simple cantilever beam.

In section 2 the RBF by [14] is presented together with a reduction of the formulation taking symmetry conditions into account. In section 3 an approach to include higher order terms to the linear normal modes are presented. Finally in section 4 and 5 the examples of the composite and cantilever beams, respectively, are described, analysed and discussed. In section 6 the conclusion is given.

2 REDUCED BASIS FORMULATION

In the following section the RBF developed by [14] is used to reduce a set of discretized kinematic nonlinear equations of motion. Furthermore an improvement of the formulation taking into account symmetry conditions is presented.

2.1 Nonlinear modal equations

The starting point of the method is the global set of discretized nonlinear equations of motion in physical coordinates containing n dofs written in matrix notation

$$\mathbf{M}\ddot{\mathbf{V}} + \mathbf{C}\dot{\mathbf{V}} + \mathbf{g}(\mathbf{V}) = \mathbf{F}(t) \tag{1}$$

where **M** and **C** are *n x n* mass and damping matrices, **F**(t) a *n x 1* external load vector which is a function of time and **g**(**V**) a *n x 1* vector containing internal restoring forces. Finally **V** is a *n x 1* vector representing the nodal displacement in global format where a dot above the vector denotes a time derivative. In the given case the discretized system in (1) is based on continuum mechanics with Green strain characterizing the state of deformation and with the Second Piola-Kirchoff stresses as conjugate stress components, cf. Appendix 1.

In the present only the internal restoring forces, **g**(**V**), are assumed to be a nonlinear function of the nodal displacements. The nonlinear restoring forces consist of a constant, linear and a quadratic stiffness matrix contribution in **V**

$$\mathbf{g}(\mathbf{V}) = (\mathbf{K}^0 + \mathbf{K}^1(\mathbf{V}) + \mathbf{K}^2(\mathbf{V},\mathbf{V}))\mathbf{V} \tag{2}$$

where $\mathbf{K}^0$ is the constant stiffness matrix known from linear elastic theory and $\mathbf{K}^1$ and $\mathbf{K}^2$ are linear and quadratic functions of the **V**, respectively, introduced due to the kinematic nonlinearities.

The discretized nonlinear equation of motion in physical coordinates can be projected onto a reduced subspace by introducing a relation between the physical and reduced coordinates given as

$$\mathbf{V} = \mathbf{\Phi}\mathbf{S} = \sum_{i=1}^{m} \boldsymbol{\varphi}_i s_i \tag{3}$$

where **Φ** is a *m x m* matrix containing m basis', $\boldsymbol{\varphi}_i$, arranged as columns and **S** a *m x 1* vector containing the m reduced

coordinates, s_i. The number of reduced basis are usually much smaller than the number of dofs, i.e. $m << n$.

Projecting the discretized equations in (1) onto the reduced subspace represented by (3) yields the general formulation

$$\tilde{\mathbf{M}}\ddot{\mathbf{S}} + \tilde{\mathbf{C}}\dot{\mathbf{S}} + \tilde{\mathbf{g}}(\mathbf{S}) = \tilde{\mathbf{F}}(t) \tag{4}$$

with the introduced vectors and matrices

$$\begin{aligned} \tilde{\mathbf{M}} &= \mathbf{\Phi}^T \mathbf{M} \mathbf{\Phi} \\ \tilde{\mathbf{C}} &= \mathbf{\Phi}^T \mathbf{C} \mathbf{\Phi} \\ \tilde{\mathbf{g}}(\mathbf{S}) &= \mathbf{\Phi}^T \mathbf{g}(\mathbf{\Phi}\mathbf{S}) \end{aligned} \tag{5}$$

In [14] the nodal restoring forces in (5) are written as a sum using the right hand side of (3). This leads to the general formulation for the reduced internal nodal forces

$$\tilde{\mathbf{g}}(\mathbf{S}) = (\tilde{\mathbf{K}}^0 + \sum_{i=1}^{m} \tilde{\mathbf{K}}_i^1 s_i + \sum_{i=1}^{m}\sum_{j=1}^{m} \tilde{\mathbf{K}}_{ij}^2 s_i s_j)\mathbf{S} \tag{6}$$

where all matrices appearing in (6) are constants. In Appendix 2 the formulation of the matrices based on Continuum mechanics are presented.

As the matrices appearing in (6) are constants these can be built before initiating the time integration if keeping the same basis throughout the analysis. This allows for a fast assembling of the nodal forces in (6) between each time step compared to the usual costly assembling of the internal nodal forces performed element by element.

2.2 Symmetry reduction of quadratic sum

The formulation of the restoring forces in (6) can compacted even further by taking advantage of the symmetry of the products of the reduced coordinates

$$s_i s_j = s_j s_i \tag{7}$$

By introducing the definition

$$\tilde{\mathbf{K}}_{ij}^{2*} = \tilde{\mathbf{K}}_{ij}^2 + (1-\delta_{ij})\tilde{\mathbf{K}}_{ji}^2 \tag{8}$$

The symmetry condition in (7) allows the quadratic sum in (6) to be written as

$$\sum_{i=1}^{m}\sum_{j=1}^{m} \tilde{\mathbf{K}}_{ij}^2 s_i s_j = \sum_{i=1}^{m}\left(\sum_{j=1}^{i} \tilde{\mathbf{K}}_{ij}^{2*} s_i s_j\right) \tag{9}$$

This reduces the number of sums by the number

$$m_{reduced} = m^2 - \frac{m^2 - m}{2} = \frac{m^2 - m}{2} \tag{10}$$

corresponding to a relative reduction of magnitude

$$r = \frac{m_{reduced}}{m^2} = \frac{(\mathrm{m}-1)}{2m} \tag{11}$$

In the limit state this approaches a reduction of magnitude

$$\lim_{m\to\infty} r = \frac{1}{2} = 50\% \tag{12}$$

3 MODES INCLUDING HIGHER ORDER EFFECTS

Choosing a reduction basis consisting of linear modes from the undeformed stage might causes the nonlinear coupling effects of the structure to be locked as these effects are not accounted for by the linear normal modes. This will increase the stiffness of the system and thereby affect the accuracy of the results. To prevent these locking phenomena modes containing higher order terms can be included.

Considering a linear normal mode i, $\mathbf{\Phi}_i$, an estimate for a mode, $\mathbf{\Phi}_i^h$, representing the higher order terms of the linear mode can be found by performing a nonlinear static calculation considering an equivalent formulation of the eigenvalue problem (EVP). Considering the mass times the considered linear mode as an external load and replacing the square of the natural frequency by a scaling factor α a nonlinear static system of equations can be arranged as

$$\mathbf{K}(\mathbf{\Phi})\mathbf{\Phi} = \alpha \mathbf{M}\mathbf{\Phi}_i \tag{13}$$

By scaling the load factor α such that the solution vector $\mathbf{\Phi}$ deviates slightly from the linear solution a vector estimate for the higher order terms of $\mathbf{\Phi}_i$, can be taken as the difference between the linear normal mode and the static solution

$$\mathbf{\Phi}_i^h = \mathbf{\Phi} - \mathbf{\Phi}_i \tag{14}$$

These modes will be applied in the analysis of the cantilever beam in section 5. The modes $\mathbf{\Phi}_i^h$ used in this example case are based on solutions where the maximum deviation in a discretization point between the linear and nonlinear response, $\mathbf{\Phi}$ and $\mathbf{\Phi}_i$, was around 1%.

4 ANALYSIS OF COMPOSITE BEAM

In the following section a composite beam is analysed to illustrate the potential of the RBF described in section 2 in a real-time perspective. Furthermore the example illustrates the consequence of locking introduced if the chosen basis cannot represent the nonlinear coupling effects.

First is presented the description of the composite geometry, boundary conditions, general stiffness parameters and loading. Next the numerical modeling of the beam and the analysis approach is described. In the final section the analysis results are presented and discussed.

4.1 Geometry and boundary conditions of composite beam

In Figure 1 is sketched the composite beam in the x-z plane. The beam is of length L and simply supported at the beam ends with the rotation axis arranged in the bottom of the composite. The distance L_c marks a part of the beam where a section cut is made to increase the effect of the kinematic nonlinearities.

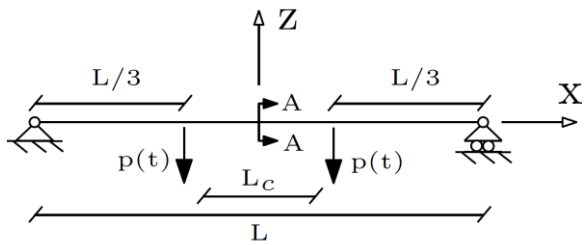

Figure 1. Composite beam in x-z plane.

In Figure 2 the cross section through section A-A marked in Figure 1 is sketched. From the figure the composite is seen to be hollow with an exterior height B and a width H. The wall thicknesses are t_1 and t_2 along the height and width respectively and the curvature along the edges of the profile is r. The introduced section cut is of width h and is placed in the flange in a distance t_2+r from the outer edge of the web. Finally point A marks an edge point at the section cut which will be considered in the analysis.

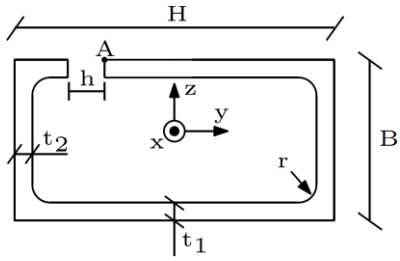

Figure 2. Composite cross section at section A-A.

In Table 1 are listed the geometry parameters of the composite beam.

Table 1. Geometry parameters of composite beam

Parameter	Magnitude	Unit
L	5	m
L_c	1	m
H	0.132	m
B	0.054	m
R	0.006	m
t_1, t_2	0.002	m
H	0.004	m
A	680	mm^2

4.2 *Loading of composite beam*

The beam is loaded by a periodic loading

$$p(t) = F_1 \sin(\omega_1 t) + F_2 \sin(\omega_2 t) \tag{15}$$

with F_1 and F_2 denoting the load amplitudes and ω_1 and ω_2 the load frequencies

Table 2. Loading parameters for composite beam

Parameter	Magnitude	Unit
F_1	2	kN
F_2	1.25	kN
ω_1	5.20	Hz
ω_2	58.20	Hz

As illustrated in Figure 1 the resultant loads are applied a distance L/3 from the beam edges. They are distributed over a square area of size $(0.4 \times H)^2$ at the bottom flange. The load parameters are presented in Table 2. The load frequencies span the frequency domain of the ten first modes of the composite in the undeformed stage.

4.3 *Stiffness parameters*

The composite beam consists of a synthetic matrix material reinforced with longitudinal fibers in one direction of the beam. In Table 3 are listed the stiffness's parameters used in the analysis with the subscript referring the global direction indicated in Figure 1 and Figure 2. The parameters are taken from [19].

Table 3. Stiffness and material parameters of composite

Parameter	Magnitude	Unit
E_x	23	GPa
E_y, E_z	8.5	GPa
G	3	GPa
ν_{xy}, ν_{xz}	0.230	-
ν_{yx}, ν_{zx}	0.085	-
ν_{yz}, ν_{zy}	0.230	-
ρ	1825	kg/m^3

E_x, E_y, E_z denote the orthotropic moduli of elasticity and G denote the orthotropic shear moduli for shear deformation assumed equal in all planes, respectively. The term ν_{xy} is a Poisson ratio characterizing the strain in the y-direction produced by the stress in the x-direction. Similar interpretations are given for the remaining Poison ratios listed in Table 3. Finally ρ denotes the density of the composite.

In the given case it is assumed that the fibers are aligned parallel with the length of the beam leading to maximum stiffness moduli in the x-direction

4.4 *Numerical Modeling*

The composite beam is modeled in a local MATLAB based finite element program named BYGFEM. To model the structure the 10-nodal isoparametric tetrahedral element sketched in Figure 3 is used. The element can describe displacement fields up to 2nd order and stress fields up to 1st order correctly. Three translations describe the deformation in each node. For a more thorough description of the element, see e.g. [15].

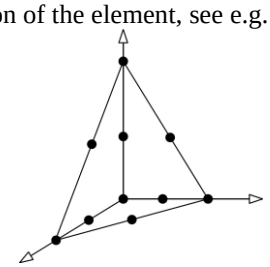

Figure 3. 10-nodal tetrahedral element.

To perform the time integration when using the RBF is used the *central difference method* (CDM) which is an explicit 2nd order method, see e.g. [15]. The reason for picking this integration scheme is that it is simple whereas the disadvantage is that the time step has to be below a critical value in order to prevent instability. To check the accuracy of the RBF solution this is compared to a full solution found with an implicit Newmark algorithm (NA).

In Table 4 are listed some of the algorithm parameters used in the analysis with t_{act} denoting the actual time simulated, Δt the time step magnitude with the superscript referring to the method applied and the algorithm parameters α and β applied in the full implicit analysis. The latter two are set equal to a magnitude corresponding to unconditionally stability in the linear analysis case. Finally ϵ is the equilibrium tolerance.

Table 4. Algorithm parameters

Parameter	Magnitude	Unit
t_{act}	0.25	s
Δt^{NA} / Δt^{CDM}	10^{-3} / $3 \cdot 10^{-5}$	s
ϵ	10^{-3}	-
γ	½	-
β	¼	-

Two different mesh sizes were used in the analysis. In the region spanning the section cut of length L_c (cf. Figure 1) the mesh density is set to ten times finer than in the remaining structure in order to model the curvature at the section cut sufficient. A total of 65523 dofs were contained in the model.

The basis used in the RBF is taken as the lowest 25 linear normal modes of the composite in the undeformed stage.

4.5 Analysis results and discussion

In Figure 4 is plotted the displacement, u_z, in point A (cf. Figure 2) in the time interval $t \in [0, 0.04]$ sec. The blue curve shows the solution obtained with the implicit NA representing the full solution. The red curve shows the RBF solution.

From the figure it is observed that the RBF curve starts to deviate significantly from the full model solution already from around t = 0.02 seconds. Around this point the RBF curve reaches a local maximum whereas the NA response keeps increasing rapidly. The behavior of the two curves indicate that the RBF solution exhibits a much higher stiffer than the NA solution. As indicated previously and as will be demonstrated in the example in the next section the increased stiffness is introduced through the choice of modes included in the model. Due to the kinematic nonlinearities coupling of the transverse and axial deformations take place. If the chosen modes do not represent these coupling effects sufficiently locking will appear increasing the stiffness of the system.

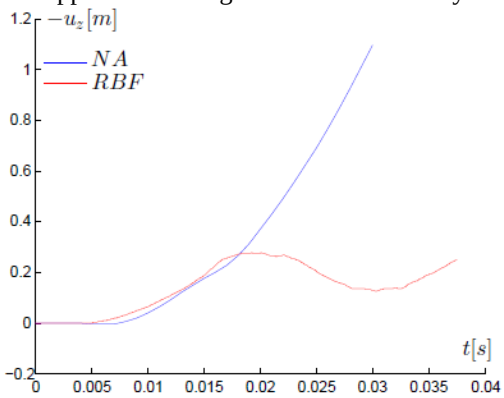

Figure 4. Displacement, u_z, at point A in the composite beam found using a NA and the RBF, respectively.

One way to overcome the locking phenomena is by increasing the number of modes until a sufficiently number of modes can represent these nonlinear effects. However, in order for the RBF to be performed in real time it is necessary to keep the number of modes as few as possible while still being able to describe the response as good as possible.

In Table 5 is presented how many modes that can be contained in the model for different time step magnitudes if the RBF should be executed in real time. It should be stressed that the results are based on simulations on a standard PC.

Table 5. Mode limit vs. time step magnitude

Time step [s]	No. of modes
10^{-3}	35
10^{-4}	12
10^{-5}	1

The table shows a decrease in number of modes as the time step is decreased, which should be expected. For a time step of magnitude $\Delta t = 10^{-5}$ a model approximated by one mode only can be executed in real time, whereas by increasing the time step to $\Delta t = 10^{-4}$ sec enables one to describe the response with up to 12 modes. Decreasing the time step further to $\Delta t = 10^{-3}$ sec up to 35 modes can be applied. As the time step is dictated by the highest frequency of the system through the stability requirement, the time step that can be applied is restricted by the nature of the considered system. Thus, the RBF is most suitable for low frequency ranges as this allows for larger time steps. From the table it is also evident that 25 modes are way beyond the limit for real time execution for the given time step applied analyzing the composite beam. However, the example in the next section indicates that by using only a few higher order modes the results can be improved significantly.

5 ANALYSIS OF CANTILEVER BEAM

A cantilever beam exposed to a harmonic loading is analysed next. The example serves to illustrate that the locking effect of a nonlinear response can be reduced significantly by introducing few modes including higher order effects.

5.1 Geometry, loading & stiffness parameters of cantilever

The cantilever is of length L and has a cross section of width and height w and h, cf. Figure 5.

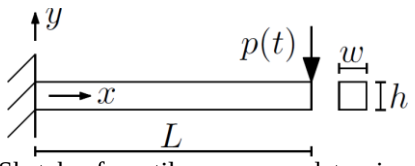

Figure 5. Sketch of cantilever exposed to sinusoidal load (left) and it cross section dimensions (right).

It is exposed to a sinusoidal load with amplitude F and excitation frequency ω.

$$p(t) = F \sin(\omega \cdot t) \tag{16}$$

The cantilever is isotropic and made from steel. The load amplitude F is chosen such that the response is significantly nonlinear. The frequency, ω, corresponds to 1/25 of the lowest natural frequency in the undeformed stage.

In Table 6 are presented the beam and load parameters.

Table 6. Cantilever parameters

Parameter	Magnitude	Unit
E	210	GPa
ν	0.3	GPa
h, w	1	m
L	4	m
F	2	GPa
ω	2	Hz

5.2 *Numerical modeling*

The cantilever is modeled with a mesh consisting of four elements along the height, twelve elements along the length and one element in the width direction with the tetrahedral element presented previously.

As for the composite beam the response of the cantilever beam is analysed numerically using the implicit NA and the CDM algorithm for the RBF with the algorithm parameters in Table 4.

In the present analysis the basis chosen for the RBF analysis consists of a varying number of modes. To reduce the locking effects linear modes and their corresponding higher order modes are included as determined by (13)-(14) using a Newton-Raphson algorithm. In Table 7 are listed three combinations of modes used.

Table 7. Modes included in RBF solutions

Case	Linear modes no.	Higher order modes no.
RBF 1	1-4	-
RBF 2	1	1
RBF 3	1, 4	1, 4

In the 'RBF 1'-case the linear modes 1 to 4 are included without higher order terms. These modes constitute bending modes in the load direction (mode 1 and 4) whereas mode 2 and 3 constitute a bending mode opposite to the load direction and a torsional load around the beam axis. In the 'RBF 2'- and 'RBF 3'-case only the bending modes in the load plane together with their higher order modes are considered.

5.3 *Analysis of Cantilever*

In Figure 6 is plotted the response of the cross-sectional midpoint node at the loaded beam end. The blue curve represents NA solution whereas the remaining curves represent the RBF solutions.

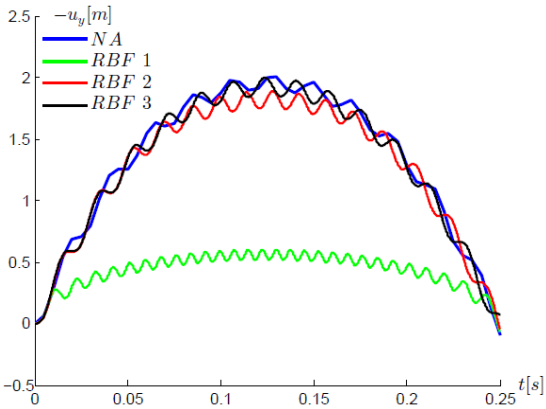

Figure 6. Deformation of midpoint node at loaded end.

Considering the full response the deformation it is seen to be dominated by a frequency equal to the excitation frequency with amplitude around 2 m corresponding to the static nonlinear response of the beam if exposed to the load amplitude, F. Local oscillations appear with a frequency around 50 Hz corresponding to the first linear bending mode of the beam. This mode is only slightly excited due to the relatively slower load frequency. The response in the 'RBF 1'-case identifies a similar locking phenomenon indicated by the relatively small global amplitude and the increased local frequency response. By including the higher order modes the locking effects are seen to be significantly reduced as the curves 'RBF 2' and 'RBF 3' attain amplitudes close to the NA solution. The solutions 'RBF 2' and 'RBF 3' are not fully converged, but their results indicate that by adding few additional modes with higher order terms the response can improved significantly.

6 CONCLUSION

It has been demonstrated how to reduce a set of kinematic nonlinear equations of motion applying a reduced basis formulation (RBF) introduced by [14] making it possible to perform fast nodal force assembling. The formulation was improved using a symmetry condition reducing the number of assembling terms by fifty percent in the limit state. A composite beam exposed to a periodic loading was used as example to demonstrate the potential of the RBF. The results were influenced by locking introduced through the choice of included linear modes increasing the stiffness of the model. However, by adding a few higher order modes to the basis it was shown that the locking could be significantly reduced. This was illustrated in a simple example considering a cantilever beam. Furthermore it was concluded that time steps of magnitude 10^{-3} s, 10^{-4} s and 10^{-5} s allow the simulations to be performed in real time with up to around 35, 12 and 1 mode(s), respectively, on a standard PC. Based on this it is concluded that the RBF has potential to perform real time simulations if choosing a sufficient basis and if possible to go beyond a time step of 10^{-5} sec.

7 APPENDICES

In Appendix 1 the Continuum mechanics theory required for a finite element formulation is presented. In Appendix 2 the discretized equations of motion are derived based on the presented Continuum mechanics. Finally in Appendix 3 the definitions of the constant matrices in the sum-formulation in (6) are presented.

7.1 *Appendix 1 – Generalized Strains and Stresses*

In the present Continuum theory required to arrange the finite element formulations is presented. The Green Strain measure is chosen to characterize the state of deformation of the continuum considered with the conjugate stress given as the Second-Piola Kirchoff stress measure. A detailed description of the theory can be seen in e.g. [16-17].

The starting point is the general Green strain tensor

$$E_{ij} = \frac{1}{2}\left(\frac{\partial u_i}{\partial x_j^0} + \frac{\partial u_j}{\partial x_i^0}\right) + \frac{1}{2}\frac{\partial u_\gamma}{\partial x_j^0}\frac{\partial u_\gamma}{\partial x_i^0} = \frac{1}{2}\left(F_{ik}^T F_{kj} - \delta_{ij}\right) \tag{17}$$

and its variation

$$\delta E_{ij} = \frac{1}{2}\left(\frac{\partial x_\gamma}{\partial x_i^0}\frac{\partial(\delta u_\gamma)}{\partial x_j^0} + \frac{\partial(\delta u_\gamma)}{\partial x_i^0}\frac{\partial x_\gamma}{\partial x_j^0}\right) = \frac{1}{2}\left(F_{ik}^T \delta D_{kj} + \delta D_{ik}^T F_{kj}\right) \tag{18}$$

Where δ_{ij} is Kronecker's delta, F the deformation gradient, and D the displacement gradient given as

$$F_{ij} = \frac{\partial x_i}{\partial x_j^0} = \delta_{ij} + D_{ij} = [\boldsymbol{\delta}_1 + \mathbf{d}_1 \;\; \boldsymbol{\delta}_2 + \mathbf{d}_2 \;\; \boldsymbol{\delta}_3 + \mathbf{d}_3] \tag{19}$$

$$D_{ij} = \frac{\partial u_i}{\partial x_j^0} = [\mathbf{d}_1 \quad \mathbf{d}_2 \quad \mathbf{d}_3] \tag{20}$$

$$\delta D_{ij} = \frac{\partial(\delta u_i)}{\partial x_j^0} = [\delta\mathbf{d}_1 \quad \delta\mathbf{d}_2 \quad \delta\mathbf{d}_3] \tag{21}$$

As stated on the right hand side of (19)-(21) the tensors can be arranged as column vectors. This formulation is used to organize the finite element formulation in the following section.

The seond Piola-Kirchoff stress measure, S, is related to the Green strain tensor, E, through the constitutive relation assuming a *Saint Venant-Kirchoff material*

$$S_{ij} = C_{ijkl} E_{kl} \tag{22}$$

where C_{ijkl} is a fourth-order tensor of elastic moduli which are constant. It is often computationally convenient to represent the stress and strain components as a one-dimensional array. These are therefore organized in Voigt notation. For the given case considering orthotropic material this is given as, se e.g. [18]

$$C = \frac{1}{\nu_{12}\nu_{23}\nu_{31} + \nu_{13}\nu_{21}\nu_{32} + \nu_{12}\nu_{21} + \nu_{13}\nu_{31} + \nu_{23}\nu_{32} - 1} \times \begin{bmatrix} E_x(\nu_{yz}\nu_{zy} - 1) & -E_x(\nu_{yz}\nu_{zx} + \nu_{yx}) & -E_x(\nu_{yx}\nu_{zy} + \nu_{zx}) & 0 & 0 & 0 \\ & E_y(\nu_{xz}\nu_{zx} - 1) & -E_y(\nu_{xy}\nu_{zx} + \nu_{zy}) & 0 & 0 & 0 \\ & & E_z(\nu_{xy}\nu_{yx} - 1) & 0 & 0 & 0 \\ & & & G_{yz} & 0 & 0 \\ & sym & & & G_{xz} & 0 \\ & & & & & G_{xy} \end{bmatrix} \tag{23}$$

Introducing the definition in (19)-(20) into the green strain tensor in (17) this can be written in Voigt notation as

$$\mathbf{E} = \left[E_{11}\, E_{22}\, E_{33}\, 2E_{23}\, 2E_{13}\, 2E_{12}\right]^T = \begin{Bmatrix} \boldsymbol{\delta}_1^T\mathbf{d}_1 \\ \boldsymbol{\delta}_2^T\mathbf{d}_2 \\ \boldsymbol{\delta}_3^T\mathbf{d}_3 \\ \boldsymbol{\delta}_2^T\mathbf{d}_3 + \boldsymbol{\delta}_3^T\mathbf{d}_2 \\ \boldsymbol{\delta}_1^T\mathbf{d}_3 + \boldsymbol{\delta}_3^T\mathbf{d}_1 \\ \boldsymbol{\delta}_1^T\mathbf{d}_2 + \boldsymbol{\delta}_2^T\mathbf{d}_1 \end{Bmatrix} + \frac{1}{2}\begin{Bmatrix} \mathbf{d}_1^T\mathbf{d}_1 \\ \mathbf{d}_2^T\mathbf{d}_2 \\ \mathbf{d}_3^T\mathbf{d}_3 \\ 2\mathbf{d}_2^T\mathbf{d}_3 \\ 2\mathbf{d}_1^T\mathbf{d}_3 \\ 2\mathbf{d}_1^T\mathbf{d}_2 \end{Bmatrix} = \mathbf{E}_{lin} + \mathbf{E}_{nonlin} \tag{24}$$

7.2 Appendix 2 – Finite Element Formulation

In the present appendix the formulation of the element local discretized equations of motion are presented. The element local variation, **u**, is interpolated in terms of the end point nodal degrees of freedom contained in the vector **v** as

$$\mathbf{u} = \mathbf{N}\mathbf{v} \tag{25}$$

Where **N** is the displacement interpolation matrix **N** for an element with m degrees of freedom. With this the vectors $\mathbf{d}_j$ in (18) can be formulated as

$$\mathbf{d}_j = \frac{\partial u_i}{\partial x_j^0} = \frac{\partial}{\partial x_j^0}\mathbf{N}\mathbf{v} = \mathbf{B}_j\mathbf{v} \tag{26}$$

The corresponding virtual components to (27) is

$$\delta\mathbf{d}_j = \mathbf{B}_j\delta\mathbf{v} \tag{27}$$

Introducing the notations

$$2\mathbf{d}_i^T\mathbf{d}_j = \mathbf{d}_i^T\mathbf{d}_j + \mathbf{d}_j^T\mathbf{d}_i = \mathbf{v}^T\mathbf{B}_i^T\mathbf{B}_j\mathbf{v} + \mathbf{v}^T\mathbf{B}_j^T\mathbf{B}_i\mathbf{v} = \mathbf{v}^T(\mathbf{B}_i^T\mathbf{B}_j + \mathbf{B}_j^T\mathbf{B}_i)\mathbf{v} \tag{28}$$

$$\left(1 - \frac{1}{2}\delta_{ij}\right)\left(\mathbf{B}_i\mathbf{B}_j + \mathbf{B}_j\mathbf{B}_i\right) = \mathbf{B}_{ij} \tag{29}$$

The nonlinear vector $\mathbf{E}_{nonlin}$ in (24) can be written as

$$\mathbf{E}_{non} = \frac{1}{2}\left[\mathbf{v}^T\mathbf{B}_{11}\;\; \mathbf{v}^T\mathbf{B}_{22}\;\; \mathbf{v}^T\mathbf{B}_{33}\;\; \mathbf{v}^T\mathbf{B}_{23}\;\; \mathbf{v}^T\mathbf{B}_{13}\;\; \mathbf{v}^T\mathbf{B}_{12}\right]^T\mathbf{v} = \frac{1}{2}\mathbf{C}(\mathbf{v})\mathbf{v} \tag{30}$$

Where **C(v)** is a linear function of **v**. Furthermore by introducing the general expression for the linear strains known linear elastic theory

$$\mathbf{E}_{lin} = \mathbf{B}\mathbf{v} \tag{31}$$

With **B** denoting the strain interpolation matrix. The Green strain tensor in (24) can then be written in compact form as

$$\mathbf{E} = \mathbf{B}\mathbf{v} + \frac{1}{2}\mathbf{C}(\mathbf{v})\mathbf{v} \tag{32}$$

Due to symmetry of matrices in (33) the virtual Green strains on Voigt notation can be found as

$$\delta\mathbf{E} = \mathbf{B}\delta\mathbf{v} + \frac{1}{2}\delta\mathbf{C}(\mathbf{v})\mathbf{v} + \frac{1}{2}\mathbf{C}(\mathbf{v})\delta\mathbf{v} \qquad (33)$$
$$= \mathbf{B}\delta\mathbf{v} + \mathbf{C}(\mathbf{v})\delta\mathbf{v}$$

Now the internal nodal load vector **g**(**v**) can be organized from the virtual work equation in static context

$$\delta V_{\text{int}} = \int_{V_0} \delta\mathbf{E}^T \mathbf{S}\ dV_0$$
$$= \int_{V_0} (\mathbf{B}\delta\mathbf{v} + \mathbf{C}\delta\mathbf{v})^T \mathbf{D}(\mathbf{B}\mathbf{v} + \frac{1}{2}\mathbf{C}\mathbf{v})\ dV_0 \qquad (34)$$
$$= \delta\mathbf{v}^T \mathbf{g}(\mathbf{v})$$

With **D** denoting the material stiffness matrix. The matrix contribution in **g**(**v**) are constant terms, terms linear in **v** and terms quadratic in **v**, respectively. These are defined as

$$\mathbf{k}^0 = \int_{V_0} \mathbf{B}^T\mathbf{D}\mathbf{B}\ dV_0$$
$$\mathbf{k}^1(\mathbf{v}) = \int_{V_0} \mathbf{C}(\mathbf{v})^T\mathbf{D}\mathbf{B} + \frac{1}{2}\mathbf{B}^T\mathbf{D}\mathbf{C}(\mathbf{v})\ dV_0 \qquad (35)$$
$$\mathbf{k}^2(\mathbf{v},\mathbf{v}) = \frac{1}{2}\int_{V_0} \mathbf{C}(\mathbf{v})^T\mathbf{D}\mathbf{C}(\mathbf{v})$$

The nonlinear equations of motion are found by adding inertia and damping terms

$$\mathbf{m}\ddot{\mathbf{v}} + \mathbf{c}\dot{\mathbf{v}} + \mathbf{g}(\mathbf{v}) = \mathbf{f}(t) \qquad (36)$$

With **m** being the mass matrix, **c** the damping matrix and **f**(t) the external load vector.

7.3 Appendix 3 – Formulation of modal matrices

In the following the expressions for the modal matrices in (6) based on the continuum theory presented in Appendix 1 are identified.

The local element dofs in **v** and the global dofs **V** are related through the element local topology array **L**

$$\mathbf{v} = \mathbf{L}\mathbf{V} = \mathbf{L}\boldsymbol{\varphi}_i s_i \qquad (37)$$

Where the reduced basis formulation in (3) is introduced. Introducing this relation into the nonlinear part of the nodal forces in (33) and projecting this onto the reduced basis in (3) yields the expression

$$\boldsymbol{\Phi}^T\mathbf{g}^{non}(\mathbf{v}) = \boldsymbol{\Phi}^T(\int_{V_0}\sum_{i=1}^{m}(\mathbf{C}^T(\mathbf{L}\boldsymbol{\varphi}_i)\mathbf{D}\mathbf{B} + \frac{1}{2}\mathbf{B}^T\mathbf{D}\mathbf{C}(\mathbf{L}\boldsymbol{\varphi}_i))\mathrm{s}_i +$$
$$\sum_{i=1}^{m}\sum_{j=1}^{m}\frac{1}{2}\mathbf{C}^T(\mathbf{L}\boldsymbol{\varphi}_i)\mathbf{D}\mathbf{C}(\mathbf{L}\boldsymbol{\varphi}_j)\mathrm{s}_i\mathrm{s}_j)\boldsymbol{\Phi}\mathbf{s} \qquad (38)$$

From where the local element stiffness's in reduced coordinates are identified as

$$\tilde{\mathbf{k}}^1_{i,el} = \boldsymbol{\Phi}^T(\int_{V_0}\mathbf{C}^T(\mathbf{L}\boldsymbol{\varphi}_i)\mathbf{D}\mathbf{B} + \frac{1}{2}\mathbf{B}^T\mathbf{D}\mathbf{C}(\mathbf{L}\boldsymbol{\varphi}_i))\boldsymbol{\Phi}^T$$
$$\tilde{\mathbf{k}}^2_{ij,el} = \boldsymbol{\Phi}^T(\int_{V_0}\frac{1}{2}\mathbf{C}^T(\mathbf{L}\boldsymbol{\varphi}_i)\mathbf{D}\mathbf{C}(\mathbf{L}\boldsymbol{\varphi}_j))\boldsymbol{\Phi} \qquad (39)$$

The global stiffnesses in reduced coordinates presented in general form in (6) are found by summing over the total number of elements (nel)

$$\tilde{\mathbf{K}}^1_i = \sum_{el=1}^{nel}\tilde{\mathbf{k}}^1_{i,\text{el}}, \quad \tilde{\mathbf{K}}^2_{ij} = \sum_{el=1}^{nel}\tilde{\mathbf{k}}^2_{ij,el} \qquad (40)$$

REFERENCES

[1] Hakuno, M. Shidawara, M. and Hara, T., *Dynamic destructive test of a cantilever beam, controlled by an analog-computer*, Transactions of the Japan Society of Civil Engineers, vol. 171, pp. 1-9, 1969 (in Japanese)

[2] C. Chen, J. M. Rickles, T. L. Karavasilis, Y. Chae, and R. Sause, *Evaluation of a real-time hybrid simulation system for performance evaluation of structures with rate dependent devices subjected to seismic loading*, Engineering Structures, Vol. 35, pp. 71-82, 2012.

[3] M. Verma and R. Rajasankar et al., *Improved Model for real-time sub-structuring testing system*, Engineering Structures, Vol. 41, pp. 258-269, 2012.

[4] R.-Y. Jung, P. B. Shing, E. Staufer and B. Thoen. *Performance of a real-time pseudodynamic test system considering nonlinear structural response*, Earthquake Engineering, Vol. 36, Issue 12, , pp. 1785-1809, 2007.

[5] D. Combescure & P. Pegon, *alpha-Operator Splitting time integration technique for pseudodynamic testing - Error propagation analysis*, Soil Dynamics & Earthquake Engineering, Vol. 16, Issue 7-8, pp. 427-443, 1997.

[6] R. Sajeeb, D. Roy & C.S. Manohar, *Numerical aspects of a real-time sub-structuring technique in structural dynamics*, International Journal for Numerical Methods In Engineering, Vol. 72, Issue 11, pp. 1261-1313, 2007.

[7] B. Wu, G.S. Xu, Q.Y. Wang, *Operator-splitting method for real-time substructure testing*, Earthquake Engineering and Structural Dynamics, Vol. 35, Issue 3, pp. 293-314, 2006.

[8] B. Wu, H. Bao, J. Ou, *Stability and accuracy analysis of the central difference method for real-time substructure testing*, Vol. 34, Issue 7, pp. 705-718, 2005.

[9] G. Mosqueda and M. Ahmadizadeh, *Combined Implicit or Explicit Integration Steps for Hybrid Simulation*, Earthquake Engineering and Structural Dynamics, Vol. 36, Issue 15, pp. 2325-2343, 2007.

[10] P. A. Bonnet, M. S. Williams & A. Blakeborough. *Evaluation of numerical time-integration schemes for real-time hybrid testing*, Earthquake Engineering And Structural Dynamics, vol. 37, Issue 13, pp. 1467-1490, 2008.

[11] C. Chen, J. M. Ricles, M. M. Thomas and M. Oya, *Real-time hybrid testing using the unconditionally stable explicit CR integration algorithm*, Earthquake Engineering And Structural Dynamics, Vol. 38, pp. 23-44, 2009.

[12] F. A. Lülf, T. Duch-Minh and R. Ohayon, *Reduced bases for nonlinear structural dynamic systems: A comparative study*, Journal of Sound and Vibration, Volume 332, Issue 15, pp. 3897-3921, 2013.

[13] A. Blakeborough, M. S. Williams, A. P. Darby, *The development of real-time substructure testing*, Philosophical Transactions of the Royal Society A: Mathematical, Physical and Engineering Sciences, Volume 359, Issue 1786, pp. 1869-1891, 2001.

[14] Y. Shi & C. Mei, *A finite element time domain modal formulation for large amplitude free vibrations of beams and plates*, Journal of Sound and Vibration, Volume 193, Issue 2, pp. 453-464, 1996

[15] R. D. Cook, D. S. Malkus, M. E. Plesha and R. J. Witt, *Concepts and Applications Of Finite Element Analysis*, John Wiley & Sons, fourth edition, New York, USA, 1974.

[16] S. Krenk, *Non-linear Modeling and Analysis of Solids and Structures*, Cambridge University Press, Cambridge, UK, first edition, 2009.

[17] T. Belytschko, W. K. Liu, B. Moran, *Nonlinear Finite Elements for Continua and Structures*, John Wiley & Sons, Chicester, England, first edition, 2000.

[18] A. P. Boresi et al., *Advanced Mechanics Of Materials*, John Wiley & Sons, New York, USA, sixth edition, 1993.

[19] www.fiberline.com, date: 12/15/13.

Paper II

"Reduction Method for Kinematic Nonlinear Real-time Simulations"

S. Andersen & P. N. Poulsen

Submitted: *International Journal for Numerical Methods in Engineering, 2015*

INTERNATIONAL JOURNAL FOR NUMERICAL METHODS IN ENGINEERING
Int. J. Numer. Meth. Engng 2010; **00**:1–26
Published online in Wiley InterScience (www.interscience.wiley.com). DOI: 10.1002/nme

Reduction Method for Kinematic Nonlinear Real-time Simulations

S. Andersen*† and P. N. Poulsen ‡

Department of Civil Engineering, Technical University of Denmark, 2800 Kgs. Lyngby, Denmark

SUMMARY

Despite todays computational power, only small nonlinear numerical substructures in finite element analysis can be simulated in real time. The size restriction of the substructures is primarily due to the time-consuming evaluation of the internal restoring forces performed element-by-element. In the present is presented a method to simulate kinematic nonlinear structures more efficiently. It entails applying a reduced basis with modal derivatives, representing the nonlinearities to reduce the number of degrees of freedom. Previously, the modal derivatives have been determined from a set of approximate governing equations. In this work, by introducing a Taylor series into the free undamped kinematic nonlinear equations of motion, is derived a novel set of equations representing the complete system of equations governing the modal derivatives. Furthermore is used a reduced basis formulation (RBF) in order to evaluate the internal restoring forces efficiently as a sum of constant equivalent force vectors multiplied by reduced co-ordinates. By way of an example it is shown that only the modal derivatives determined from the complete set of equations are consistent with the Taylor series. Furthermore, the present method allows up to 70 degrees of freedom to run in real-time on a standard PC. Copyright © 2010 John Wiley & Sons, Ltd.

Received . . .

KEY WORDS: Kinematic Nonlinearities; Real-time Simulations; Basis Reduction; Modal Derivatives; Finite Element Analysis

1. INTRODUCTION

Hybrid testing is a testing method developed by Japanese scientists in the 1960s by combining a physical component with a numerical simulation, see [1]. If conducted in real time in order to include dynamic effects, the method is often referred to as real-time hybrid testing (RTHT) or real-time hybrid simulation.

The principle of the method consists of partitioning a test structure into two parts. One is a physical part of the structure that is considered to be a black box displaying complicated or unknown structural behavior. This substructure, therefore, has to be tested in a physical test setup. The other part is well understood, and its structural response can be determined by analytical means. Thus, this substructure does not have to be tested in a physical test setup, but can instead be modeled numerically, and its response can be determined by time integration techniques.

During the hybrid test, a high frequent iteration loop exchanges data between the numerical and physical substructures. The displacement response of the numerical substructure found from time integration is imposed onto the physical substructure at the common interface of the substructures through servo-hydraulic actuators at a finite number of points. The force response from the physical substructure due to the imposed displacements is then measured by the actuators, and sent to the

*Correspondence to: Sebastian Andersen, Department of Civil Engineering, Technical University of Denmark, 2800 Kgs. Lyngby, Denmark. Tel.: +45 25 50 48, E-mail: seba@byg.dtu.dk
†PhD Student
‡Associate Professor

Copyright © 2010 John Wiley & Sons, Ltd.

numerical model ending the loop. The following loop is then initiated including the measured force response of the structure in the numerical simulation. Together, the experimental substructure(s), the numerical substructure(s), the integration algorithm and the servo-hydraulic actuators, are integrated through an IT control system to form the RTHT system. For further details about the principle of hybrid testing see for example [2, 3].

One crucial aspect for RTHT to be successful is that the time integration is robust, accurate and fast in order to ensure real-time execution. However, when nonlinear behavior is included, the real-time execution requirement significantly limits the size of the numerical substructures. A large part of the computational time in nonlinear analysis is spent on evaluating the internal nodal restoring forces element-by-element, followed by assembling the global set of equations before conducting each time step. By increasing the size of the numerical models, the assembling time is obviously increased as well. Simultaneously, increasing the model size and complexity introduces higher frequencies, which calls for smaller time steps in the integration schemes in order to maintain stability and accuracy. This again increases the computational time as the assembling frequency of the internal nodal forces is increased.

Researchers in the RTHT context have considered both implicit and explicit algorithms, and combinations of these, see for example [4–10]. In [10] a number of implicit and explicit integration schemes are evaluated in a RTHT setup with nonlinear finite element substructures. The study concludes that explicit schemes are preferable as these do not require equilibrium iterations, making them less time-consuming than implicit algorithms. However, the downside of explicit schemes is that smaller time steps are required to maintain stability of the system compared with implicit schemes. Yet, the capacity with respect to degrees of freedom (dofs) in the study in [10] is very modest with an upper limit of around 50 dofs. The largest number of dofs applied in a RTHT with a nonlinear numerical substructure found by the present authors is 134, see [11]. In many cases, this can be considered as a modest model size.

One way to lessen the computational time of nonlinear systems is to reduce the number of dofs in the models. This is also referred to as a reduced order model. This can be done by projecting the discretized nonlinear equations of motion onto a subspace represented by a reduced basis. The concept is well known from linear theory, and provides a simple way to reduce the number of dofs and at the same time cuts off some of the higher frequency content in the model not representing real physics. The first use of the concept to kinematic nonlinear structural systems can be dated back to the work of Horri [12], and later to that of Nickell [13]. In both cases, eigenvectors constituted the basis.

Projection-based methods have been applied in a RTHT context. The authors of [14] use a basis consisting of linear normal modes, and plastic deformation modes found from static considerations, to reduce a 50 dof material nonlinear numerical substructure and to perform the simulations in real time. However, the plastic modes possessed high frequencies, which had to be decreased artificially by including additional inertia in order to be able to perform real-time simulations.

Since the work with projection-based reduction of kinematic nonlinear equations presented in [12, 13], a variety of different bases have been developed, and applied in the nonlinear context. [15] presents an overview and evaluation of the most commonly used bases applied for kinematic nonlinear structures considering robustness and accuracy. Among these are bases consisting of Ritz vectors [16], and vectors based on the proper orthogonal decomposition method and modal derivatives, [17] to mention a few.

In the present article, to simulate kinematic nonlinear systems, is applied a set of eigenvector modes fulfilling the linearized eigenvalue problem and their modal derivatives. So far, the modal derivatives have been determined as the solution of the linearized eigenvalue problem in differentiated form introduced by Idelsohn & Cardona, see [17, 18]. However, by default this system of equations contains a singular matrix, and the modal derivatives cannot be solved directly. The most common approach to circumvent this problem has been to neglect the inertia of the system, leading to a sought of static modal derivative, see for example [17, 19–21]. The authors of [22] suggest a numerical approach by evaluating the modal derivative as the difference between two tangent modes at two equilibrium stages separated by a small displacement increment. Furthermore,

Copyright © 2010 John Wiley & Sons, Ltd.

DOI: 10.1002/nme

[17, 22] discuss the possibility of counteracting the singularity by predefining a component in the modal derivatives to a value free of choice, and determine the remaining components through a reduced set of equations. The authors of [18] assume a linear expression for the acceleration. They insert this into the equations of motion, and differentiating these leads to a recurrence relationship on static form, from which the modal derivatives can be determined. However, all of the mentioned approaches lead to approximate solutions. In the present work, the singularity problem is solved by introducing an additional condition using the Lagrange multiplier method. This allows the modal derivatives to be determined without introducing any approximations.

More importantly it should be stressed that the equations introduced by Idelsohn & Cardona, see [17, 18], are based on a linearized set of equations. This means that the equations can only serve as a set of approximated governing equations for the modal derivatives. In the following discussion, the modal derivatives determined from this system of equations are referred to as the approximate modal derivatives.

In the present work, is derived a set of equations representing the complete system of equations governing the modal derivatives. This is done by introducing a Taylor series into the free undamped kinematic nonlinear equations of motion, and putting forward the argument that all the generated coefficients in the system should be zero. Each coefficient represents a governing set of equations. The zero order proportional coefficients represent the equations of motion; the first order proportional coefficients represent the eigenvalue problem; and the second order proportional coefficients represent the system of equations governing the modal derivatives. In the following discussion, the modal derivatives determined from these equations are referred to as the complete modal derivatives'. The complete set of governing equations derived is nonsingular and the modal derivatives can easily be determined without having to introduce a number of approximations. Furthermore, in contrast to the former applied approximate modal derivatives, the complete modal derivatives are consistent with the Taylor series.

When introducing a basis into the nonlinear equations of motion, the projection-based reformulation technique presented by Nash [23] can be applied to further reduce the computational time. The concept consists of introducing a reduced basis into the global equations of motion, and then reformulating the internal nonlinear stiffness as a sum of constant equivalent stiffness coefficients multiplied by reduced co-ordinates up to a quadratic order. By simple manipulation the internal restoring forces can be expressed as a sum of constant equivalent force vectors multiplied by reduced co-ordinates up to a cubic order. With this global formulation, the time consuming assembly of the internal nodal restoring forces between each time step can be heavily reduced compared with the usual element-by-element assembling approach.

Because of its computational saving, the reformulation technique introduced by Nash [23] has been applied by several researchers; see for example [24–27]. However, there are many ways to determine the coefficients. In [21, 23, 24] the coefficients are identified by directly manipulating the nonlinear finite element formulation. The coefficients can alternatively be found from static solutions by indirect identification [26–28], or from experimental data [25].

The authors of [21] use the reformulation technique of [23] to perform real-time simulations in a graphical context. They record impressive simulation times. However, they do not enter into discussion or present detailed information on how large models can be simulated in real time with the given formulation. The present work will investigate this.

In the following section, is presented the derivation of the novel set of equations representing the complete set of equations governing the modal derivatives. Next, is presented the differentiated eigenvalue problem with an additional condition introduced through the Lagrange multiplier method. Then, in section three, is presented the RBF method. Finally, in section four, is given an example considering a kinematic nonlinear cable exposed to harmonic loading. The example is used to exemplify and evaluate the real-time potential of the RBF method. Furthermore, the example demonstrates that only the co-ordinates of the complete modal derivatives are consistent with the prediction of the Taylor series. It should be stressed that the RBF method is only applicable for kinematic nonlinear systems, and not material nonlinear systems, since the effects of stiffness change due to cracking or plasticity are not included.

Copyright © 2010 John Wiley & Sons, Ltd.

DOI: 10.1002/nme

2. REDUCED BASIS AND MODAL DERIVATIVES

In the following section, is presented the concept of projecting the nonlinear equations of motion onto a reduced basis. Next, is derived a complete system of equations governing the modal derivatives by introducing a Taylor series into the free undamped equations of motion. Finally, is considered the linearized eigenvalue problem in differentiated form, and its singularity is removed by introducing an innovative geometric restriction using the Lagrange multiplier method. To exemplify the method with a practical example a plane beam element based on Euler-Bernoulli theory is considered.

2.1. The Governing Equations of Motion

The starting point of the method is the governing equations of motion. Considering an Euler-Bernoulli beam, the governing equations including the axial strain, ε, and the curvature, κ, are given as in, see for example [29]:

$$\rho(x)\frac{\partial^2 w}{\partial t^2} + \frac{\partial^2}{\partial x^2}\left(EI(x)\kappa\right) = p(x) \tag{1}$$

$$\rho(x)\frac{\partial^2 u}{\partial t^2} - \frac{\partial}{\partial x}\left(EA(x)\varepsilon\right) = q(x) \tag{2}$$

where x is the local beam co-ordinate, w and u are respectively the transverse and the axial deformation along the un-deformed beam axis, EI(x) is the bending stiffness, EA(x) is the axial stiffness, ρ(x) is the density per unit length, t is the time, and p(x) and q(x) are the external load in the transverse and axial directions of the beam, respectively. Assuming the Lagrange strain measures to be valid the strains are given as

$$\varepsilon = \frac{\partial u}{\partial x} + \frac{1}{2}\left(\frac{\partial w}{\partial x}\right)^2 \quad , \quad \kappa = \frac{\partial^2 w}{\partial x^2} \tag{3}$$

With the strain definitions in (3) the governing equations of motion in (1) and (2) are seen to couple.

2.2. The Kinematic Nonlinear Equations of Motion

By using the principle of virtual work, the governing equations can be organized in discretized form. Using matrix notation, the global set of discretized kinematic nonlinear equations in physical co-ordinates containing n dofs can be generalized as:

$$\mathbf{M}\ddot{\mathbf{V}} + \mathbf{C}\dot{\mathbf{V}} + \mathbf{g}(\mathbf{V}) = \mathbf{F}(t) \tag{4}$$

where $\mathbf{V}$ is an n$\times$1 vector representing the nodal displacement in global format, with the standard notation $\dot{()} = d()/dt$. Furthermore, $\mathbf{M}$ and $\mathbf{C}$ are n$\times$n mass and damping matrices, $\mathbf{F}$(t) is an n$\times$1 external load vector which is a function of time, and $\mathbf{g}(\mathbf{V})$ is an n$\times$1 vector containing the internal nodal restoring forces. Appendix B gives an example on the discretized equations of motion based on the 2-dimensional Euler-Bernoulli beam element, including viscous damping.

For the present, only the internal restoring forces, $\mathbf{g}(\mathbf{V})$, are assumed to be nonlinear functions of the nodal displacements due to the kinematic nonlinearities. Furthermore, it is assumed that $\mathbf{g}(\mathbf{V})$ contributes a linear, a quadratic and a cubic polynomial in $\mathbf{V}$. The general formula is:

$$\mathbf{g}(\mathbf{V}) = (\mathbf{K}_0 + \mathbf{K}_1(\mathbf{V}) + \mathbf{K}_2(\mathbf{V},\mathbf{V}))\mathbf{V} \tag{5}$$

where $\mathbf{K}_0$ is a constant stiffness matrix and $\mathbf{K}_1(\mathbf{V})$ and $\mathbf{K}_2(\mathbf{V},\mathbf{V})$ are matrices linear and quadratic in the vector $\mathbf{V}$, respectively. (5) will be used in section 3 in the presentation of the reduced basis formulation.

Copyright © 2010 John Wiley & Sons, Ltd.

DOI: 10.1002/nme

2.3. Projection of Nonlinear Equations of Motion

The number of dofs contained in the discretized equations of motion in (4) can be reduced by projecting them onto a reduced subspace. This is done by introducing a relationship between the physical and the reduced co-ordinates, for example of the form

$$\mathbf{V} \approx \mathbf{\Phi s} = \sum_{i=1}^{N} \boldsymbol{\varphi}_i s_i \tag{6}$$

where $\mathbf{\Phi}$ is a n×N matrix containing N base vectors, $\boldsymbol{\varphi}_i$, arranged as columns. Furthermore $\mathbf{s}$ is a N×1 vector containing the N reduced co-ordinates, s_i, i ϵ [1,N]. The number of reduced bases required to obtain a good approximate solution is usually much smaller than the number of dofs, that is, N $\ll$ n. The size of the ratio N/n will however be dependent on the case considered. Typically, the modes with a shape and frequency similar to the loading should be included to obtain a good solution. Furthermore the modes representing the nonlinear effects are important. This is discussed in more detail in the following section.

In the example presented in section 4, the matrix $\mathbf{\Phi}$ contains the eigenvectors fulfilling the linearized eigenvalue problem in equation (7), and their associated derivatives.

$$(\mathbf{K}_T - \omega_i^2 \mathbf{M})\boldsymbol{\varphi}_i = \mathbf{0} \tag{7}$$

In the following the modes constituted by the eigenvectors of equation (7) are referred to as the linear modes, and their derivatives are referred to as the modal derivatives'.

Projecting the discretized equations in (4) onto the reduced subspace represented by (6), and multiplying by $\mathbf{\Phi}^T$ on the left hand side, yields the general formulation for the projected nonlinear equations of motion:

$$\tilde{\mathbf{m}}\ddot{\mathbf{s}} + \tilde{\mathbf{c}}\dot{\mathbf{s}} + \tilde{\mathbf{g}}(\mathbf{s}) = \tilde{\mathbf{f}}(t) \tag{8}$$

where the following matrix definitions have been introduced

$$\tilde{\mathbf{m}} = \mathbf{\Phi}^T\mathbf{M}\mathbf{\Phi} \quad , \quad \tilde{\mathbf{c}} = \mathbf{\Phi}^T\mathbf{C}\mathbf{\Phi} \quad , \quad \tilde{\mathbf{g}}(\mathbf{s}) = \mathbf{\Phi}^T\mathbf{g}(\mathbf{\Phi}s) \quad , \quad \tilde{\mathbf{f}}(t) = \mathbf{\Phi}^T\mathbf{F}(t) \tag{9}$$

2.4. Modal Derivatives

When choosing a reduced basis for the analysis of kinematic nonlinear structures, it is important to take into consideration the effects from the nonlinear behavior. In the case of the Euler-Bernoulli beam, it was demonstrated that the nonlinearity introduced a coupling between the transverse and longitudinal deformations through the axial strain, see equation (3). Modes representing coupling-activated deformations are, therefore, important. Not including these may lead to locking, and result in a heavily increased stiffness of the system, affecting the accuracy of the results.

It can be a difficult task to evaluate which modes are required to represent the deformations activated due to coupling effects. One approach is to include modal derivatives since these represent the higher order effects of the system. This can be shown by first expanding the displacement field $\mathbf{V}(\mathbf{s})$ as a Taylor series in the reduced co-ordinates s_j

$$\mathbf{V}(\mathbf{s}) = \mathbf{V}_0 + \sum_{j=1}^{N} \frac{\partial \mathbf{V}_0}{\partial s_j}(s_j - s_{j0}) + \frac{1}{2}\sum_{j=1}^{N}\sum_{k=1}^{N} \frac{\partial^2 \mathbf{V}_0}{\partial s_j \partial s_k}(s_j - s_{j0})(s_k - s_{k0}) + ... \tag{10}$$

By inserting the basis in (6) into (10), the displacement derivatives can be written in the form:

$$\frac{\partial \mathbf{V}}{\partial s_j} = \frac{\partial}{\partial s_j}\left(\sum_{i=1}^{N} \boldsymbol{\varphi}_i s_i\right) = \sum_{i=1}^{N} \frac{\partial \boldsymbol{\varphi}_i}{\partial s_j} s_i + \boldsymbol{\varphi}_j \tag{11}$$

$$\frac{\partial^2 \mathbf{V}}{\partial s_j \partial s_k} = \frac{\partial}{\partial s_k}\left(\frac{\partial \mathbf{V}}{\partial s_j}\right) = \sum_{i=1}^{N} \frac{\partial^2 \boldsymbol{\varphi}_i}{\partial s_j s_k} s_i + \frac{\partial \boldsymbol{\varphi}_k}{\partial s_j} + \frac{\partial \boldsymbol{\varphi}_j}{\partial s_k} \tag{12}$$

From (11) and (12), the displacement derivatives are seen to include the linear modes and their modal derivatives up to the second order.

Copyright © 2010 John Wiley & Sons, Ltd.

DOI: 10.1002/nme

2.5. Governing Equations Based on Taylor Series

The following presents a novel set of equations representing the complete system of equations governing the modal derivatives in (11) and (12). Only the main steps are presented here. Readers who are interested in the full details are referred to Appendix A.

The starting point of the approach is to consider the free undamped kinematic nonlinear equations of motion:

$$\mathbf{M}\ddot{\mathbf{V}} + \mathbf{g}(\mathbf{V}) = \mathbf{0} \tag{13}$$

A higher order displacement field is chosen to be introduced into (13). In the given case, the Taylor series in (10) is taken as the natural choice, including the terms up to second order. The acceleration is found by differentiating this twice with respect to time:

$$\ddot{\mathbf{V}}(\mathbf{s}) = \sum_{j=1}^{N} \frac{\partial \mathbf{V}_0}{\partial s_j}\ddot{s}_j + \sum_{j=1}^{N}\sum_{k=1}^{N} \frac{1}{2}\frac{\partial^2 \mathbf{V}_0}{\partial s_j \partial s_k}\left[\ddot{s}_j(s_k - s_{k0}) + 2\dot{s}_j\dot{s}_k + (s_j - s_{j0})\ddot{s}_k\right] \tag{14}$$

It is then assumed that the co-ordinates s_j are given in the form

$$s_j = A_j e^{i\omega_j(s_k)t} \tag{15}$$

with A_j denoting the amplitude. This is multiplied by the complex exponential function dependent on the time, t, and the frequency $\omega_j(s_k)$. As the free and undamped system is considered the amplitude is assumed to be constant. The frequency will, however, be a function of the displacement field since kinematic nonlinearities are included. By considering the system of equations at time t = 0, and by introducing the definition

$$s_j = s_j(t=0) \quad , \quad \dot{s}_j = \dot{s}_j(t=0) \quad , \quad \ddot{s}_j = \ddot{s}_j(t=0) \tag{16}$$

the velocity and acceleration can be evaluated from (15) as:

$$\dot{s}_j = i\omega_j(s_k)s_j \quad , \quad \ddot{s}_j = i2\frac{\partial \omega_j(s_k)}{\partial t}s_j - \omega_j^2(s_k)s_j \tag{17}$$

By expanding the frequency $\omega_j(s_k)$, raised to the first and second powers respectively, into a Taylor series, and by introducing (10), (14), (15) and (17) into (13), this can be expressed as a polynomial in the co-ordinates s_j of the form:

$$\mathbf{A} + \sum_{j=1}^{N}\mathbf{B}_j s_j + \sum_{j=1}^{N}\sum_{k=1}^{N}\mathbf{C}_{jk}s_j s_k + ... = \mathbf{0} \tag{18}$$

$\mathbf{A}$, $\mathbf{B}_j$ and $\mathbf{C}_{jk}$ in (18) are vector coefficients. Since the co-ordinates s_j can take on any value, it can be argued that all of the vector coefficients should be zero in order for the equations to be satisfied in all cases. Replacing each coefficient with zero, yields a set of governing equations. The zero order proportional coefficients represent the equations of motion; the first order proportional coefficients represent the eigenvalue problem and the second order proportional coefficients represent the equations governing the modal derivatives.

In Appendix A, the second order proportional coefficients are derived using the Euler-Bernoulli beam element that will be used in the example in section 4. These coefficients lead to a system of equations governing the first and second order displacement fields $\partial^2\mathbf{V}/(\partial s_j \partial s_k)$ and $\partial\mathbf{V}/\partial s_j$ of the form:

$$\left[\mathbf{K}_T(\mathbf{V}_0) + \left(E_{jk} - (\omega_j + \omega_k)^2\right)\mathbf{M}\right]\frac{1}{2}\frac{\partial^2 \mathbf{V}_0}{\partial s_j \partial s_k} = -\left[C_{jk}\mathbf{M} + \frac{\partial \mathbf{K}_S(s_k)}{\partial s_k} + \partial \mathbf{K}_A(s_k)\right]\frac{\partial \mathbf{V}_0}{\partial s_j} \tag{19}$$

Copyright © 2010 John Wiley & Sons, Ltd.

DOI: 10.1002/nme

where $\mathbf{K}_T(\mathbf{V})$ is the tangent stiffness matrix, E_{jk} and C_{jk} are constants, ω_j and ω_k are the linear frequencies belonging respectively to the linear modes numbers j and k, $\partial\mathbf{K}_S(s_k)/\partial s_j$ is the differentiated secant stiffness, and $\partial\mathbf{K}_A(s_k)$ is an additional stiffness contribution.

Since $\partial^2\mathbf{V}/(\partial s_j\partial s_k)$ and $\partial\mathbf{V}/\partial s_j$ both contain unknown modal derivatives of different orders, as seen in (11)-(12), it is not by default possible to determine the modal derivatives from the system of equations in (19). However, by inserting (11) and (12), and by considering the special case with zero initial deformation, the equations in (19) can be simplified to:

$$\left[\mathbf{K}_{T0}(\mathbf{0}) - (\omega_j + \omega_k)^2\mathbf{M}\right]\frac{1}{2}\left(\frac{\partial\boldsymbol{\varphi}_{k0}}{\partial s_j} + \frac{\partial\boldsymbol{\varphi}_{j0}}{\partial s_k}\right) = \left[2\frac{\partial\omega_{j0}}{\partial s_k}(\omega_{j0} - \omega_{k0})\mathbf{M} - \frac{\partial\mathbf{K}_{S0}(0)}{\partial s_k}\right]\boldsymbol{\varphi}_{j0} \quad (20)$$

As seen from (20), the modal derivatives only appear as a sum on the left hand side. These are easily determined by inverting the matrix $[\mathbf{K}_{T0}(\mathbf{0}) - (\omega_j + \omega_k)^2\mathbf{M}]$, consisting of the difference between the tangent stiffness and the mass matrix multiplied by the squared sum of the linear natural frequencies. The right hand side consists of the mass matrix multiplied by the difference between two times the linear frequencies of modes j and k, and multiplied by the natural frequency of mode j differentiated with respect to the co-ordinate s_k. The differentiated secant stiffness is subtracted from this, before multiplying by the j-th linear mode.

2.6. *Determination of Differentiated Frequency*

The differentiated natural frequency on the right hand side of (20) is an unknown quantity. The symmetry of the governing equations can be used to determine this. It is obvious that the left hand side of (20) is symmetric with respect to the subindeces j and k. In order for the equations to be consistent, this requires the right hand side also to be symmetric with respect to these indeces. It is therefore valid that:

$$\left[2\frac{\partial\omega_{j0}}{\partial s_k}(\omega_{j0} - \omega_{k0})\mathbf{M} - \frac{\partial\mathbf{K}_{S0}}{\partial s_k}\right]\boldsymbol{\varphi}_{j0} = \left[2\frac{\partial\omega_{k0}}{\partial s_j}(\omega_{k0} - \omega_{j0})\mathbf{M} - \frac{\partial\mathbf{K}_{S0}}{\partial s_j}\right]\boldsymbol{\varphi}_{k0} \quad (21)$$

Multiplying (21) through by $\boldsymbol{\varphi}_{j0}^T$ and introducing the orthogonality relationship known from linear theory:

$$\boldsymbol{\varphi}_{j0}^T\mathbf{M}\boldsymbol{\varphi}_{k0} = 0 \quad (22)$$

which is valid when $\omega_j \neq \omega_k$, and the following relation is found:

$$2\frac{\partial\omega_{j0}}{\partial s_k}(\omega_{j0} - \omega_{k0}) = \frac{1}{m_j}\left(\frac{\partial k_{S0j}}{\partial s_k} - \boldsymbol{\varphi}_j^T\frac{\partial\mathbf{K}_{S0}}{\partial s_j}\boldsymbol{\varphi}_k\right) \quad (23)$$

where

$$m_j = \boldsymbol{\varphi}_{j0}^T\mathbf{M}\boldsymbol{\varphi}_{j0} \quad , \quad \frac{\partial k_{S0j}}{\partial s_k} = \boldsymbol{\varphi}_{j0}^T\frac{\partial\mathbf{K}_{s0j}}{\partial s_k}\boldsymbol{\varphi}_{j0} \quad (24)$$

Inserting (23) into (21) one arrives at the formula

$$\left[\mathbf{K}_{T0}(\mathbf{0}) - (\omega_{j0} + \omega_{k0})^2\mathbf{M}\right]\frac{1}{2}\left(\frac{\partial\boldsymbol{\varphi}_{k0}}{\partial s_j} + \frac{\partial\boldsymbol{\varphi}_{j0}}{\partial s_k}\right) = \left[\frac{1}{m_j}\left(\frac{\partial k_{S0j}}{\partial s_k} - \boldsymbol{\varphi}_j^T\frac{\partial\mathbf{K}_{S0}}{\partial s_j}\boldsymbol{\varphi}_k\right)\mathbf{M} - \frac{\partial\mathbf{K}_{S0}(0)}{\partial s_k}\right]\boldsymbol{\varphi}_{j0} \quad (25)$$

The system of equations (25) represents the final expression for the equations governing the modal derivatives.

2.7. *The Differentiated Eigenvalue Problem*

The complete modal derivatives determined from (25) are compared with the approximate modal derivatives. The latter are determined from the linearized eigenvalue problem in differentiated form

Copyright © 2010 John Wiley & Sons, Ltd.

DOI: 10.1002/nme

introduced by Idelsohn & Cardona, see [17, 18]. The starting point is the linearized eigenvalue problem

$$\left(\mathbf{K}_T(\mathbf{V}) - \omega_i^2\mathbf{M}\right)\boldsymbol{\varphi}_i = \mathbf{0} \tag{26}$$

If the modal derivative of mode $\boldsymbol{\varphi}_i$ with respect to the reduced co-ordinate s_j is required the eigenvalue problem in (26) is differentiated with respect to s_j. This leads to the system of first order differential equations:

$$\left(\mathbf{K}_T(\mathbf{V}) - \omega_i^2\mathbf{M}\right)\frac{\partial\boldsymbol{\varphi}_i}{\partial s_j} = \left(\frac{\partial\omega_i^2}{\partial s_j}\mathbf{M} - \frac{\partial\mathbf{K}_T(\mathbf{V})}{\partial s_j}\right)\boldsymbol{\varphi}_i \tag{27}$$

The desired modal derivative is seen to appear on the left hand side, multiplied by the matrix appearing in the eigenvalue problem in (26). The right hand side of (27) consists of a matrix, which is the difference between the product of the squared natural frequency and the mass matrix, and the tangent stiffness in differentiated form. This matrix is multiplied by the linear mode.

As the matrix on the left hand side of (27) appears in the eigenvalue problem the system of equations is by default singular. Thus, it is not possible to invert the matrix and determine the higher order mode from this system of equations. However, by introducing a geometric restriction on the modal derivatives it is possible to eliminate the singularity.

2.8. *Geometric Restriction on Modal Derivatives*

The full solution to the modal derivative in (27) is given as a sum of the homogeneous solution and its particular solution

$$\frac{\partial\boldsymbol{\varphi}_i}{\partial s_j} = \left\{\frac{\partial\boldsymbol{\varphi}_i}{\partial s_j}\right\}_{Hom} + \left\{\frac{\partial\boldsymbol{\varphi}_i}{\partial s_j}\right\}_{Part} \tag{28}$$

As the homogeneous system of equations (27) corresponds to the eigenvalue problem in (26), the homogeneous solution must be of the form

$$\left\{\frac{\partial\boldsymbol{\varphi}_i}{\partial s_j}\right\}_{Hom} = \beta\varphi_i \tag{29}$$

where β is a scalar free of choice.

A restriction could be to anticipate that the homogenous and the particular solutions might be orthogonal, that is, their scalar product is zero. An argument in support of this is that, if the particular solution includes information already present in the homogenous solution, this information would be redundant, and vice versa. Thus, a geometric restriction can be expressed as:

$$\left\{\frac{\partial\boldsymbol{\varphi}_i}{\partial s_j}\right\}_{Hom}^T \left\{\frac{\partial\boldsymbol{\varphi}_i}{\partial s_j}\right\}_{Part} = 0 \tag{30}$$

Assuming the particular mode to have a frequency different from the homogenous mode, the mass and stiffness orthogonality conditions also apply

$$\boldsymbol{\varphi}_i^T\mathbf{K}_T(\mathbf{V})\left\{\frac{\partial\boldsymbol{\varphi}_i}{\partial s_j}\right\}_{Part} = \boldsymbol{\varphi}_i^T\mathbf{M}\left\{\frac{\partial\boldsymbol{\varphi}_i}{\partial s_j}\right\}_{Part} = 0 \tag{31}$$

Considering the system of equations in (27) to be derived from a minimization condition with the modal derivative as the variable parameter, the Lagrange multiplier method can be applied to introduce a geometric condition, see for example [30]. Introducing the condition presented in (30), together with (29) into (27), leads to the following system of equations:

$$\begin{bmatrix}\left(\mathbf{K}_T(\mathbf{V}) - \omega_i^2\mathbf{M}\right) & \boldsymbol{\varphi}_i \\ \boldsymbol{\varphi}_i^T & 0\end{bmatrix}\begin{Bmatrix}\left\{\frac{\partial\boldsymbol{\varphi}_i}{\partial s_j}\right\}_{Part} \\ \lambda\end{Bmatrix} = \begin{Bmatrix}\left(\frac{\partial\omega_i^2}{\partial s_j}\mathbf{M} - \frac{\partial\mathbf{K}_T(\mathbf{V})}{\partial s_j}\right)\boldsymbol{\varphi}_i \\ 0\end{Bmatrix} \tag{32}$$

Copyright © 2010 John Wiley & Sons, Ltd.

DOI: 10.1002/nme

with λ being the Lagrange multiplier, which is an additional unknown introduced. In the present case, this is a scalar. This matrix system is nonsingular.

It should be stressed that, due to the introduction of the geometric condition into (30), the modal derivative in (32) only represents the particular solution. To obtain the full modal derivative, this can be added to the homogenous solution in (29).

2.9. The Differentiated Natural Frequency

An expression is determined for the differentiated natural frequency in (32). For this it is assumed that the eigenvalues ω_i^2 have geometric multiplicity of one. For a further generalisation to the cases with geometric and algebraic multiplicity higher than one, the reader is referred to [22]. Thus, in the present case the matrix $(\mathbf{K} - \omega_i^2\mathbf{M})$ is assumed to be singular with a rank of N-1. This implies that the right hand side of (27) has to fulfill one condition in order for a solution $\partial\boldsymbol{\varphi}_i/\partial s_j$ to exist. This condition is found by multiplying equation (27) by $\boldsymbol{\varphi}_i^T$, and inserting (28) and (29). This yields:

$$\boldsymbol{\varphi}_i^T \left(\mathbf{K}_T(\mathbf{V}) - \omega_i^2\mathbf{M}\right)\left(\beta\boldsymbol{\varphi}_i + \left\{\frac{\partial\boldsymbol{\varphi}_i}{\partial s_j}\right\}_{Part}\right) = \boldsymbol{\varphi}_i^T\left(\frac{\partial\omega_i^2}{\partial s_j}\mathbf{M} - \frac{\partial\mathbf{K}_T(\mathbf{V})}{\partial s_j}\right)\boldsymbol{\varphi}_i \tag{33}$$

Inserting the eigenvalue problem (26) and the orthogonality conditions (31) into (33), the left hand side becomes zero, and an expression for the natural frequency in differentiated form can then be found as:

$$\frac{\partial\omega_i^2}{\partial s_j} = m_i^{-1}\frac{\partial k_{Ti}}{\partial s_j} \tag{34}$$

where the following definitions have been introduced

$$m_i = \boldsymbol{\varphi}_i^T\mathbf{M}\boldsymbol{\varphi}_i \quad , \quad \frac{\partial k_{Ti}}{\partial s_j} = \boldsymbol{\varphi}_i^T\frac{\partial\mathbf{K}_T(\mathbf{V})}{\partial s_j}\boldsymbol{\varphi}_i \tag{35}$$

Inserting (34) into (32), the system of equations governing the partial modal derivatives is written as

$$\begin{bmatrix}\left(\mathbf{K}_T(\mathbf{V}) - \omega_i^2\mathbf{M}\right) & \boldsymbol{\varphi}_i \\ \boldsymbol{\varphi}_i^T & 0\end{bmatrix}\begin{Bmatrix}\left\{\frac{\partial\boldsymbol{\varphi}_i}{\partial s_j}\right\}_{Part} \\ \lambda\end{Bmatrix} = \begin{Bmatrix}\left(m_i^{-1}\frac{\partial k_{Ti}}{\partial s_j}\mathbf{M} - \frac{\partial\mathbf{K}_T(\mathbf{V})}{\partial s_j}\right)\boldsymbol{\varphi}_i \\ 0\end{Bmatrix} \tag{36}$$

Several significant differences can be observed when (36) is compared with (25). First of all, it is the tangent stiffness that appears on the right hand side of the approximate equations in (36), whereas the secant stiffness appears in the complete set of equations (25). Furthermore, on the left hand side of (36), only a single mode appears, whereas in (25) the modal derivatives appear as a sum of modes, and the corresponding linear natural frequencies appear as a squared sum.

3. THE REDUCED BASIS FORMULATION

The following section presents the concept behind inserting a reduced basis into the internal restoring forces, and manipulating these into a cubic polynomial in the reduced co-ordinates. The concept is based on the works of Nash, Shi & Mei and Slaats et al. [22–24] and the formulation is referred to as the reduced basis formulation (RBF).

3.1. The Equivalent Force Vector Coefficients

The internal restoring forces present in the projected equations of motion in (8) are expressed as a cubic polynomial in the reduced co-ordinates. Complying with equation (5), the projected internal restoring forces contain the three projected stiffness matrices presented in (37):

$$\boldsymbol{\Phi}^T\mathbf{K}_0\boldsymbol{\Phi} = \tilde{\mathbf{K}}_0 \quad , \quad \boldsymbol{\Phi}^T\mathbf{K}_1(\boldsymbol{\Phi}\mathbf{s})\boldsymbol{\Phi} = \sum_{i=1}^{N}\tilde{\mathbf{K}}_{1,i}s_i \quad , \quad \boldsymbol{\Phi}^T\mathbf{K}_2(\boldsymbol{\Phi}\mathbf{s},\boldsymbol{\Phi}\mathbf{s})\boldsymbol{\Phi} = \sum_{i=1}^{N}\sum_{j=1}^{N}\tilde{\mathbf{K}}_{2,ij}s_is_j \tag{37}$$

Copyright © 2010 John Wiley & Sons, Ltd.

DOI: 10.1002/nme

As shown, the matrices $\mathbf{K}_1(\mathbf{V})$ and $\mathbf{K}_2(\mathbf{V},\mathbf{V})$ on projected form can be expressed as a sum of coefficients multiplied by the scalars s_i. The matrices $\tilde{\mathbf{K}}_0$, $\tilde{\mathbf{K}}_{1,i}$ and $\tilde{\mathbf{K}}_{2,ij}$ denote the equivalent stiffness matrix coefficients and are constant. With the above introduced definitions, the internal restoring forces after projection are given by the expression:

$$\tilde{\mathbf{g}}(\mathbf{s}) = \left(\tilde{\mathbf{K}}_0 + \sum_{i=1}^{N}\tilde{\mathbf{K}}_{1,i}s_i + \sum_{i=1}^{N}\sum_{j=1}^{N}\tilde{\mathbf{K}}_{2,ij}s_is_j\right)\mathbf{s} \tag{38}$$

In order to express $\tilde{\mathbf{g}}(\mathbf{s})$ as a sum of equivalent force vectors is introduced the following vector $\mathbf{s}$

$$\mathbf{s} = \sum_{k=1}^{N}\mathbf{i}_k s_k \qquad , \qquad \mathbf{i}_k = \begin{bmatrix}\delta_{1k}, & \delta_{2k}, & \dots & \delta_{Nk}\end{bmatrix}^T \tag{39}$$

with δ_{ij} denoting the Kronecker delta. This allows the internal restoring forces to be written in cubic form with respect to the reduced co-ordinates:

$$\tilde{\mathbf{g}}(\mathbf{s}) = \sum_{i=1}^{N}\tilde{\mathbf{q}}_{1,i}s_i + \sum_{i=1}^{N}\sum_{j=1}^{N}\tilde{\mathbf{q}}_{2,ij}s_is_j + \sum_{i=1}^{N}\sum_{j=1}^{N}\sum_{k=1}^{N}\tilde{\mathbf{q}}_{3,ijk}s_is_js_k \tag{40}$$

with the constant equivalent force vector coefficients defined by:

$$\tilde{\mathbf{q}}_{1,i} = \tilde{\mathbf{K}}_0\mathbf{i}_i, \qquad \tilde{\mathbf{q}}_{2,ij} = \tilde{\mathbf{K}}_{1,i}\mathbf{i}_j, \qquad \tilde{\mathbf{q}}_{3,ijk} = \tilde{\mathbf{K}}_{2,ij}\mathbf{i}_k \tag{41}$$

Equation (40) is referred to as the RBF. It is very convenient since it allows all the equivalent force vector coefficients to be arranged before starting the time integration. Thus, the usual time-consuming evaluation of the internal restoring force contribution performed element-by-element for every time step is replaced by a simple summation where only the reduced co-ordinates vary. As will be illustrated in the example in section 4 the equation (40) makes it possible to perform real-time simulations on a standard personal computer (PC).

An important aspect regarding the evaluation of the internal restoring forces in real-time is that the matrices $\tilde{\mathbf{q}}_{1i}$, $\tilde{\mathbf{q}}_{2,ij}$ and $\tilde{\mathbf{q}}_{3,ijk}$ do not exceed the memory capacity. However, for the size of systems considered in the given article, this is not seen to be an issue. For the largest model presented in section 4.8 that contains 78 modes, these matrices only use approximately 50 MB in total.

3.2. Reduction of Quadratic and Cubic Summations

The number of summation terms in (40) can be reduced further by taking advantage of the symmetry of the products between the reduced co-ordinates. The symmetry implies that:

$$s_is_j = s_js_i \tag{42}$$

$$s_is_js_k = s_is_ks_j = s_js_is_k = s_js_ks_i = s_ks_is_j = s_ks_js_i \tag{43}$$

and allows for the quadratic and cubic summations in (40) to be written as the expressions on the right hand sides of (44) and (45):

$$\sum_{i=1}^{N}\sum_{j=1}^{N}\tilde{\mathbf{q}}_{2,ij}s_is_j = \sum_{i=1}^{N}\sum_{j=1}^{i}\tilde{\mathbf{q}}^*_{2,ij}s_is_j \tag{44}$$

$$\sum_{i=1}^{N}\sum_{j=1}^{N}\sum_{k=1}^{N}\tilde{\mathbf{q}}_{3,ijk}s_is_js_k = \sum_{i=1}^{N}\sum_{j=1}^{i}\sum_{k=1}^{j}\tilde{\mathbf{q}}^*_{3,ijk}s_is_js_k \tag{45}$$

The interior summation indeces on the right hand side now run from 1 to the value of the exterior neighbor index. The outermost index still runs from 1 to N. The equivalent force vector coefficients

Copyright © 2010 John Wiley & Sons, Ltd.

DOI: 10.1002/nme

on the right hand sides of (44) and (45) are defined by:

$$\tilde{\mathbf{q}}^{*}_{2,ij} = \tilde{\mathbf{q}}_{2,ij} + (1-\delta_{ij})\tilde{\mathbf{q}}_{2,ji} \tag{46}$$

$$\tilde{\mathbf{q}}^{*}_{3,ijk} = \tilde{\mathbf{q}}_{3,ijk} + (\tilde{\mathbf{q}}_{3,jki}+\tilde{\mathbf{q}}_{3,kij})(1-\delta_{ij}\delta_{jk}) + (\tilde{\mathbf{q}}_{3,ikj} + \tilde{\mathbf{q}}_{3,kji} + \tilde{\mathbf{q}}_{3,jik})(1-\delta_{ij})(1-\delta_{jk}) \tag{47}$$

Introducing (44) and (45) into the projected restoring forces in (40), these are reduced to

$$\tilde{\mathbf{g}}(\mathbf{s}) = \sum_{i=1}^{N} \tilde{\mathbf{q}}_{1,i} s_i + \sum_{i=1}^{N}\sum_{j=1}^{i} \tilde{\mathbf{q}}^{*}_{2,ij} s_i s_j + \sum_{i=1}^{N}\sum_{j=1}^{i}\sum_{k=1}^{j} \tilde{\mathbf{q}}^{*}_{3,ijk} s_i s_j s_k \tag{48}$$

The number of terms, T_x, in the first, second and third order summation expressions, respectively, in (48) are given by the formula:

$$T_{\mathrm{x}}(N) = \prod_{i=0}^{\mathrm{x}-1} \frac{N+i}{1+i} \tag{49}$$

where x denotes the order of the summation expression. Thus, the total number of summations in (48) equates to:

$$T_3 = \sum_{\mathrm{x}=1}^{3} T_{\mathrm{x}}(N) = \frac{11}{6}N + N^2 + \frac{1}{6}N^3 \tag{50}$$

The number of terms in (50) should be compared with the N+N^2+N^3 terms present in (40). Thus, when the product symmetry is utilized, there is a drastic reduction in the number of terms as N increases.

4. ILLUSTRATIVE EXAMPLE - SIMPLE SUPPORTED CABLE

This section considers the example of a simple supported cable modeled with plane beam elements, with two nodes exposed to a transverse harmonic line load. The purpose of the example is to compare the solutions obtained using the complete modal derivatives and the approximate modal derivatives. Furthermore, it is used to consider the real-time simulation potential of the RBF presented in section 3.

Firstly, is presented the beam element formulation. From this is established an example based on the equivalent force vectors in (41), and the differentiated secant stiffness and tangent stiffness present in (27) and (36), respectively. This is followed by a description of the cable example under consideration, including geometries, stiffness parameters, and loading. Next is considered a short description of the model parameters, covering mesh and integration scheme details. Finally, is presented an analysis of the results and a discussion focusing on the accuracy and the computational time.

4.1. Finite Element Formulation for Plane Beam Element

The plane beam element shown in Figure 1 is used to model a simple supported cable. The element

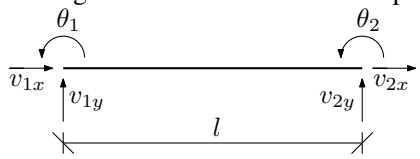

Figure 1. Plane beam element.

has two nodes, each with two translational dofs, v_{ix} and v_{iy}, and one rotational dof, θ_i, i ϵ {1,2}. It

Copyright © 2010 John Wiley & Sons, Ltd.

DOI: 10.1002/nme

spans the domain Ω_{el} of length l. Shape functions of second order are used to describe the bending deformation and shape functions of the first order are used to describe the axial deformation.

The generalized stresses consist of the normal force, N, and the moment, M. The work conjugate strains are the axial strain, ε, and the curvature, κ. To include kinematic nonlinear effects, is used the Lagrange strain measure introduced in equation (3). The stresses and strains are collected in the vectors $\boldsymbol{\sigma}$ and $\boldsymbol{\varepsilon}$, using the notation $()' = \partial()/\partial x$:

$$\boldsymbol{\sigma} = \begin{Bmatrix} N \\ M \end{Bmatrix}, \quad \boldsymbol{\varepsilon} = \begin{Bmatrix} \varepsilon \\ \kappa \end{Bmatrix} = \begin{Bmatrix} u' + \frac{1}{2}(w')^2 \\ w'' \end{Bmatrix} \tag{51}$$

Through the concept of virtual work, the element local equations of motion can now be derived. However, details of this are not presented here, but can be found in Appendix B. The introduced strain and stress definitions lead to the element local's internal restoring forces, of the form

$$\mathbf{g}_{el}(\mathbf{v}_{el}) = \int_{\Omega_{el}} \left(\mathbf{B}^T\mathbf{D}\mathbf{B} + \frac{EA}{2}\left(\mathbf{B}_\epsilon^T\mathbf{v}^T\mathbf{G} + 2\mathbf{G}\mathbf{v}\mathbf{B}_\epsilon + \mathbf{G}\mathbf{v}\mathbf{v}^T\mathbf{G}\right)\right)_{el} \mathbf{v}_{el}\, d\Omega_{el} \tag{52}$$

where $\mathbf{B}$ and $\mathbf{B}_\varepsilon$ are strain interpolation matrices, $\mathbf{D}$ is a material stiffness matrix, $\mathbf{v}$ is the dof vector, and $\mathbf{G}$ is a symmetric matrix representing a mixed product of the element displacement field in differentiated form. The matrices $\mathbf{B}$ and $\mathbf{B}_\varepsilon$ stem from the linear strain measures u' and w'' in (51), and $\mathbf{G}$ from the nonlinear term $\frac{1}{2}(w')^2$.

To transform the element contribution into global form, is introduced a transformation matrix, $\tilde{\mathbf{L}}_{el}$, that relates the element local dof vector $\mathbf{v}_{el}$ and the global dof vector $\mathbf{V}$:

$$\mathbf{v}_{el} = \tilde{\mathbf{L}}_{el}\mathbf{V} = \tilde{\mathbf{V}}_{el} \tag{53}$$

The global internal restoring forces are found by introducing (53) into the internal restoring forces in (52), and summing over the total number of elements (nel):

$$\mathbf{g}(\mathbf{V}) = \sum_{el=1}^{nel} \tilde{\mathbf{L}}_{el}^T \int_{\Omega_{el}} \left(\mathbf{B}^T\mathbf{D}\mathbf{B} + \frac{EA}{2}\left(\mathbf{B}_\epsilon^T\tilde{\mathbf{V}}^T\mathbf{G} + 2\mathbf{G}\tilde{\mathbf{V}}\mathbf{B}_\epsilon\right) + \frac{EA}{2}\mathbf{G}\tilde{\mathbf{V}}\tilde{\mathbf{V}}^T\mathbf{G}\right)_{el} \tilde{\mathbf{L}}_{el}\mathbf{V}\, d\Omega_{el} \tag{54}$$

By identifying the following matrices from (54):

$$\mathbf{K}_0 = \sum_{el=1}^{nel} \tilde{\mathbf{L}}_{el}^T \int_{\Omega_{el}} \left(\mathbf{B}^T\mathbf{D}\mathbf{B}\right)_{el} \tilde{\mathbf{L}}_{el}\, d\Omega_{el} \tag{55}$$

$$\mathbf{K}_1(\mathbf{V}) = \sum_{el=1}^{nel} \tilde{\mathbf{L}}_{el}^T \int_{\Omega} \frac{EA}{2}\left(\mathbf{B}_\epsilon^T\tilde{\mathbf{V}}^T\mathbf{G} + 2\mathbf{G}\tilde{\mathbf{V}}\mathbf{B}_\epsilon\right)_{el} \tilde{\mathbf{L}}_{el}\, d\Omega_{el} \tag{56}$$

$$\mathbf{K}_2(\mathbf{V},\mathbf{V}) = \sum_{el=1}^{nel} \tilde{\mathbf{L}}_{el}^T \int_{\Omega_{el}} \frac{EA}{2}\left(\mathbf{G}\tilde{\mathbf{V}}\tilde{\mathbf{V}}^T\mathbf{G}\right)_{el} \tilde{\mathbf{L}}_{el}\, d\Omega_{el} \tag{57}$$

it is recognized that (54) is of the form presented in (5).

4.2. Equivalent Force Vectors

The equivalent force vectors defined in (41) can now be identified for the considered plane beam element. This is done in two steps. Firstly, the stiffness matrices in (55) to (57) are transformed into the reduced co-ordinate system defined in (6), as was done in (37). Then the projected stiffness

Copyright © 2010 John Wiley & Sons, Ltd.

DOI: 10.1002/nme

matrix coefficients are multiplied by $\mathbf{i}_k$, and the equivalent force vectors are identified as:

$$\tilde{\mathbf{q}}_{1,i} = \mathbf{\Phi}^T \sum_{el=1}^{nel} \int_{\Omega_{el}} \tilde{\mathbf{L}}_{el}^T \left(\mathbf{B}^T\mathbf{D}\mathbf{B}\right)_{el} \tilde{\mathbf{L}}_{el}\, d\Omega_{el} \mathbf{\Phi}\mathbf{i}_i \tag{58}$$

$$\tilde{\mathbf{q}}_{2,ij} = \mathbf{\Phi}^T \sum_{el=1}^{nel} \tilde{\mathbf{L}}_{el}^T \int_{\Omega_{el}} \left(\frac{EA}{2}\left(\mathbf{B}_\varepsilon^T \boldsymbol{\varphi}_i^T \tilde{\boldsymbol{L}}^T \mathbf{G} + 2\mathbf{G}\tilde{\boldsymbol{L}}\boldsymbol{\varphi}_i \mathbf{B}\right)\right)_{el} \tilde{\mathbf{L}}_{el}\, d\Omega_{el} \mathbf{\Phi}\mathbf{i}_j \tag{59}$$

$$\tilde{\mathbf{q}}_{3,ijk} = \mathbf{\Phi}^T \sum_{el=1}^{nel} \tilde{\mathbf{L}}_{el}^T \int_{\Omega_{el}} \left(\frac{EA}{2}\mathbf{G}\tilde{\boldsymbol{L}}\boldsymbol{\varphi}_i \boldsymbol{\varphi}_j^T \tilde{\boldsymbol{L}}^T \mathbf{G}\right)_{el} \tilde{\mathbf{L}}_{el}\, d\Omega_{el} \mathbf{\Phi}\mathbf{i}_k \tag{60}$$

When evaluating the internal restoring forces in (48) in the MATLAB simulations, is applied the following matrix format:

$$\tilde{\mathbf{g}}(\mathbf{s}) = \mathbf{Q}_1\mathbf{s} + \mathbf{Q}_2\mathbf{s}_q + \mathbf{Q}_3\mathbf{s}_c \tag{61}$$

with the matrix definitions:

$$\mathbf{Q}_1 = \begin{bmatrix}\tilde{\mathbf{q}}_{1,1} & \tilde{\mathbf{q}}_{1,2} & \cdots & \tilde{\mathbf{q}}_{1,N}\end{bmatrix} \tag{62}$$

$$\mathbf{Q}_2 = \begin{bmatrix}\tilde{\mathbf{q}}_{2,11}^* & \tilde{\mathbf{q}}_{2,21}^* & \tilde{\mathbf{q}}_{2,22}^* & \tilde{\mathbf{q}}_{2,31}^* & \cdots & \tilde{\mathbf{q}}_{2,NN}^*\end{bmatrix} \tag{63}$$

$$\mathbf{Q}_3 = \begin{bmatrix}\tilde{\mathbf{q}}_{3,111}^* & \tilde{\mathbf{q}}_{3,211}^* & \tilde{\mathbf{q}}_{3,221}^* & \tilde{\mathbf{q}}_{3,222}^* & \tilde{\mathbf{q}}_{3,311}^* & \cdots & \tilde{\mathbf{q}}_{3,NNN}^*\end{bmatrix} \tag{64}$$

and the vector definitions

$$\mathbf{s}_q = \begin{bmatrix}s_1s_1 & s_2s_1 & s_2s_2 & s_3s_1 & \cdots & s_Ns_N\end{bmatrix}^T \tag{65}$$

$$\mathbf{s}_c = \begin{bmatrix}s_1s_1s_1 & s_2s_1s_1 & s_2s_2s_1 & s_2s_2s_2 & s_3s_1s_1 & \cdots & s_Ns_Ns_N\end{bmatrix}^T \tag{66}$$

Evaluation of the internal restoring forces in (61) involves $\mathcal{O}\left(\mathrm{N}^4\right)$ operations. Furthermore the generation of the vectors $\mathbf{s}_q$ and $\mathbf{s}_c$ involve $\mathcal{O}(\mathrm{N}^2)$ and $\mathcal{O}(\mathrm{N}^3)$ operations, respectively.

4.3. Differentiated Secant Stiffness Matrix

Equations (25) and (36) require the secant and tangent stiffness matrices, differentiated with respect to the reduced co-ordinate, s_j. From (54), the global secant stiffness can be identified as:

$$\mathbf{K}_s(\mathbf{V}) = \sum_{el=1}^{nel} \tilde{\mathbf{L}}_{el}^T \int_{\Omega_{el}} \left(\mathbf{B}^T\mathbf{D}\mathbf{B} + \frac{EA}{2}\left(\mathbf{B}_\epsilon^T\tilde{\mathbf{V}}^T\mathbf{G} + 2\mathbf{G}\tilde{\mathbf{V}}\mathbf{B}_\epsilon + \mathbf{G}\tilde{\mathbf{V}}\tilde{\mathbf{V}}^T\mathbf{G}\right)\right)_{el} \tilde{\mathbf{L}}_{el}\, d\Omega_{el} \tag{67}$$

and the tangent stiffness is given by, see Appendix B equation (124):

$$\mathbf{K}_T(\mathbf{V}) = \sum_{el=1}^{nel} \int_{\Omega_{el}} \tilde{\mathbf{L}}_{el}^T \Bigg(\mathbf{B}^T\mathbf{D}\mathbf{B} + EA\left(\mathbf{B}_\epsilon^T\tilde{\mathbf{V}}^T\mathbf{G} + \mathbf{G}\tilde{\mathbf{V}}\mathbf{B}_\epsilon + \mathbf{G}\tilde{\mathbf{V}}\tilde{\mathbf{V}}^T\mathbf{G} + \mathbf{B}_\epsilon\tilde{\mathbf{V}}\mathbf{G} + \frac{1}{2}\tilde{\mathbf{V}}^T\mathbf{G}\tilde{\mathbf{V}}\mathbf{G}\right)\Bigg)_{el} \tilde{\mathbf{L}}_{el}\, d\Omega_{el} \tag{68}$$

According to (6), $\mathbf{V}$ is a function of s_i. Thus, when differentiating (67) with respect to s_j, only the vectors, $\mathbf{V}$, are considered to be variables. Therefore, the secant stiffness in (67) in differentiated form becomes:

$$\frac{\partial\mathbf{K}_s(\mathbf{s})}{\partial s_j} = \sum_{el=1}^{nel} \tilde{\mathbf{L}}_{el}^T \int_{\Omega_{el}} \frac{EA}{2}\left(\mathbf{B}_\epsilon^T \frac{\partial\tilde{\mathbf{V}}}{\partial s_j}^T \mathbf{G} + 2\mathbf{G}\frac{\partial\tilde{\mathbf{V}}}{\partial s_j}\mathbf{B}_\epsilon + \mathbf{G}\left(\frac{\partial\tilde{\mathbf{V}}}{\partial s_j}\tilde{\mathbf{V}}^T + \tilde{\mathbf{V}}\frac{\partial\tilde{\mathbf{V}}}{\partial s_j}^T\right)\mathbf{G}\right)_{el} \tilde{\mathbf{L}}_{el}\, d\Omega_{el} \tag{69}$$

Copyright © 2010 John Wiley & Sons, Ltd.

DOI: 10.1002/nme

and the tangent stiffness in (68) when differentiated becomes

$$\frac{\partial \mathbf{K}_T(\mathbf{s})}{\partial s_j} = \sum_{el=1}^{nel} \tilde{\mathbf{L}}_{el}^T \int_{\Omega_{el}} EA \left(\mathbf{B}_\epsilon^T \frac{\partial \tilde{\mathbf{V}}}{\partial s_j}^T \mathbf{G} + \mathbf{G} \frac{\partial \tilde{\mathbf{V}}}{\partial s_j} \mathbf{B}_\epsilon + \mathbf{G} \left(\frac{\partial \tilde{\mathbf{V}}}{\partial s_j} \tilde{\mathbf{V}}^T + \tilde{\mathbf{V}} \frac{\partial \tilde{\mathbf{V}}}{\partial s_j}^T \right) \mathbf{G} + \right.$$
$$\left. \mathbf{B}_\epsilon \frac{\partial \tilde{\mathbf{V}}}{\partial s_j} \mathbf{G} + \tilde{\mathbf{V}}^T \mathbf{G} \frac{\partial \tilde{\mathbf{V}}}{\partial s_j} \mathbf{G} \right)_{el} \tilde{\mathbf{L}}_{el} \, d\Omega_{el} \tag{70}$$

where the symmetry of $\mathbf{G}$ has been utilized.

4.4. Cable Geometry and Loading

Next, is considered a simple supported cable of length l exposed to a transverse uniform load p(t) along half of its length, see Figure 2.

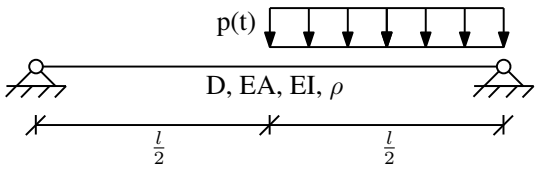

Figure 2. Simple supported cable.

The cable has a diameter, D, Young's modulus, E, cross-sectional area, A, second moment of area, I, and a density, ρ. The load, p(t), consists of two harmonic load contributions in phase with the first and second natural bending frequencies ω_1 and ω_2, respectively. The formula for p(t) is:

$$p(t) = F_1 sin(\omega_1 t) + F_2 sin(\omega_2 t) \tag{71}$$

where F_1 and F_2 denote the load amplitudes. Table I presents the applied cable and load parameters.

To enhance the kinematic nonlinearities, the bending stiffness is set to be very small compared with the axial stiffness.

4.5. Time integration

To perform the analysis of the cable, is used the implicit Newmark integration method and the explicit central difference method (CDM). The algorithms are implemented into a local MATLAB-based finite element method (FEM) program. In this regard, it should be stressed that the code cannot be considered fully optimized. Therefore, it is expected that, if the code is optimized and implemented in a faster programming language, the simulation times of both the full and reduced FEM models presented in the following can be further decreased.

To ensure the algorithms are implemented correctly in MATLAB, an ABAQUS model is made for comparison. In this context, in order to interpolate both the transverse and longitudinal displacement fields, is used a three-dimensional element, denoted by B31, with two nodes and linear shape functions.

To perform real-time simulations the RBF is integrated into the CDM scheme. The reason for using an explicit scheme to perform the real-time simulations is based on the recommendation from [10], as was also discussed in the introduction.

In Table II is presented the algorithm parameters used. Δt refers to the time step magnitude and is listed as an interval covering all the conducted simulations presented in the following. The weighting parameters required when applying the Newmark time integration method are denoted γ and β. The values chosen correspond to the *average acceleration* case in linear problems, with unconditional stability with respect to time-step magnitude, see for example [31]. The nel used to model the cable is also given as an interval of 20 to 30 elements. The solution converged for 20 elements in the MATLAB code. However, the nel had to be increased in the real-time analysis in order to increase

Copyright © 2010 John Wiley & Sons, Ltd.

DOI: 10.1002/nme

the number of modes, and to find the real-time limit with respect to the number of modes. With four boundary restrictions and three dofs at each node the number of modes are increased from 59 to 89 going from 20 to 30 elements.

According to [2,3,32,33], in the RTHT context, the range for the time step magnitude, Δt, is often between 10^{-2} and 10^{-3} seconds. Thus, the given time step interval applied should be representative of the RTHT context. It should however be stressed that the required time step magnitude will be dependent on the structure considered.

4.6. Implementation Check and Case Validation

The implementation of the different algorithms is checked to start with. Furthermore it is investigated whether the cable example displays sufficient nonlinear behavior to be considered as a relevant case study for kinematic nonlinearities.

In Figure 3 are plotted the linear and nonlinear transverse deformation of the cable midpoint, v_m, considering a 10-second interval, using respectively the linear Newmark (LN), nonlinear Newmark (NN), linear CDM (LC) and nonlinear CDM (NC) schemes. Furthermore are plotted a linear ABAQUS (LA) and nonlinear ABAQUS (NA) solution.

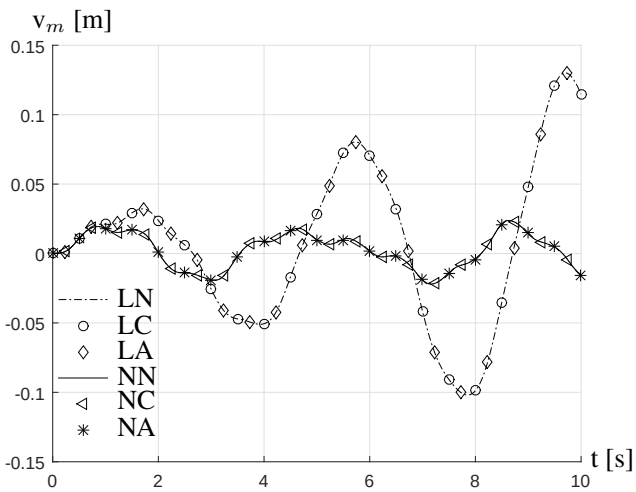

Figure 3. Transverse deformation of beam midpoint from linear Newmark (LN), linear CDM (LC), linear ABAQUS (LA), nonlinear Newmark (NN), nonlinear CDM (NC) and nonlinear ABAQUS (NA) solutions for a time step magnitude Δt=10^{-4} sec..

The responses represent the full solution in the converged state with respect to both time step magnitude (Δt =10^{-4} s), iteration residual and the number of elements. To converge, the MATLAB models required 20 elements, and the ABAQUS models required 30. This is assumed to be due to different element formulations.

From the graph it can be seen that all of the linear solutions are identical. The same is true for all of the nonlinear solutions. This confirms the implementation to be correct. In the nonlinear case, the amplitude is seen to be more or less bounded; whereas, in the linear case the amplitude continues to increase during the entire time interval considered. The significantly different behavior in the linear and the nonlinear cases verifies that the structure is a relevant case study for kinematic nonlinearities.

Copyright © 2010 John Wiley & Sons, Ltd.

DOI: 10.1002/nme

4.7. ROM-Based Beam Response

In the following, the solutions obtained using the complete modal derivatives and the approximate modal derivatives are considered and compared. Figure 4 shows the nonlinear case using the RBF with a different number of linear modes and their modal derivatives determined from equation (25). Figure 4(a) shows the full 10-seconds time interval, and Figure 4(b) shows a close-up of the section of the graph marked by the box in Figure 4(a).

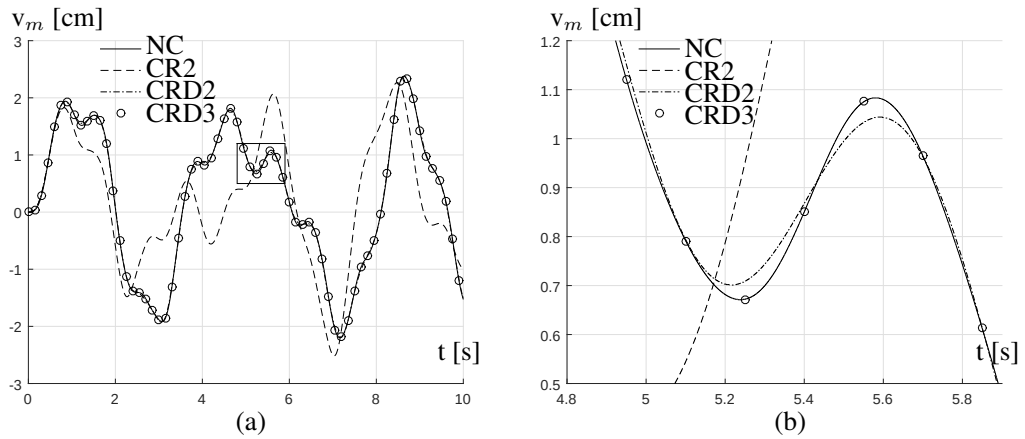

Figure 4. Transverse deformation of beam midpoint with nonlinear CDM (NC) and nonlinear CDM integration schemes with modal derivatives (CRD) and without (CR) considering (a) the full 10 seconds interval and (b) a close up.

The CR2-curve represents the response obtained using only the first and second linear bending modes. The CRD2-curve and CRD3-curve represent the responses including respectively the first two and first three linear bending modes and their associated modal derivatives. The definition of the *associated modal derivatives* are those comprising all the possible combinations of $\partial\boldsymbol{\varphi}_i/\partial s_j$ for i,j ϵ [1,N] with N being the number of linear modes applied.

From the plots shown in Figure 4, it can be observed that the CR2-curve is significantly different from the others. The amplitude is within the same range as the other solutions, but the response frequency and shape are different. The response is greatly improved by adding the associated modal derivatives. This can be observed by considering the CRD2-curve, which is almost identical to that of Newmark solution, except for small deviations close to the local maxima and local minima, as seen in Figure 4(b). By including the third linear mode and the associated modal derivatives, the response (CRD3) becomes almost fully identical to the NC solution.

The CRD3 response was executed with a time step of magnitude $\Delta t = 3 \cdot 10^{-4}$ s, so as to maintain precision and stability. This is three times the time step applied for the full NC solution response plotted in Figure 3. Increasing the time step is possible because some of the high frequency content is filtered out when projecting the equations of motion onto the reduced basis applied. Furthermore, the simulation time spent on the CRD3 curve was 0.8 s. This is more than 100 times faster than the NC simulation which lasted for 129 s.

In the given case, the approximate modal derivatives are identical with the complete modal derivatives with respect to shape, but have a different amplitude. Thus, with the approximate modal derivatives applied to generate the solution curves in Figure 4, is found identical deformation responses. However, for more complex structures, it is expected that the shape will also differ between the complete modal derivatives and the approximate modal derivatives, leading to different responses. In the given case it is also found that only the complete modal derivatives fulfill the relationship between the co-ordinates of the linear modes and the modal derivatives predicted by the Taylor series in equation (10).

Copyright © 2010 John Wiley & Sons, Ltd.

DOI: 10.1002/nme

When three linear modes and their modal derivatives were applied to obtain the CRD3 curve, the following approximation was used

$$\mathbf{V} = \begin{bmatrix} \boldsymbol{\varphi}_1 & \boldsymbol{\varphi}_2 & \boldsymbol{\varphi}_3 & \frac{\partial \boldsymbol{\varphi}_1}{\partial s_1} & \left(\frac{\partial \boldsymbol{\varphi}_1}{\partial s_2} + \frac{\partial \boldsymbol{\varphi}_2}{\partial s_1}\right) & \left(\frac{\partial \boldsymbol{\varphi}_1}{\partial s_3} + \frac{\partial \boldsymbol{\varphi}_3}{\partial s_1}\right) & \left(\frac{\partial \boldsymbol{\varphi}_2}{\partial s_3} + \frac{\partial \boldsymbol{\varphi}_3}{\partial s_2}\right) & \frac{\partial \boldsymbol{\varphi}_3}{\partial s_3} \end{bmatrix} \begin{Bmatrix} s_1 \\ s_2 \\ s_3 \\ s_4 \\ s_5 \\ s_6 \\ s_7 \\ s_8 \end{Bmatrix} \tag{72}$$

with a matrix containing the three linear modes in the first three places and the modal derivatives in the final places. These were multiplied by a vector containing eight independent co-ordinates, s_i, i ϵ [1,8].

It should be stressed that the modal derivative $\partial\boldsymbol{\varphi}_2/\partial s_2$ was left out of the basis when using both (25) and (36) to determine the modal derivatives. The reason for this is that a Gauss elimination on the matrix in (72), including $\partial\boldsymbol{\varphi}_2/\partial s_2$ in both cases, revealed the following linear relationship:

$$\frac{\partial \boldsymbol{\varphi}_2}{\partial s_2} = -\frac{3}{8}\left(\frac{\partial \boldsymbol{\varphi}_1}{\partial s_3} + \frac{\partial \boldsymbol{\varphi}_3}{\partial s_1}\right) - \frac{1}{4}\frac{\partial \boldsymbol{\varphi}_1}{\partial s_1} \tag{73}$$

Thus, in order to avoid singularities, the mode $\partial\boldsymbol{\varphi}_2/\partial s_2$ is not included in (72). By inserting the relationship in (73) into the Taylor series in (10) for $s_{k0} = 0$, and by comparing this with the expression in (72), predicts the following relationships between the co-ordinates of the linear modes and the modal derivatives:

$$s_4 = s_1^2 - \frac{1}{4}s_2^2 \quad , \quad s_5 = s_1 s_2 \quad , \quad s_6 = s_1 s_3 - \frac{3}{8}s_2^2 \quad , \quad s_7 = s_2 s_3 \quad , \quad s_8 = s_3^2 \tag{74}$$

The s_4 relationship in (74) is plotted in Figure 5(a) for the case where the modal derivatives are determined from the complete system of equations in (25). From the graph it is obvious that the two curves are identical. The same relationship is plotted in Figure 5(b), but based on the solution with the approximate modal derivatives. It can be seen from the graph that the relationship is not fulfilled in the given case. The shapes of the two curves are almost identical, but a factor of two separates them.

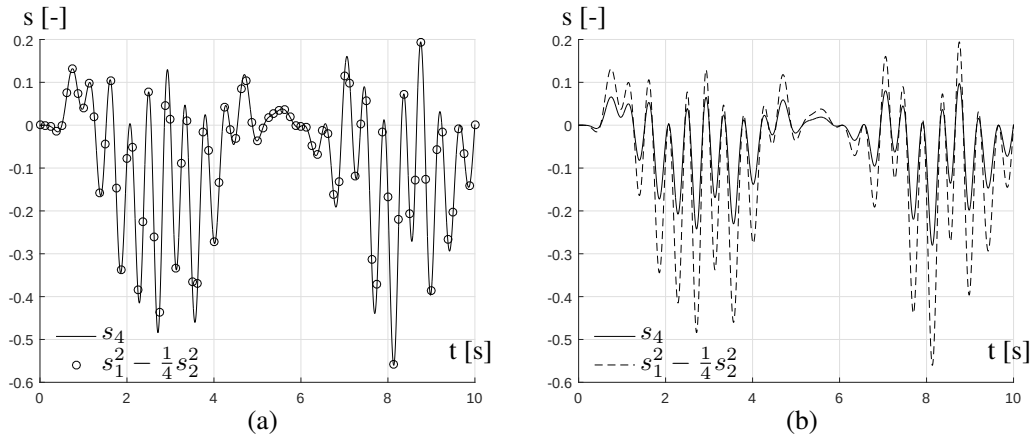

Figure 5. Plot of the co-ordinates s_4 and $s_1^2 - \frac{1}{4}s_2^2$ based on (a) the complete modal derivatives and (b) the approximate modal derivatives.

The same pattern shown in Figure 5 is seen when the remaining relationships in (74) are plotted. It can be concluded from these observations that the governing system of equations in (25) are seen to fulfill the Taylor series, whereas the equations in (36) do not.

Copyright © 2010 John Wiley & Sons, Ltd.

Int. J. Numer. Meth. Engng (2010)
DOI: 10.1002/nme

4.8. Real-time Analysis Using The RBF

Next, is considered the real-time potential of the RBF with the internal restoring forces of the form presented in equation (48). The simulations are executed on a PC with an Intel Core I7 3036QM processer with 4 cores, 2.4 GHz and 8 GB RAM.

The real-time potential is considered as the maximum number of modes that can be included in the RBF if the simulations should run in real time. The analysis is performed by considering the harmonic loaded cable for different time-step magnitudes. In this regard it should be stressed that the response errors have not been considered. Therefore, the results based on models applying fewer elements and higher time steps than those shown in Figure 4, may include deviations in their responses.

Three curves are plotted in Figure 6, representing the time spent on simulating the $t_{sim} = 10$ second cable response time as a function of the sum of linear modes and modal derivatives, N_T. The time-step magnitudes considered are $\Delta t = 10^{-2}$ s, $\Delta t = 10^{-3}$ s and $\Delta t = 10^{-4}$ s, respectively.

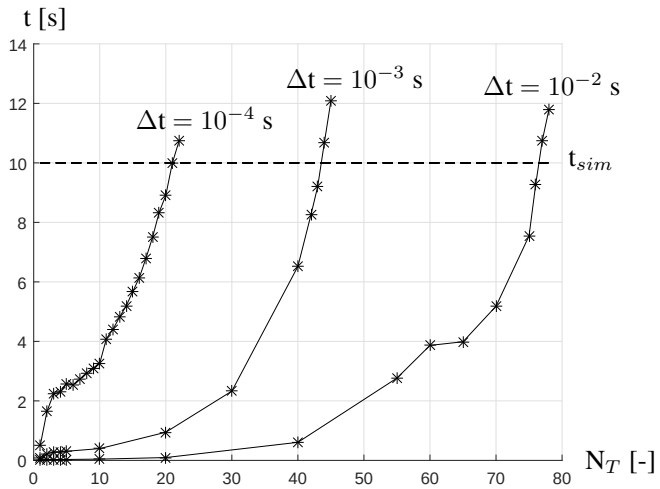

Figure 6. Computational time spent on simulating t_{sim} =10 seconds as function of the total number of modes, N_T, using the RBF for the step magnitudes $\Delta t = 10^{-4}$ s, $\Delta t = 10^{-3}$ s and $\Delta t = 10^{-2}$ s.

The horizontal dashed line represents the time of the simulation. Result points below this line represent the simulations that can run in real time, whereas the result points above the line are those that exceed the real-time limit.

From the plots it can be seen that the computational time is a nonlinear function of the total number of modes, N_T, in the basis. This is as expected since the evaluation of the restoring forces in equation (61) and the organization of the reduced coordinates in equation (65) and (66) are nonlinear functions of the number of modes. However, from the curve representing the smallest time-step, it is evident that the curves start out following the graph of an approximate linear function of N_T, and then follow the graph of a more nonlinear function from around $N_T \approx 3$, and values beyond. This could be explained by the fact that the remaining operations in the time integration algorithm dominate for small values of N_T. Furthermore, as expected, the smaller the time-step is, the fewer modes can be included before the real-time limit is exceeded. For the smallest time-step magnitude, Δt=10^{-4} s, around 20 modes can be contained in the model when run in real time. Using a time-step magnitude of Δt=10^{-2} s, the number of modes is increased to about 76. When simulating the latter curve the mass of the structure was increased in order to decrease the frequencies. Otherwise, the simulations became unstable.

Again, it should be stressed that the simulations are executed on a standard PC. Furthermore, the in-house MATLAB code is probably not optimized. Thus, it should be expected that the number of dofs could be increased when implementing the method on faster devices, and optimizing the code. Thus, with this in mind, it can be concluded that the method exhibits high real-time potential within kinematic nonlinear structures.

Copyright © 2010 John Wiley & Sons, Ltd.

DOI: 10.1002/nme

5. CONCLUSION

A method to reduce the computational time of kinematic nonlinear equations has been presented. The first step of the method consists of introducing a reduced basis, including the modal derivatives, into the nonlinear equations of motion, and thereby reduces the number of dofs. As an alternative to determining a set of approximate modal derivatives by solving the usual applied singular and linearized eigenvalue problem in differentiated form, a complete system of equations were derived. These were found by inserting a Taylor series for the displacement field into the free undamped kinematic nonlinear equations of motion, and arguing that all coefficients should be zero to fulfill the system of equations.

The second step in the method was to reduce the computational time further by applying a reduced basis formulation. Using this, the global restoring forces were expressed as a sum of constant equivalent force vectors multiplied by reduced co-ordinates up to a cubic order. This allowed for a fast assembling of the internal forces between each time-step compared with the usual element-by-element assembling approach.

A example with a simple supported cable exposed to harmonic loading modeled by beam elements was used to compare the complete modal derivatives with the approximate modal derivatives. Furthermore, the real-time potential of the method was demonstrated. From the example, it was concluded that using different modal derivatives produced identical solutions. However, only the modes determined from the complete system of equations fulfilled the relationship between the co-ordinates of the linear modes and modal derivatives predicted by the Taylor series. Furthermore it was found that, for a kinematic nonlinear system, a model with up to around seventy dofs can run in real time on a standard PC for a time step magnitude of $\Delta t = 10^{-2}$ seconds.

A. DERIVATION OF GOVERNING EQUATIONS FOR THE MODAL DERIVATIVES

The system of equations governing the modal derivatives are derived. The free undamped kinematic nonlinear equations of motion are considered:

$$\mathbf{M}\ddot{\mathbf{V}} + \mathbf{g}(\mathbf{V}) = \mathbf{0} \tag{75}$$

with the internal restoring forces $\mathbf{g}(\mathbf{V})$ as defined in (52).

Then is introduced a Taylor series up to second order to express the displacement field, $\mathbf{V}(\mathbf{s})$, as a function of the reduced co-ordinates collected in the vector $\mathbf{s}$:

$$\mathbf{V}(\mathbf{s}) = \mathbf{V}_0 + \sum_{j=1}^{N} \frac{\partial \mathbf{V}_0}{\partial s_j}(s_j - s_{j0}) + \frac{1}{2}\sum_{j=1}^{N}\sum_{k=1}^{N} \frac{\partial^2 \mathbf{V}_0}{\partial s_j \partial s_k}(s_j - s_{j0})(s_k - s_{k0}) + ... \tag{76}$$

where the subindex 0 indicates the value at the initial stage, and represents the notation

$$\mathbf{V}_0 = \mathbf{V}(\mathbf{s}_0) \tag{77}$$

The differentiated displacement fields of first and second order in equation (76) contain both linear modes and modal derivatives up to the second order. This is realized by inserting the reduced basis introduced in (6).

$$\frac{\partial \mathbf{V}}{\partial s_j} = \frac{\partial}{\partial s_j}\left(\sum_{i=1}^{N} \boldsymbol{\varphi}_i s_i\right) = \left(\sum_{i=1}^{N} \frac{\partial \boldsymbol{\varphi}_i}{\partial s_j} s_i + \boldsymbol{\varphi}_j\right) \tag{78}$$

$$\frac{\partial^2 \mathbf{V}}{\partial s_j \partial s_k} = \frac{\partial}{\partial s_k}\left(\frac{\partial \mathbf{V}}{\partial s_j}\right) = \sum_{i=1}^{N} \frac{\partial^2 \boldsymbol{\varphi}_i}{\partial s_j s_k} s_i + \frac{\partial \boldsymbol{\varphi}_k}{\partial s_j} + \frac{\partial \boldsymbol{\varphi}_j}{\partial s_k} \tag{79}$$

Copyright © 2010 John Wiley & Sons, Ltd.

DOI: 10.1002/nme

From equation (76), the acceleration is found by differentiating twice with respect to time

$$\ddot{\mathbf{V}}(\mathbf{s}) = \sum_{j=1}^{N} \frac{\partial \mathbf{V}_0}{\partial s_j} \ddot{s}_j + \sum_{j=1}^{N} \sum_{k=1}^{N} \frac{1}{2} \frac{\partial^2 \mathbf{V}_0}{\partial s_j \partial s_k} \left[\ddot{s}_j (s_k - s_{k0}) + 2\dot{s}_j \dot{s}_k + (s_j - s_{j0}) \ddot{s}_k \right] \tag{80}$$

It is then assumed that the solution to the reduced co-ordinates is given in the form:

$$s_j = A_j e^{i\omega_j(s_k)t} \tag{81}$$

with A_j denoting the amplitude, and $\omega_j(s_k)$ denoting the associated frequency. When the free and undamped system of equations is considered, the amplitude is assumed to be constant. As kinematic nonlinearities are included, the stiffness, and thus also the natural frequency, will be dependent on the displacements, s_k.

Based on equation (81), the velocity and acceleration can be expressed as:

$$\dot{s}_j = i \left(\frac{\partial \omega_j(s_k)}{\partial t} t + \omega_j(s_k) \right) s_j \tag{82}$$

$$\ddot{s}_j = i \left(\frac{\partial^2 \omega_j(s_k)}{\partial t^2} t + 2 \frac{\partial \omega_j(s_k)}{\partial t} \right) s_j - \left(\frac{\partial \omega_j(s_k)}{\partial t} t + \omega_j(s_k) \right)^2 s_j \tag{83}$$

Introducing the notation

$$s_j = s_j(t=0) \quad , \quad \dot{s}_j = \dot{s}_j(t=0) \quad , \quad \ddot{s}_j = \ddot{s}_j(t=0) \tag{84}$$

and considering the system of equations at time $t = 0$, the equations (82) to (83) can be simplified to:

$$\dot{s}_j = i\omega_j(s_k) s_j \tag{85}$$

$$\ddot{s}_j = i2 \frac{\partial \omega_j(s_k)}{\partial t} s_j - \omega_j^2(s_k) s_j \tag{86}$$

with the time derivative of the natural frequency given by:

$$\frac{\partial \omega_j(s_k)}{\partial t} = \sum_{r=1}^{N} \frac{\partial \omega_j(s_k)}{\partial s_r} \dot{s}_r \tag{87}$$

In order to evaluate the expressions for $\dot{s}_j$ and $\ddot{s}_j$ in (85) and (86), is introduced a Taylor series for the natural frequency and the squared natural frequency:

$$\omega_j(s_k) = \omega_{j0} + \sum_{l=1}^{N} \frac{\partial \omega_{j0}}{\partial s_l} (s_l - s_{l0}) + \frac{1}{2} \sum_{l=1}^{N} \sum_{p=1}^{N} \frac{\partial^2 \omega_{j0}}{\partial s_l \partial s_p} (s_l - s_{l0})(s_p - s_{p0}) + \ldots \tag{88}$$

$$\omega_j^2(s_k) = \omega_{j0}^2 + \sum_{l=1}^{N} \frac{\partial \omega_{j0}^2}{\partial s_l} (s_l - s_{l0}) + \frac{1}{2} \sum_{l=1}^{N} \sum_{p=1}^{N} \frac{\partial^2 \omega_{j0}^2}{\partial s_l \partial s_p} (s_l - s_{l0})(s_p - s_{p0}) + \ldots \tag{89}$$

Using equation (88), the time derivative of the natural frequency in equation (91) can be written on the form:

$$\frac{\partial \omega_j(s_k)}{\partial t} = i \sum_{r=1}^{N} A_r s_r + \ldots \tag{90}$$

where A_r are constants of the form:

$$\begin{aligned} A_r = & i \sum_{r=1}^{N} \left[\frac{\partial \omega_{j0}}{\partial s_r} \omega_{r0} - \sum_{n=1}^{N} \left(\frac{\partial^2 \omega_{j0}}{\partial s_r \partial s_n} \omega_{r0} + \frac{\partial \omega_{j0}}{\partial s_r} \frac{\partial \omega_{r0}}{\partial s_n} \right) s_{n0} + \right. \\ & \left. \sum_{n=1}^{N} \sum_{l=1}^{N} \left(\frac{\partial^2 \omega_{j0}}{\partial s_r \partial s_n} \frac{\partial \omega_{r0}}{\partial s_l} + \frac{1}{2} \frac{\partial^2 \omega_{r0}}{\partial s_n \partial s_l} \frac{\partial \omega_{j0}}{\partial s_r} \right) s_{n0} s_{l0} - \frac{1}{2} \sum_{n=1}^{N} \sum_{l=1}^{N} \sum_{m=1}^{N} \frac{\partial^2 \omega_{j0}}{\partial s_n \partial s_r} \frac{\partial^2 \omega_{r0}}{\partial s_l \partial s_m} s_{n0} s_{l0} s_{m0} \right] \end{aligned} \tag{91}$$

Copyright © 2010 John Wiley & Sons, Ltd.

DOI: 10.1002/nme

With the above introduced parameters and definitions, the acceleration can now be written in the form:

$$\ddot{s}_j = [B_j - \omega_{j0}^2]s_j + \sum_{r=1}^{N} C_{jr} s_r s_j + ... \tag{92}$$

with the constants B_j and C_{jr} defined as:

$$B_j = \sum_{l=1}^{N} \left[\frac{\partial \omega_{j0}^2}{\partial s_l} - \frac{1}{2} \sum_{p=1}^{N} \frac{\partial^2 \omega_{j0}^2}{\partial s_l \partial s_p} s_{p0} \right] s_{l0} \quad , \quad C_{jr} = \left(2A_r - \frac{\partial \omega_{j0}^2}{\partial s_r} \right) + \sum_{l=1}^{N} \frac{\partial^2 \omega_{j0}^2}{\partial s_l \partial s_r} s_{l0} \tag{93}$$

The velocity product consists of second-order terms and above, and its formula is:

$$\dot{s}_j \dot{s}_k = i^2 \omega_j(s_z)\omega_k(s_z) s_j s_k = [D_{jk} - \omega_{j0}\omega_{k0}] s_j s_k + ... \tag{94}$$

with D_{jk} defined as:

$$\begin{aligned} D_{jk} = & \sum_{p=1}^{N} \left[\omega_{j0} \frac{\partial \omega_{k0}}{\partial s_p} + \omega_{k0} \frac{\partial \omega_{j0}}{\partial s_p} - \sum_{q=1}^{N} \left(\frac{1}{2} \frac{\partial^2 \omega_{k0}}{\partial s_p \partial s_q} \omega_{j0} + \frac{1}{2} \frac{\partial^2 \omega_{j0}}{\partial s_p \partial s_q} \omega_{k0} + \frac{\partial \omega_{j0}}{\partial s_p} \frac{\partial \omega_{k0}}{\partial s_q} \right) s_{q0} - \right. \\ & \sum_{q=1}^{N} \sum_{m=1}^{N} \frac{1}{2} \left(\frac{\partial \omega_{j0}}{\partial s_p} \frac{\partial^2 \omega_{k0}}{\partial s_q \partial s_m} + \frac{\partial \omega_{k0}}{\partial s_p} \frac{\partial^2 \omega_{j0}}{\partial s_q \partial s_m} \right) s_{q0} s_{m0} - \\ & \left. \sum_{q=1}^{N} \sum_{m=1}^{N} \sum_{n=1}^{N} \frac{1}{4} \frac{\partial^2 \omega_{j0}}{\partial s_p \partial s_q} \frac{\partial^2 \omega_{k0}}{\partial s_m \partial s_n} s_{q0} s_{m0} s_{n0} \right] s_{p0} + ... \end{aligned} \tag{95}$$

The equations (92) and (94) are then inserted into (80), leading to the acceleration formula:

$$\ddot{\mathbf{V}} = ... + \sum_{j=1}^{N} \sum_{k=1}^{N} \left[\frac{\partial \mathbf{V}_0}{\partial s_j} C_{jk} + \frac{1}{2} \frac{\partial^2 \mathbf{V}_0}{\partial s_j \partial s_k} \left(E_{jk} - (\omega_{j0} + \omega_{k0})^2 \right) \right] s_j s_k + ... \tag{96}$$

with the introduced constants:

$$E_{jk} = 2C_{jk}\bar{s}_{r0} + B_j + B_k + 2D_{jk} \quad , \quad \bar{s}_{r0} = \sum_{r=1}^{N} s_{r0} \tag{97}$$

Only the second order terms in equation (96) are considered since these are the terms required for arranging the equations governing the modal derivatives up to the second order.

Next, is evaluated the internal restoring forces $\mathbf{g}(\mathbf{V})$ when inserting the Taylor series for the displacement field in (76) into the expression (54).

To evaluate of $\mathbf{g}(\mathbf{V})$ it can be split into three parts to start with. These are the linear part, $\mathbf{K}_0\mathbf{V}$, the quadratic part, $\mathbf{K}_1(\mathbf{V})\mathbf{V}$, and the cubic part, $\mathbf{K}_2(\mathbf{V},\mathbf{V})\mathbf{V}$, in accordance with the general definition given in equation (5). When considering the second order proportional terms, the linear part becomes:

$$\mathbf{K}_0\mathbf{V} = \sum_{el=1}^{nel} \int_{\Omega_{el}} \tilde{\mathbf{L}}^T \mathbf{B}^T \mathbf{D} \mathbf{B} \tilde{\mathbf{L}} \, d\Omega_{el} \mathbf{V} = ... + \sum_{j=1}^{N} \sum_{k=1}^{N} \left[\sum_{el=1}^{nel} \int_{\Omega_{el}} \tilde{\mathbf{L}}^T \mathbf{B}^T \mathbf{D} \mathbf{B} \tilde{\mathbf{L}} \, d\Omega_{el} \right] \frac{1}{2} \frac{\partial^2 \mathbf{V}_0}{\partial s_j \partial s_k} s_j s_k + ... \tag{98}$$

Copyright © 2010 John Wiley & Sons, Ltd.

DOI: 10.1002/nme

The quadratic part is:

$$\mathbf{K}_1(\mathbf{V})\mathbf{V} = \sum_{el=1}^{nel} \int_{\Omega_{el}} \frac{EA}{2}\tilde{\mathbf{L}}^T \left(\mathbf{B}_\epsilon^T \mathbf{V}^T \tilde{\mathbf{L}}^T \mathbf{G}\tilde{\mathbf{L}} + 2\mathbf{G}\tilde{\mathbf{L}}\mathbf{V}\mathbf{B}_\epsilon\tilde{\mathbf{L}}\right)_{el} d\Omega_{el}\mathbf{V}$$
$$=\ldots + \sum_{j=1}^{N}\sum_{k=1}^{N}\left[\sum_{el=1}^{nel}\int_{\Omega_{el}} \frac{EA}{2}\tilde{\mathbf{L}}^T\left(2\mathbf{B}_\epsilon^T\mathbf{V}_0^T\tilde{\mathbf{L}}^T\mathbf{G}\tilde{\mathbf{L}}\frac{1}{2}\frac{\partial^2\mathbf{V}_0}{\partial s_j\partial s_k} + \mathbf{B}_\epsilon^T\frac{\partial\mathbf{V}_0^T}{\partial s_k}\tilde{\mathbf{L}}^T\mathbf{G}\tilde{\mathbf{L}}\frac{\partial\mathbf{V}_0}{\partial s_j} + \right.\right.$$
$$\left.\left. 2\mathbf{G}\tilde{\mathbf{L}}\mathbf{V}_0\mathbf{B}_\epsilon\tilde{\mathbf{L}}\frac{1}{2}\frac{\partial^2\mathbf{V}_0}{\partial s_j\partial s_k} + 2\mathbf{G}\tilde{\mathbf{L}}\frac{\partial\mathbf{V}_0}{\partial s_k}\mathbf{B}_\epsilon\tilde{\mathbf{L}}\frac{\partial\mathbf{V}_0}{\partial s_j} + 2\mathbf{G}\tilde{\mathbf{L}}\frac{1}{2}\frac{\partial^2\mathbf{V}_0}{\partial s_j\partial s_k}\mathbf{B}_\epsilon\tilde{\mathbf{L}}\mathbf{V}_0\right)_{el} d\Omega_{el}\right] s_j s_k + \ldots \tag{99}$$

The cubic term is expressed in the form

$$\mathbf{K}_2(\mathbf{V},\mathbf{V})\mathbf{V} = \sum_{el=1}^{nel}\int_{\Omega_{el}} \frac{EA}{2}\tilde{\mathbf{L}}^T\left(\mathbf{G}\tilde{\mathbf{L}}\mathbf{V}\mathbf{V}^T\tilde{\mathbf{L}}\mathbf{G}\tilde{\mathbf{L}}\right)_{el} d\Omega_{el}\mathbf{V}$$
$$=\ldots + \sum_{j=1}^{N}\sum_{k=1}^{N}\left[\sum_{el=1}^{nel}\int_{\Omega_{el}} \frac{EA}{2}\tilde{\mathbf{L}}^T\mathbf{G}\left(2\tilde{\mathbf{L}}\mathbf{V}_0\mathbf{V}_0^T\tilde{\mathbf{L}}\mathbf{G}\tilde{\mathbf{L}}\frac{1}{2}\frac{\partial^2\mathbf{V}_0}{\partial s_j\partial s_k} + \tilde{\mathbf{L}}\mathbf{V}_0\frac{\partial\mathbf{V}_0^T}{\partial s_k}\tilde{\mathbf{L}}\mathbf{G}\tilde{\mathbf{L}}\frac{\partial\mathbf{V}_0}{\partial s_j} + \right.\right.$$
$$\left.\left. 2\tilde{\mathbf{L}}\frac{\partial\mathbf{V}_0}{\partial s_k}\mathbf{V}_0^T\tilde{\mathbf{L}}\mathbf{G}\tilde{\mathbf{L}}\frac{\partial\mathbf{V}_0}{\partial s_j} + \tilde{\mathbf{L}}\frac{1}{2}\frac{\partial^2\mathbf{V}_0}{\partial s_j\partial s_k}\mathbf{V}_0^T\tilde{\mathbf{L}}\mathbf{G}\tilde{\mathbf{L}}\mathbf{V}_0\right)_{el} d\Omega_{el}\right] s_j s_k + \ldots \tag{100}$$

Adding together (98) to (100), and collecting the terms proportional to $\frac{\partial\mathbf{V}_0}{\partial s_j}$ and $\frac{1}{2}\frac{\partial^2\mathbf{V}_0}{\partial s_j\partial s_k}$, respectively, the internal restoring forces can be written in the form

$$\mathbf{g}(\mathbf{V}) =\ldots + \sum_{j=1}^{N}\sum_{k=1}^{N}\left[\left(\sum_{el=1}^{nel}\int_{\Omega_{el}} \frac{EA}{2}\tilde{\mathbf{L}}^T\left(\mathbf{B}_\epsilon^T\frac{\partial\mathbf{V}_0^T}{\partial s_k}\tilde{\mathbf{L}}_{el}^T\mathbf{G} + 2\mathbf{G}\tilde{\mathbf{L}}_{el}\frac{\partial\mathbf{V}_0}{\partial s_k}\mathbf{B}_\epsilon + \mathbf{G}\tilde{\mathbf{L}}_{el}\mathbf{V}_0\frac{\partial\mathbf{V}_0^T}{\partial s_k}\tilde{\mathbf{L}}_{el}^T\mathbf{G} + \right.\right.\right.$$
$$\left.\left. 2\mathbf{G}\tilde{\mathbf{L}}_{el}\frac{\partial\mathbf{V}_0}{\partial s_k}\mathbf{V}_0^T\tilde{\mathbf{L}}_{el}^T\mathbf{G}\right)\tilde{\mathbf{L}}\, d\Omega\right)_{el}\frac{\partial\mathbf{V}_0}{\partial s_j} +$$
$$\left(\sum_{el=1}^{nel}\int_{\Omega_{el}}\tilde{\mathbf{L}}_{el}^T\left(\mathbf{B}^T\mathbf{D}\mathbf{B}\tilde{\mathbf{L}} + EA\left(\mathbf{B}_\epsilon^T\mathbf{V}_0^T\tilde{\mathbf{L}}^T\mathbf{G} + \mathbf{G}\tilde{\mathbf{L}}\mathbf{V}_0\mathbf{B}_\epsilon + \mathbf{G}\tilde{\mathbf{L}}\mathbf{V}_0\mathbf{V}_0^T\tilde{\mathbf{L}}^T\mathbf{G} + \mathbf{B}_\epsilon\tilde{\mathbf{L}}\mathbf{V}_0\mathbf{G} + \right.\right.\right.$$
$$\left.\left.\left.\left.\frac{1}{2}\mathbf{V}_0^T\tilde{\mathbf{L}}^T\mathbf{G}\tilde{\mathbf{L}}\mathbf{V}_0\mathbf{G}\right)\tilde{\mathbf{L}}\right)_{el} d\Omega_{el}\right)\frac{1}{2}\frac{\partial^2\mathbf{V}_0}{\partial s_j\partial s_k}\right] s_j s_k + \ldots \tag{101}$$

In equation (101), the term proportional to $\frac{\partial\mathbf{V}_0}{\partial s_j}$ can be identified as the secant stiffness differentiated with respect to s_k, as defined in equation (69), plus an additional contribution. The term proportional to $\frac{1}{2}\frac{\partial^2\mathbf{V}_0}{\partial s_j\partial s_k}$ can be identified as the tangent stiffness matrix in equation (124). Furthermore, by introducing the stiffness definition:

$$\partial\mathbf{K}_A = \sum_{el=1}^{nel}\int_{\Omega_{el}} \mathbf{G}\tilde{\mathbf{L}}_{el}\frac{\partial\mathbf{V}_0}{\partial s_k}\mathbf{V}_0^T\tilde{\mathbf{L}}_{el}^T\mathbf{G}\tilde{\mathbf{L}}_{el}\, d\Omega_{el} \tag{102}$$

the expression in (101) simplifies to

$$\mathbf{g}(\mathbf{V}) = \ldots + \sum_{j=1}^{N}\sum_{k=1}^{N}\left[\left(\frac{\partial\mathbf{K}_{S0}}{\partial s_k} + \partial\mathbf{K}_A\right)\frac{\partial\mathbf{V}_0}{\partial s_j} + \mathbf{K}_T\frac{1}{2}\frac{\partial^2\mathbf{V}_0}{\partial s_j\partial s_k}\right] s_j s_k + \ldots \tag{103}$$

Now, by inserting the expressions in equations (103) and (96) into equation (75) and setting the terms proportional to the second order product $s_j s_k$ equal to zero, leads to the following system of equations:

Copyright © 2010 John Wiley & Sons, Ltd.

DOI: 10.1002/nme

$$\left[\mathbf{K}_{T0} + \left(E_{jk} - (\omega_j + \omega_k)^2\right)\mathbf{M}\right]\frac{1}{2}\frac{\partial^2 \mathbf{V}_0}{\partial s_j \partial s_k} = -\left[C_{jk}\mathbf{M} + \frac{\partial \mathbf{K}_{S0}}{\partial s_k} + \partial \mathbf{K}_A\right]\frac{\partial \mathbf{V}_0}{\partial s_j} \tag{104}$$

B. FORMULATION OF 2D BEAM ELEMENT

A plane beam of length l spanning the domain Ω_{el}, as shown in Figure 7, is considered. The element has one rotational and two translational dofs at each of its two nodes at the beam ends. It is exposed to concentrated forces in the nodes and a line loads, p, along the element. The local element dofs

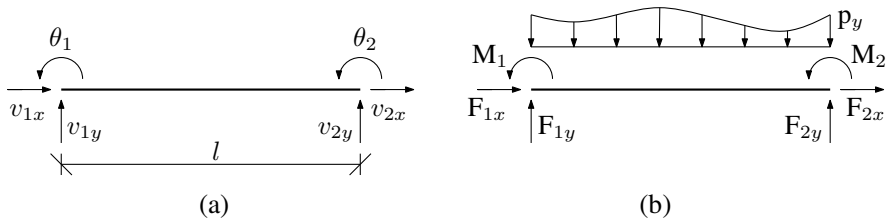

Figure 7. 2D Beam element illustrating (a) the degrees of freedoms and (b) the loading.

are collected in the vector, $\mathbf{v}$, and the loading components in the vectors, $\mathbf{f}$ and $\mathbf{p}$:

$$\mathbf{v} = \begin{bmatrix} v_{1x}, & v_{1y}, & \theta_1, & v_{2x}, & v_{2y}, & \theta_2 \end{bmatrix}^T \tag{105}$$

$$\mathbf{f} = \begin{bmatrix} F_{1x}, & F_{1y}, & M_1, & F_{2x}, & F_{2y}, & M_2 \end{bmatrix}^T \tag{106}$$

$$\mathbf{p} = \begin{bmatrix} p_x, & p_y \end{bmatrix}^T \tag{107}$$

The displacement field over the element is interpolated as

$$\mathbf{u} = \begin{bmatrix} u \\ w \end{bmatrix} = \mathbf{N}\mathbf{v} = \begin{bmatrix} N_1 & 0 & 0 & N_4 & 0 & 0 \\ 0 & N_2 & N_3 & 0 & N_5 & N_6 \end{bmatrix}\mathbf{v} \quad , \quad \mathbf{N} = \begin{bmatrix} \mathbf{N}_u \\ \mathbf{N}_w \end{bmatrix} \tag{108}$$

where u is the horizontal deformation, w is the transverse deformations, and $\mathbf{N}$ is the displacement interpolation matrix containing six shape functions N_i, i ϵ [1,6]. $\mathbf{N}$ can be divided into two matrices, $\mathbf{N}_u$ and $\mathbf{N}_w$, relating to the horizontal and transverse deformations, respectively. The shape functions applied for the horizontal deformation are linear, see for example Cook [34]

$$N_1 = 1 - s \quad , \quad N_4 = s \tag{109}$$

and the transverse shape functions of the second order are:

$$N_2 = 1 - 3s^2 + 2s^3 \quad , \quad N_3 = l(s - 2s^2 + s^3) \quad , \quad N_5 = 3s^2 - 2s^3 \quad , \quad N_6 = l(-s^2 + s^3) \tag{110}$$

The governing equations of motion on discretized form are found from the concept of virtual work, see for example Cook [34]. Considering the element of length l with the possibility of being exposed to line load and concentrated forces, the virtual work is given by

$$\int_{\Omega_{el}} \left(\delta\mathbf{u}^T \rho \ddot{\mathbf{u}} + \delta\mathbf{u}^T d\dot{\mathbf{u}} + \delta\boldsymbol{\varepsilon}^T \sigma\right)\, c\Omega_{el} = \left[\delta\mathbf{u}^T \mathbf{f}\right]_0^l + \int_{\Omega_{el}} \delta\mathbf{u}^T \mathbf{p}\, d\Omega_{el} \tag{111}$$

with ρ defining the density of the material per unit length, d being a material damping parameter analogous to viscosity and $\boldsymbol{\varepsilon}$ being a vector containing the work conjugate strain fields. The domain of the element is denoted by Ω_{el}.

The generalized stresses consist of the normal force, N, and the moment, M. The work conjugate stresses are the axial strain, ε, and the curvature, κ. To include kinematic nonlinear effects, is used

Copyright © 2010 John Wiley & Sons, Ltd.

DOI: 10.1002/nme

the Lagrange strain measure for plane beams. The work conjugate strains and stresses are collected in the vectors σ and $\boldsymbol{\varepsilon}$:

$$\sigma = \begin{Bmatrix} N \\ M \end{Bmatrix}, \quad \boldsymbol{\varepsilon} = \begin{Bmatrix} \varepsilon \\ \kappa \end{Bmatrix} = \begin{Bmatrix} u' + \frac{1}{2}(w')^2 \\ w'' \end{Bmatrix} \tag{112}$$

where $()' = \partial()/\partial x$. The material is assumed to be hyper-elastic, that is, a linear relationship between the stresses and strains, leading to the constitutive relationship:

$$\sigma = \mathbf{D}\boldsymbol{\varepsilon} \quad , \quad \mathbf{D} = \begin{bmatrix} EA & 0 \\ 0 & EI \end{bmatrix} \tag{113}$$

By interpolating the displacement, velocity and acceleration fields as a set of interpolation functions that are functions of space multiplied by an element of a local dof vector that is a function of both time and space, this gives:

$$\mathbf{u} = \mathbf{N}\mathbf{v} \quad , \quad \ddot{\mathbf{u}} = \mathbf{N}\ddot{\mathbf{v}} \quad , \quad \dot{\mathbf{u}} = \mathbf{N}\dot{\mathbf{v}} \tag{114}$$

The variation of $\mathbf{u}$ is evaluated using principles from the Calculus of Variations:

$$\delta\mathbf{u} = \mathbf{N}\delta\mathbf{v} \tag{115}$$

Introducing equation (114) into (112), the generalized form can be written as:

$$\boldsymbol{\varepsilon}_{el} = \mathbf{B}_{el}\mathbf{v}_{el} + \frac{1}{2}\mathbf{e}\mathbf{v}_{el}^T\mathbf{G}_{el}\mathbf{v}_{el}, \qquad \mathbf{e} = \begin{Bmatrix} 1 \\ 0 \end{Bmatrix} \tag{116}$$

From (116), the variational strains are found to be:

$$\delta\boldsymbol{\varepsilon}_{el} = \mathbf{B}_{el}\delta\mathbf{v}_{el} + \mathbf{e}\mathbf{v}_{el}^T\mathbf{G}_{el}\delta\mathbf{v}_{el} \tag{117}$$

where $\mathbf{B}_{el}$ and $\mathbf{G}_{el}$ are defined as:

$$\mathbf{B}_{el} = \begin{bmatrix} \mathbf{N}_u' \\ \mathbf{N}_w'' \end{bmatrix} = \begin{bmatrix} \mathbf{B}_\varepsilon \\ \mathbf{B}_\kappa \end{bmatrix}, \quad \mathbf{G}_{el} = (\mathbf{N}_w')^T\,\mathbf{N}_w' \tag{118}$$

Inserting equations (113) to (118) into equation (111), the element local mass and damping matrices, $\mathbf{m}_{el}$ and $\mathbf{c}_{el}$ and the loading vector, $\mathbf{r}_{el}$, can be identified as:

$$\mathbf{m}_{el} = \rho\int_0^l \mathbf{N}^T\mathbf{N}\,dx_{el} \quad , \quad \mathbf{c}_{el} = d\int_0^l \mathbf{N}^T\mathbf{N}\,dx_{el} \quad , \quad \mathbf{r}_{el} = [\mathbf{N}^T\mathbf{f}]_0^l + \int_0^l \mathbf{N}^T\mathbf{p}\,d\Omega \tag{119}$$

and the internal nodal restoring forces $\mathbf{g}_{el}(\mathbf{x}_{el})$ as

$$\mathbf{g}_{el}(\mathbf{v}_{el}) = \int_{\Omega_{el}} \left(\mathbf{B}^T\mathbf{D}\mathbf{B} + \frac{EA}{2}\left(\mathbf{B}_\epsilon^T\mathbf{v}^T\mathbf{G} + 2\mathbf{G}\mathbf{v}\mathbf{B}_\epsilon + \mathbf{G}\mathbf{v}\mathbf{v}^T\mathbf{G}\right)\right)\mathbf{v}\,d\Omega_{el} \tag{120}$$

B.1. The Tangent Stiffness Matrix

The element tangent stiffness matrix is defined as the stiffness relating the change in deformation, $\mathbf{dv}$, to the change in the loading, $\mathbf{dr}$, in a static context:

$$\mathbf{k}_T d\mathbf{v} = d\mathbf{r} \tag{121}$$

To determine kt is considered the differential form of the static internal work in (111):

$$d\left(\int_{\Omega_{el}} \delta\boldsymbol{\varepsilon}^T\boldsymbol{\sigma}\,d\Omega_{el}\right) = \int_{\Omega_{el}} d\delta\boldsymbol{\varepsilon}^T\boldsymbol{\sigma} + \delta\boldsymbol{\varepsilon}^T d\boldsymbol{\sigma}\,d\Omega_{el} \tag{122}$$

Copyright © 2010 John Wiley & Sons, Ltd.

DOI: 10.1002/nme

Considering the matrices $\mathbf{D}$, $\mathbf{G}$ and $\mathbf{B}$, and the variation $\delta\mathbf{v}$ as constants with respect to differentiation, leads to the following relationship

$$d(\delta\boldsymbol{\varepsilon}) = d\delta\boldsymbol{\varepsilon} = \mathbf{e}d\mathbf{v}^T\mathbf{G}\delta\mathbf{v} \quad , \quad d\boldsymbol{\sigma} = \mathbf{D}d\boldsymbol{\varepsilon} \quad , \quad d\boldsymbol{\varepsilon} = \mathbf{B}d\mathbf{v} + \mathbf{e}\mathbf{v}^T\mathbf{G}d\mathbf{v} \tag{123}$$

Inserting equations (113), (117) and (123) into equation (122), the element local tangent stiffness matrix can be identified as:

$$\mathbf{k}_{T,el} = \int_{\Omega_{el}} \mathbf{B}^T\mathbf{D}\mathbf{B} + EA\left(\mathbf{B}_\varepsilon^T\mathbf{v}^T\mathbf{G} + \mathbf{G}\mathbf{v}\mathbf{B}_\varepsilon + \mathbf{G}\mathbf{v}\mathbf{v}^T\mathbf{G} + \mathbf{B}_\varepsilon\mathbf{v}\mathbf{G} + \frac{1}{2}\mathbf{v}^T\mathbf{G}\mathbf{v}\mathbf{G}\right) d\Omega_{el} \tag{124}$$

B.2. Global Equations of Motion

The element local work contributions are transformed into global co-ordinates by relating the element dofs in the global co-ordinate system, $\mathbf{v}_{el}^g$, to the element dofs in the local co-ordinate system, $\mathbf{v}_{el}$. This is achieved through a transformation matrix $\mathbf{T}_{el}$:

$$\mathbf{v}_{el} = \mathbf{T}_{el}\mathbf{v}_{el}^g \tag{125}$$

Furthermore, is introduced a topology array, $\mathbf{L}_{el}$, relating the local elements dofs, $\mathbf{v}_{el}^g$, to the global element dof of vector $\mathbf{V}$:

$$\mathbf{v}_{el}^g = \mathbf{L}_{el}\mathbf{V} \tag{126}$$

Introducing the relationships of equations (125) and (126) into equation (111), and summing over the nel, the global set of virtual work can be found using equation (4) with the mass and damping matrices, $\mathbf{M}$ and $\mathbf{C}$, given by:

$$\mathbf{M} = \sum_{el=1}^{nel} \mathbf{L}_{el}^T\mathbf{T}_{el}^T\mathbf{m}_{el}\mathbf{T}_{el}\mathbf{L}_{el} \quad , \quad \mathbf{C} = \sum_{el=1}^{nel} \mathbf{L}_{el}^T\mathbf{T}_{el}^T\mathbf{c}_{el}\mathbf{T}_{el}\mathbf{L}_{el} \tag{127}$$

and internal restoring forces, and external forces given by:

$$\mathbf{g}(\mathbf{V}) = \sum_{el=1}^{nel} \left(\mathbf{L}_{el}^T\mathbf{T}_{el}^T\mathbf{k}_s(\mathbf{v}_{el})\mathbf{T}_{el}\mathbf{L}_{el}\right)\mathbf{V} \quad , \quad \mathbf{F}(t) = \sum_{el=1}^{nel} \mathbf{L}_{el}^T\mathbf{T}_{el}^T\mathbf{r}_{el} \tag{128}$$

REFERENCES

1. M. Hakuno, M. Shidawara, T. Hara, Dynamic destructive test of a cantilever beam, controlled by an analog-computer (in japanese), Transactions of the Japan Society of Civil Engineers 171 (1969) 1–9.
2. C. Chen, J. M. Ricles, T. L. Karavasilis, Y. Chae, R. Sause, Evaluation of a real-time hybrid simulation system for performance evaluation of structures with rate dependent devices subjected to seismic loading, Engineering Structures 35 (2012) 71–82. doi:10.1016/j.engstruct.2011.10.006.
3. M. Verma, J. Rajasankar, Improved model for real-time substructuring testing system, Engineering Structures 41 (2012) 258–269. doi:10.1016/j.engstruct.2012.03.031.
4. R.-y. Jung, P. B. Shing, E. Stauffer, B. Thoen, Performance of a real-time pseudodynamic test system considering nonlinear structural response, Earthquake Engineering & Structural Dynamics 36 (June) (2007) 1785–1809. doi:10.1002/eqe.
5. D. Combescure, P. Pegon, Alpha-Operator Splitting time integration technique for pseudodynamic testing Error propagation analysis, Soil Dynamics & Earthquake Engineering 16 (1997) 427–443. doi:Doi:10.1016/s0267-7261(97)00017-1.
6. R. Sajeeb, D. Roy, C. S. Manohar, Numerical aspects of a real-time sub-structuring technique in structural dynamics R., International Journal for Numerical Methods in Engineering 72 (11) (2007) 1261–1313. doi:10.1002/nme.2038.
7. B. Wu, G. Xu, Q. Wang, M. S. Williams, Operator-splitting method for real-time substructure testing, Earthquake Engineering and Structural Dynamics 35 (August 2005) (2006) 293–314. doi:10.1002/eqe.519.
8. B. Wu, H. Bao, J. Ou, S. Tian, Stability and accuracy analysis of the central difference method for real-time substructure testing, Earthquake Engineering and Structural Dynamics 34 (7) (2005) 705–718. doi:10.1002/eqe.451.

Copyright © 2010 John Wiley & Sons, Ltd.

9. G. Mosqueda, M. Ahmadizadeh, Combined implicit or explicit integration steps for hybrid simulation, Earthquake Engineering & Structural Dynamics 36 (15) (2007) 2325–2343. doi:10.1002/eqe.731.
10. P. A. Bonnet, M. S. Williams, A. Blakeborough, Evaluation of numerical time-integration schemes for real-time hybrid testing, Earthquake Engineering & Structural Dynamics 37 (13) (2008) 1467–1490. doi:10.1002/eqe.821.
11. C. Chen, J. M. Ricles, T. M. Marullo, O. Mercan, Real-time hybrid testing using the unconditionally stable explicit CR integration algorithm, Earthquake Engineering & Structural Dynamics 38 (2009) 23–44. doi:10.1002/eqe.838.
12. K. Horri, M. Kawahara, A numerical analysis on the dynamic response of structures, Proceedings of 19th Japan National Congress for Applied Mechanics (1969) 17–22.
13. R. E. Nickell, Nonlinear Dynamics By Mode Superposition, Computer Methods in Applied Mechanics and Engineering 7 (1976) 107–129.
14. B. A. Blakeborough, M. S. Williams, A. P. Darby, D. M. Williams, The development of real-time substructure testing, Philosophical Transactions of the Royal Society A: Mathematical, Physical and Engineering Sciences 359 (1786) (2001) 1869–1891. doi:10.1098/rsta.2001.0877.
15. F. A. Lülf, D.-M. Tran, R. Ohayon, Reduced bases for nonlinear structural dynamic systems: A comparative study, Journal of Sound and Vibration 332 (15) (2013) 3897–3921. doi:10.1016/j.jsv.2013.02.014.
16. E. L. Wilson, M.-W. Yuan, J. M. Dickens, Dynamic Analysis by Direct Superposition of Ritz Vectors, Earthquake Engineering & Structural Dynamics 10 (1982) 813–821.
17. S. R. Idelsohn, A. Cardona, Recent advances in reduction methods in nonlinear structural dynamics, in: Proceedings of the Second International Conference on: Recent Advances in Structural Dynamics, Vol. 2, University of Southampton, 1984, pp. 475–482.
18. S. R. Idelsohn, A. Cardona, A Reduction Method for Nonlinear Structural Dynamic Analysis, Computer Methods in Applied Mechanics and Engineering 49 (1985) 253–279.
19. S. R. Idelsohn, A. Cardonas, A load-dependent basis for reduced nonlinear structural dynamics, Computers & Structures 20 (1-3) (1985) 203–210.
20. O. Weeger, U. Wever, B. Simeon, Nonlinear frequency response analysis of structural vibrations, Computational Mechanics 54 (2014) 1477–1495. doi:10.1007/s00466-014-1070-9.
21. J. Barbic, D. James, Real-Time Subspace Integration for St . Venant-Kirchhoff Deformable Models c, ACM Transactions on Graphics 24 (3) (2005) 982–990.
22. P. M. A. Slaats;, J. de Jongh;, A. A. H. J. Sauren, Model Reduction Tools For Nonlinear Structural Dynamics, Computer and Structures 54 (6) (1995) 1155–1171.
23. M. Nash, Nonlinear structural dynamics by finite element modal synthesis, Ph.D. thesis, Imperial College, The University of London (1977).
24. Y. Shi, C. Mei, A finite element time domain modal formulation for large amplitude free vibrations of beams and plates, Journal of Sound and Vibration 193 (2) (1996) 453–464. doi:10.1006/jsvi.1996.0295.
25. S. Spottswood, R. Allemang, Identification of nonlinear parameters for reduced order models, Journal of Sound and Vibration 295 (2006) 226–245. doi:10.1016/j.jsv.2006.01.009.
26. M. Mcewan, J. Wright, J. Cooper, a.Y.T. Leung, a Combined Modal/Finite Element Analysis Technique for the Dynamic Response of a Non-Linear Beam To Harmonic Excitation, Journal of Sound and Vibration 243 (4) (2001) 601–624. doi:10.1006/jsvi.2000.3434.
27. A. A. Muravyov, S. A. Rizzi, Determination of nonlinear stiffness with application to random vibration of geometrically nonlinear structures, Computers & Structures 81 (15) (2003) 1513–1523. doi:10.1016/S0045-7949(03)00145-7.
28. M. R. Brake, D. J. Segalman, Nonlinear Model Reduction of von Kármán Plates Under Quasi-Steady Fluid Flow, AIAA Journal 48 (10) (2010) 2339–2347. doi:10.2514/1.J050357.
29. D. J. Inman, Engineering Vibrations, 3rd Edition, Pearson Education, New York, USA, 2009.
30. T. Belytschko, W. K. Liu, B. Moran, Nonlinear Finite Elements for Continua and Structures, 1st Edition, John Wiley & Sons, Chicester, England, 2000.
31. S. Krenk, Non-linear Modeling and Analysis of Solids and Structures, 1st Edition, Cambridge University Press, Cambridge, UK, 2009.
32. M. Ahmadizadeh, G. Mosqueda, A. M. Reinhorn, Compensation of actuator delay and dynamics for real-time hybrid structural simulation, Earthquake Engineering and Structural Dynamics 37 (2008) 21–42. doi:10.1002/eqe.
33. O. Mercan, J. M. Ricles, Stability and accuracy analysis of outer loop dynamics in real-time pseudodynamic testing of SDOF systems, Earthquake Engineering and Structural Dynamics 36 (May) (2007) 1523–1543. doi:10.1002/eqe.701.
34. R. D. Cook, D. S. Malkus, M. E. Plesha, R. J. Witt, Concepts and Applications Of Finite Element Analysis, 4th Edition, John Wiley & Sons, New York, USA, 1974.

Copyright © 2010 John Wiley & Sons, Ltd.

Table I. Cable and load parameters.

Parameter	Unit	Formula	Magnitude
l	m	-	20
E	GPa	-	210
D	m	-	$50{\cdot}10^{-3}$
A	m^2	$\pi(D/2)^2$	$2{\cdot}10^{-3}$
I	m^4	$\pi\frac{D^4}{64}$	$3.07{\cdot}10^{-7}$
F_1	N/m	-	1
F_2	N/m	-	3
ω_1	rad/s	$\left(\frac{\pi}{l}\right)^2\sqrt{EI/(\rho A)}$	1.60
ω_2	rad/s	$\left(\frac{2\pi}{l}\right)^2\sqrt{EI/(\rho A)}$	6.40
ρ	kg/m^3	-	7800

Table II. Algorithm Parameters.

Parameter	Unit	Magnitude
γ	-	$\frac{1}{2}$
β	-	$\frac{1}{4}$
Δt	s	10^{-2} - 10^{-5}
nel	-	20-30

Copyright © 2010 John Wiley & Sons, Ltd.

Int. J. Numer. Meth. Engng (2010)
DOI: 10.1002/nme

Paper III

"Nonlinear Real-time Simulations Using a Taylor Basis"

S. Andersen & P. N. Poulsen

Submitted: *International Journal for Numerical Methods in Engineering, 2016*

INTERNATIONAL JOURNAL FOR NUMERICAL METHODS IN ENGINEERING
Int. J. Numer. Meth. Engng 2010; **00**:1–26
Published online in Wiley InterScience (www.interscience.wiley.com). DOI: 10.1002/nme

Nonlinear Real-time Simulations Using a Taylor Basis

S. Andersen*† and P. N. Poulsen ‡

Department of Civil Engineering, Technical University of Denmark, 2800 Kgs. Lyngby, Denmark

SUMMARY

Real-time simulations are used to a significant extent in many engineering fields. However, if nonlinearities are included, the real-time requirement significantly limits the size and complexity of numerical models. The main reason for this limitation is the costly evaluation of the internal restoring forces in each time increment. In the present work, an efficient basis reduction method is applied for kinematic nonlinear structures that enables the size of the basis to be increased without increasing the number of unknown variables. Therefore, larger numerical models can be run in real time. The basis is organized from a Taylor series that predicts a linear relation between the co-ordinates of the linear modes and the modal derivatives. Thus, a full solution is known by solely determining the co-ordinates of the linear modes, which significantly minimizes the computational costs. An example illustrates that computational time can be decreased by one order of magnitude using a Taylor basis compared with former applied basis reduction methods. Copyright © 2010 John Wiley & Sons, Ltd.

Received . . .

KEY WORDS: Kinematic Nonlinearities; Basis Reduction; Taylor Series; Real-time Simulations; Finite Element Analysis; Modal Derivatives

1. INTRODUCTION

Along with rapidly increasing computational speed over the last decades the use of real-time simulations in the industry and research community within engineering fields is increasing. Real time means that the simulation time spent producing the model's output is shorter than or equal to the simulated time. Real-time simulations are applied in engineering fields, such as aircraft design and simulation, motor drive controller design, space robot integration, computer graphics and structural testing to mention some applications, cf. [1–3].

The motivation for the present work relates specifically to the engineering field of hybrid testing in which physical and numerical substructures are combined in structural testing. This proces is also referred to as online-testing, hardware in the loop and pseudo-dynamic testing. If the behavior of the physical substructure is rate dependent, then the structural test and the numerical simulations must to be performed in real-time. The testing is then referred to as real-time hybrid testing or real-time hybrid simulation (RTHS).

The concept of hybrid testing was introduced by Japanese scientists at the end of the 1960s as an alternative to using shaking tables for the seismic analysis of structures, cf. [4]. Typically, the physical substructure represents a part of the structure to be tested that is too complex to be modeled numerically. Thus, this part is considered a black box and must be included physically in the test

*Correspondence to: Department of Civil Engineering, Technical University of Denmark, 2800 Kgs. Lyngby, Denmark. E-mail: seba@byg.dtu.dk
†PhD Student
‡Associate Professor

Copyright © 2010 John Wiley & Sons, Ltd.

setup, whereas the remaining part of the structure is modeled numerically. This substructural testing concept is very appealing for a number of reasons. One benefit is the cost and space reduction achieved because only part of the structure must be build. Furthermore, issues such as scaling problems experienced in shaking tables, are avoided.

During the test the substructures are coupled through actuators installed at the physical substructure at the common substructure interface(s). The actuators impose a kinematic response of the numerical simulations onto physical substructure and measure its force response. The response forces are then included in the following numerical time-step integration. This iterative interchange of data proceeds throughout the test. For a more in-depth description of the principles behind Hybrid testing see e.g. [5, 6].

Since its introduction the field of hybrid testing has experienced significant development. In [7, 8] part of the development during the first couple of decades is summarized. In this period only the pseudo-dynamic (slow rate) testing was considered among researchers. In 1992 Nakashima et al. conducted the first real-time hybrid test with a viscous damper coupled to a single degree of freedom (SDOF) substructure, cf. [9]. Further real-time experiments followed during the 1990s through the the work of Horiuchi et al., Darby et al. and Nakashima and Masaoka, cf. [10–12]. In [12] nonlinearities were successfully included in the numerical substructure. A superstructure of a base-isolated building was modeled as a five DOF numerical model with bilinear constitutive material behavior.

Nonlinear DOF capacity has significantly increased since the work in [12]; however, in many cases it is still considered as modest. In 2001 [13] simulated a material nonlinear system with 50 DOFs, in 2009 [14] simulated a material nonlinear structure with 134 DOFs, in 2012 [3] simulated a material nonlinear system with 405 DOFs and in 2013 [15] included a kinematic and material nonlinear substructure with 514 DOFs. The modest DOF capacity can be viewed as a consequence of the fact that significant research effort in hybrid testing has concentrated on control and communication, whereas the numerical field has received less attention. One of the major factors limiting the nonlinear real-time models is the time-consuming evaluation of the internal restoring forces performed element by element at each time step. Most of the focus in the numerical field has been on time integration. For RTHS to be successfull the applied time integration schemes have to be robust, accurate and fast. Both implicit and explicit schemes have been used including various integration strategies. [16] introduced an approach using an implicit scheme with a fixed number of iterations to apply the initial stiffness in the iterations. [17] suggested a procedure that combines explicit and implicit integration and [18] introduced a noniterative implicit time integration scheme by combining the operator-splitting method with the alpha modified Newmark scheme. [14, 19, 20] proposed unconditional stable explicit algorithms. In [21] implicit and explicit schemes are discussed and compared in real-time through consideration of factors such as accuracy, stability and computational costs. Explicit schemes were concluded as being generally preferable.

Reduction methods also found some interest in research. In [2, 13, 22, 23] the concept of modal transformation is used to reduce the size of the numerical DOFs. In [22] the concept was used to reduce a linear system. In [13] a basis consisting of linear modes and Ritz vectors was applied to represent material nonlinear behavior. In [2, 23] a basis consisting of linear modes and modal derivatives representing kinematic nonlinearities is applied. Furthermore, the basis projection was combined with a mathematical reformulation of the internal restoring forces initially introduced by Nash [24]. The formulation enabled the internal restoring forces to be organized in a global form. In this manner, element by element assembling was avoided and the computational time was significantly decreased. The difference between the work in [2] and [23] is the use of different modal derivatives. In [2] the modal derivatives are determined from a set of equations introduced by Idelsohn and Cardona in [25, 26] whereas a novel set of governing equations are derived and used in [23]. In [23] the different modal derivatives are compared. Only with the modal derivatives based on the novel set of governing equations are the co-ordinates of the modal derivatives shown as given as a quadratic product of the linear mode co-ordinates, as predicted by the Taylor series.

The aim of the present work is to utilize the findings made in [23] and to introduce an efficient basis method that improves on the computational simulation time of kinematic nonlinear systems.

Copyright © 2010 John Wiley & Sons, Ltd.

DOI: 10.1002/nme

For this aim, the relation between the co-ordinates of the linear modes and the modal derivatives is utilized to include the modal derivatives in a basis without introducing further unknowns. This basis formulation introduces a significant reduction in computational time. In [27] a similar approach was adopted for the special case that considers Von Kármán plates. In this case, the membrane displacements are assumed to be given as the sum of the displacement fields proportional to a quadratic product of the out-of-plane deformation co-ordinates. The higher order displacement fields are calculated from a number of nonlinear static deformation cases using finite difference approximations.

The approach introduced in the present work differs from the approach in [27] by being simpler and more general. By using the modal derivatives to represent the higher order displacement fields, these fields can be evaluated using a single computation from their governing equations instead of having to evaluate them from multiple static deformation cases. Furthermore, when applying modal derivatives a general procedure for organizing the equations of motion is available that is independent of the element type considered, such as for example beams, plates or solids.

The following section presents a general form for the kinematic nonlinear equations of motion and how these are organized when projected onto a reduced basis. Next, the Taylor basis including the modal derivatives is presented and introduced into the kinematic nonlinear equations of motion (EOM). In relation to these EOM, a co-ordinate transformation of the equations of motion, an approximation for the velocity required in explicit time integration and the novel equations governing the modal derivatives are presented. Next, the internal restoring forces are organized in a global form using the Taylor basis. Finally, a simple frame example using plane Euler-Bernoulli beam elements is considered to illustrate the precision of the basis and the computational time savings compared with former basis formulations applied in [2, 23].

2. KINEMATIC NONLINEAR EQUATIONS OF MOTION

In the following section, the concept of projecting nonlinear EOM onto a reduced basis, is presented. The derivations are given in reference to the Euler-Bernoulli beam element for which kinematic nonlinear effects are included through a nonlinear axial strain measure that depends on the transverse deformations. The effect of the nonlinear strain measure on the deformations is discussed.

2.1. Governing Equations of Motion

The Euler-Bernoulli beam is considered a reference point. The governing equations including the axial strain, ε, and the curvature, κ, are given as in for example [28]

$$\rho(x)\frac{\partial^2 w}{\partial t^2} + \frac{\partial^2}{\partial x^2}\left(EI(x)\kappa\right) = p(x) \tag{1}$$

$$\rho(x)\frac{\partial^2 u}{\partial t^2} - \frac{\partial}{\partial x}\left(EA(x)\varepsilon\right) = q(x) \tag{2}$$

where x represents the local beam co-ordinate, w and u are the transverse and the axial deformations along the un-deformed beam axis, EI(x) is the bending stiffness, EA(x) is the axial stiffness, ρ(x) is the density per length unit, t is time and p(x) and q(x) represent the external load in the transverse and axial directions of the beam, respectively. To include nonlinear kinematics the Lagrange strain measures are introduced

$$\varepsilon = \frac{\partial u}{\partial x} + \frac{1}{2}\left(\frac{\partial w}{\partial x}\right)^2 \quad , \quad \kappa = \frac{\partial^2 w}{\partial x^2} \tag{3}$$

The transverse and axial deformations are observed to couple through the nonlinear axial strain measure in (3).

Copyright © 2010 John Wiley & Sons, Ltd.

DOI: 10.1002/nme

Using the Calculus of Variations, equations (1)-(2) can be written in discretized form with n DOFs as

$$\mathbf{M}\ddot{\mathbf{V}} + \mathbf{C}\dot{\mathbf{V}} + \mathbf{g}(\mathbf{V}) = \mathbf{F}(t) \tag{4}$$

where $\mathbf{V}$ is a n$\times$1 global displacement vector with $\dot{()} = d()/dt$, $\mathbf{M}$ and $\mathbf{C}$ are n$\times$n mass and damping matrices, $\mathbf{F}$(t) is the time-dependent external load vector of dimensions n$\times$1 and $\mathbf{g}(\mathbf{V})$ is a n$\times$1 vector representing the internal nodal restoring forces.

Kinematic nonlinearities cause the vector $\mathbf{g}(\mathbf{V})$ to be a nonlinear function of the nodal displacements. This vector consist of a linear, quadratic and cubic contribution in $\mathbf{V}$

$$\mathbf{g}(\mathbf{V}) = (\mathbf{K}_0 + \mathbf{K}_1(\mathbf{V}) + \mathbf{K}_2(\mathbf{V},\mathbf{V}))\mathbf{V} \tag{5}$$

where $\mathbf{K}_0$, $\mathbf{K}_1(\mathbf{V})$ and $\mathbf{K}_2(\mathbf{V},\mathbf{V})$ are all stiffness matrices that are independent, linearly dependent and quadratically dependent, respectively, on the vector $\mathbf{V}$.

2.2. *Projection of Nonlinear Equations of Motion*

The EOM in (4) can be projected onto a reduced basis to lower the amount of DOFs in the numerical substructure. Typically, a linear basis is applied in which the relation between the physical and reduced co-ordinates is formulated as

$$\mathbf{V}(s_i) \approx \mathbf{\Phi}\mathbf{s} = \sum_{i=1}^{N} \boldsymbol{\varphi}_i s_i \tag{6}$$

$\mathbf{\Phi}$ is the basis matrix of dimension n$\times$N where N is the number of basis vectors, $\boldsymbol{\varphi}_i$, i ϵ [1;N], which are independent of time. Each vector has an associated reduced co-ordinate, s_i, which depends on time. The reduced co-ordinates are collected in the vector $\mathbf{s}$ of dimension N$\times$1. The discretized equations in (4) are projected onto the linear basis in (6)

$$\tilde{\mathbf{m}}\ddot{\mathbf{s}} + \tilde{\mathbf{c}}\dot{\mathbf{s}} + \tilde{\mathbf{g}}(\mathbf{s}) = \tilde{\mathbf{f}}(t) \tag{7}$$

where the projected matrices and vectors are defined as

$$\tilde{\mathbf{m}} = \mathbf{\Phi}^T\mathbf{M}\mathbf{\Phi} \quad , \quad \tilde{\mathbf{c}} = \mathbf{\Phi}^T\mathbf{C}\mathbf{\Phi} \quad , \quad \tilde{\mathbf{g}}(\mathbf{s}) = \mathbf{\Phi}^T\mathbf{g}(\mathbf{\Phi}s) \quad , \quad \tilde{\mathbf{f}}(t) = \mathbf{\Phi}^T\mathbf{F}(t) \tag{8}$$

When using the linear basis in (6) for the projection in (7), this is referred to as the linear basis projection in the following. A natural choice for the basis vectors applied in (6) are the eigenvectors fulfilling the linearized eigenvalue problem with the tangent stiffness matrix, $\mathbf{K}_T$, and the ith natural frequency, ω_i:

$$\left(\mathbf{K}_T - \omega_i^2\mathbf{M}\right)\boldsymbol{\varphi}_i = \mathbf{0} \tag{9}$$

The eigenvectors, $\boldsymbol{\varphi}_i$, are referred to as the linear mode-shape vectors in the following section.

Solely including the N modes, $\boldsymbol{\varphi}_i$, which contribute significantly to the displacement field $\mathbf{V}$, makes it generally possible to achieve an accurate solution with a substantially reduced number of DOFs, that is, N $\ll$ n. For linear systems, these N modes are typically modes with frequencies in the domain of the excitation frequencies and with a relatively high modal load $|\boldsymbol{\varphi}_i^T F(t)|$. The same modes are significant to the response of kinematic nonlinear systems. However, in nonlinear structures, representing the coupling activated deformations, is also important.

To illustrate the nonlinear effects, a cantilever beam exposed to a transverse deformation, Δw, at the beam end, is sketched; see Figure 1. By assuming that no axial forces are present along the local beam axis, the axial strains are zero throughout the beam.

$$\varepsilon = \frac{\partial u}{\partial x} + \frac{1}{2}\left(\frac{\partial w}{\partial x}\right)^2 = 0 \tag{10}$$

Copyright © 2010 John Wiley & Sons, Ltd.

DOI: 10.1002/nme

For the axial strain to be zero, the derivative of the horizontal displacement, u, must be nonzero. An expression for u along the beam is found from (10) by integrating over the beam length:

$$u(x) = -\frac{1}{2}\int_0^x \left(\frac{\partial w}{\partial x}\right)^2 dx \tag{11}$$

Thus, the kinematic nonlinearities are viewed as introducing a negative axial deformation, in other words, a beam contraction in the case of transverse deformation.

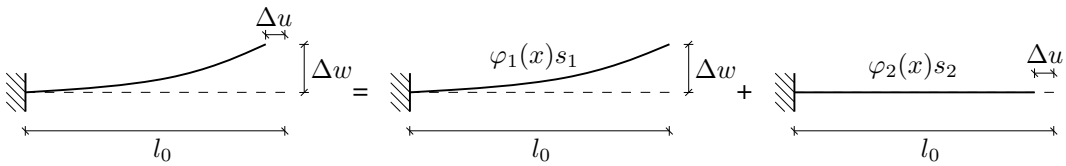

Figure 1. Kinematic Nonlinear Cantilever Beam.

That the basis vectors evaluated from (9) represent these coupling activated deformations, is very important. Otherwise, the system may experience so-called membrane locking, in which the stiffness of the system is increased; see [29]. The possible consequences of locking are poorly predicted displacements or an unstable system.

However, the basis vectors representing the nonlinear effects are not necessarily easy to pick out, particularly not for complex systems. When evaluating the basis vectors from the linearized equations (9), these vectors are typically divided in transverse and axial displacement fields. Thus, if these modes are used to represent the nonlinear coupling effects, a minimum of two modes are required, as sketched in Figure 1.

One way to identify the required basis vectors is to utilize the information contained in a Taylor series of $\mathbf{V}$. The Taylor series reveals the basis vectors required to represent the coupling effects through its higher order terms and suggests a basis including higher order effects without including further unknowns into the system. This concept is discussed in the following section.

3. MODAL DERIVATIVES AND THE TAYLOR BASIS

In this section, a basis including kinematic nonlinear higher order effects is presented without introducing further unknowns. Furthermore, in order to perform an explicit time integration, a transformation of the equations into linear co-ordinates and an approximate evaluation of the velocity are introduced.

3.1. Modal Derivatives and the Taylor Relation

A basis including the higher order displacement effects of kinematic nonlinear structures is identified. For this bases, a second-order Taylor series of the displacement field $\mathbf{V}(s_i)$ is evaluated with point of origin in s_{i0}

$$\mathbf{V}(s_i) = \mathbf{V}(s_{i0}) + \sum_{j=1}^{N} \frac{\partial \mathbf{V}(s_{i0})}{\partial s_j}(s_j - s_{j0}) + \frac{1}{2}\sum_{j=1}^{N}\sum_{k=1}^{N} \frac{\partial^2 \mathbf{V}(s_{i0})}{\partial s_j \partial s_k}(s_j - s_{j0})(s_k - s_{k0}) \tag{12}$$

Copyright © 2010 John Wiley & Sons, Ltd.

DOI: 10.1002/nme

By inserting the linear basis in (6) into, respectively, the zero-order, first-order and second-order displacement fields in (12), these fields can be written as

$$\mathbf{V}(s_{i0}) = \sum_{i=1}^{N} \boldsymbol{\varphi}_{i0} s_{i0} \tag{13}$$

$$\frac{\partial \mathbf{V}(s_{i0})}{\partial s_j} = \frac{\partial}{\partial s_j}\left(\sum_{i=1}^{N} \boldsymbol{\varphi}_{i0} s_{i0}\right) = \sum_{i=1}^{N} \frac{\partial \boldsymbol{\varphi}_{i0}}{\partial s_j} s_{i0} + \boldsymbol{\varphi}_{j0} \tag{14}$$

$$\frac{\partial^2 \mathbf{V}(s_{i0})}{\partial s_j \partial s_k} = \frac{\partial}{\partial s_k}\left(\frac{\partial \mathbf{V}(s_{i0})}{\partial s_j}\right) = \sum_{i=1}^{N} \frac{\partial^2 \boldsymbol{\varphi}_{i0}}{\partial s_j s_k} s_{i0} + \frac{\partial \boldsymbol{\varphi}_{k0}}{\partial s_j} + \frac{\partial \boldsymbol{\varphi}_{j0}}{\partial s_k} \tag{15}$$

Equation (13) is a constant term representing the initial deformation of the system. The first-order term in (14) is viewed as consisting of a linear mode-shape vector and a sum of the first-order modal derivatives. By inserting this term into (12) with zero initial deformations, $s_i = 0$, the well-known linear basis formulation in (6) appears. The second-order contribution in (15) consists of the first- and second-order basis vector derivatives. These vectors are required to represent the nonlinear effects up to the second order.

In the work by [2, 23, 26] the terms in (14) and (15) were included in a linear basis to analyze kinematic nonlinear structures. Because a linear basis was used, the terms had independent modal co-ordinates, s_k, associated with them. However, as the Taylor formulation in (12) suggests, including the higher-order terms in (15) can be done more efficiently. The Taylor series predicts that the co-ordinates of the second order displacement field are given as a quadratic product of the co-ordinates associated with the first-order displacement field (14). Thus, the higher order effects represented by (15) can be included without introducing further unknowns into the system.

In the following section, a basis based on the second-order Taylor series in (12) is set up and is referred to as the Taylor basis. When using the Taylor basis, significant computational time is saved with the same precision as the response achieved by including the higher-order effects directly in a linear basis, as was done by [2, 23, 26].

3.2. Second-Order Taylor Basis

A basis utilizing the relation between the co-ordinates of the linear terms and the higher order terms predicted by the Taylor series in (12) is arranged. The basis is taken as the Taylor series including the terms up to the second order with an initial zero deformation state, in other words, for $s_{k0} = 0$. Inserting (13)-(15) into (12) a second-order basis with respect to the reduced co-ordinates, s_k, can be written in the form

$$\mathbf{V}(\mathbf{s}) = \sum_{i=1}^{N} \boldsymbol{\varphi}_i s_i + \frac{1}{2} \sum_{i=1}^{N} \sum_{j=1}^{N} \left(\frac{\partial \boldsymbol{\varphi}_i}{\partial s_j} + \frac{\partial \boldsymbol{\varphi}_j}{\partial s_i}\right) s_i s_j \tag{16}$$

The basis contains N linear mode-shape vectors, $\boldsymbol{\varphi}_i$, and N^2 first order mode-shape vectors, $\partial \boldsymbol{\varphi}_k / \partial s_l$. The vectors are weighted by N modal co-ordinates s_k on linear and quadratic forms. Utilizing the symmetry of the products $s_i s_j = s_j s_i$ the amount of quadratic summation terms in (16) is reduced and the basis takes the form

$$\mathbf{V}(\mathbf{s}) = \sum_{i=1}^{N} \boldsymbol{\varphi}_i s_i + \sum_{i=1}^{N} \sum_{j=1}^{i} \left(\frac{\partial \boldsymbol{\varphi}_i}{\partial s_j} + (1 - \delta_{ij}) \frac{\partial \boldsymbol{\varphi}_j}{\partial s_i}\right) s_i s_j \tag{17}$$

where δ_{ij} is Kronecker's delta. In the quadratic summation the inner index j is observed to run from 1 to i instead of to N, which was the case in (16). This phenomenon leaves the formulation with N linear summations plus $\frac{1}{2}(N + N^2)$ quadratic summations from the higher-order terms.

As is subsequently demonstrated, the first-order mode-shape vectors, $\partial \boldsymbol{\varphi}_i / \partial s_j$, are not determined as separate vectors. Instead, they are evaluated as the sum in which they appear in

Copyright © 2010 John Wiley & Sons, Ltd.

DOI: 10.1002/nme

(16). Therefore, each sum of the first-order mode-shape vectors is accounted for in the following section as only a single basis vector. Thus, $\frac{1}{2}(N+N^2)$ first-order modes are present in (16) when the symmetry terms of the quadratic sum are considered. The formulation in (17) is organized in matrix form as

$$\mathbf{V}(\mathbf{s}) = \mathbf{V}_T = \mathbf{\Phi}_T \mathbf{s}_T \quad , \quad \mathbf{\Phi}_T = [\mathbf{\Phi}_L \, , \, \mathbf{\Phi}_H] \quad , \quad \mathbf{s}_T = \begin{Bmatrix} \mathbf{s} \\ \mathbf{s}_H \end{Bmatrix} \tag{18}$$

where the Taylor basis matrix, $\mathbf{\Phi}_T$, is of dimension $n \times \left(\frac{3}{2}N + \frac{1}{2}N^2\right)$. This matrix consists of the matrices $\mathbf{\Phi}_L$ and $\mathbf{\Phi}_H$ containing N linear modes and $\frac{1}{2}(N+N^2)$ modal derivatives, respectively. The submatrices $\mathbf{\Phi}_L$ and $\mathbf{\Phi}_H$ are organized as

$$\mathbf{\Phi}_L = [\varphi_1, \;\; \varphi_2, \;\; \ldots \;\; \varphi_N] \tag{19}$$

$$\mathbf{\Phi}_H = \left[\frac{\partial \varphi_1}{\partial s_1}, \;\; \frac{\partial \varphi_2}{\partial s_1} + \frac{\partial \varphi_1}{\partial s_2}, \;\; \frac{\partial \varphi_2}{\partial s_2}, \;\; \frac{\partial \varphi_3}{\partial s_1} + \frac{\partial \varphi_1}{\partial s_3}, \;\; \frac{\partial \varphi_3}{\partial s_2} + \frac{\partial \varphi_2}{\partial s_3}, \;\; \ldots \;\; \frac{\partial \varphi_N}{\partial s_N} \right] \tag{20}$$

The vector $\mathbf{s}_T$ in (18) consists of the vectors $\mathbf{s}$ and $\mathbf{s}_H$, which contain the co-ordinates related to the modes in $\mathbf{\Phi}_L$ and $\mathbf{\Phi}_H$, that is

$$\mathbf{s}^T = \begin{bmatrix} s_1, & s_2, & \ldots & s_N \end{bmatrix} \tag{21}$$

$$\mathbf{s}_H^T = \begin{bmatrix} s_1 s_1, & s_2 s_1, & s_2 s_2, & s_3 s_1, & s_3 s_2, & \ldots & s_N s_N \end{bmatrix} \tag{22}$$

Projecting the EOM in (4) onto the basis in (18) gives the following formulation

$$\hat{\mathbf{m}} \ddot{\mathbf{s}}_T + \hat{\mathbf{c}} \dot{\mathbf{s}}_T + \hat{\mathbf{g}}(\mathbf{s}_T) = \hat{\mathbf{f}}(t) \tag{23}$$

with the introduced matrix definitions

$$\hat{\mathbf{m}} = (\mathbf{\Phi}_T)^T \, \mathbf{M} \mathbf{\Phi}_T \tag{24}$$

$$\hat{\mathbf{c}} = (\mathbf{\Phi}_T)^T \, \mathbf{C} \mathbf{\Phi}_T \tag{25}$$

$$\hat{\mathbf{g}}(\mathbf{s}_T) = (\mathbf{\Phi}_T)^T \, \mathbf{g}(\mathbf{\Phi}_T \mathbf{s}_T) \tag{26}$$

$$\hat{\mathbf{f}}(t) = (\mathbf{\Phi}_T)^T \, \mathbf{F}(t) \tag{27}$$

Furthermore the velocity and acceleration vectors $\dot{\mathbf{s}}_T$ and $\ddot{\mathbf{s}}_T$ in (23) are given in the form

$$\dot{\mathbf{s}}_T = \begin{Bmatrix} \dot{\mathbf{s}} \\ \dot{\mathbf{s}}_H \end{Bmatrix} = \begin{Bmatrix} \dot{s}_1 \\ \dot{s}_2 \\ . \\ \dot{s}_N \\ \dot{s}_1 s_1 + s_1 \dot{s}_1 \\ \dot{s}_2 s_1 + s_2 \dot{s}_1 \\ \dot{s}_2 s_2 + s_2 \dot{s}_2 \\ \dot{s}_3 s_1 + s_3 \dot{s}_1 \\ . \\ \dot{s}_N s_N + s_N \dot{s}_N \end{Bmatrix}, \quad \ddot{\mathbf{s}}_T = \begin{Bmatrix} \ddot{\mathbf{s}} \\ \ddot{\mathbf{s}}_H \end{Bmatrix} = \begin{Bmatrix} \ddot{s}_1 \\ \ddot{s}_2 \\ . \\ \ddot{s}_N \\ \ddot{s}_1 s_1 + 2\dot{s}_1 \dot{s}_1 + s_1 \ddot{s}_1 \\ \ddot{s}_2 s_1 + 2\dot{s}_2 \dot{s}_1 + s_2 \ddot{s}_1 \\ \ddot{s}_2 s_2 + 2 s_2 \ddot{s}_2 + s_2 \ddot{s}_2 \\ \ddot{s}_3 s_1 + 2\dot{s}_3 \dot{s}_1 + s_3 \ddot{s}_1 \\ . \\ \ddot{s}_N s_N + 2\dot{s}_N \dot{s}_N + s_N \ddot{s}_N \end{Bmatrix} \tag{28}$$

From the introduced definitions in (21), (22) and (28) all unknowns $(s_i, \dot{s}_i, \ddot{s}_i)$ appear multiple times. Therefore, the system of equations in (23) must be transformed from the $(\mathbf{s}_T, \dot{\mathbf{s}}_T, \ddot{\mathbf{s}}_T)$ co-ordinate system to the $(\mathbf{s}, \dot{\mathbf{s}}, \ddot{\mathbf{s}})$ co-ordinate system before it is solved. This transformation can be performed using straightforward mathematical approaches presented in the following section.

3.3. Transformation of Equations of Motion

When transforming the projected system of equations in (23) onto the $(\mathbf{s}, \dot{\mathbf{s}}, \ddot{\mathbf{s}})$ co-ordinate system, these equations are initially written in a variational form by multiplying them with the virtual

Copyright © 2010 John Wiley & Sons, Ltd.

DOI: 10.1002/nme

component vector $\delta\mathbf{s}_T$

$$(\delta\mathbf{s}_T)^T\left(\hat{\mathbf{m}}\ddot{\mathbf{s}}_T+\hat{\mathbf{c}}\dot{\mathbf{s}}_T+\hat{\mathbf{g}}(\mathbf{s}_T)-\hat{\mathbf{f}}\right)=0 \tag{29}$$

The vector $\delta\mathbf{s}_T$ is arranged by taking the variation of the vector $\mathbf{s}_T$ introduced in (18)

$$\delta\mathbf{s}_T=\left[\delta s_1,\quad \delta s_2,\quad \ldots\quad \delta s_N,\quad 2\delta s_1 s_1,\quad \delta s_2 s_1+s_2\delta s_1,\quad 2\delta s_2 s_2,\quad \ldots\quad 2\delta s_N s_N\right]^T \tag{30}$$

Next, a set of relations between the vectors ($\mathbf{s}$, $\dot{\mathbf{s}}$, $\ddot{\mathbf{s}}$, $\delta\mathbf{s}$) and ($\mathbf{s}_T$, $\dot{\mathbf{s}}_T$, $\ddot{\mathbf{s}}_T$, $\delta\mathbf{s}_T$) are arranged. As shown in detail in Appendix A, such relations can be written in the form

$$\mathbf{s}_T=\mathbf{Q}(\mathbf{s})\mathbf{s} \tag{31}$$
$$\delta\mathbf{s}_T=\mathbf{U}(\mathbf{s})\delta\mathbf{s} \tag{32}$$
$$\dot{\mathbf{s}}_T=\mathbf{U}(\mathbf{s})\dot{\mathbf{s}} \tag{33}$$
$$\ddot{\mathbf{s}}_T=\mathbf{U}(\mathbf{s})\ddot{\mathbf{s}}+2\mathbf{P}(\dot{\mathbf{s}})\dot{\mathbf{s}} \tag{34}$$

where $\mathbf{Q}(\mathbf{s})$, $\mathbf{U}(\mathbf{s})$ and $\mathbf{P}(\dot{\mathbf{s}})$ are all matrices of dimension $\left(\frac{3}{2}\mathrm{N}+\frac{1}{2}\mathrm{N}^2\right)\times\mathrm{N}$. As indicated, these matrices are functions of the vectors $\mathbf{s}$ and $\dot{\mathbf{s}}$, which entails that they must be evaluated in every time step during the simulations. To minimize the computational time spent on their evaluation, they are manipulated and written in the form

$$\mathbf{Q}(\mathbf{s})=\sum_{k=1}^{N}\mathbf{A}_k s_k+\mathbf{H} \tag{35}$$
$$\mathbf{P}(\dot{\mathbf{s}})=\sum_{k=1}^{N}\mathbf{A}_k \dot{s}_k \tag{36}$$
$$\mathbf{U}(\mathbf{s})=\sum_{k=1}^{N}\mathbf{B}_k s_k+\mathbf{H} \tag{37}$$

where $\mathbf{H}$, $\mathbf{A}_k$ and $\mathbf{B}_k$ are all constant matrices of dimension $\left(\frac{3}{2}\mathrm{N}+\frac{1}{2}\mathrm{N}^2\right)$ x N. Inserting the relations in (31)-(34) into (29) yields the expression

$$(\mathbf{U}(\mathbf{s})\delta\mathbf{s})^T\left(\hat{\mathbf{m}}\big(\mathbf{U}(\mathbf{s})\ddot{\mathbf{s}}+2\mathbf{P}(\dot{\mathbf{s}})\dot{\mathbf{s}}\big)+\hat{\mathbf{c}}\mathbf{U}(\mathbf{s})\dot{\mathbf{s}}+\hat{\mathbf{g}}\left(\mathbf{s}_T\right)-\hat{\mathbf{f}}(t)\right)=\mathbf{0} \tag{38}$$

The terms proportional to the vectors $\mathbf{s}$, $\dot{\mathbf{s}}$ and $\ddot{\mathbf{s}}$ are then collected

$$\delta\mathbf{s}^T\left(\mathbf{U}(\mathbf{s})^T\hat{\mathbf{m}}\mathbf{U}(\mathbf{s})\ddot{\mathbf{s}}+\mathbf{U}(\mathbf{s})^T\left(2\hat{\mathbf{m}}\mathbf{P}(\dot{\mathbf{s}})+\hat{\mathbf{c}}\mathbf{U}(\mathbf{s})\right)\dot{\mathbf{s}}+\mathbf{U}(\mathbf{s})^T\hat{\mathbf{g}}(\mathbf{s}_T)-\mathbf{U}(\mathbf{s})^T\hat{\mathbf{f}}(t)\right)=\mathbf{0} \tag{39}$$

Introducing the definitions

$$\bar{\mathbf{m}}(\mathbf{s})=\mathbf{U}(\mathbf{s})^T\hat{\mathbf{m}}\mathbf{U}(\mathbf{s}) \tag{40}$$
$$\bar{\mathbf{c}}(\mathbf{s},\dot{\mathbf{s}})=\mathbf{U}(\mathbf{s})^T\left(2\hat{\mathbf{m}}\mathbf{P}(\dot{\mathbf{s}})+\hat{\mathbf{c}}\mathbf{U}(\mathbf{s})\right) \tag{41}$$
$$\bar{\mathbf{g}}(\mathbf{s})=\mathbf{U}(\mathbf{s})^T\hat{\mathbf{g}}\left(\mathbf{s}_T\right) \tag{42}$$
$$\bar{\mathbf{f}}(\mathbf{s},t)=\mathbf{U}(\mathbf{s})^T\hat{\mathbf{f}}(t) \tag{43}$$

enables the governing EOM projected onto the Taylor basis to be written in the ($\mathbf{s}$, $\dot{\mathbf{s}}$, $\ddot{\mathbf{s}}$) co-ordinates as

$$\bar{\mathbf{m}}(\mathbf{s})\ddot{\mathbf{s}}+\bar{\mathbf{c}}(\mathbf{s},\dot{\mathbf{s}})\dot{\mathbf{s}}+\bar{\mathbf{g}}(\mathbf{s})=\bar{\mathbf{f}}(\mathbf{s},t) \tag{44}$$

Copyright © 2010 John Wiley & Sons, Ltd.

DOI: 10.1002/nme

As is illustrated in section 5, a considerable amount of computational time can be saved by solving the system of equations in (44) instead of a system projected onto a linear basis containing $N+\frac{1}{2}N+N^2$ modes with equally many unknowns.

Importantly, note that after the transformation, the mass and damping matrices in (44) now depend on $\mathbf{s}$ and $\dot{\mathbf{s}}$. If using an explicit integration scheme, such as the central difference method (CDM) the velocity vector is not available at the present time, t_i. Therefore, the vector $\dot{\mathbf{s}}_i$ must be approximated, which is described in the following section with the CDM as a reference.

3.4. Evaluation of Velocity using the CDM

An approximation for the velocity vector $\dot{\mathbf{s}}_i$ is arranged. For this approximation, a second-order Taylor series of the displacement vector $\mathbf{s}$ is considered, with time, t_i, taken as the point of reference

$$\mathbf{s}(t) = \mathbf{s}_i + \dot{\mathbf{s}}_i(t - t_i) + \frac{1}{2}\ddot{\mathbf{s}}_i(t - t_i)^2 \tag{45}$$

The vectors $\dot{\mathbf{s}}_i$, $\ddot{\mathbf{s}}_i$ are unknowns and should be determined. As sketched in Figure 2, both the displacement $\mathbf{s}_{i-1}$ and the velocity $\dot{\mathbf{s}}_{i-1}$ in the time state $t_{i-1} = t_i - \Delta t$ are assumed to be known. By using the Taylor series in (45) to evaluate the displacement and velocity at the time state t_{i-1}

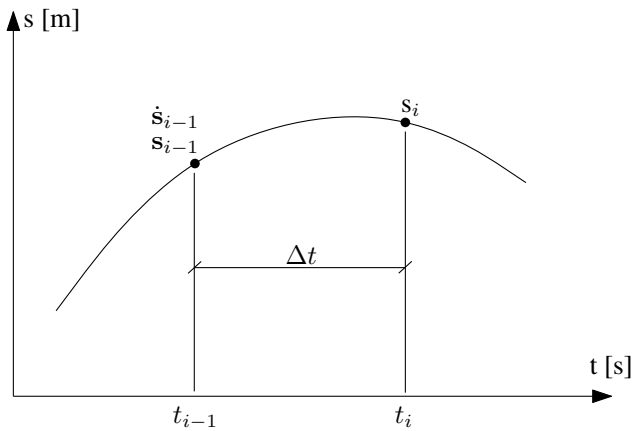

Figure 2. Time response.

two equations including the unknowns $\dot{\mathbf{s}}_i$ and $\ddot{\mathbf{s}}_i$ can be arranged as

$$\mathbf{s}(t_{i-1}) = \mathbf{s}_i + \dot{\mathbf{s}}_i(-\Delta t) + \frac{1}{2}\ddot{\mathbf{s}}_i(-\Delta t)^2 = \mathbf{s}_{i-1} \tag{46}$$

$$\dot{\mathbf{s}}(t_{i-1}) = \dot{\mathbf{s}}_i + \ddot{\mathbf{s}}_i(-\Delta t) = \dot{\mathbf{s}}_{i-1} \tag{47}$$

Isolating $\ddot{\mathbf{s}}_i$ in (47) and inserting it into (46) enables the desired velocity at time t_i to be found as a function of known displacements and velocities

$$\dot{\mathbf{s}}_i = \frac{2}{\Delta t}(\mathbf{s}_i - \mathbf{s}_{i-1}) - \dot{\mathbf{s}}_{i-1} \tag{48}$$

However, evaluating the velocity solely on the basis of displacements is desired. Using the CDM as an explicit integration scheme, the displacement vectors are related to the velocity by

$$\dot{\mathbf{s}}_{i-1} = \frac{1}{2\Delta t}(\mathbf{s}_i - \mathbf{s}_{i-2}) \tag{49}$$

Inserting (49) into (48) gives an approximation for the velocity vector at the time state t_i in the form

$$\dot{\mathbf{s}}_i = \frac{1}{\Delta t}\left(\frac{3}{2}\mathbf{s}_i - 2\mathbf{s}_{i-1} + \frac{1}{2}\mathbf{s}_{i-2}\right) \tag{50}$$

As is observed from (50) the velocity is now purely based on the displacements at times t_i, t_{i-1} and t_{i-2}. The velocity approximation is applied in the examples presented in section 5.

Copyright © 2010 John Wiley & Sons, Ltd.

DOI: 10.1002/nme

3.5. Governing Equations of Modal Derivatives

The following section presents the main steps in the derivation of the complete system of equations governing the modal derivatives, as introduced in [23]. The free undamped kinematic nonlinear equations of motion are considered

$$\mathbf{M}\ddot{\mathbf{V}} + \mathbf{g}(\mathbf{V}) = \mathbf{0} \tag{51}$$

The Taylor series in (12) including up to second-order terms, are then introduced into (51) under the assumption that the co-ordinates s_j are in the complex form

$$s_j = A_j e^{i\omega_j(s_i)t} \tag{52}$$

where A_j is the amplitude, $\omega_j(s_i)$ is the frequency, and t is the time. The amplitude is assumed to be constant given a free and undamped system. However, the kinematic nonlinearities of the system cause the natural frequency, $\omega_j(s_i)$, to depend on the displacement field represented by the reduced co-ordinates, s_i. Expanding the natural frequency as a Taylor series with respect to the reduced co-ordinates s_i evaluated at time t = 0 s enables the equations in (51) to be written as a vector polynomial of the form

$$\mathbf{A} + \sum_{j=1}^{N} \mathbf{B}_j s_j + \sum_{j=1}^{N}\sum_{k=1}^{N} \mathbf{C}_{jk} s_j s_k + ... = \mathbf{0} \tag{53}$$

where $\mathbf{A}$, $\mathbf{B}_j$ and $\mathbf{C}_{jk}$ are constant vector coefficients that include the initial displacement field s_{i0} in their formulation. The reduced co-ordinates, s_{i0}, are introduced through the Taylor series of $\omega_j(s_i)$. Then, arguably, each vector coefficient should be zero for (53) to be fulfilled for any value of s_j. For each vector coefficient set equal to zero, a system of governing equations is given. The zero-order proportional coefficient $\mathbf{A}$ represents the force equilibrium equations, the first-order proportional coefficients $\mathbf{B}_j$ represent the eigenvalue problem and the second-order proportional coefficients $\mathbf{C}_{jk}$ represent the system of equations governing the modal derivatives.

Inserting the Euler-Bernoulli beam element formulation as presented in section 5.2 into (53) enables an expression for $\mathbf{C}_{jk}$ that governs modal derivatives to be revealed. The equations are considered with an initial zero deformation, $s_{i0} = 0$, because this case is the only one in which an explicit solution for the first-order modal derivatives can be determined. The system of equations found by setting $\mathbf{C}_{jk}$ equal to zero is

$$\left[\mathbf{K}_{T0} - (\omega_{j0} + \omega_{k0})^2\mathbf{M}\right]\frac{1}{2}\left(\frac{\partial\boldsymbol{\varphi}_{k0}}{\partial s_j} + \frac{\partial\boldsymbol{\varphi}_{j0}}{\partial s_k}\right) = \left[2\frac{\partial\omega_{j0}}{\partial s_k}(\omega_{j0} - \omega_{k0})\mathbf{M} - \frac{\partial\mathbf{K}_{S0}}{\partial s_k}\right]\boldsymbol{\varphi}_{j0} \tag{54}$$

where $\mathbf{K}_{T0}$ is the tangent stiffness, $\mathbf{M}$ is the mass matrix, $\mathbf{K}_{S0}$ is the secant stiffness and ω_{j0} and ω_{k0} are the linear natural frequencies of modes j and k. The subindex 0 indicates the initial deformation state evaluation.

On the left-hand side of (54) the sum of two modal derivatives with switched indices appears. These figures are multiplied by the tangent stiffness subtracted by the product of the mass matrix times the squared sum of the natural frequencies. On the right-hand side is the linear mode $\boldsymbol{\varphi}_{j0}$ multiplied by a matrix that includes the mass matrix, the zero- and first-order derivatives of the natural frequencies, and the secant stiffness in differentiated form. The first-order derivative of the natural frequency is an unknown quantity that can be determined using the symmetry of the governing equations. As is observed, the left-hand side is symmetric with respect to the subindexes j and k. To ensure consistency, the right-hand side must also be symmetric with respect to the indexes. As shown in [23] the symmetry can be used to determine the following relation.

$$2\frac{\partial\omega_{j0}}{\partial s_k}(\omega_{j0} - \omega_{k0}) = \frac{1}{m_j}\left(\frac{\partial k_{S0j}}{\partial s_k} - \frac{\partial k_{S0jk}}{\partial s_j}\right) \tag{55}$$

Copyright © 2010 John Wiley & Sons, Ltd.

DOI: 10.1002/nme

with the included definitions

$$m_j = \boldsymbol{\varphi}_{j0}^T \mathbf{M} \boldsymbol{\varphi}_{j0} \quad , \quad \frac{\partial k_{S0j}}{\partial s_k} = \boldsymbol{\varphi}_{j0}^T \frac{\partial \mathbf{K}_{S0j}}{\partial s_k} \boldsymbol{\varphi}_{j0} \quad , \quad \frac{\partial k_{S0jk}}{\partial s_j} = \boldsymbol{\varphi}_j^T \frac{\partial \mathbf{K}_{S0}}{\partial s_j} \boldsymbol{\varphi}_k \tag{56}$$

Inserting the relation in (55) into (54) enables the sum of the first-order modal derivatives to be directly determined by inverting the matrix on the left hand side.

3.6. Linear Dependent Basis Vectors

In given cases, some of the modal derivatives in (20) appear to be linearly dependent on each other. In those cases the Taylor basis $\boldsymbol{\Phi}_T$ in (18) becomes singular. In conventional basis formulations, the linear dependent vectors are taken out of the basis to remove the singularity. However, in the given case the singularity is automatically removed when transforming the system of equations into the linear co-ordinate system ($\mathbf{s}$, $\dot{\mathbf{s}}$, $\ddot{\mathbf{s}}$), cf. (44). It is, therefore, not necessary to remove the linear dependent basis vectors. In order to fulfill the Taylor series in (17) it is also required to include the terms.

In the case where linear dependent vectors are present, the Taylor basis is formulated as a matrix product of the form

$$\boldsymbol{\Phi}_T = \check{\boldsymbol{\Phi}}_T \mathbf{T} \tag{57}$$

where $\check{\boldsymbol{\Phi}}_T$ is a matrix containing all basis vectors but the P linear dependent modal derivatives in $\boldsymbol{\Phi}_T$. $\mathbf{T}$ is a matrix containing the coefficients in the linear combinations. The matrices $\check{\boldsymbol{\Phi}}_T$ and $\mathbf{T}$ are of dimension $n \times \left(\frac{3}{2}N + \frac{1}{2}N^2 - P\right)$ and $\left(\frac{3}{2}N + \frac{1}{2}N^2 - P\right) \times \left(\frac{3}{2}N + \frac{1}{2}N^2\right)$ respectively. Utilizing the formulation in (57) the relation in (18) is transformed into the $\check{\mathbf{s}}_T$ co-ordinates

$$\mathbf{V}(\mathbf{s}) = \check{\boldsymbol{\Phi}}_T \check{\mathbf{s}}_T \quad , \quad \check{\mathbf{s}}_T = \mathbf{T}\mathbf{s}_T \tag{58}$$

As a direct consequence of the relation in (58) the transformation matrices in (35)-(37) are replaced by the matrices in (59).

$$\check{\mathbf{Q}}(\mathbf{s}) = \mathbf{T}\mathbf{Q}(\mathbf{s}) \quad , \quad \check{\mathbf{U}}(\mathbf{s}) = \mathbf{T}\mathbf{U}(\mathbf{s}) \quad , \quad \check{\mathbf{P}}(\dot{\mathbf{s}}) = \mathbf{T}\mathbf{P}(\dot{\mathbf{s}}) \tag{59}$$

In the examples presented in section 5, used to illustrate the method, linear dependencies exist. In these cases it is important to stress, that the linear dependent modes are not included in the counting of DOFs.

4. REDUCED BASIS FORMULATION

In the following section the so-called reduced basis formulation (RBF) based on the work by Nash, Shi and Mei and Slaats et al. [24, 30, 31] is presented. The principle of the RBF is to manipulate the internal restoring forces into a global vector polynomial. Significant computational costs can be saved by evaluating the internal restoring forces on this form compared with the usual element by element evaluation.

Initially, the formulation is presented when a linear basis is applied. Next, the formulation based on a Taylor basis is considered. The two formulations are used for a comparison in section 5 analyzing a simple frame structure exposed to dynamic loading in a real-time context.

4.1. RBF with a Linear Basis

The internal restoring forces in (5) are projected onto the basis in (6) which consists of purely linear modes. Doing so enables the projected stiffness matrices to be written in the form

$$\boldsymbol{\Phi}^T \mathbf{K}_0 \boldsymbol{\Phi} = \tilde{\mathbf{K}}_0 \quad , \quad \boldsymbol{\Phi}^T \mathbf{K}_1(\boldsymbol{\Phi}\mathbf{s}) \boldsymbol{\Phi} = \sum_{i=1}^{N} \tilde{\mathbf{K}}_{1,i} s_i \quad , \quad \boldsymbol{\Phi}^T \mathbf{K}_2(\boldsymbol{\Phi}\mathbf{s}, \boldsymbol{\Phi}\mathbf{s}) \boldsymbol{\Phi} = \sum_{i=1}^{N} \sum_{j=1}^{N} \tilde{\mathbf{K}}_{2,ij} s_i s_j \tag{60}$$

Copyright © 2010 John Wiley & Sons, Ltd.

DOI: 10.1002/nme

where the matrices $\tilde{\mathbf{K}}_0$, $\tilde{\mathbf{K}}_{1,i}$ and $\tilde{\mathbf{K}}_{2,ij}$ are constant stiffness coefficients of dimension N×N. The latter two are defined as

$$\tilde{\mathbf{K}}_{1,i} = \mathbf{\Phi}^T \mathbf{K}_1(\boldsymbol{\varphi}_i)\mathbf{\Phi} \quad , \quad \tilde{\mathbf{K}}_{2,ij} = \mathbf{\Phi}^T \mathbf{K}_2(\boldsymbol{\varphi}_i, \boldsymbol{\varphi}_j)\mathbf{\Phi} \tag{61}$$

With the formulation in (60) the projected internal restoring forces take the form

$$\tilde{\mathbf{g}}(\mathbf{s}) = \mathbf{\Phi}^T \mathbf{g}(\mathbf{\Phi}\mathbf{s}) = \left(\tilde{\mathbf{K}}_0 + \sum_{i=1}^{N} \tilde{\mathbf{K}}_{1,i} s_i + \sum_{i=1}^{N}\sum_{j=1}^{N} \tilde{\mathbf{K}}_{2,ij} s_i s_j \right) \mathbf{s} \tag{62}$$

By introducing the relation for $\mathbf{s}$ in (63) with δ_{ij} to denote the Kronecker delta

$$\mathbf{s} = \sum_{k=1}^{N} \mathbf{i}_k s_k \qquad , \qquad \mathbf{i}_k = \begin{bmatrix} \delta_{1k}, & \delta_{2k}, & \dots & \delta_{Nk} \end{bmatrix}^T \tag{63}$$

the projected restoring forces in (62) can be expanded to a cubic vector polynomial

$$\tilde{\mathbf{g}}(\mathbf{s}) = \sum_{i=1}^{N} \tilde{\mathbf{q}}_{1,i} s_i + \sum_{i=1}^{N}\sum_{j=1}^{N} \tilde{\mathbf{q}}_{2,ij} s_i s_j + \sum_{i=1}^{N}\sum_{j=1}^{N}\sum_{k=1}^{N} \tilde{\mathbf{q}}_{3,ijk} s_i s_j s_k \tag{64}$$

The $\tilde{\mathbf{q}}$ vectors in (64) are constant equivalent force vector coefficients of dimension N×1 defined as

$$\tilde{\mathbf{q}}_{1,i} = \tilde{\mathbf{K}}_0 \mathbf{i}_i, \qquad \tilde{\mathbf{q}}_{2,ij} = \tilde{\mathbf{K}}_{1,i} \mathbf{i}_j, \qquad \tilde{\mathbf{q}}_{3,ijk} = \tilde{\mathbf{K}}_{2,ij} \mathbf{i}_k \tag{65}$$

The co-ordinate products $s_i s_j$ and $s_i s_j s_k$ in (64) remain unchanged when switching the indexes i, j and k. Utilizing this product symmetry enables the number of summations in (64) to be reduced by formulating the vector polynomial as

$$\tilde{\mathbf{g}}(\mathbf{s}) = \sum_{i=1}^{N} \tilde{\mathbf{q}}_{1,i} s_i + \sum_{i=1}^{N}\sum_{j=1}^{i} \tilde{\mathbf{q}}^*_{2,ij} s_i s_j + \sum_{i=1}^{N}\sum_{j=1}^{i}\sum_{k=1}^{j} \tilde{\mathbf{q}}^*_{3,ijk} s_i s_j s_k \tag{66}$$

with the introduced equivalent force vectors

$$\tilde{\mathbf{q}}^*_{2,ij} = \tilde{\mathbf{q}}_{2,ij} + (1-\delta_{ij})\tilde{\mathbf{q}}_{2,ji} \tag{67}$$

$$\tilde{\mathbf{q}}^*_{3,ijk} = \tilde{\mathbf{q}}_{3,ijk} + (\tilde{\mathbf{q}}_{3,jki} + \tilde{\mathbf{q}}_{3,kij})(1-\delta_{ij}\delta_{jk}) - (\tilde{\mathbf{q}}_{3,ikj} + \tilde{\mathbf{q}}_{3,kji} + \tilde{\mathbf{q}}_{3,jik})\varepsilon_{ijk} \tag{68}$$

where ε_{ijk} is a permutation symbol fulfilling the conditions

$$\varepsilon_{ijk} = 1 \quad if \;\; (i,j,k) = (1,2,3) \;\vee\; (2,3,1) \;\vee\; (3,1,2) \tag{69}$$

$$\varepsilon_{ijk} = -1 \quad if \;\; (i,j,k) = (3,2,1) \;\vee\; (2,1,3) \;\vee\; (1,3,2) \tag{70}$$

$$\varepsilon_{ijk} = 0 \quad if \;\; i = j \;\vee\; i = k \;\vee\; j = k \tag{71}$$

Application of the cubic vector polynomial (66) in equation (7), is referred to as the *linear reduced basis formulation* (LRBF). Because the equivalent force vectors are constant, they can be organized before the simulation. Only the reduced co-ordinates vary during the simulations. Evaluating the internal restoring forces using (66) is significantly faster than the usual element by element evaluation.

The amount of vector-scalar products contained in each summation term in (66) is given by the formula

$$T_{\mathrm{x}}(N) = \prod_{i=0}^{\mathrm{x}-1} \frac{N+i}{1+i} \tag{72}$$

Copyright © 2010 John Wiley & Sons, Ltd.

DOI: 10.1002/nme

where x refers to the summation order, which is 3 for the formulation in equation (66). For N modes, the equivalent force vectors in equation (66) are of dimension N×1 and the amount of operations, when evaluating $\tilde{\mathbf{g}}(\mathbf{s})$, accumulates to

$$O_{\text{LRBF}}(N) = N \times \sum_{i=1}^{3} T_i(N) = \frac{11}{6}N^2 + N^3 + \frac{1}{6}N^4 \tag{73}$$

The amount of operations is viewed as a fourth-order polynomial in the number of modes, N. Because the evaluation of $\tilde{\mathbf{g}}(\mathbf{s})$ dominates for an increasing number of modes, the computational time is expected to be proportional to N^4.

4.2. RBF with a Second-Order Taylor basis

Taylor basis is considered next. The procedure is the same as in the LRBF case but with a different result given the quadratic co-ordinate products introduced with the modal derivatives. The projected internal restoring forces in (26) can be written as a fourth order matrix polynomial

$$\begin{aligned}\hat{\mathbf{g}}(s_m) = \Bigg(&\hat{\mathbf{K}}_0 + \sum_{i=1}^{N}\hat{\mathbf{K}}_{1,i}s_i + \sum_{i=1}^{N}\sum_{j=1}^{N}\hat{\mathbf{K}}_{2,ij}s_is_j + \sum_{i=1}^{N}\sum_{j=1}^{N}\sum_{k=1}^{N}\hat{\mathbf{K}}_{3,ijk}s_is_js_k + \\ &\sum_{i=1}^{N}\sum_{j=1}^{N}\sum_{k=1}^{N}\sum_{l=i}^{N}\hat{\mathbf{K}}_{4,ijkl}s_is_js_ks_l\Bigg)\mathbf{s}_T\end{aligned} \tag{74}$$

The matrices $\hat{\mathbf{K}}_0$, $\hat{\mathbf{K}}_1$, $\hat{\mathbf{K}}_{2,ij}$, $\hat{\mathbf{K}}_{3,ijk}$ and $\hat{\mathbf{K}}_{4,ijkl}$ are all constant and of dimension $(\frac{3}{2}N + \frac{1}{2}N^2) \times (\frac{3}{2}N + \frac{1}{2}N^2)$. Given the definition $\partial\boldsymbol{\varphi}_{ij} = \frac{1}{2}(\frac{\partial\boldsymbol{\varphi}_i}{\partial s_j} + \frac{\partial\boldsymbol{\varphi}_j}{\partial s_i})$, the matrices are defined as

$$\hat{\mathbf{K}}_0 = (\boldsymbol{\Phi}_T)^T\mathbf{K}_0\boldsymbol{\Phi}_T \tag{75}$$

$$\hat{\mathbf{K}}_{1,i} = (\boldsymbol{\Phi}_T)^T\mathbf{K}_1(\boldsymbol{\varphi}_i)\boldsymbol{\Phi}_T \tag{76}$$

$$\hat{\mathbf{K}}_{2,ij} = (\boldsymbol{\Phi}_T)^T\left(\mathbf{K}_1\left(\partial\boldsymbol{\varphi}_{ij}\right) + \mathbf{K}_2(\boldsymbol{\varphi}_i, \boldsymbol{\varphi}_j)\right)\boldsymbol{\Phi}_T \tag{77}$$

$$\hat{\mathbf{K}}_{3,ijk} = (\boldsymbol{\Phi}_T)^T\left(\mathbf{K}_2\left(\boldsymbol{\varphi}_i, \partial\boldsymbol{\varphi}_{jk}\right) + \mathbf{K}_2\left(\partial\boldsymbol{\varphi}_{jk}, \boldsymbol{\varphi}_i\right)\right)\boldsymbol{\Phi}_T \tag{78}$$

$$\hat{\mathbf{K}}_{4,ijkl} = (\boldsymbol{\Phi}_T)^T\left(\mathbf{K}_2(\partial\boldsymbol{\varphi}_{ij}, \partial\boldsymbol{\varphi}_{kl}) + \mathbf{K}_2\left(\partial\boldsymbol{\varphi}_{kl}, \partial\boldsymbol{\varphi}_{ij}\right)\right)\boldsymbol{\Phi}_T \tag{79}$$

The expression in (74) is converted into a vector polynomial by introducing the co-ordinate vector $\mathbf{s}_T$ of the form

$$\mathbf{s}_T = \begin{Bmatrix}\mathbf{s}\\ \mathbf{s}_H\end{Bmatrix} = \begin{Bmatrix}\mathbf{s}\\ \mathbf{0}_a\end{Bmatrix} + \begin{Bmatrix}\mathbf{0}_b\\ \mathbf{s}_H\end{Bmatrix} = \sum_{i=1}^{N}\mathbf{i}_is_i + \sum_{i=1}^{N}\sum_{n=1}^{i}\mathbf{i}_{ij}s_is_j \tag{80}$$

where $\mathbf{0}_a$ and $\mathbf{0}_b$ are zero vectors of dimension $\frac{1}{2}(N + N^2)\times 1$ and N×1, respectively. Moreover the vectors $\mathbf{i}_m$ and $\mathbf{i}_{mn}$ are given in the form

$$\mathbf{i}_i = \begin{bmatrix}\delta_{1i} & \delta_{2i} & \dots & \delta_{Ni} & \mathbf{0}_a^T\end{bmatrix}^T \tag{81}$$

$$\mathbf{i}_{ij} = \begin{bmatrix}\mathbf{0}_b^T & \delta_{1i}\delta_{j1} & \delta_{2i}\delta_{j1} & \delta_{2i}\delta_{j2} & \delta_{3i}\delta_{j1} & \delta_{3i}\delta_{j2} & \delta_{3i}\delta_{j3} & \delta_{4i}\delta_{j1} & \dots & \delta_{Ni}\delta_{jN}\end{bmatrix}^T \tag{82}$$

By introducing the formulation in (80) into (74), the following six types of constant equivalent force vectors can be organized as

$$\hat{\mathbf{q}}_{1,i} = \hat{\mathbf{K}}_0\mathbf{i}_i \tag{83}$$

$$\mathbf{q}_{2,ij} = \hat{\mathbf{K}}_{1,i}\mathbf{i}_j + \hat{\mathbf{K}}_0\mathbf{i}_{ij} \tag{84}$$

$$\hat{\mathbf{q}}_{3,ijk} = \hat{\mathbf{K}}_{2,ij}\mathbf{i}_k + \hat{\mathbf{K}}_{1,i}\mathbf{i}_{jk} \tag{85}$$

$$\hat{\mathbf{q}}_{4,ijkl} = \hat{\mathbf{K}}_{3,ijk}\mathbf{i}_l + \hat{\mathbf{K}}_{2,ij}\mathbf{i}_{kl} \tag{86}$$

$$\hat{\mathbf{q}}_{5,ijklm} = \hat{\mathbf{K}}_{4,ijkl}\mathbf{i}_m + \hat{\mathbf{K}}_{3,ijk}\mathbf{i}_{lm} \tag{87}$$

$$\hat{\mathbf{q}}_{6,ijklmn} = \hat{\mathbf{K}}_{4,ijkl}\mathbf{i}_{mn} \tag{88}$$

Copyright © 2010 John Wiley & Sons, Ltd.

DOI: 10.1002/nme

Utilizing the symmetry of the co-ordinate products in (74) enables the restoring forces to be written in on the reduced polynomial vector form

$$\begin{aligned}\hat{\mathbf{g}}(s_p) = &\sum_{i=1}^{N} \mathbf{q}_{1,i} s_i + \sum_{i=1}^{N}\sum_{j=1}^{i} \mathbf{q}^*_{2,ij} s_i s_j + \sum_{i=1}^{N}\sum_{j=1}^{i}\sum_{k=1}^{j} \mathbf{q}^*_{3,ijk} s_i s_j s_k + \\ &\sum_{i=1}^{N}\sum_{j=1}^{i}\sum_{k=1}^{j}\sum_{l=1}^{k} \mathbf{q}^*_{4,ijkl} s_i s_j s_k s_l + \sum_{i=1}^{N}\sum_{j=1}^{i}\sum_{k=1}^{k}\sum_{l=1}^{k}\sum_{m=1}^{l} \mathbf{q}^*_{5,ijklm} s_i s_j s_k s_l s_m + \\ &\sum_{i=1}^{N}\sum_{j=1}^{i}\sum_{k=1}^{j}\sum_{l=1}^{k}\sum_{m=1}^{l}\sum_{n=1}^{m} \mathbf{q}^*_{6,ijklmn} s_i s_j s_k s_l s_m s_n \end{aligned} \tag{89}$$

with $()^*$ denoting the assemblage of the equivalent force vectors adjusted to the symmetry organization. In the following section, the formulation in (89) is referred to as the *Taylor reduced basis formulation* (TRBF). The TRBF can also be written in the more compact matrix format

$$\hat{\mathbf{g}}(s_p) = \hat{\mathbf{Q}}\hat{\mathbf{s}} \tag{90}$$

with the matrix definitions

$$\begin{aligned}\hat{\mathbf{Q}} &= \begin{bmatrix}\hat{\mathbf{q}}^*_{1,1} & \hat{\mathbf{q}}^*_{1,2} & \cdots & \hat{\mathbf{q}}^*_{1,N} & \hat{\mathbf{q}}^*_{2,11} & \hat{\mathbf{q}}^*_{2,21} & \hat{\mathbf{q}}^*_{2,22} & \cdots & \hat{\mathbf{q}}^*_{2,NN} & \hat{\mathbf{q}}^*_{3,111} & \cdots & \hat{\mathbf{q}}^*_{6,NNNNNN}\end{bmatrix} \\ \hat{\mathbf{s}} &= \begin{bmatrix}s_1 & s_2 & \cdots & s_N & s_1 s_1 & s_2 s_1 & s_2 s_2 & \cdots & s_N s_N & s_1 s_1 s_1 & \cdots & s_N s_N s_N s_N s_N s_N\end{bmatrix}^T\end{aligned}$$

The formulation in (90) is used in the numerical simulations presented in the following section. The vector $\hat{\mathbf{s}}$ must be organized in every integration step, whereas $\hat{\mathbf{Q}}$ is constant.

When evaluating the internal restoring forces in the TRBF, the number of operations is taken as the number of operations in (89) plus those from the transformation in (42). For N linear modes and $\frac{1}{2}\left(N + N^2\right)$ modal derivatives, the equivalent force vectors are of dimension $(\frac{3}{2}N + \frac{1}{2}N^2) \times 1$ and the number of operations is evaluated from the polynomial

$$\begin{aligned}O_{\text{TRBF}}(N) &= \left(\frac{3}{2}N + \frac{1}{2}N^2\right) \times \sum_{i=1}^{6} T_i(N) + N \times \left(\frac{3}{2}N + \frac{1}{2}N^2\right) \\ &= \frac{227}{40}N^2 + \frac{553}{120}N^3 + \frac{3829}{1440}N^4 + \frac{7}{8}N^5 + \frac{119}{720}N^6 + \frac{1}{60}N^7 + \frac{1}{1440}N^8\end{aligned} \tag{91}$$

The number of operations in (91) is significantly higher than in (73) for N modes. However, (91) also includes additional $\frac{1}{2}(N + N^2)$ modal derivatives.

In the case where P linear dependent modes appear, the equivalent force vectors will be reduced to be of dimension $(\frac{3}{2}N + \frac{1}{2}N^2 - P) \times 1$. This will reduce the amount of operations in (89) as well. Furthermore, by replacing the transformation matrix $\mathbf{U}$ in (42) by $\check{\mathbf{U}}$ in (59), a further reduction is introduced, because the dimensions of the latter transformation matrix are smaller. The effect is illustrated with an example in section 5.

4.3. Computational Savings

An estimate is made for the relative computational savings achieved if using the TRBF instead of the LRBF. The estimate is taken as the ratio of the number of operations included in the formulations of the internal restoring forces in (89) and (66), respectively. A main portion of the the time integration is spent on the internal restoring forces, which should provide a good estimate.

When considering the ratio between the products in (91) and (73) an equal number of modes should be included. Therefore, $\frac{1}{2}(N + N^2)$ additional modes should be introduced in (73) to account for the modal derivatives implicitly contained in (91). Thus, the ratio between the number of products in (91) and (73) for an infinite number of modes converges toward the value

$$\lim_{N\to\infty} \frac{O_{\text{TRBF}}(N)}{O_{\text{LRBF}}(N_s)} \to \frac{1}{15} \quad , \quad N_s = N + \frac{1}{2}(N + N^2) \tag{92}$$

Copyright © 2010 John Wiley & Sons, Ltd.

DOI: 10.1002/nme

the number of operations is viewed as being reduced to approximately 1/15 using a Taylor basis instead of a linear basis formulation in the limit state. However, because the generation of the transformation matrices in (35)-(37) and the co-ordinate vector $\hat{s}$ in (90) are not included in the relative estimate in (92), the ratio represents a lower bound value for the relative computational time. Furthermore, an important point to stress is that the estimate in (92) is based on the assumptions that no linear dependent modes are present.

5. ILLUSTRATIVE EXAMPLE - SIMPLE FRAME

In the following section the computational time, stability, and precision of the TRBF and the LRBF are considered. For this purpose a simple example with a kinematic nonlinear frame modelled using two-dimensional Euler-Bernoulli beam elements is studied. The simulations are executed on an in-house MATLAB code on a standard PC with an Intel Core I7 3036QM processor with four cores, 2.4 GHz and 8 GB RAM. The code cannot be considered optimized and faster devices further increase the real-time capacity than that which is presented in the following section. However, the result are good indicators of the real-time potential of the formulations applied.

First, cable geometry, loading and other factors are presented. Then, the element formulation and an example of the various equivalent force vectors in the TRBF and LRBF are given. Finally, the simulation results are presented with a focus on precision, stability, and simulation times.

5.1. Frame Geometry and Loading

Figure 3 indicates that a frame of two equally long elements of length l are connected vertically to each other. The horizontal element is referred to as the frame beam and the vertical element as the frame column. Both elements have solid circular cross-sections with diameter D, Young's modulus E, cross sectional area A, second moment of area I and density per length ρ. The frame is simple supported. To enhance the kinematic nonlinear effects, the frame corner is restricted against the horizontal displacements. Furthermore, the beam is loaded by a harmonic line load, p(t), with amplitude, A, of the form

$$p(t) = A \cdot sin(\omega t) \tag{93}$$

In Table I the applied load and frame parameters are presented.

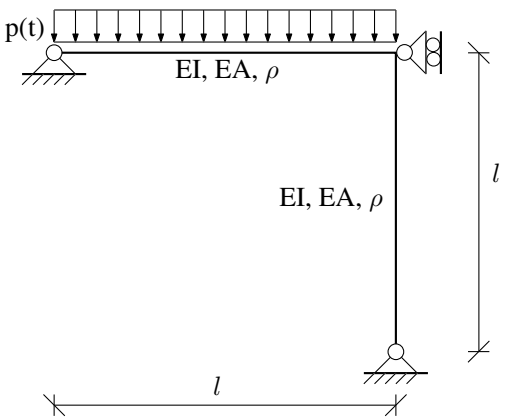

Figure 3. Simple frame.

5.2. Plane Beam Finite Element Formulation

The plane beam element illustrated in Figure 4 is used to model the simple frame. This element is identical to the one used in [23], which presents the full details of the element formulation. In the

Copyright © 2010 John Wiley & Sons, Ltd.

DOI: 10.1002/nme

present study, only a brief description is provided. The element has two nodes with three DOFs at

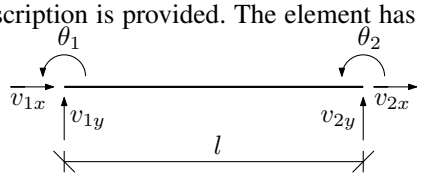

Figure 4. Plane beam element.

each node consisting of the translational DOFs v_{ix} and v_{iy} and the rotational DOFs θ_i, i ϵ [1;2]. The element spans the domain Ω_{el} and is of length l_{el}. To describe the transverse and axial beam deformations, denoted w and u, are used second-order and first-order shape functions, respectively.

The kinematic nonlinear EOM in (4) are organized through the concept of virtual work, such as in [32]

$$\int_{\Omega_{el}} \left(\delta\mathbf{u}^T\rho\ddot{\mathbf{u}} + \delta\mathbf{u}^T d\dot{\mathbf{u}} + \delta\boldsymbol{\varepsilon}^T\boldsymbol{\sigma}\right)\, d\Omega_{el} = \left[\delta\mathbf{u}^T\mathbf{f}\right]_0^l + \int_{\Omega_{el}} \delta\mathbf{u}^T\mathbf{p}\, d\Omega_{el} \tag{94}$$

$\delta()$ represents the virtual components, ρ represents the material density per length unit, d is a material damping parameter analogous to viscosity, $\boldsymbol{\varepsilon}$ represents the work conjugate strain fields, and $\boldsymbol{\sigma}$ represents the generalized stresses. Furthermore the external forces are collected in vectors with $\mathbf{f}$ representing the concentrated forces at the nodes and $\mathbf{p}$ representing the transverse and horizontal line loads along the beam element.

The generalized stresses and work conjugate strains consist of the normal force N, the moment M, the axial strain ε, and the curvature κ. Using the previously introduced Lagrange strain measures for plane beams

$$\boldsymbol{\varepsilon} = \begin{Bmatrix} \varepsilon \\ \kappa \end{Bmatrix} = \begin{Bmatrix} u' + \frac{1}{2}(w')^2 \\ w'' \end{Bmatrix} \tag{95}$$

with $()' = \partial()/\partial x$, the element local internal restoring forces can be derived as

$$\mathbf{g}_{el}(\mathbf{v}_{el}) = \int_{\Omega_{el}} \left(\mathbf{B}^T\mathbf{D}\mathbf{B} + \frac{EA}{2}\left(\mathbf{B}_\epsilon^T\mathbf{v}^T\mathbf{G} + 2\mathbf{G}\mathbf{v}\mathbf{B}_\epsilon + \mathbf{G}\mathbf{v}\mathbf{v}^T\mathbf{G}\right)\right)_{el} \mathbf{v}_{el}\, d\Omega_{el} \tag{96}$$

where $\mathbf{D}$ is a material stiffness matrix and $\mathbf{v}$ is the element local DOF vector. Furthermore, $\mathbf{B}$, $\mathbf{B}_\varepsilon$, and $\mathbf{G}$ are strain interpolation matrices originating from the strain measures u', w'', and $\frac{1}{2}(w')^2$, respectively. Furthermore, the matrix $\mathbf{G}$ is symmetric.

The global internal restoring forces are found by introducing the transformation matrix $\tilde{\mathbf{L}}_{el}$ that relates the local DOF vector $\mathbf{v}_{el}$ with the global DOF vector $\mathbf{V}$.

$$\mathbf{v}_{el} = \tilde{\mathbf{L}}_{el}\mathbf{V} = \tilde{\mathbf{V}}_{el} \tag{97}$$

Inserting (97) into (96) and adding all local element contributions together the internal restoring forces on the global form, with nel denoting the number of elements, are given as

$$\mathbf{g}(\mathbf{V}) = \sum_{el=1}^{nel} \tilde{\mathbf{L}}_{el}^T \int_{\Omega_{el}} \left(\mathbf{B}^T\mathbf{D}\mathbf{B} + \frac{EA}{2}\left(\mathbf{B}_\epsilon^T\tilde{\mathbf{V}}^T\mathbf{G} + 2\mathbf{G}\tilde{\mathbf{V}}\mathbf{B}_\epsilon\right) + \frac{EA}{2}\mathbf{G}\tilde{\mathbf{V}}\tilde{\mathbf{V}}^T\mathbf{G}\right)_{el} \tilde{\mathbf{V}}_{el}\, d\Omega_{el} \tag{98}$$

The formulation in (98) is in the same form as in (5) with the following matrix definitions

$$\mathbf{K}_0 = \sum_{el=1}^{nel} \tilde{\mathbf{L}}_{el}^T \int_{\Omega_{el}} \left(\mathbf{B}^T\mathbf{D}\mathbf{B}\right)_{el} \tilde{\mathbf{L}}_{el}\, d\Omega_{el} \tag{99}$$

$$\mathbf{K}_1(\mathbf{V}) = \sum_{el=1}^{nel} \tilde{\mathbf{L}}_{el}^T \int_{\Omega} \frac{EA}{2}\left(\mathbf{B}_\epsilon^T\tilde{\mathbf{V}}^T\mathbf{G} + 2\mathbf{G}\tilde{\mathbf{V}}\mathbf{B}_\epsilon\right)_{el} \tilde{\mathbf{L}}_{el}\, d\Omega_{el} \tag{100}$$

$$\mathbf{K}_2(\mathbf{V},\mathbf{V}) = \sum_{el=1}^{nel} \tilde{\mathbf{L}}_{el}^T \int_{\Omega_{el}} \frac{EA}{2}\left(\mathbf{G}\tilde{\mathbf{V}}\tilde{\mathbf{V}}^T\mathbf{G}\right)_{el} \tilde{\mathbf{L}}_{el}\, d\Omega_{el} \tag{101}$$

Copyright © 2010 John Wiley & Sons, Ltd.

DOI: 10.1002/nme

From (99)-(101) the equivalent force vectors are organized.

5.3. Taylor Equivalent Force Vectors

On the basis of the introduced stiffness matrices in (99)-(101) the equivalent force vectors defined in (83)-(88) are identified. Using the definitions

$$\tilde{\mathbf{\Phi}}_{T,el} = \tilde{\mathbf{L}}_{el}\mathbf{\Phi}_T \quad , \quad \tilde{\boldsymbol{\varphi}}_{i,el} = \tilde{\mathbf{L}}_{el}\boldsymbol{\varphi}_i \tag{102}$$

the equivalent force vectors are identified as

$$\hat{\mathbf{q}}_{1,i} = \sum_{el=1}^{nel} \tilde{\mathbf{\Phi}}_{T,el}^T \int_{\Omega_{el}} \left(\mathbf{B}^T\mathbf{D}\mathbf{B}\tilde{\mathbf{\Phi}}_T \right)_{el} \mathbf{i}_i \, d\Omega_{el} \tag{103}$$

$$\hat{\mathbf{q}}_{2,ij} = \sum_{el=1}^{nel} \tilde{\mathbf{\Phi}}_{T,el}^T \int_{\Omega_{el}} \left(\frac{EA}{2} \left(\mathbf{B}_\epsilon^T \tilde{\boldsymbol{\varphi}}_i^T \mathbf{G} + 2\mathbf{G}\tilde{\boldsymbol{\varphi}}_i \mathbf{B}_\epsilon \right) \tilde{\mathbf{\Phi}}_T \mathbf{i}_j + \mathbf{B}^T\mathbf{D}\mathbf{B}\tilde{\mathbf{\Phi}}_T \mathbf{i}_{ij} \right)_{el} d\Omega_{el} \tag{104}$$

$$\begin{aligned} \hat{\mathbf{q}}_{3,ijk} = \sum_{el=1}^{nel} \tilde{\mathbf{\Phi}}_{T,el}^T \int_{\Omega_{el}} \frac{EA}{2} \Big(& \left(\mathbf{B}_\epsilon^T \tilde{\boldsymbol{\varphi}}_i^T \mathbf{G} + 2\mathbf{G}\tilde{\boldsymbol{\varphi}}_i \mathbf{B}_\epsilon \right) \tilde{\mathbf{\Phi}}_T \mathbf{i}_{jk} + \\ & \left(\mathbf{B}_\epsilon^T \partial\tilde{\boldsymbol{\varphi}}_{ij}^T \mathbf{G} + 2\mathbf{G}\partial\tilde{\boldsymbol{\varphi}}_{ij}\mathbf{B}_\epsilon + \mathbf{G}\tilde{\boldsymbol{\varphi}}_i \tilde{\boldsymbol{\varphi}}_j^T \mathbf{G} \right) \tilde{\mathbf{\Phi}}_T \mathbf{i}_k \Big)_{el} d\Omega_{el} \end{aligned} \tag{105}$$

$$\begin{aligned} \hat{\mathbf{q}}_{4,ijkl} = \sum_{el=1}^{nel} \tilde{\mathbf{\Phi}}_{T,el}^T \int_{\Omega_{el}} \frac{EA}{2} \Big(& \mathbf{G}(\tilde{\boldsymbol{\varphi}}_i \partial\tilde{\boldsymbol{\varphi}}_{jk}^T + \partial\tilde{\boldsymbol{\varphi}}_{jk}\tilde{\boldsymbol{\varphi}}_i^T)\mathbf{G}\tilde{\mathbf{\Phi}}_T \mathbf{i}_l + \\ & \left(\mathbf{B}_\epsilon^T \partial\tilde{\boldsymbol{\varphi}}_{ij}^T \mathbf{G} + 2\mathbf{G}\partial\tilde{\boldsymbol{\varphi}}_{ij}\mathbf{B}_\epsilon + \mathbf{G}\tilde{\boldsymbol{\varphi}}_i \tilde{\boldsymbol{\varphi}}_j^T \mathbf{G} \right) \tilde{\mathbf{\Phi}}_T \mathbf{i}_{kl} \Big)_{el} d\Omega_{el} \end{aligned} \tag{106}$$

$$\begin{aligned} \hat{\mathbf{q}}_{5,ijklm} = \sum_{el=1}^{nel} \tilde{\mathbf{\Phi}}_{T,el}^T \int_{\Omega_{el}} \frac{EA}{2} \mathbf{G} \Big(& \left(\partial\tilde{\boldsymbol{\varphi}}_{ij}\partial\tilde{\boldsymbol{\varphi}}_{kl}^T + \partial\tilde{\boldsymbol{\varphi}}_{kl}\partial\tilde{\boldsymbol{\varphi}}_{ij}^T \right) \mathbf{G}\tilde{\mathbf{\Phi}}_T \mathbf{i}_m + \\ & (\tilde{\boldsymbol{\varphi}}_i \partial\tilde{\boldsymbol{\varphi}}_{jk}^T + \partial\tilde{\boldsymbol{\varphi}}_{jk}\tilde{\boldsymbol{\varphi}}_i^T)\mathbf{G}\tilde{\mathbf{\Phi}}_T \mathbf{i}_{lm} \Big)_{el} d\Omega_{el} \end{aligned} \tag{107}$$

$$\hat{\mathbf{q}}_{6,ijklmn} = \sum_{el=1}^{nel} \tilde{\mathbf{\Phi}}_{T,el}^T \int_{\Omega_{el}} \frac{EA}{2} \left(\mathbf{G} \left(\partial\tilde{\boldsymbol{\varphi}}_{ij}\partial\tilde{\boldsymbol{\varphi}}_{kl}^T + \partial\tilde{\boldsymbol{\varphi}}_{kl}\partial\tilde{\boldsymbol{\varphi}}_{ij}^T \right) \mathbf{G}\tilde{\mathbf{\Phi}}_T \right)_{el} \mathbf{i}_{mn} \, d\Omega_{el} \tag{108}$$

The equivalent force vectors in (103)-(108) are evaluated and then organized into symmetry force vectors $\hat{\mathbf{q}}^*$ as introduced in equation (89). The present authors use a simple algorithm for this purpose.

The equivalent force vectors defined in (65) for the LRBF are given as the terms in (103)-(105) with $\mathbf{\Phi}_T$ replaced by $\mathbf{\Phi}$, and $\partial\tilde{\boldsymbol{\varphi}}_{ij}$ and $\mathbf{i}_{ij}$ set to zero.

5.4. Secant stiffness of Differentiated Form

To determine the modal derivatives from the equations in (54), the secant stiffness matrix, is required and differentiated with respect to the reduced co-ordinate s_j. The secant stiffness is given as the sum of the stiffness matrices in (99)-(101)

$$\mathbf{K}_s(\mathbf{V}) = \sum_{el=1}^{nel} \tilde{\mathbf{L}}_{el}^T \int_{\Omega_{el}} \left(\mathbf{B}^T\mathbf{D}\mathbf{B} + \frac{EA}{2} \left(\mathbf{B}_\epsilon^T \tilde{\mathbf{V}}^T \mathbf{G} + 2\mathbf{G}\tilde{\mathbf{V}}\mathbf{B}_\epsilon + \mathbf{G}\tilde{\mathbf{V}}\tilde{\mathbf{V}}^T\mathbf{G} \right) \right)_{el} \tilde{\mathbf{L}}_{el} \, d\Omega_{el}$$

Differentiating this equation with respect to s_j results in the formulation

$$\frac{\partial \mathbf{K}_s(\mathbf{V})}{\partial s_j} = \sum_{el=1}^{nel} \tilde{\mathbf{L}}_{el}^T \int_{\Omega_{el}} \frac{EA}{2} \left(\mathbf{B}_\epsilon^T \frac{\partial\tilde{\mathbf{V}}}{\partial s_j}^T \mathbf{G} + 2\mathbf{G}\frac{\partial\tilde{\mathbf{V}}}{\partial s_j}\mathbf{B}_\epsilon + \mathbf{G} \left(\frac{\partial\tilde{\mathbf{V}}}{\partial s_j}\tilde{\mathbf{V}}^T + \tilde{\mathbf{V}}\frac{\partial\tilde{\mathbf{V}}}{\partial s_j}^T \right) \mathbf{G} \right)_{el} \tilde{\mathbf{L}}_{el} \, d\Omega_{el}$$

Copyright © 2010 John Wiley & Sons, Ltd.

DOI: 10.1002/nme

with the displacement vector of the differentiated form given as

$$\begin{aligned}\frac{\partial \mathbf{V}(s_l)}{\partial s_k} =& \frac{\partial}{\partial s_k}\left(\sum_{i=1}^{N}\boldsymbol{\varphi}_i s_i + \frac{1}{2}\sum_{i=1}^{N}\sum_{j=1}^{N}\left(\frac{\partial \boldsymbol{\varphi}_i}{\partial s_j} + \frac{\partial \boldsymbol{\varphi}_j}{\partial s_i}\right) s_i s_j\right) \\ =& \boldsymbol{\varphi}_k + \sum_{i=1}^{N}\left(2\frac{\partial \boldsymbol{\varphi}_i}{\partial s_k} + \frac{\partial \boldsymbol{\varphi}_k}{\partial s_i}\right) s_i + \frac{1}{2}\sum_{i=1}^{N}\sum_{j=1}^{N}\left(\frac{\partial^2 \boldsymbol{\varphi}_i}{\partial s_j \partial s_k} + \frac{\partial^2 \boldsymbol{\varphi}_j}{\partial s_i \partial s_k}\right) s_i s_j \end{aligned} \tag{109}$$

From the content of (109), the differentiated secant stiffness is viewed as implicitly dependent on the modal derivatives in the case that a nonzero displacement field is introduced, that is, $s_i \neq 0$. In contrast, if $s_i = 0$, the secant stiffness is only a function of the linear modes, $\boldsymbol{\varphi}_k$.

5.5. *Case Validation of the Simple Frame*

Whether the simple frame presented in section 5.1 displays sufficiently nonlinear behavior to be considered a relevant case study for testing, the precision and computational speed of the TRBF was determined. For this determination the linear and nonlinear responses of the simple frame are compared. The beam element used for this purpose was tested and validated against a commercial finite element program in [23].

Figure 5 plots the linear and nonlinear responses to the transverse center deformation in the frame beam. The responses are based on a finite element model using 20 elements to model both the frame beam and the column. Time integration is conducted using the implicit Newmark scheme and the explicit CDM scheme. Both time integration schemes are implemented in linear and nonlinear versions. The four responses represent the linear Newmark response (LN), the nonlinear Newmark response (NN), the linear CDM response (LC), and the nonlinear CDM response (NC). All simulations are performed with a time step $\Delta t = 4.5 \cdot 10^{-5}$ s, and a ten-second period is considered. Furthermore, the integration parameters used in the Newmark scheme correspond to the *average acceleration* case.

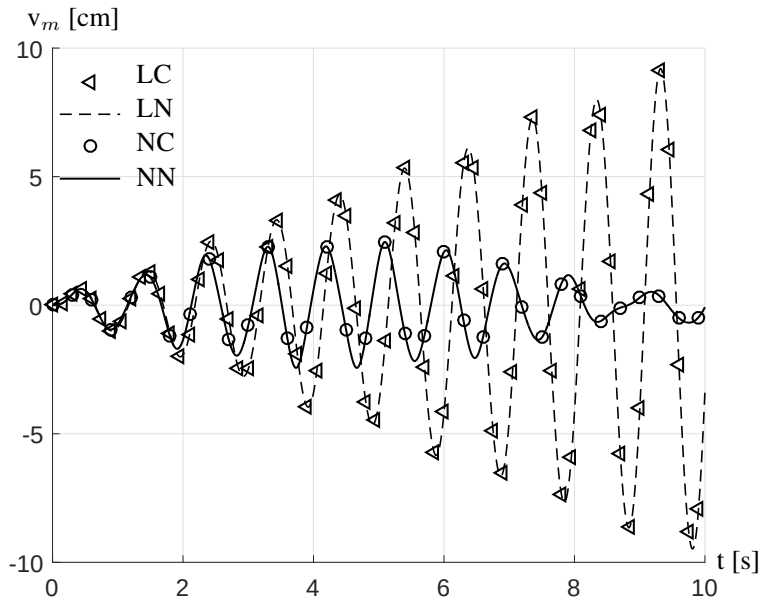

Figure 5. Transverse deformation of the frame beam midpoint using linear Newmark (LN), linear CDM (LC), nonlinear Newmark (NN) and nonlinear CDM (NC) integration schemes.

From the plot in Figure 5, the linear responses are observed to be identical, as are the nonlinear responses. Furthermore, the linear and nonlinear responses are viewed as significantly different. In the linear case, the amplitude appears to grow unbounded, whereas the amplitude is bounded in the

Copyright © 2010 John Wiley & Sons, Ltd.

DOI: 10.1002/nme

nonlinear case and reaches its maximum after approximately five seconds. The smaller amplitude in the nonlinear response compared with the linear response indicates an increasing stiffness attributable to the frame deformation. The stiffness increase also increases the frequency which causes the maxima and minima of the nonlinear response to be "ahead of" the linear maxima and minima. Altogether, the nonlinear behavior of the system is significant and the frame is considered a relevant case study.

5.6. Precision and Stability of Reduced Basis Formulations

In the following section, the LRBF and TRBF, as presented in section 4, are used to analyze the simple frame with a focus on precision and stability. For this purpose, implementing the reduced basis formulations in the CDM integration scheme, is selected. The argument for selecting an explicit scheme is that it is simple to implement and equilibrium iterations are avoided.

When executing the simulations using the TRBF, always including all of the modal derivatives associated with the N included linear modes, is selected. *Associated modal derivatives* means all of the terms $(\partial\boldsymbol{\varphi}_i/\partial s_j + (1-\delta_{ij})\partial\boldsymbol{\varphi}_j/\partial s_i)$ for i, j ϵ [1;N] $\wedge$ i $\geq$ j. Therefore, in the event that N linear modes are included in the basis, then adding one additional linear mode increases the number of modes by the number N+2 .

First, the precision of the TRBF and the LRBF is evaluated by considering the transverse deformation of the frame beam midpoint. For this purpose, the FEM model introduced in the previous section is used.

In Figure 6, three responses are plotted on the basis on the TRBF containing one, three, and six linear modes. The numbers at the end of the figure legends refer to the number of linear modes included. The LRBF responses are found to be identical with the TRBF responses. Therefore, only a single LRBF response including six linear modes and the associated modal derivatives is included in the figure. To check the precision of the reduced basis formulations the NC solution presented in Figure 5, is also plotted.

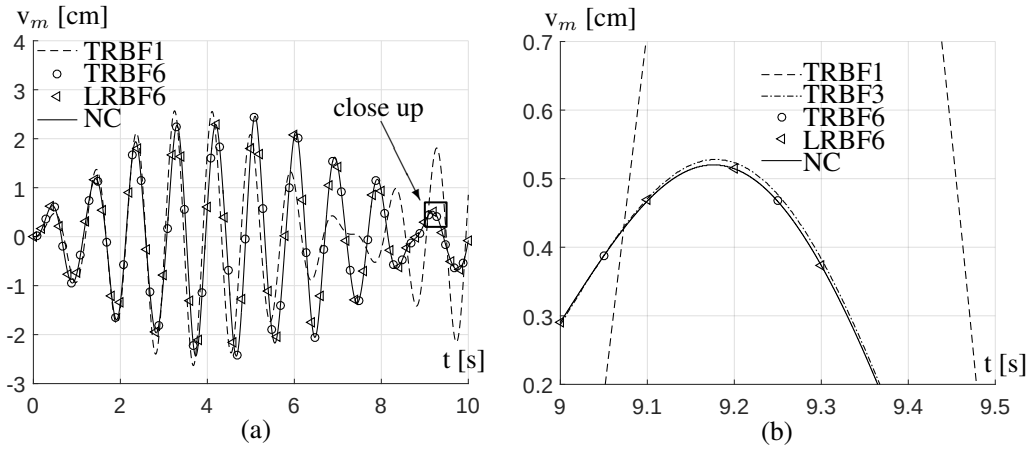

Figure 6. Transverse deformation of beam midpoint considering (a) a 10 second interval and (b) a close up.

The TRBF1 curve is observed to diverge significantly from the remaining responses as time elapses because it does not contain a sufficient number of modes to represent the nonlinear solution. However, the TRBF curves are observed to rapidly converge towards the NC solution as the number of modes increase. A close-up of Figure 6b shows that the TRBF is more or less identical with the NC solution for three or more linear modes. Thus, the conclusion is made that the TRBF and LRBF exhibit equal precision and that they work as intended.

The simulation times of the TRBF6, the LRBF6, and NC responses were 0.7 s, 13.4 s, and 559.5 s, respectively. Thus, in the given case, the TRBF is approximately 20 times faster than the LRBF and approximately 800 times faster than the NC algorithm. The simulations were executed with the time step magnitudes $\Delta t_{\text{TRBF}} = 10^{-3}$ s, $\Delta t_{\text{LRBF}} = 10^{-4}$ s and $\Delta t_{\text{NC}} = 4.5 \cdot 10^{-5}$ s. Increasing the time step magnitudes for the NC algorithm and the LRBF algorithm, resulted in instability.

Copyright © 2010 John Wiley & Sons, Ltd.

DOI: 10.1002/nme

However, the time step of the TRBF could be further increased up to a magnitude of Δt=28·10^{-3} s, before instability occurred. However, the further increase in time step magnitude resulted in response deviations. From this observation it appears that the TRBF exhibits significantly higher stability than the other algorithms. The immediate explanation for this view is that the TRBF is transformed into the linear co-ordinate system of equations in (44). This system of equations only represent the frequencies of the linear modes, which are usually lower than the frequencies of the modal derivatives.

A more in-depth analysis of the stability of the TRBF and the LRBF are presented in Figure 7, which indicates the maximum allowed time step magnitudes, Δt_{TRBF} and Δt_{LRBF}, before instability occurs as a function of the frequencies, ω_{L} and ω_{H}, given in the unit Hz. The former frequency refers to the highest frequency associated with the linear modes of the system, and ω_{H} refers to the highest frequency associated with the modal derivatives in the system. These frequencies can be evaluated directly using the applied FEM program or by Rayleigh's quotient as

$$\omega_L^2 = \frac{\boldsymbol{\varphi}_i^T \mathbf{K}_0 \boldsymbol{\varphi}_i}{\boldsymbol{\varphi}_i^T \mathbf{M} \boldsymbol{\varphi}_i} \quad , \quad \omega_H^2 = \frac{\partial \boldsymbol{\varphi}_{ij}^T \mathbf{K}_0 \partial \boldsymbol{\varphi}_{ij}}{\partial \boldsymbol{\varphi}_{ij}^T \mathbf{M} \partial \boldsymbol{\varphi}_{ij}} \tag{110}$$

For simplicity, only a single linear mode and its associated modal derivative are included in the analysis.

Two analytical stability limits, Δt_{L} and Δt_{H}, are also plotted in Figure 7. These limits are taken as the stability requirement for the CDM method in the linear case, see e.g. [33], with the frequencies in (110) inserted with the unit Hz

$$\Delta t_{\mathrm{L}} = \frac{1}{\pi \omega_{\mathrm{L}}} \quad , \quad \Delta t_{\mathrm{H}} = \frac{1}{\pi \omega_{\mathrm{H}}} \tag{111}$$

To investigate the stability of the algorithms for a wide range of frequencies, the mass was scaled during the analysis. Furthermore a time interval of 100 s was used for each frequency "state" considered.

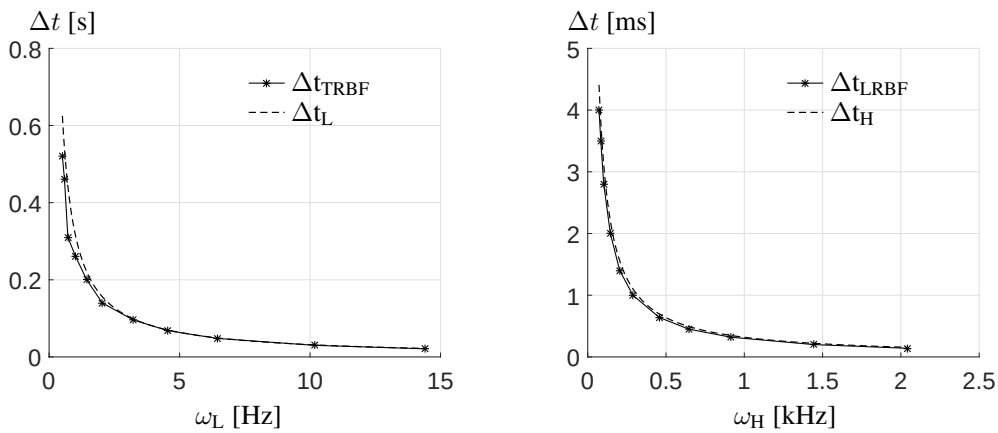

Figure 7. Stability Curves for the TRBF (left) and the LRBF (right).

From the left plot in Figure 7 the time step applied in the TRBF, Δt_{TRBF}, is viewed as having the same order of magnitude as the analytical time step, Δt_{L}. In particular for frequencies $\omega_{\mathrm{L}} > 2.5$ Hz the Δt_{TRBF} curve and the Δt_{L} curve are very close, with the former curve deviating by a maximum of 10 percent. For $\omega_{\mathrm{L}} < 2.5$ Hz, the deviation between the curves is slightly more significant, with a maximum relative deviation of 30 percent for ω_{L} =0.72 Hz, corresponding to the third mark from the left. The time step of the LRBF, Δt_{TRBF}, shown on the right plot in Figure 7, is viewed as in the same order of magnitude as the analytical time step Δt_{L} on basis of the frequency of the modal derivatives. The relative deviation between the curves is in the 8-10 percent interval for the frequency domain considered.

Copyright © 2010 John Wiley & Sons, Ltd.

DOI: 10.1002/nme

The observations indicate that the stability of the TRBF is independent of the included modal derivative. Furthermore, an approximate magnitude for the ratio between the time step magnitudes is given as the ratio between the two analytical stability limits

$$\frac{\Delta t_{\text{TRBF}}}{\Delta t_{\text{LRBF}}} \approx \frac{\Delta t_{\text{L}}}{\Delta t_{\text{H}}} = \frac{\omega_H}{\omega_L} \tag{112}$$

As indicated by the magnitudes of the frequencies in Figure 7, that $\omega_H \gg \omega_L$ is not unlikely. Thus, potentially the time steps applied in the TRBF can be significantly increased compared with when using, for instance, the LRBF or the NC algorithm. In the given case the frequency of the sixth linear mode was ω_6 = 10.76 Hz, which corresponds to at time step stability limit of magnitude

$$\Delta t_{\text{lim}} = \frac{1}{\pi \cdot 10.76 \text{ Hz}} = 30 \cdot 10^{-3} \text{ s} \tag{113}$$

The time step magnitude in (113) is close to the above reported stability limit for the TRBF.

5.7. Real-time Simulations

Next, a more in-depth analysis of the simulation times using the TRBF and LRBF are considered for a varying number of modes. In this context, stressing that the response precision is not in focus, is important. The analysis is intended to provide a general idea of the real-time capacity of the presented methods. Furthermore, for simplicity, ignoring the apparent higher stability properties of the TRBF compared with the LRBF, with respect to time step magnitudes, is chosen. Thus, the comparison of the methods is based on equal time step magnitudes.

Two cases are considered in the analysis. In the first case the present frame structure including linear dependent modes is considered. During the analysis it was found that for seven or more linear modes, some of the modal derivatives became linear dependent. In the second case an idealised frame without linear dependent modes are considered. It was possible to 'remove' the linear dependencies by adjusting a tolerance applied in the simulations. The point of considering a case without linear dependent modes, is to have an idea of the full potential of the TRBF. It is expected, that for larger structures with increased complexity, a higher number of modes can be included, before linear dependencies are introduced. This is supported by the fact, that in [23] the first linear dependent mode was already introduced for three linear modes, considering a simple horizontal cable. It is therefore valid to consider the real-time potential of the TRBF method when no linear dependencies exist.

Figure 8a plots the time spent on simulating the ten-second long response of the considered frame as a function of the sum of linear modes and modal derivatives, $N_S = \frac{3}{2}N + \frac{1}{2}N^2$. The horizontal dashed line represents the simulation time. Result points below this line represent real-time simulations, whereas the result points above the line exceed the real-time execution. All simulations are executed with a time step magnitude of Δt=10^{-3} s, because it is a commonly applied time step magnitude in hybrid testing, such as in [5,6,34,35]. However, that the time step depends on the structure considered, should be stressed. To keep simulations stable with the given time step, the density of the frame was continuously increased when increasing the modes to lower the frequencies of the system.

Three curves are shown in Figure 8a; one referring to simulations with the LRBF, t_{LRBF}, and two representing the simulation times, when using the TRBF, referred to as t^*_{TRBF} and t_{TRBF}, respectively. The t^*_{TRBF} curve represents the simple frame including the linear dependent modes, whereas the t_{TRBF} curve represents the case without linear dependent modes. The marks a, b and c in Figure 8a represent the equivalent points of the two curves, i.e. the points with the same number of modes. However, in the t^*_{TRBF} curve, the linear dependent modes are not included in the counting, and the curve is therefore shifted towards the left compared to the t_{TRBF} curve. Furthermore, as discussed in the end of section 4.2, the computational time, when using the TRBF, is smaller when linear dependencies are included. For seven linear modes, two linear dependent modal derivatives exist. This is increased to twenty-eight linear dependent modes for twelve linear modes (point a).

Copyright © 2010 John Wiley & Sons, Ltd.

DOI: 10.1002/nme

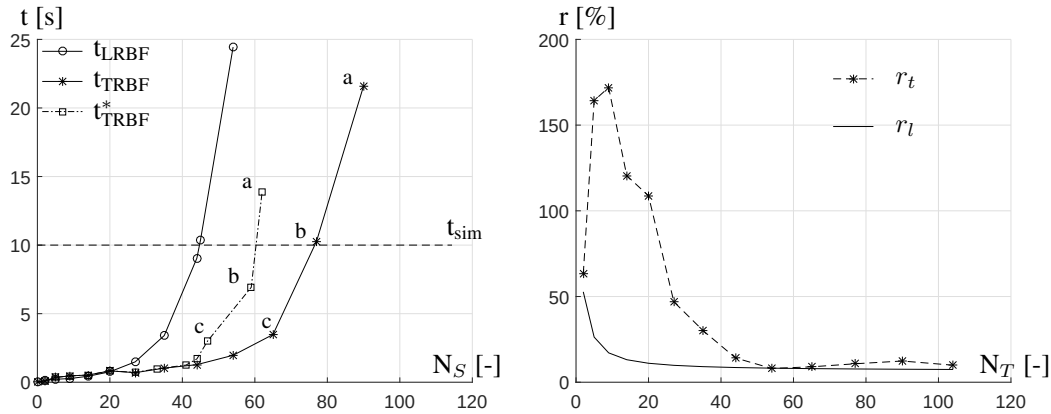

Figure 8. Simulation time using Taylor formulation, t_{TRBF}, and symmetry formulation, t_{LRBF}, as a function of the sum of the number of linear modes and modal derivatives, N_s.

Thus, a rapid increase in the number of linear dependent modes exist. This must be due to the simple structural system considered.

The simulation times from Figure 8a are viewed as a nonlinear function of the number of modes. This observation is expected because the number of operations involved in the evaluation of the internal restoring forces in (66) and (89) is a nonlinear function of the number of modes. The t_{LRBF} curve exceeds the real-time limit that goes from 44 to 45 modes, the t^*_{TRBF} curve exceeds the real-time limit that goes from 59 to 62 modes, and the t_{TRBF} curve exceeds the real-time limit that goes from 65 to 77 modes. The 44 and 59 modes as real-time capacities correspond to a relative modal increase of 34 percent when using the TRBF compared with the LRBF. Considering the 44 and 65 modes as the real-time capacities, correspond to a relative modal increase of 45 percent.

The simulation times presented in Figure 8a indicate that the horizontal distance between curves, t_{LRBF} and t_{TRBF}, keeps increasing when going beyond the real-time limit, t_{sim}. Thus, in a sense an unresolved time reduction potential is present. Therefore, implementing the algorithms on faster devices makes it possible to include further modes in real-time simulations and to increasingly utilize the time reduction potential of the Taylor basis. The gradient of the t^*_{TRBF} curve, on the other hand, is seen to increase faster than the other curves. This is because the number of linear dependent modes increases.

Figure 8b plots the relative simulation time, r_t, and the lower bound estimate for the relative time, r_l, which was introduced previously. These variables are defined as

$$r_t = \frac{t_{\text{TRBF}}(N_s)}{t_{\text{LRBF}}(N_s)} \quad , \quad r_l = \frac{O_{\text{TRBF}}(N_s)}{O_{\text{LRBF}}(N_s)} \tag{114}$$

To begin to understand the full time reduction potential, the relative simulation times in (114) can be considered. The plot in Figure 8b indicates that the r_t curve initially increases up to nine modes and reaches a maximum value of approximately 170 percent. In other words at this point, the LRBF is much faster than the TRBF. Then, a rapid decrease occurs for an increasing number of modes and continues until reaching a local minima of 7 percent ($\approx$ 1/15) at 54 modes. At this point, the r_t curve is also viewed as intersecting with the r_l curve. Beyond this point, the r_t curve fluctuates slightly; but is observed as remaining in the domain of one order of magnitude, which is slightly higher than the lower bound estimate, r_l.

The initial increase in the r_t curve can be partly explained by the transformations required in the TRBF. The involved transformation operations are relatively significant for a small number of modes and, therefore, significantly increase the ratio. For an increasing number of modes, the evaluation of the internal restoring forces becomes dominant given its nonlinear formulation. This dominance is indicated by the fact that the r_t curve starts to rapidly approach the r_l curve beyond nine modes. The irregular behavior beyond this point is attributed to the fluctuating computational performance.

Copyright © 2010 John Wiley & Sons, Ltd.

DOI: 10.1002/nme

6. CONCLUSION

In the present work the real-time potential of using a Taylor basis on kinematic nonlinear systems was investigated. The advantage of using a Taylor basis is that additional modes can be included as modal derivatives with the corresponding reduced co-ordinates given as a product of the linear mode co-ordinates. This relation can be utilized to project a discretized system onto a Taylor basis representing N linear modes and $\frac{1}{2}$(N+N^2) modal derivatives containing only N unknowns. The Taylor basis formulation has been implemented and tested against a former arranged linear basis method applicable for real-time simulations. The tests showed that the Taylor basis improves the efficiency of the simulations significantly. In a real-time analysis of a nonlinear frame, the number of modes in the Taylor basis could be increased by more than thirty percent, compared with the usual linear basis, with a time step of magnitude Δt $= 10^{-3}$ s on a standard PC. Furthermore, the Taylor basis exhibits much higher stability than the linear basis method. A simple analysis indicated that an approximate magnitude for the ratio between the time steps applied when using a Taylor basis and a linear basis method, is given as the ratio between the frequencies of the modal derivatives and the linear modes included in the model. Because the frequencies of the modal derivatives are typically significant higher than the linear mode frequencies, this difference potentially allows for a significantly higher time step to be applied with a Taylor basis. By utilizing this stability improvement in the analysis of the nonlinear frame, the computational time was shown to be reduced by one order of magnitude if the Taylor basis was used instead of the linear basis formulation.

A. TRANSFORMATION OF THE TAYLOR-BASED EQUATIONS OF MOTION

In the following appendix it is illustrated how the EOM projected onto the Taylor basis is transformed from the ($\mathbf{s}_T$, $\dot{\mathbf{s}}_T$, $\ddot{\mathbf{s}}_T$) co-ordinates to the ($\mathbf{s}$, $\dot{\mathbf{s}}$, $\ddot{\mathbf{s}}$) co-ordinates. The starting point is the system of equations in (23)

$$\hat{\mathbf{m}}\ddot{\mathbf{s}}_T + \hat{\mathbf{c}}\dot{\mathbf{s}}_T + \hat{\mathbf{g}}(\mathbf{s}_T) = \hat{\mathbf{f}}(t) \tag{115}$$

For the purpose, two matrices are introduced

$$\mathbf{H} = \begin{bmatrix} \mathbf{I} \\ \mathbf{0} \end{bmatrix}, \quad \mathbf{E}_{ij} = \mathbf{E}_{ji}^T = \begin{bmatrix} \delta_{1i}\delta_{j1} & \delta_{1i}\delta_{j2} & \delta_{1i}\delta_{j3} & \dots & \delta_{1i}\delta_{jN} \\ \delta_{2i}\delta_{j1} & \delta_{2i}\delta_{j2} & \delta_{2i}\delta_{j3} & \dots & \delta_{2i}\delta_{jN} \\ . & . & . & \dots & . \\ \delta_{Ni}\delta_{j1} & \delta_{Ni}\delta_{j2} & \delta_{Ni}\delta_{j3} & \dots & \delta_{Ni}\delta_{jN} \end{bmatrix} \tag{116}$$

with $\mathbf{I}$ being a unit matrix of dimension N$\times$N, $\mathbf{0}$ a zero matrix of dimension $\frac{1}{2}$(N+N^2)$\times$N and $\mathbf{E}_{ij}$ a N$\times$N matrix of the Kronecker's delta products. Furthermore, the vectors

$$\mathbf{e}_{ij} = \begin{Bmatrix} \mathbf{0} \\ \mathbf{d}_{ij} \end{Bmatrix}, \quad \mathbf{d}_{ij} = \begin{Bmatrix} \delta_{1i}\delta_{j1} \\ \delta_{2i}\delta_{j1} \\ \delta_{2i}\delta_{j2} \\ \delta_{3i}\delta_{j1} \\ \delta_{3i}\delta_{j2} \\ . \\ \delta_{Ni}\delta_{jN} \end{Bmatrix} \tag{117}$$

are introduced, with $\mathbf{d}_{ij}$ being a vector of dimension $\frac{1}{2}$(N+N^2)$\times$1, $\mathbf{0}$ a zero vector of dimension N$\times$1 and $\mathbf{e}_{ij}$ a vector of dimension $\left(\frac{3}{2}\mathrm{N} + \frac{1}{2}\mathrm{N}^2\right)\times 1$. The vector $\mathbf{s}$ is also introduced in a sum format written in the following manner

$$\mathbf{s} = \sum_{k=1}^{N} \mathbf{h}_k s_k, \quad \mathbf{h}_k^T = \begin{bmatrix} \delta_{1k} & \delta_{2k} & \dots & \delta_{Nk} \end{bmatrix} \tag{118}$$

Copyright © 2010 John Wiley & Sons, Ltd.

DOI: 10.1002/nme

Given these defined vectors and matrices, the relation between $\mathbf{s}_T$ and $\mathbf{s}$ is written as

$$\begin{aligned}\mathbf{s}_T &= \left(\mathbf{H} + \sum_{i=1}^{N}\sum_{j=1}^{i} \mathbf{e}_{ij}\mathbf{s}^T\mathbf{E}_{ij}\right)\mathbf{s} \\ &= (\mathbf{H} + \mathbf{W}(\mathbf{s}))\,\mathbf{s} \\ &= \mathbf{Q}(\mathbf{s})\mathbf{s}\end{aligned} \tag{119}$$

with the introduced definitions

$$\mathbf{W}(\mathbf{s}) = \sum_{i=1}^{N}\sum_{j=1}^{i} \mathbf{e}_{ij}\mathbf{s}^T\mathbf{E}_{ij} \quad , \quad \mathbf{Q}(\mathbf{s}) = \mathbf{H} + \mathbf{W}(\mathbf{s}) \tag{120}$$

Furthermore, the relation between $\dot{\mathbf{s}}_T$ and $\mathbf{s}$ is

$$\begin{aligned}\dot{\mathbf{s}}_T &= \left(\mathbf{H} + \sum_{i=1}^{N}\sum_{j=1}^{i} \mathbf{e}_{ij}\mathbf{s}^T(\mathbf{E}_{ij} + \mathbf{E}_{ji})\right)\dot{\mathbf{s}} \\ &= (\mathbf{H} + \mathbf{R}(\mathbf{s}))\,\dot{\mathbf{s}} \\ &= \mathbf{U}(\mathbf{s})\dot{\mathbf{s}}\end{aligned} \tag{121}$$

where

$$\mathbf{U}(\mathbf{s}) = \mathbf{H} + \mathbf{R}(\mathbf{s}) \quad , \quad \mathbf{R}(\mathbf{s}) = \sum_{i=1}^{N}\sum_{j=1}^{i} \mathbf{e}_{ij}\mathbf{s}^T(\mathbf{E}_{ij} + \mathbf{E}_{ji}) \tag{122}$$

The $\mathbf{s}_T$ vector is related to the ($\mathbf{s}$, $\dot{\mathbf{s}}$, $\ddot{\mathbf{s}}$) coordinates through the relation

$$\begin{aligned}\ddot{\mathbf{s}}_T &= \mathbf{U}(\mathbf{s})\ddot{\mathbf{s}} + 2\sum_{i=1}^{N}\sum_{j=1}^{i} \mathbf{e}_{ij}\dot{\mathbf{s}}^T\mathbf{E}_{ij}\dot{\mathbf{s}} \\ &= \mathbf{U}(\mathbf{s})\ddot{\mathbf{s}} + 2\mathbf{P}(\dot{\mathbf{s}})\dot{\mathbf{s}}\end{aligned} \tag{123}$$

where

$$\mathbf{P}(\dot{\mathbf{s}}) = \sum_{i=1}^{N}\sum_{j=1}^{i} \mathbf{e}_{ij}\dot{\mathbf{s}}^T\mathbf{E}_{ij} \tag{124}$$

Finally the variation $\delta\mathbf{s}_T$ can be related using the expression

$$\delta\mathbf{s}_T = \mathbf{U}(\mathbf{s})\delta\mathbf{s} \tag{125}$$

Introducing the sum formulation in (118) into the definitions for the matrices $\mathbf{W}(\mathbf{s})$, $\mathbf{R}(\mathbf{s})$ and $\mathbf{P}(\dot{\mathbf{s}})$ enables them to be written in a more compact form as

$$\mathbf{W}(\mathbf{s}) = \sum_{k=1}^{N}\mathbf{A}_k s_k, \quad \mathbf{R}(\mathbf{s}) = \sum_{k=1}^{N}\mathbf{B}_k s_k, \quad \mathbf{P}(\dot{\mathbf{s}}) = \sum_{k=1}^{N}\mathbf{A}_k \dot{s}_k \tag{126}$$

with the constant matrices

$$\mathbf{A}_k = \sum_{i=1}^{N}\sum_{j=1}^{i} \mathbf{e}_{ij}\mathbf{h}_k^T\mathbf{E}_{ij}, \qquad \mathbf{B}_k = \sum_{i=1}^{N}\sum_{j=1}^{i} \mathbf{e}_{ij}\mathbf{h}_k^T(\mathbf{E}_{ij} + \mathbf{E}_{ji}) \tag{127}$$

REFERENCES

Copyright © 2010 John Wiley & Sons, Ltd.

DOI: 10.1002/nme

1. C. Dufour, C. Andrade, J. Blanger, Real-Time Simulation Technologies in Education: a Link to Modern Engineering Methods and Practices, in: Proceedings of the 11th International Conference on Engineering and Technology Education, Vol. 11, Ilhus, Brazil, 2010, pp. 114–118.
2. J. Barbic, D. James, Real-Time Subspace Integration for St. Venant-Kirchhoff Deformable Models, ACM Transactions on Graphics 24 (3) (2005) 982–990. doi:10.1145/1073204.1073300.
3. V. Saouma, D.-H. Kang, G. Haussmann, A Computational Finite-Element Program For Hybrid Simulation, Earthquake Engineering and Structural Dynamics 41 (2012) 375–389. doi:10.1002/eqe.1134.
4. M. Hakuno, M. Shidawara, T. Hara, Dynamic destructive test of a cantilever beam, controlled by an analog-computer (in japanese), Transactions of the Japan Society of Civil Engineers 171 (1969) 1–9.
5. C. Chen, J. M. Ricles, T. L. Karavasilis, Y. Chae, R. Sause, Evaluation of a real-time hybrid simulation system for performance evaluation of structures with rate dependent devices subjected to seismic loading, Engineering Structures 35 (2012) 71–82. doi:10.1016/j.engstruct.2011.10.006.
6. M. Verma, J. Rajasankar, Improved model for real-time substructuring testing system, Engineering Structures 41 (2012) 258–269. doi:10.1016/j.engstruct.2012.03.031.
7. K. Takanashi, M. Nakashima, Real-time substructure tests using hydraulic actuator, Journal Of Engineering Mechanics 113 (1987) 1014–1032.
8. S. A. Mahin, P.-S. B. Shing, C. R. Thewalt, R. D. Hanson, Pseudodynamic test method. Current status and future directions, Journal Of Structural Engineering 115 (8) (1989) 2113–2128.
9. M. Nakashima, H. Kato, E. Takaoka, Development Of Real-Time Pseudo Dynamic Testing, Earthquake Engineering And Structural Dynamics 21 (1992) 79–92. doi:10.1002/eqe.4290210106.
10. T. Horiuchi, M. Nakagawa, M. Sugano, T. Konno, Development Of A Real-Time Hybrid Experimental System With Actuator Delay Compensation, in: Eleventh World Conference on Earthquake Engineering, Acapulco, Mexico, 1996.
11. A. P. Darby, A. Blakeborough, M. S. Williams, Real-time substructure tests using hydraulic actuator, Journal Of Engineering Mechanics 125 (10) (1999) 1133–1139. doi:10.1061/(ASCE)0733-9399(1999)125:10(1133).
12. M. Nakashima, N. Masaoka, Real-Time On-Line Test For MDOF Systems, Earthquake Engineering and Structural Dynamics 28 (4) (1999) 393–420. doi:10.1002/(sici)1096-9845(199904)28:4<393::aid-eqe823>3.0.co;2-c.
13. B. A. Blakeborough, M. S. Williams, A. P. Darby, D. M. Williams, The development of real-time substructure testing, Philosophical Transactions of the Royal Society A: Mathematical, Physical and Engineering Sciences 359 (1786) (2001) 1869–1891. doi:10.1098/rsta.2001.0877.
14. C. Chen, J. M. Ricles, T. M. Marullo, O. Mercan, Real-time hybrid testing using the unconditionally stable explicit CR integration algorithm, Earthquake Engineering & Structural Dynamics 38 (2009) 23–44. doi:10.1002/eqe.838.
15. Y. Chae, K. Kazemibidokhti, J. M. Ricles, Adaptive time series compensator for delay compensation of servo-hydraulic actuator systems for real-time hybrid simulation, Earthquake Engineering And Structural Dynamics 42 (2013) 1697–1715. doi:10.1002/eqe.2294.
16. P. B. Shing, Z. Wei, R.-Y. Jung, E. Stauffer, Nees Fast Hybrid Test System At The Univeristy of Colorado, in: 13th World Conference on Earthquake Engineering, Vancouver, B.C., Canada, 2004.
17. G. Mosqueda, M. Ahmadizadeh, Combined implicit or explicit integration steps for hybrid simulation, Earthquake Engineering & Structural Dynamics 36 (15) (2007) 2325–2343. doi:10.1002/eqe.731.
18. D. Combescure, P. Pegon, Alpha-Operator Splitting time integration technique for pseudodynamic testing Error propagation analysis, Soil Dynamics & Earthquake Engineering 16 (1997) 427–443. doi:Doi:10.1016/s0267-7261(97)00017-1.
19. S.-Y. Chang, Explicit Pseudodynamic Algorithm with Unconditional Stability, Journal Of Engineering Mechanics 128 (9) (2002) 935–947. doi:10.1061/(ASCE)0733-9399(2002)128:9(935).
20. C. Chen, J. M. Ricles, Development of Direct Integration Algorithms for Structural Dynamics Using Discrete Control Theory, Journal of Engineering Mechanics 134 (8) (2008) 676–683. doi:10.1061/(ASCE)0733-9399(2008)134:8(676).
21. P. A. Bonnet, M. S. Williams, A. Blakeborough, Evaluation of numerical time-integration schemes for real-time hybrid testing, Earthquake Engineering & Structural Dynamics 37 (13) (2008) 1467–1490. doi:10.1002/eqe.821.
22. A. Darby, A. Blakeborough, M. Williams, Improved control algorithm for real-time substructure testing, Earthquake Engineering and Structural Dynamics 30 (3) (2001) 431–448.
23. S. Andersen, P. N. Poulsen, Reduction Method For Kinematic Nonlinear Real-time Simulations [UNDER REVIEW], International Journal For Numerical Methods In Engineering.
24. M. Nash, Nonlinear structural dynamics by finite element modal synthesis, Ph.D. thesis, Imperial College, The University of London (1977).
25. S. R. Idelsohn, A. Cardona, Recent advances in reduction methods in nonlinear structural dynamics, in: Proceedings of the Second International Conference on: Recent Advances in Structural Dynamics, Vol. 2, University of Southampton, 1984, pp. 475–482.
26. S. R. Idelsohn, A. Cardona, A Reduction Method for Nonlinear Structural Dynamic Analysis, Computer Methods in Applied Mechanics and Engineering 49 (1985) 253–279.
27. M. Brake, D. Segalman, Nonlinear model reduction of von kármán plates under quasi-steady fluid flow, The American Institute of Aeronautics and Astronautics 48 (2010) 2339–2347.
28. D. J. Inman, Engineering Vibrations, 3rd Edition, Pearson Education, New York, USA, 2009.
29. T. Belytschko, W. K. Liu, B. Moran, Nonlinear Finite Elements for Continua and Structures, 1st Edition, John Wiley & Sons, Chicester, England, 2000.
30. Y. Shi, C. Mei, A finite element time domain modal formulation for large amplitude free vibrations of beams and plates, Journal of Sound and Vibration 193 (2) (1996) 453–464. doi:10.1006/jsvi.1996.0295.

Copyright © 2010 John Wiley & Sons, Ltd.

31. P. M. A. Slaats;, J. de Jongh;, A. A. H. J. Sauren, Model Reduction Tools For Nonlinear Structural Dynamics, Computer and Structures 54 (6) (1995) 1155–1171.
32. R. D. Cook, D. S. Malkus, M. E. Plesha, R. J. Witt, Concepts and Applications Of Finite Element Analysis, 4th Edition, John Wiley & Sons, New York, USA, 1974.
33. A. K. Chopra, Dynamics of Structures: Theory and Application to Earthquake Engineering, 2nd Edition, Vol. 1, Prentice-Hall, 1995.
34. M. Ahmadizadeh, G. Mosqueda, A. M. Reinhorn, Compensation of actuator delay and dynamics for real-time hybrid structural simulation, Earthquake Engineering and Structural Dynamics 37 (2008) 21–42. doi:10.1002/eqe.
35. O. Mercan, J. M. Ricles, Stability and accuracy analysis of outer loop dynamics in real-time pseudodynamic testing of SDOF systems, Earthquake Engineering and Structural Dynamics 36 (May) (2007) 1523–1543. doi:10.1002/eqe.701.

Table I. Frame and load parameters.

Parameter	Unit	Formula	Magnitude
l	m	-	10
E	GPa	-	210
D	m	-	0.05
A	m^2	$\frac{\pi}{4}D^2$	$2{\cdot}10^{-3}$
I	m^4	$\frac{\pi}{64}D^4$	$3.07{\cdot}10^{-7}$
F	N/m	-	3
ω	rad/s		6.40
ρ	kg/m^3	-	7800

Copyright © 2010 John Wiley & Sons, Ltd.

Paper IV

"Single-component Multi-rate Real-Time Hybrid Simulation Pilot Test on a Composite Structure"

J. P. Waldbjoern, S. Andersen, J. H. Hoegh, J. W. Schmidt & C. Berggreen

To be submitted: *Strain, 2016*

Single-component Multi-rate Real-Time Hybrid Simulation Pilot Test on a Composite Structure

Jacob P. Waldbjoern[1], Sebastian Andersen[1], Jacob Herold Høgh[2], Jacob Wittrup Schmidt[1] and Christian Berggreen[2]

[1]Department of Civil Engineering, Technical University of Denmark, Kgs. Lyngby, Denmark

[2]Department of Mechanical Engineering, Technical University of Denmark, Kgs. Lyngby, Denmark

Keywords: *multi-rate real-time hybrid simulation, hardware-in-the-loop, performance evaluation, experimental substructure, numerical substructure, Taylor basis*

Abstract

This paper represents a single component multi-rate real-time hybrid simulation (mrRTHS) strategy for experimental assessment of a cantilever Glass Fiber Reinforced Polymer (GFRP) beam loaded at the tip by a sinusoidal point load. This emulated structure is implemented as a simplified wind turbine blade in terms of geometry, scale and load – here with special attention paid to the root and max-chord section. For that reason the experimental substructure comprises the clamped end of the GFRP beam while the free end makes up the numerical substructure. The partitioning between the numerical and experimental substructure – referred to here as the shared boundary - includes a discrete point with 3 degrees-of-freedom (dof). The numerical substructure generates a displacement signal through a Taylor basis with a coarse time step of Δt = 20 msec to optimize computational resources. Using the current and three previous displacement data points, a finer control signal is generated with a time step of δt = 2 msec to ensure accurate actuator control in the transfer system. The hybrid simulation communication loop is operated through a Laboratory Engineering Workshop (LabVIEW) real-time target which combines an onboard reconfigurable field-programmable gate array (FPGA) and real-time single-core processor within the same chassis. A DIC and inertia compensator is implemented to account for the compliance and dynamics imposed by the load train in the transfer system. The structural response is investigated by mrRTHS for an execution frequency in the range: 0.074Hz – 2.96Hz for the sinusoidal point load. The system performance is evaluated against a numerical model of the emulated structure – referred to here as the reference. For the translational dofs at the shared boundary a root-mean-square (RMS) error of 19.37% to 21.59% in the x-direction and 15.01% to 16.23% in the y-direction is identified between the mrRTHS and reference. The rotation at the shared boundary exhibits an RMS error of 56.84% to 67.99%. This is a significant RMS error which is induced in the mrRTHS given that the commanded rotation defined by the numerical substructure was erroneously reduced by a factor of π/180. However the overall system performance proved successful which is an important milestone in the effort of performing a successful single component mrRTHS on a wind turbine blade.

1. Introduction

Hybrid simulation is a substructuring technique where a structure of interest is emulated by combining the advantages of numerical modelling with those of experimental testing [1], [2]. The coupling governed through the interface between the numerical and experimental substructure – referred to here as the shared boundary – is achieved by maintaining the compatibility and equilibrium at the interface. During the test, a predefined external load is applied the numerical substructure and the corresponding response computed. Through a communication loop, the displacement at the shared boundary is acquired and applied to the experimental substructure through a servo-hydraulic transfer system. The forces required to deform the experimental substructure – referred to here as the reaction force – are fed back to the numerical substructure to reveal the response of the emulated structure. The experimental and numerical substructure, communication loop and servo-hydraulic transfer system combine to form the hybrid simulation.

The research within hybrid simulation has primary been focusing on testing of seismic protection of building structures on a real-time and extended time-scale [3], [4], [5], [6]. Here the shared boundary between the numerical and experimental substructure typically consist of a discrete point with a few degree-of-freedom (dof) referred to here as multi-component hybrid simulation. For this application, the load bearing structure has been simulated in a numerical model while e.g. damping fixtures has been tested experimentally including: elastomer [7], stud types [8], [9] and magneto-rheological [10], [11], [12]. However multi-component hybrid simulation is becoming a mature and reliable technology, which opens the opportunity to spread the hybrid simulation technique within other application areas [13].

Wind turbines are progressively used as a substitute to fossil fuels and the demand for larger and more energy producing turbines are needed. Thus demands for optimization yields test methods able to accurately determine the wind turbine blade response to major static and dynamic forces acting on the blade during service. The ambition to improve the structural and operational performance within the industry of wind turbines [14] has resulted in extensive research within large-scale and high performance composite structures. In these efforts, testing has primary been focusing on two scales: full scale and coupon material testing [15]. However to address shortcomings in full scale and material testing, the hybrid simulation concept is implemented as a substructural technique for large scale composite structures – referred to here as single component hybrid simulation.

Single component hybrid simulation is a substructuring technique, capable of evaluating the global response of the emulated structure when exposed to local effects and advanced load configurations. However the single component hybrid simulation technique highly complicates the numerical and experimental substructure due to the complex geometry and material characterization [16]. Furthermore, the transferring of response at the shared boundary is continues along the edge instead of e.g. a clearly defined hinge as mentioned above. The operation of the shared boundary justifies the need for advanced measuring techniques to ensure a high degree of accuracy in the displacement imposed on the shared boundary of the experimental substructure [17], [18]. Previous research has been done within the field of single component hybrid simulation on a composite structure with the shared boundary covering; a single discrete point with multiple and single axis control. However both publications only cover the quasi-static regime which is inadequate given the significance of strain rate and inertia effects on composite structures [19].

To include the dynamic effects on both the numerical and experimental substructure, Real Time Hybrid Simulation (RTHS) is implemented. RTHS includes critical time constraints throughout the entire system to ensure accuracy and stability of the experiment [20]. Given the increased complexity of the numerical substructure within single component hybrid simulation, this time constraints can be difficult to meet with the available on-board computational resources due to the implementation of e.g. non-linear effects along with numerous degrees of freedom. For that reason, the numerical substructure may require an extended integration time to be solved in real-time. However another principle aspect in the RTHS lies in the shared boundary, which needs to follow a continuous time history of displacement, velocity or acceleration [21]. Given that the output from the numerical substructure is discrete, fine time steps is required to ensure accurate actuator control. To optimize the available computational resources and enhance flexibility to the RTHS architecture, the numerical substructure and shared boundary is executed at different rates – referred to here as multi-rate real-time hybrid simulation (mrRTHS) [22].

The scope of this paper is to perform an experimental assessment of a cantilever thin-walled GFRP beam with a rectangular cross sectional geometry using single component mrRTHS. The cantilever beam is loaded at the tip by a sinusoidal point load representing a simplified wind turbine blade in terms of geometry, scale and loads. With the root and max-chord section as the area of special interest of the wind turbine blade [23] the clamped end of the GFRP beam is chosen as the experimental substructure while the free end makes up the numerical substructure. The partitioning between the numerical and experimental substructure is described by a discrete point with 3 dofs. The mrRTHS communication loop is operated through a Laboratory Virtual Engineering Workshop (LabVIEW) real-time target capable of providing deterministic and real-time performance for data acquisition and control systems. Digital

Image Correlation (DIC) is implemented as a method of adjusting the dynamically imposed displacement at the shared boundary, to fit the command signal received by the numerical model. Furthermore an inertia compensator is implemented to erase the dynamic effects implemented by the mass of the load train [24]. Compensation of communication delay and dynamics of the transfer system are conducted through a suitable compensator to ensure accuracy and stability in the communication loop. A so-called Taylor basis is applied in the numerical simulation of the mrRTHS, as this provides a computational efficient way of including the nonlinearities in the model, cf. [25], [26]. For verification of the single-component mrRTHS technique a numerical and experimental representation of the emulated structure is conducted – referred to here as the reference. Here a sinusoidal point load is applied the emulated structure and the global response monitored in multiple measurement points to compare with the global response of the mrRTHS.

2. Hybrid simulation setup

2.1. Emulated structure and partitioning

A cantilever beam is implemented as the emulated structure with the overall dimensions, external load and boundary conditions represented in figure 1. This configuration is studied to reduce the complexity and cost in verifying the mrRTHS communication loop for a wind turbine blade application in terms of geometry, scale and loads.

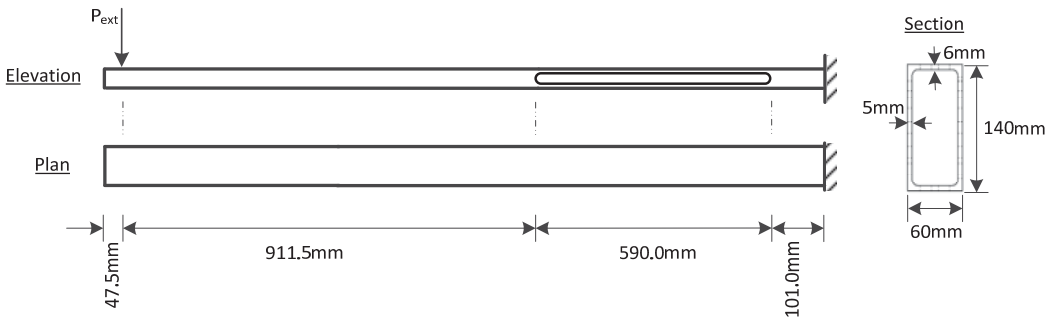

Figure 1: emulated structure representing the overall dimensions, external load and boundary conditions

The emulated structure is a 1650mm long thin-walled Glass Fiber Reinforced Polymer (GFRP) beam produced by fiber pultrusion. The in-plane stiffness properties of the GFRP beam are assumed identical to the properties identified in **[16]** given that the specimen used in both studies are from the same batch. The in-plane material properties are presented in table 1, determined in accordance with D3039/D3030M – 08 **[27]** and D5579/D5379M – 12 **[28]**. The 1-direction corresponds to the x-direction while the 2-direction corresponds to the z-direction for the compression/tension flanges and y-direction for the shear flanges in figure 2.

Table 1: In-plane stiffness properties and density for the GFRP composite

E_1 [GPa]	E_2 [GPa]	ν_{12} [-]	ν_{21} [-]	G_{12} [GPa]	G_{21} [GPa]	Dens [kg/m^3]
28.36	9.96	0.23	0.08	3.41	3.06	1825

The emulated structure is partitioned in a numerical and experimental substructure named: part A and part B respectively. In the experimental substructure a 590mm long and 40mm wide slit are initiated in both shear webs of the closed rectangular profile to weaken the shear stiffness – yielding a geometrical non-linear response. The shared boundary between the two substructures is defined by a discrete point with three dof including: translation in the x- and y-direction along with rotation around the z-axis – referred to here as d_x, d_y and φ respectively. The corresponding reaction force is defined by three dof including: normal and shear force along with a moment – referred to here as N, V and M respectively cf. figure 2.

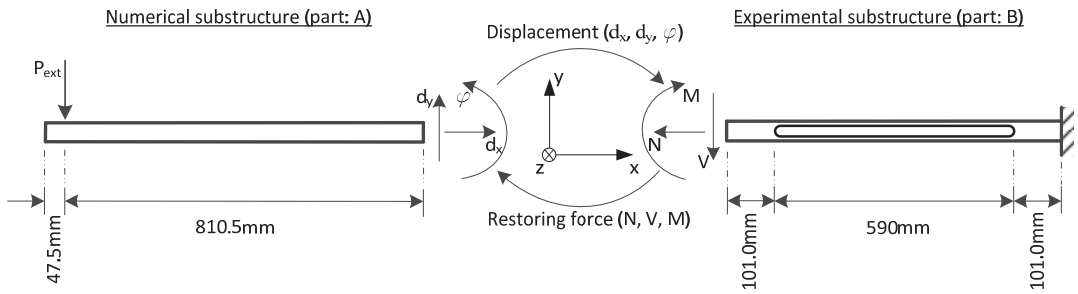

Figure 2: emulated structure and shared boundary between the numerical substructure (part A) and experimental substructure (part B)

2.2. Experimental test setup

The experimental test setup is handled in a reconfigurable stiff frame structure – capable of handle both the experimental substructure and reference structure. The clamped boundary of the GFRP beam is achieved through a rectangular steel profile which encloses the clamped end of the GFRP beam. Installation plates are fitted in between the GFRP beam and rectangular steel profile to ensure a tight fit and to avoid critical stress concentrations around the support. A stiff friction connection between the rectangular steel profile and GFRP beam is established through eighteen bolts. A more detailed description/representation of the design and dimensions of the clamped support are given in [16].

Experimental substructure (part: B)

The experimental substructure of the mrRTHS consist of a 1200mm long cantilever beam which is loaded in three dof by three actuators named: A, B and C cf. figure 3. Actuator A is a MTS model: 244.12 with a static and dynamic stroke of 182.9mm and 152mm respectively and force capacity of ±25kN. The actuator is operated by a 2 stage servo valve model: MTS 252.23G-01 with a capacity of 19l/min. The displacement of the actuator is measured by a Linear Variable Differential Transducer (LVDT) and the force obtained by an MTS load cell model: 661.19E-04 with a capacity of ±25kN. Actuator B and C is a MTS model: 242.01 with a static and dynamic stroke of 114.3 and 101.6mm respectively and force capacity of ±5kN. The actuators are operated by a 2-stage servo valve model: MTS 252.21G-01 with a capacity of 4l/min. All three actuators are operating at 3000psi pressure delivered by a hydraulic power unit (HPU). The PID controller is a MTS model: TestStar II with a three channel configuration – controlled and monitored through the real-time target. The standard deviation of the repeatability offered by the transfer system is given in table 2. The repeatability is identified from a sample of 40000 measurements, acquired under constant conditions with a sampling frequency of 0.5 kHz.

Table 2: standard deviation (std.) of the repeatability offered by the transfer system

actuator label	act. A	act. B	act. C
std. displacemet [mm]	0.0103	0.0016	0.0017
std. force [N]	1.66	1.12	3.67

The response of the shared boundary is monitored through real time tracking of the three measurement points (MP's) applied on the shared boundary, see figure 3. This is achieved through a 3D DIC system of the type: ARAMIS 12M by Gesellschaft für Optische Messtechnik mbH (GOM). Through 24mm Titanar lenses a measurement volume of 200x150mm is achieved and calibrated using a 175x140mm calibration panel. The real-time tracking of the MP's are acquired, processed and transferred through an Ethernet port using the software: PONTUS live vs. 8. The in-plane and out-of-plane standard deviation of the repeatability offered by the DIC system is given by the average of MP-1, MP-2 and MP-3: dx = 0.419µm, dx = 4.157µm and dz = 0.777µm. The repeatability is identified from a sample of 10000 measurements, acquired under constant condition with a sampling frequency of 90 Hz. The MP's are illuminated with an even and high intensity to lower the shutter time as much as possible.

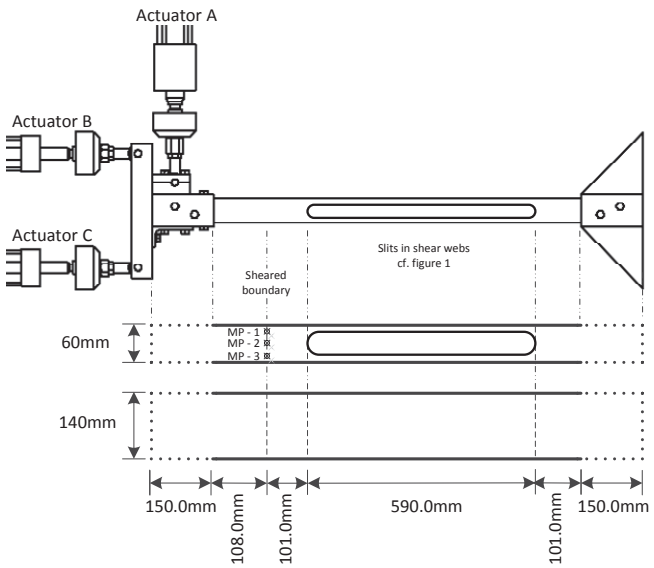

Figure 3: experimental substructure including: load train, support, specimen and MP's

A load introduction zone of 108mm is implemented between the shared boundary and the load introduction rig to erase any influence on the in-plane displacement field initiated by the rectangular steel profile. A numerical analysis of the setup verified that the influence was negligible for a load introduction zone longer than 100mm.

Experimental reference structure

A reference structure configuration is studied to reduce the complexity in verifying the mrRTHS communication loop capabilities and operation of the shared boundary. The experimental reference structure consist of a 1800mm long cantilever beam which is loaded in a single dof by actuator A cf. figure 4. The response of the loading point (MP - 4) is monitored through the LVDT and load cell on the actuator with the specifications further described in the previews section. The shared boundary is monitored through the 3D DIC system with the camera type, setup and performance as described in the previews section.

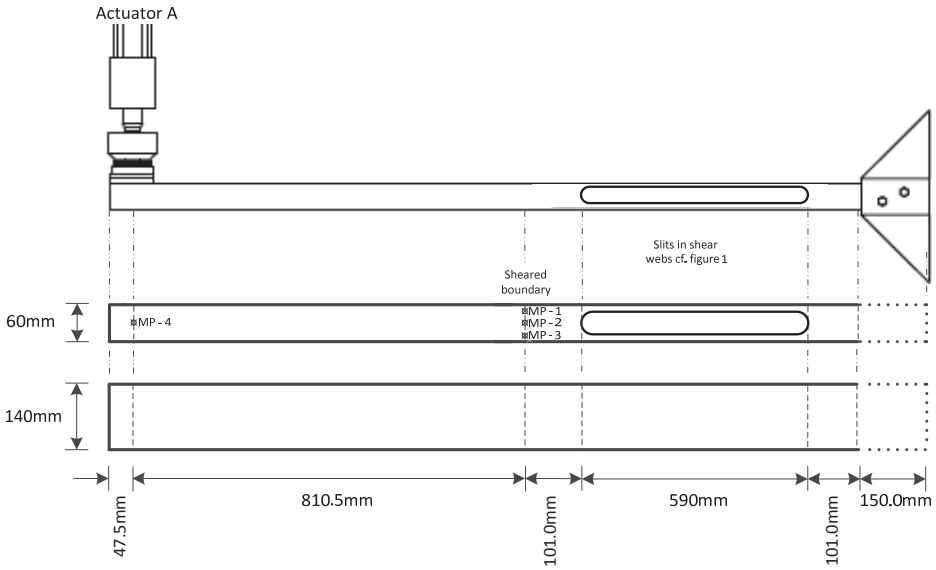

Figure 4: experimental reference structure including: load train, support, specimen and measurement points

The first and second natural frequency of the reference structure was experimentally identified to f_1 = 7.40Hz and f_2 = 47.3Hz through a vibration test further described in [24]. To access the first modal shape of the reference structure a modal analysis is performed through ANSYS 15.0 using isoparametric quadrilateral 8 node shell elements of the type: shell281. The model consists of 12841 elements and orthotropic material properties with the following extension to table 1: $E_2 = E_3$, all G-moduli are taken as the average of G_{12} and G_{21} i.e. ($G_{12}=G_{23}=G_{13}$=3.235) and all poisons ratio are taken as the average of ν_{12} and ν_{21} i.e. ($\nu_{12}=\nu_{23}=\nu_{13}$=0.15). The corresponding modal shape is presented in figure 5 with and eigenfrequency of f_1 = 8.90Hz.

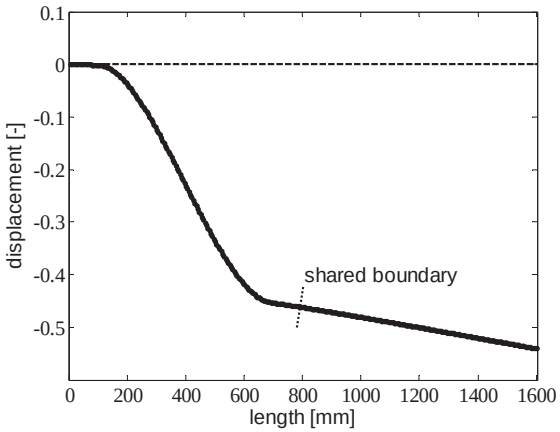

Figure 5: 1st modal shape of the cantilever beam generated by ANSYS

The increase of the Eigen frequency identified by the ANSYS model is caused by the clamped support which is modelled as infinitely stiff i.e. no rotation at the clamped end of the beam is allowed. This is not the case for the experimental reference structure where some rotation will occur in the clamped support **[16]**.

2.3. Numerical test setup

In the following is given a description of the numerical aspects of the hybrid simulation. First, the numerical substructure (part: A) is described. This part is used in the hybrid simulation. Next a finite element method (FEM) model of the full structure, used to verify the hybrid simulation, is described - referred to as the numerical reference structure.

The time integration is performed with the Central Difference Method (CDM), which is an explicit method, see e.g. [29]. This is chosen as it is simple to implement and does not require equilibrium iterations. The FEM model of the structure is modeled by two nodal plane Euler-Bernoulli beam elements with two translational dofs, v_{ix} and v_{iy}, and one rotational dof, θ_i, in each node, see Fig 1. A detailed description of the element is presented in [25].

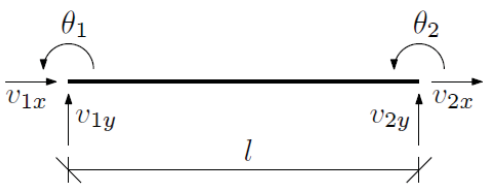

Figure 6: Plane Euler-Bernoulli Beam Element

Numerical substructure (part: A)

As described previously, the emulated structure consists of a numerical and experimental substructure. By distinguishing between the two substructures, the equations of motion (EOM) can be written as eq. (1).

$$\boldsymbol{M}_n\ddot{\boldsymbol{x}} + \boldsymbol{C}_n\dot{\boldsymbol{x}} + \boldsymbol{Q}_n + \boldsymbol{R} = \boldsymbol{F} \tag{1}$$

The matrices **M** and **C** represent the mass and damping matrices and the vectors **Q** and **F** the internal restoring forces and the external loading, respectively with the index n referring to the numerical substructure. Furthermore, **R** is a vector representing the inertia, damping and restoring forces of the experimental substructure, obtained by the actuators.

To be able to execute the simulations in real time the EOM are projected onto a reduced basis. The basis applied in the given case is a so called Taylor basis, which combines a set of linear modes and their associated modal derivatives. The modal derivatives represent the higher order effects of the deformations introduced by the linear modes. These are important to include in nonlinear systems if effects such as membrane locking should be avoided. The Taylor basis is described in full detail in [25], [26]. In the given case the linear modes are determined from the linearized eigenvalue problem presented in eq. (2).

$$(\boldsymbol{K}_T - \omega_i^2\boldsymbol{M})\boldsymbol{\varphi}_i = \boldsymbol{0} \tag{2}$$

Here $\mathbf{K}_T$ is the tangent stiffness matrix, $\boldsymbol{\varphi}_i$ is the i'th linear modal vector and ω_i its associated frequency. The modal derivative of mode number i with respect to the reduced co-ordinates, s_j, is written as, $\frac{\partial\boldsymbol{\varphi}_i}{\partial s_j}$, and can be determined from eq. (3), see [25];

$$\left(\boldsymbol{K}_T - (\omega_i + \omega_j)^2\boldsymbol{M}\right)\frac{1}{2}\left(\frac{\partial\varphi_i}{\partial s_j} + \frac{\partial\varphi_j}{\partial s_i}\right) = \left[\frac{1}{m_j}\boldsymbol{\varphi}_j^T\left(\frac{\partial\boldsymbol{K}_S}{\partial s_k}\boldsymbol{\varphi}_j - \frac{\partial\boldsymbol{K}_S}{\partial s_j}\boldsymbol{\varphi}_k\right)\boldsymbol{M} - \frac{\partial\boldsymbol{K}_S}{\partial s_k}\right]\boldsymbol{\varphi}_j \tag{3}$$

Here $\mathbf{K}_s$ is the secant stiffness and m_j is the modal mass associated with mode j. It should be stressed that the modes determined from eq. (2) and (3) are based on the full structure which includes the full FE - model including both the physical and numerical substructure. The consequences and assumptions made when including the physical substructure in the modes is discussed in detail in chapter 5. The basis vectors are organized in the matrix $\boldsymbol{\phi}$. Projecting eq. 3 on the basis, the equations take the form presented in eq. 4.

$$\boldsymbol{\phi}^T(\boldsymbol{M}_n\boldsymbol{\phi}\ddot{\boldsymbol{s}} + \boldsymbol{C}_n\boldsymbol{\phi}\dot{\boldsymbol{s}} + \boldsymbol{Q}_n + \boldsymbol{R}) = \boldsymbol{\phi}^T\boldsymbol{F} \tag{4}$$

As shown in [25] and [26] the co-ordinates of the modal derivatives are given as a product of the linear mode co-ordinates. Thus, the number of unknowns corresponds to the number of linear modes only. Therefore, before solving the EOM in eq. (4) these are transformed into a linear set of equations - for details see [26].

Numerical damping of the magnitude 20% is included to damp out the high frequent response related to the included modes. This is done in order to stabilize the hybrid simulation. The damping is included in the linear mode through the principle of '*Superposition of Modal Damping Matrices*', see e.g. [30]. As the linear modes and the modal derivatives are coupled, damping of the linear modes will have a damping effect on the modal derivatives as well.

A suitable time step increment is required to ensure precision and stability of the numerical substructure. An increasing system frequency comes with a reduced time step which requires additional onboard computational resources. In the given case the real-time target requires a time step magnitudes to be $\Delta t \leq 10^{-2}s$ to fulfill the real time criteria. To meet this criteria only the first linear mode and its associated modal derivative can be included in the basis. Further modes would introduce higher frequencies and make the system turn unstable for a time step $\Delta t \geq 10^{-2}s$. The first linear mode and associated derivative is presented in Figure 7.

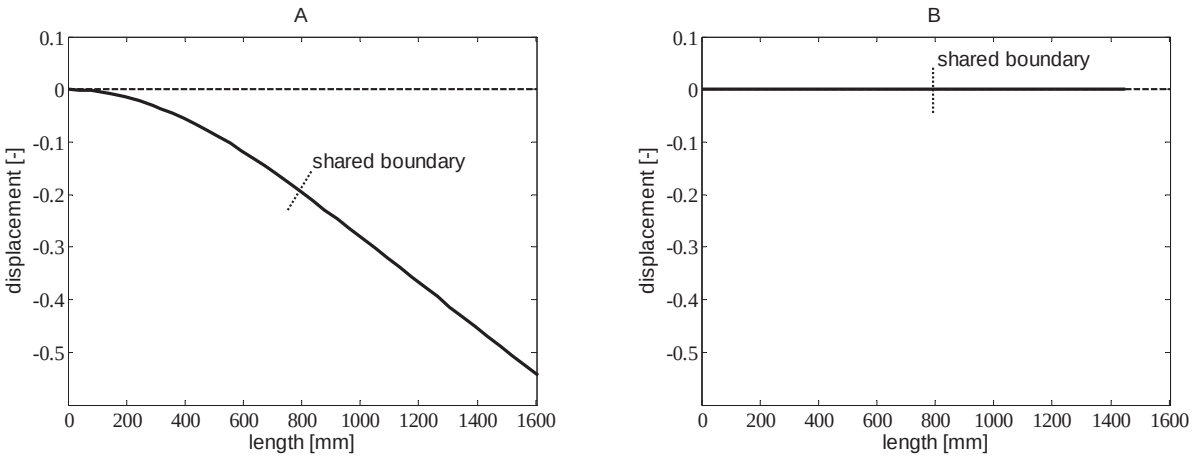

Figure 7: modal shape of the cantilever beam generated by plane Euler-Bernoulli elements: A) 1st linear mode and B) its associated derivative

The dashed line indicates the initial position of the beam, and the solid line the deformation. The linear mode is seen to be a bending mode and the modal derivative is a horizontal contraction. The horizontal deformation is kinematic nonlinear effect introduced when the beam is exposed to bending.

The linear bending mode in Figure 7 is significantly different from the first mode of the numerical reference structure presented in Figure 5. Thus, by only being able to include a single mode, displacement discontinuities at the shared boundary are expected.

Numerical reference structure

A full numerical model is organized in order to verify the output from the mrRTHS. The Euler-Bernoulli element, however, does not include the effect of shear flexibility. To account for this effect in the best way, the experimental substructure is modeled with a linear beam element in the numerical reference structure where the second moment of area I is scaled such that the deformations of the full FEM model attains the value (P,u) presented in Figure 12a in the quasi-static regime. The reference point chosen is (P,u) = (50 N, 10 mm), representing the linear regime of the experimental reference structure.

3. Overall testing strategy and equipment

3.1. Hardware

The overall hardware setup of the mrRTHS system is separated into four components including: 1) real-time target, 2) monitoring PC, 3) DIC system and 4) transfer system. A representation of the overall hardware setup and communication flow is illustrated in figure 8.

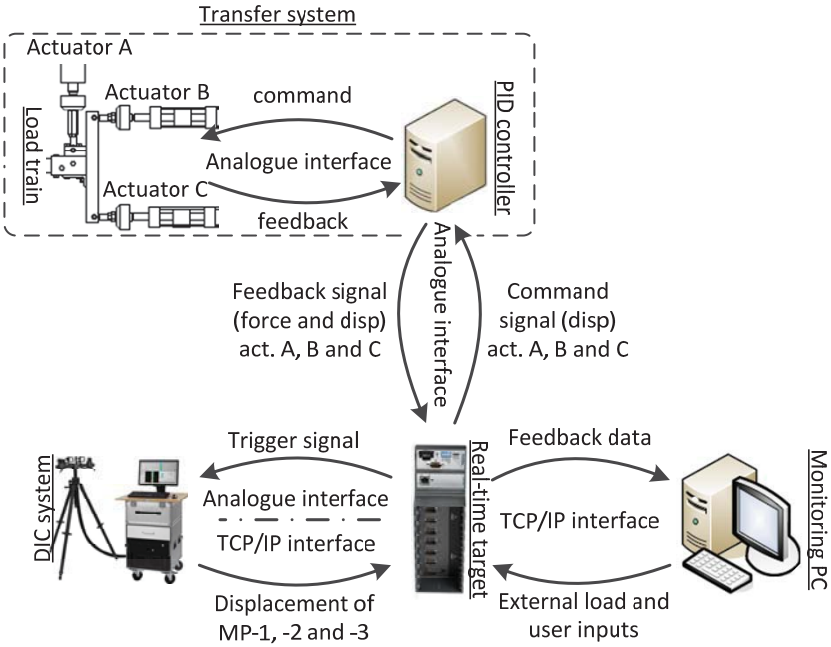

Figure 8: representation of the overall hardware setup

Here the real-time target consists of a CompactRIO 9074 (cRIO – 9074) [31] which is integrated to provide reliable, deterministic and real-time control and monitoring capabilities. The cRIO - 9074 system combines an onboard reconfigurable field-programmable gate array (FPGA) and 400MHz real-time single-core processor – referred to here as the Digital Signal Processor (DSP) – within the same chassis. An analogue interface between the DIC system, transfer system and cRIO – 9074 is handled through a digital to analogue (NI9263) [32] and analogue to digital (NI9205) [33] I/O module. The cRIO – 9074 and I/O module combine to form the real-time target.

The monitoring PC continuously transmits the predefined external load and user defined inputs, while receiving feedback data from the real-time target through Ethernet port 1. This configuration provides ample onboard memory and a graphical user interface (GUI) for the operator.

Through Ethernet port 2 in the real-time target the DIC system is connected. Here the in-plane displacement of the MP's on the shared boundary (see figure 3 and 4) are tracked in real-time and transferred to the real-time target through the TCP/IP interface. The communication delay - being the time from a displacement of the shared boundary occurs to the measurement is available to the real-time target - is quantified through an analogue trigger signal.

The transfer system consists of a load train driven by 3 servo hydraulic actuators named: A, B and C along with a PID controller cf. figure 3 and 8. The PID controller is operated and monitored by the real-time target through an analogue signal to ensure a reliable and real-time performance interface.

3.2. Communication loop and testing procedure

The main architecture of the mrRTHS communication loop is separated into three parallel processes named: 1) Main-loop, b) Outer-loop and c) transfer system. The outline of the dataflow in the mrRTHS communication loop is separated in 12 units labeled from **(1)** to **(12)** cf. figure 9.

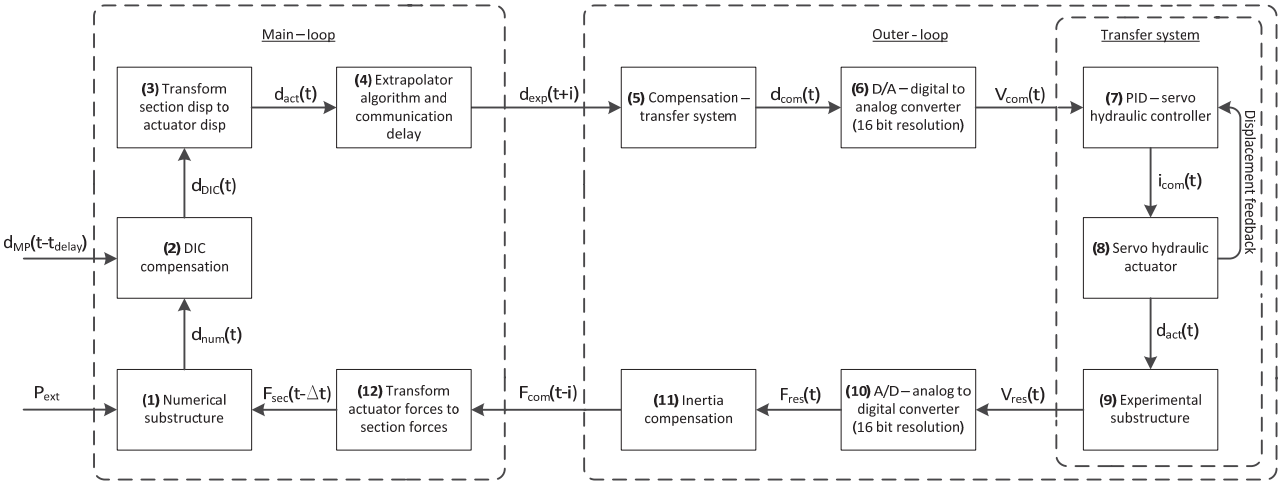

Figure 9: Schematic block diagram representing the overall architecture for the mrRTHS communication loop

The main-loop is operated in the time domain t through the DSP on the real-time target with a coarse time step of 50Hz (i.e. Δt = 0.020 sec) to save computational resources. Here the numerical substructure computes the next displacement signal $d_{num}(t)$ = [dx(t), dy(t), φ(t)] in **(1)** based on the external load P_{ext} and last available reaction force $F_{sec}(t-\Delta t)$ = [N(t-Δt),V(t-Δt),M(t-Δt)]. For stability reasons **(1)** is executed with a numerical time step of 0.010 sec (100Hz) by using the same reaction force $F_{sec}(t-\Delta t)$ twice for each main-loop iteration – see subchapter 2.3. The reaction forces from actuator A, B and C are transformed to section forces $F_{sec}(t-\Delta t)$ through a trigonometric relation in **(12)**, assuming rigid body motion [16]. To handle the effect of the compliance in the load train a DIC compensator is implemented in **(2)**. A schematic of the switching logic between the DIC compensator **(2)** and DIC – system are outlined in figure 10. Here the latest available in-plane displacement $d_{MP}(t-t_{delay})$ = [dx(t-t_{delay}), dy(t-t_{delay})] for each of the three measurement points on the shared boundary is transferred to the real-time target upon request. The real-time tracking rate achieved by the DIC system is 90Hz (dt = 0.011sec) with a time delay of t_{delay} = 160ms. The in-plane deformations $d_{MP}(t-t_{delay})$ are transformed to a 3 dof displacement on a discrete point with the format $d_{sec}(t-t_{delay})$ = [dx(t), dy(t), φ(t)] by deriving the dx and dy translation as the average of the three measurement points while the rotation around the z-axis is determine by the angle between MP-1 and MP-3 [24]. Knowing the target displacement of the shared boundary $d_{num}(t-t_{delay})$, actual measured displacement $d_{sec}(t-t_{delay})$ and previews error $d_{error}(t-\Delta T)$ the current error can be derived as $d_{error}(t) = (d_{num}(t-t_{delay}) - d_{sec}(t-t_{delay})) + d_{error}(t-\Delta T)$. Tuning of the DIC compensation is conducted with the gain K_{gain} meaning that the current compensated displacement signal is given by $d_{DIC}(t) = K_{gain} \cdot d_{error}(t) + d_{num}(t)$. The compensated displacement $d_{DIC}(t)$ = [dx(t), dy(t), φ(t)] is converted to an equivalent displacement for each of the three actuators $d_{act}(t) = [d_A(t),d_B(t),d_C(t)]$ through a trigonometric algorithm following the assumption of rigid body motion [16]. Through the current and previews data points provided for each of the three actuators by **(3)** the displacement signal is resampled through extrapolation $d_{exp}(t+i)$ in **(4)** with the time increment δt for $i \in [0;\Delta t]$. Furthermore the predicted system response after the communication delay is identified as the displacement signal and included in the $d_{exp}(t+i)$ by superposition. The extrapolator and delay compensator in **(4)** are both handled by a 3rd order polynomial fitting algorithm, further described in subchapter 4.2.

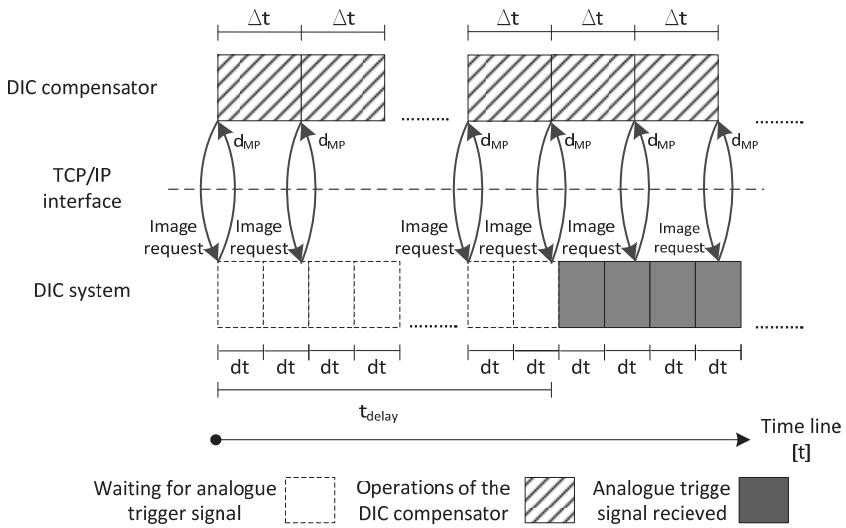

Main calculations in the DIC compensator

$$\left\{ \begin{array}{c} d_{MP} \rightarrow d_{sec} \\ \Updownarrow \\ d_{error}(t) = \left(d_{num}(t - t_{delay}) - d_{sec}(t - t_{delay})\right) + d_{error}(t - \Delta T) \\ \Updownarrow \\ d_{DIC}(t) = K_{gain} \cdot d_{error}(t) + d_{num}(t) \end{array} \right\}$$

Figure 10: Schematic of the DIC compensator and DIC system switching logic and main calculations

The outer – loop is operated through the FPGA with an execution rate of 500Hz (i.e. δt = 0.002 sec) to generate a smooth command signal for the experimental substructure. Here the dynamics of the entire transfer system is handled through a direct inverted first order compensator in **(5)** for each of the three actuators. Further details of the compensator are given in subchapter 4.1. From the data points provided by **(5)** an equivalent analogue signal $V_{com}(t)$ is generated in **(6)** to operate the transfer system. The corresponding reaction force $V_{res}(t)$ are acquired from the transfer system and converted to a digital signal $F_{res}(t)$ by **(10)**. In order to compensate for the inertia effects induced by the load train – which acts as a lumped mass applied on the tip of an cantilever beam – an inertia force compensator is implemented in **(11)** [24]. Through the vertical displacement dy(t) of $d_{num}(t)$ an equivalent acceleration is derived. Knowing the mass of the load train and current acceleration the equivalent load can be derived from newton's second law. This force is subtracted from the current vertical load V from $F_{sec}(t-\Delta t)$ by obtaining the reaction force from the specimen.

The communication interface between the main- and outer-loop which is running with a sampling frequency ratio of ($\Delta t/\delta t$ = 10) – referred to here as an execution rate of 1:10 - is handled through a producer/consumer configuration further specified in [34].

The transfer system is operated against the real-time analogue command signal $V_{com}(t)$ received from **(6)** with an execution frequency of 3 KHz. Through the PID controller in **(7)**, an electrical current $I_{com}(t)$ is generated and passed to the servo hydraulic actuators in **(8)** causing the actuators to move $d_{act}(t)$. The corresponding reaction forces induced on the load cells $V_{res}(t)$ is obtained from the experimental substructure in **(9)**.

4. System characterization

4.1. Transfer system dynamics

The dynamics of the transfer system represents a significant source of delay/lags in the mrRTHS communication loop – thus compensation is crucial to ensure accuracy and stability of the RTHS [35]. To handle the dynamics of each of the

three actuators included in the transfer system over the frequency and amplitude range of interest a direct inverted first order feed forward (FF) compensator is implemented. The discrete first order direct inverted compensator $K_i(z)$ is presented in the z-domain by eq. (5).

$$K_i(z) = \frac{\propto z-(\propto-1)}{z} \quad \text{for} \quad \text{i = actuator A, actuator B, actuator C} \tag{5}$$

Here α is calibrated for each of the three actuators so that the measured and desired displacement correlate. This calibration process is conducted through an open loop chirped sinusoidal signal with a linearly increasing frequency ranging from 0 to 3 Hz for the duration of 40 seconds and constant peak-to-peak amplitude of 19.81mm, -1.46mm and 0.92mm for actuator A, B and C respectively. The amplitude is identified on the basis of the displacement of the shared boundary identified for the reference structure (see table 3). The time domain comparison of the actuator performance is represented in figure 11.

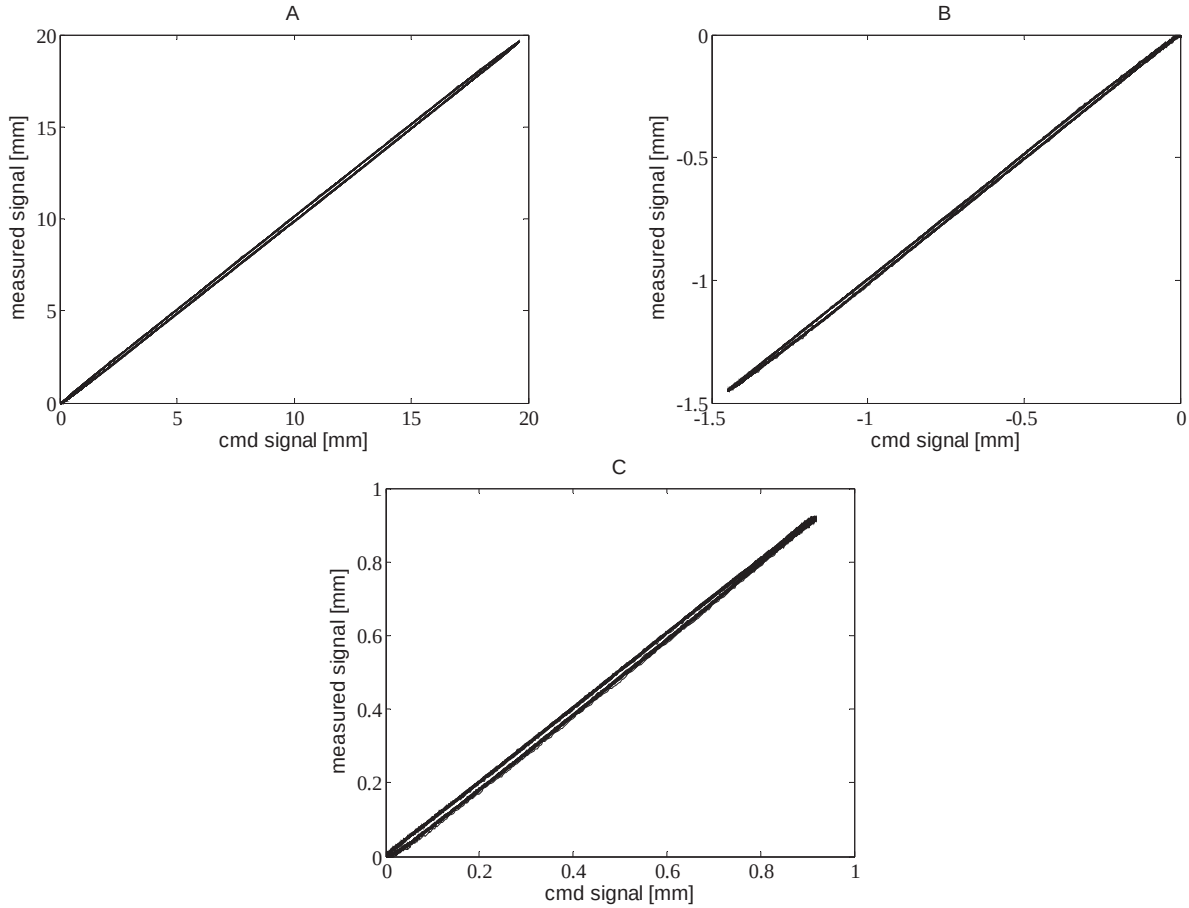

Figure 11: Time domain comparison of actuator performance with a single-order FF controller: a) act. A, b) act. B and c) act. C

Here a sound correlation between the desired and measured displacement of the actuator is identified, indicating that the single-order FF compensator is adequate for the given application.

4.2. Communication delay and extrapolation

Both the communication delay and extrapolation is handled through a forward prediction scheme of the type: third order polynomial fitting algorithm developed by [36]. Several of other prediction schemes have been investigated for the use in mrRTHS [22] – however the third order polynomial fit algorithm was identified as the best solution in terms of tracking performance and the required computational resources needed to operate the algorithm [34]. Through the

use of the current and three previews data points provided by the numerical substructure with the time step Δt, the control signal is extrapolated with a predefined time step of δt in eq. (6).

$$d_{exp} = \sum_{i=0}^{N} a_i d_i \tag{6}$$

Here d_{exp} are the control signal with the time step Δt, d_i the current and three previous data points provided by the numerical substructure and a_i the polynomial coefficients generated through the Lagrange formula. For a fully independent relation between the main loop time step Δt and outer loop time step δt, the polynomial coefficients a_i are given by eq. (7) – (10) cf. [36].

$$a_0 = \frac{\delta t}{\Delta T}\left(\frac{11}{6} + \frac{\delta t}{\Delta T} + \frac{1}{6}\left(\frac{\delta t}{\Delta T}\right)^2\right) \tag{7}$$

$$a_1 = -\frac{\delta t}{\Delta T}\left(3 + \frac{5}{2}\frac{\delta t}{\Delta T} + \frac{1}{2}\left(\frac{\delta t}{\Delta T}\right)^2\right) \tag{8}$$

$$a_2 = \frac{\delta t}{\Delta T}\left(\frac{3}{2} + 2\frac{\delta t}{\Delta T} + \frac{1}{2}\left(\frac{\delta t}{\Delta T}\right)^2\right) \tag{9}$$

$$a_3 = -\frac{\delta t}{\Delta T}\left(\frac{1}{3} + \frac{1}{2}\frac{\delta t}{\Delta T} + \frac{1}{6}\left(\frac{\delta t}{\Delta T}\right)^2\right) \tag{10}$$

The tracking performance of the polynomial fitting extrapolator is investigated in [34] through a chirped sinusoidal open loop signal for an execution rate of 1:10. Here an error between the desired and extrapolated signal were identified to 0.10% for a frequency up to 3Hz. Given that the identified error is independent of the signal amplitude an error of 0.10% will be expected for all three actuators.

5. Test results and discussion

5.1. Response of the reference structure

The reference structure represented in figure 1 is tested in two configurations including an experimental and numerical representation. Initially the correlation of the global response between the numerical and experimental reference structure are investigated in the quasi-static regime cf. figure 12a. Here the force-displacement response of MP-4 for both reference structures is linear up to approximately 100N. Beyond this point the stiffness of the experimental reference structure decreases significantly with a local maximum of around P = 230 N. The response of the numerical reference structure seems to make a slight increase in the stiffness for a load P > 100N. It is expected that the behavior of the numerical reference structure exhibits a higher stiffness than the experimental reference structure given that the former does not include shear flexibility - as discussed previously. However, the softening behavior of the experimental reference structure cannot be attributed to the shear flexibility. The significant stiffness reduction is an effect originating from geometric nonlinearities where the flange at the shear slits is exposed to a local instability. This was furthermore visually verified during the quasi-static test presented in figure 12a.

To compare the global response of the experimental and numerical reference structure in the real-time regime the GFRP beam is loaded by a sinusoidal deformation P_{ext} with a peak-to-peak amplitude of 25mm and excitation frequency including: f_1 = 0.074Hz, f_2 = 0.74Hz, f_3 = 1.48Hz, f_4 = 2.22Hz and f_5 = 2.96Hz - equivalent to 1%, 10%, 20% 30% and 40% of the first natural frequency. From figure 12b the peak-to-peak reaction force decreases as a function of an increasing excitation frequency. This is explained by fact that more inertia is introduced into the system when the excitation frequency is increased. Furthermore, the experimental reference substructure seems to be more affected by the inertia effects than the numerical reference structure. This is most likely caused by the weight of the steel and rubber plate located between the load cell and GFRP beam – see figure 4. The peak to peak reaction force of the

numerical reference structure is shifted and located slightly higher than in the experimental reference. This is in accordance with the force-displacement curve in Figure 12a, where a 25 mm displacement is seen to be outside the linear domain, indicating that the stiffness of the numerical reference is higher than the experimental reference.

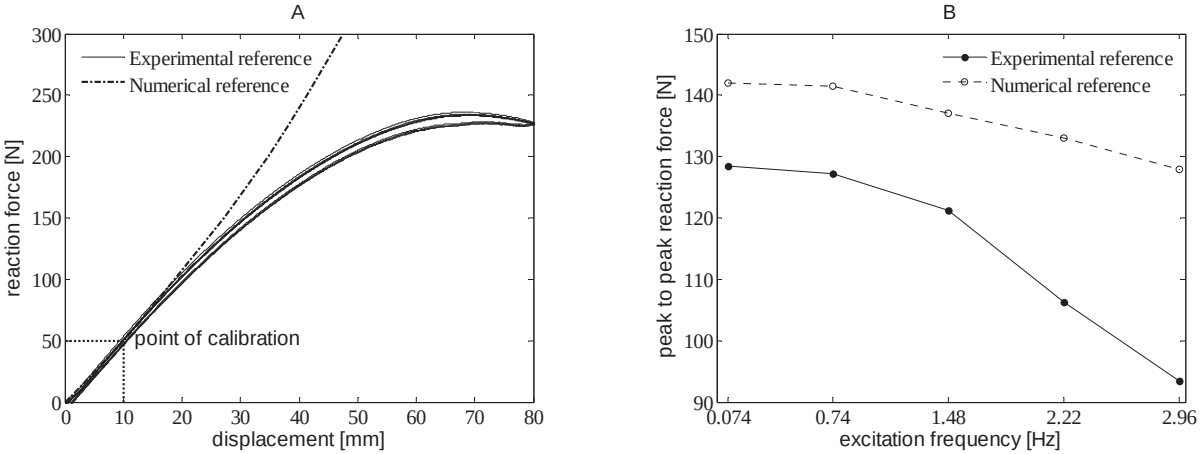

Figure 12: response of MP-4 in the reference structure: a) quasi-static response and b) peak-to-peak reaction force amplitude for a constant deformation of 25mm of MP-4

The displacement obtained at the shared boundary is represented in table 3 for a 25mm vertical displacement at MP-4. Here a large deviation between the numerical and experimental reference structure are present. The experimental reference is seen to experience the largest translations, whereas the largest rotation is found in the numerical reference. The significant deviations can be explained by the difference in the deformation shapes of the two reference structures – see figure 5 and 7. The deformation of the numerical reference is a pure bending deformation, as indicated in Figure 7a with a steady increase in both translations and rotation. The experimental reference structure, on the other hand, will experience a local deformation around the slits with large translations and rotations cf. figure 5. The rotation at the shared boundary required to reach 25 mm at MP-4, is therefore smaller than in the numerical reference.

Table 3: displacement of the shared boundary with a 25mm vertical displacement of MP-4

	dx [mm]	**dy [mm]**	**φ [rad]**
experimental reference	-0.563	-18.68	5.894e-3
numerical reference	-0.053	-8.10	18.91e-3
error [%]	90.58	56.64	220.8

Thus, by calibrating the numerical reference structure from the displacement at MP-4 as described in subchapter 2.3, discontinuities of the response at the shared boundary is inevitable introduced due to the lack of shear flexibility in the implemented element formulation.

5.2. Single component mrRTHS

The global response of the cantilever GFRP beam is evaluated in the real-time regime through a single component mrRTHS. Here the GFRP beam is loaded by a sinusoidal deformation P_{ext} with a peak-to-peak load of 130N with an excitation frequency including: f_1 = 0.074Hz, f_2 = 0.74Hz, f_3 = 1.48Hz, f_4 = 2.22Hz and f_5 = 2.96Hz - equivalent to 1%, 10%, 20% 30% and 40% of the first natural frequency. The mrRTHS is evaluated using a normalized error between the mrRTHS and numerical reference structure represented in eq. (11)

$$Error(t) = \frac{|mrRTHS(t) - REF(t)|}{max(|REF(t)|)} \cdot 100 \tag{11}$$

Due to global instability issues triggered by measurement noise and undesirable signal chattering induced by the extrapolator [22], [34] – a 75% reduction of the reaction force is introduced in the mrRTHS communication loop. An alternative approach would be to filter the generated displacement signal and/or the corresponding reaction force; however that was not possible due to the limited available computational resources offered by the real-time target.

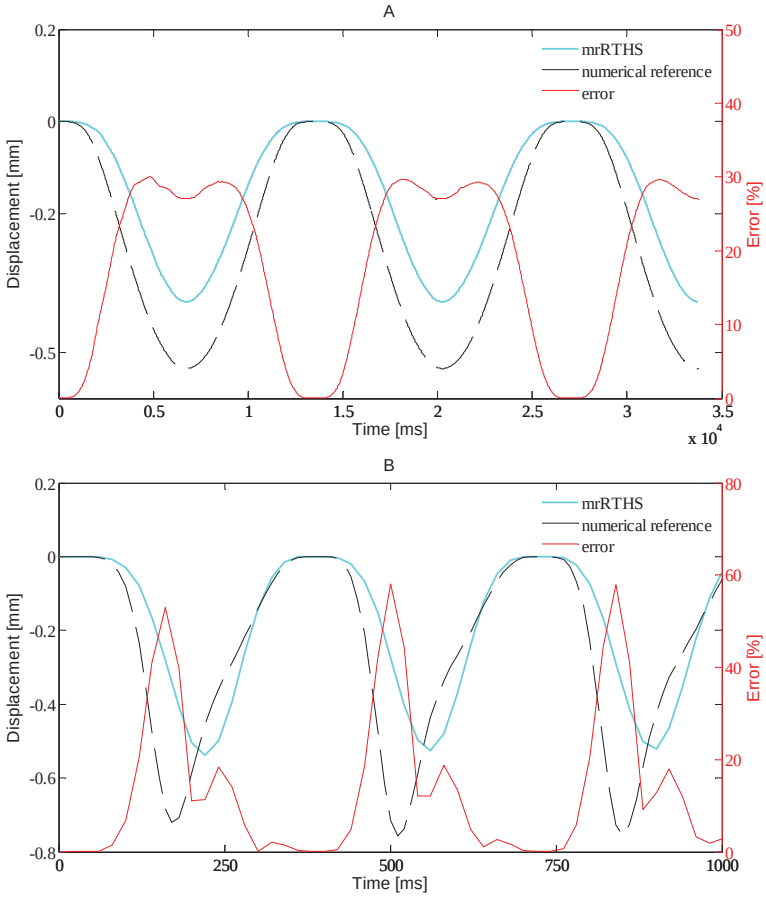

Figure 13: x-direction (dx) of the shared boundary for mrRTHS and reference including: a) f_1 = 0.074Hz and b) f_5 = 2.96Hz

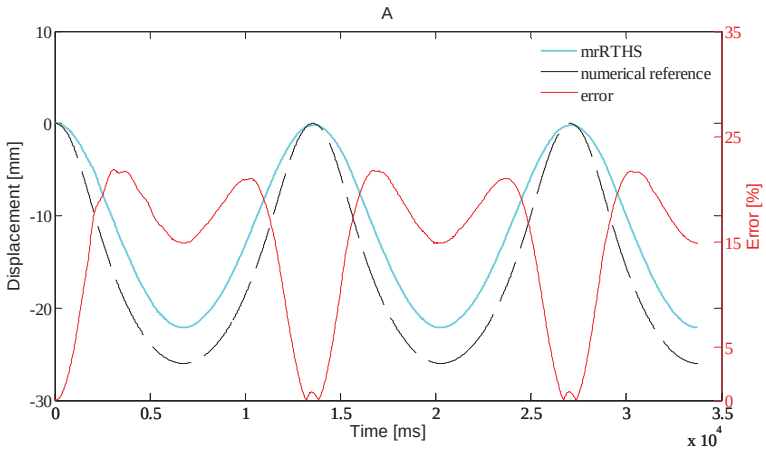

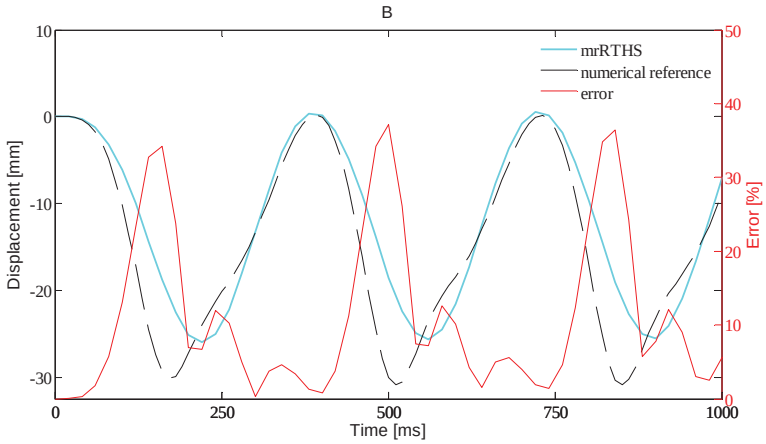

Figure 14: y-direction (dy) of the shared boundary for mrRTHS and reference including: a) f_1 = 0.074Hz and b) f_5 = 2.96Hz

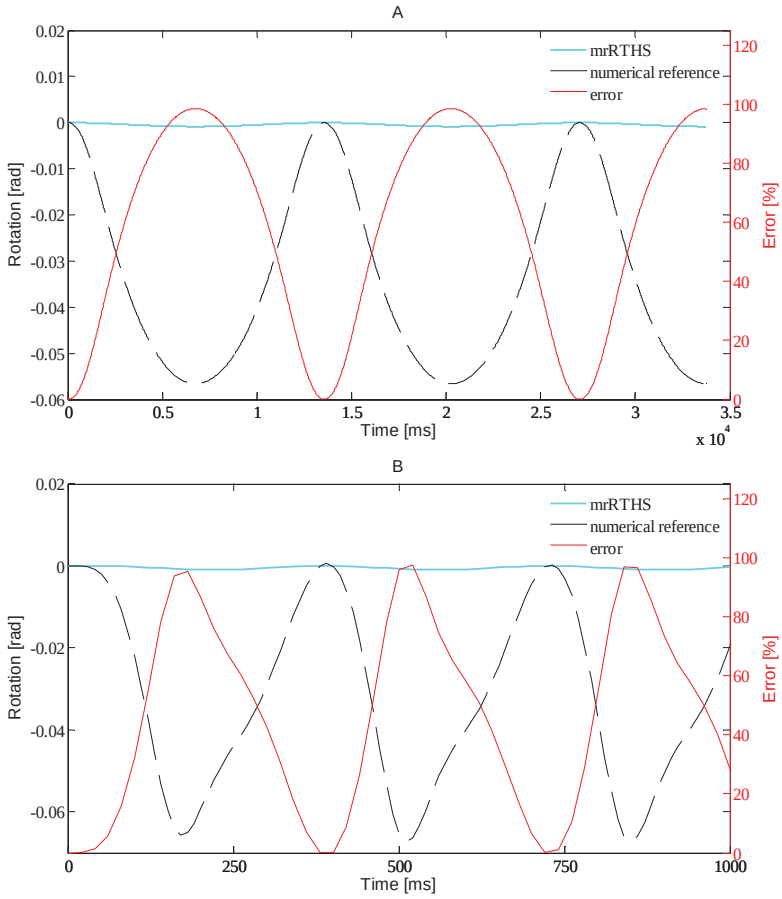

Figure 15: z-rotation (φ) of the shared boundary for mrRTHS and reference including: a) f_1 = 0.074Hz and b) f_5 = 2.96Hz

In Figure 13 through 15 the in-plane displacement of the shared boundary for the two excitation frequencies f_1 = 0.074 Hz and f_5 =2.96 Hz are represented. The key results for the remaining frequencies (f_1 to f_4) are given in table 4. From the translations of the shared boundary in figure 13 and 14, the deformations in the mrRTHS are smaller than the numerical reference structure. Furthermore the reference responses are seen to be in phase for f_1. However in the f_5 case the numerical reference response is seen to be irregular. At the minima the numerical reference response is seen to be ahead of the mrRTHS response. However, this difference vanishes more or less between the local minima and maxima, as the reference response decreases its deformation speed. This is a dynamic effect, due to an increased influence of the bending mode. The bending mode has a natural frequency of 9 Hz for the numerical reference

structure. Thus, by increasing the excitation frequency from f_1 to f_5 - more energy in introduced into the mode. By increasing the damping of the system the effect was removed, confirming the consideration. For the remaining excitation frequencies represented in table 4 the peak error is increasing as a function of the frequency. However the root-mean-square (RMS) error is approximately constant supporting the fact that the irregularity seen at minima is very local along the time scale and does not influence the remaining wave shape. The difficulties in mimicking the dynamic effects through the mrRTHS method is most likely related to experimental errors including: transfer system dynamics, communication delay, sensor miscalibration, measurement noise and random truncations in the analogue-to-digital (AD) conversion of the communication interface between the real-time target and PID controller, etc. However the overall peak-to-peak displacement amplitude obtained for an increasing excitation frequency is increasing due to the dynamics in the system cf. table 4. The same effect is observed for the experimental and numerical reference structure cf. figure 12b.

Table 4: peak-to-peak displacement and error obtained through single component mrRTHS

direction		excitation frequency [Hz]				
		0.074	0.74	1.48	2.22	2.96
x-direction	peak-to-peak disp. ampl. [mm]	0.3906	0.4540	0.5123	0.5428	0.5394
	peak error [%]	30.03	30.26	46.98	56.75	58.05
	RMS error [%]	21.59	19.86	19.37	20.34	21.54
y-direction	peak-to-peak disp. ampl. [mm]	22.13	23.86	25.34	26.09	26.96
	peak error [%]	21.86	25.14	33.48	37.09	37.25
	RMS error [%]	16.23	15.32	15.01	15.06	15.64
z-rotation	peak-to-peak rot. ampl. [rad]	8.44e-4	9.09e-4	9.79e-4	10.25e-4	10.29e-4
	peak error [%]	98.51	98.46	98.40	98.78	98.81
	RMS error [%]	67.89	67.99	67.24	62.40	56.84

Considering the rotations of the shared boundary for the mrRTHS and reference structure in Figure 15, an evident difference appears. The rotation of the mrRTHS is seen to be significant smaller than the rotation in the reference structure. The reason for this is that the rotation introduced into the transfer system was erroneously reduced by a factor $\pi/180$, as if converted from degrees to radians. However, as the output from the numerical substructure is in radians, this reduction is meaningless. The rotations in the mrRTHS are therefore approximately zero compared to the rotations in the reference structure at the shared boundary. Due to the introduced rotation errors, a discussion of the results, are based primarily on the translation plots in Figure 13 and 14.

From the translational response in figure 13 and 14, a higher stiffness of the mrRTHS is unexpected – considering the results presented in figure 12 and table 3. However, two obvious reasons for the higher stiffness in the mrRTHS are given as the lack of rotations at the shared boundary and the applied modal basis. By restricting the rotation to be more or less zero when translations are imposed onto the shared boundary, a stiffer response is expected, compared to the case were the shared boundary were assigned a rotation which is a factor $180/\pi$ higher. Furthermore as only the first bending mode and its associated derivative are included in the applied basis, the local deformation in the region of the slits cannot be properly represented. Thus, by imposing the displacements of a pure bending mode onto the physical substructure, a further stiffness increase is expected.

The tracking performance between the mrRTHS (desired) and DIC (achieved) displacement of the shared boundary when using the DIC compensator is evaluated in table 5. Furthermore the correlation between the command signal (mrRTHS) and measured signal (DIC) are presented I figure 6 for an execution frequency of 0.074Hz.

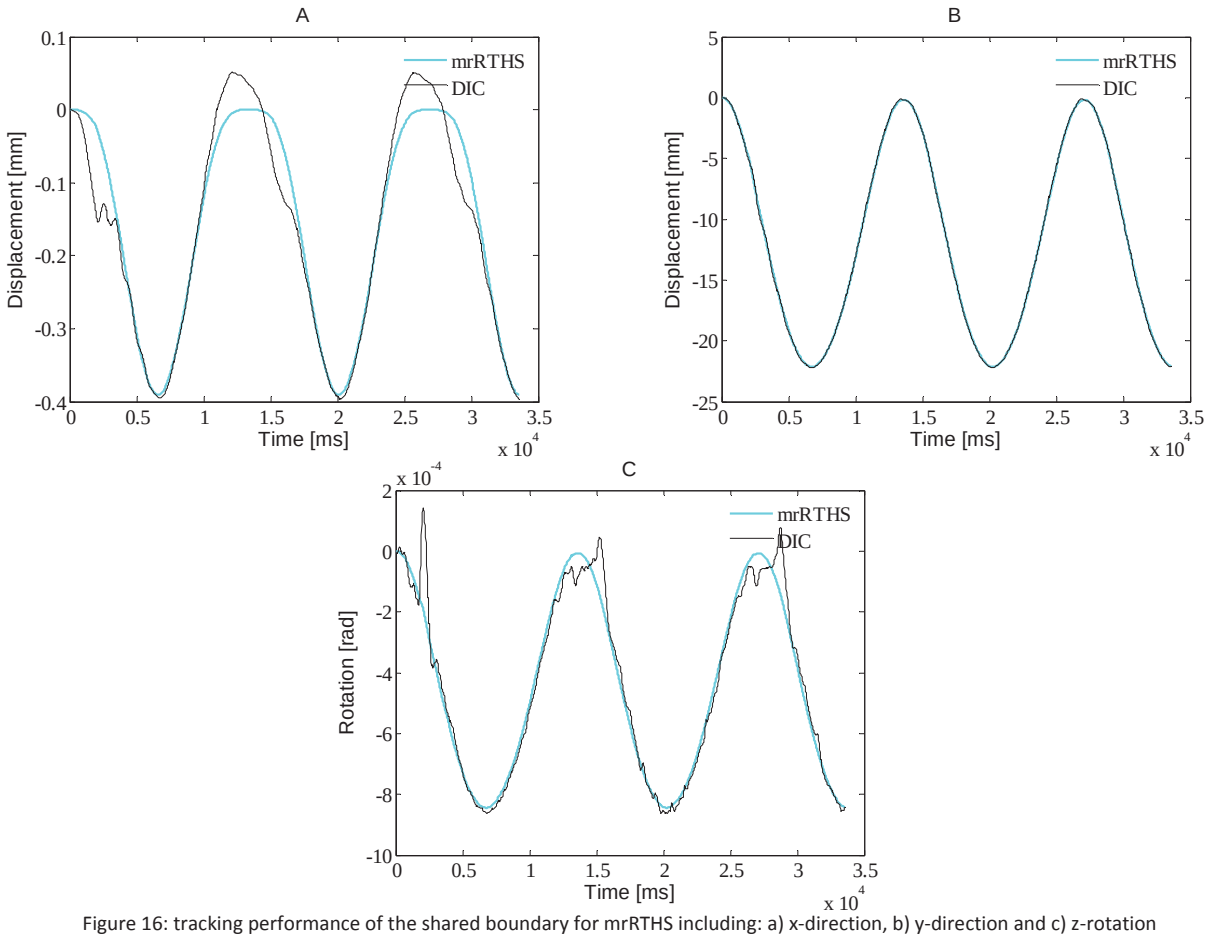

Figure 16: tracking performance of the shared boundary for mrRTHS including: a) x-direction, b) y-direction and c) z-rotation

Here a sound correlation between the desired and achieved displacement is achieved for an execution frequency of 0.074Hz. However for an increasing execution frequency the error is increasing as well due to the compliance of the test rig. This is expected due to the time delay of 160ms which is equivalent to 47.3% of a single period for an excitation frequency of 2.96 [24].

Table 5: error between the desired and achieved displacement of the shared boundary

direction		excitation frequency [Hz]				
		0.074	0.74	1.48	2.22	2.96
x-direction	peak error [%]	31.68	95.54	129.72	116.08	101.68
	RMS error [%]	9.19	30.85	40.45	26.94	22.14
y-direction	peak error [%]	2.31	9.97	16.81	32.15	31.56
	RMS error [%]	0.51	2.62	5.73	10.90	15.57
z-rotation	peak error [%]	39.74	38.54	57.38	68.22	68.85
	RMS error [%]	6.75	17.65	22.02	20.54	22.32

The missing ability to reach the target displacement due to compliance in the load train entails a reduced reaction force at the shared boundary – implying a reduced stiffness of the emulated structure.

6. Conclusion

A single component mrRTHS configuration was executed on a cantilever thin-walled GFRP beam with a rectangular cross sectional geometry loaded on the tip by a sinusoidal point load. This test configuration was chosen as a simplified substitute for a wind turbine blade in terms of geometry, scale and loads. Despite some inconsistencies

between the mrRTHS and reference the system proved successful which was an important milestone in the effort of conducting a successful single component mrRTHS on a wind turbine blade.

The mrRTHS was demonstrated on a single component structure and the performance evaluated against the corresponding reference. For the in-plane translational displacement in the shared boundary an RMS error of 19.37% to 21.59% and 15.01% to 16.23% were identified in the x- and y-direction respectively. For an increasing execution frequency of the external load a growing peak error between the mrRTHS and reference were identified. However, given that these peak errors were local along the time scale - this effect was not conclusive when measured as an RMS error. Furthermore, for an external load with constant amplitude the translational displacement were found to increase due to the inertia induced in the system. This effect was furthermore identified in the reference test presented in figure 12b. For the rotation around the z-axis a RMS errors of 56.84% to 67.99% was registered between the mrRTHS and refence. This very high error was due to the rotation received by the numerical substructure being erroneously reduced by a factor of $\pi/180$.

The error between the mrRTHS and corresponding reference in the in-plane translational displacement of the shared boundary was mainly triggered by the inconsistencies between the modal shape of the reference (see figure 5) and numerical substructure (see figure 7a). Furthermore having the rotation of the shared boundary being reduced by a factor of $\pi/180$ generated an increase of the stiffness in the mrRTHS representation outlined in figure 13 and 14. Other contributions to the identified error cover sensor miscalibration, transfer system dynamics, etc.

Due to instability issues in the mrRTHS communication loop the restoring force obtained by the experimental substructure was reduced to 15%. This instability was mainly triggered by undesirable signal chattering generated by the extrapolator. However other contributions to the instability were identified including the actuator dynamic and DIC compensator along with measurement noise and random truncations in the analogue-to-digital (AD) conversion. This instability could have been solved by e.g. filtering the command signal generated by the extrapolator – however due to the limited available computational resources offered by the real time target, this filter were not included in the mrRTHS communication loop.

7. Acknowledgement

The authors would like to acknowledge the financial support from the Danish Centre for Composite Structures and Materials (DCCSM) funded by the Danish Council for Strategic Research within Sustainable Energy and Environment (Grant: 09-067212). Furthermore, the authors acknowledge Fiberline Composites, Barmstedt Allé 5, 5500 Middelfart, DK, for the donation of the GFRP test specimens.

8. References

[1] X. Shao, A. M. Reinhorn and M. V. Sivaselvan, "Real-time Hybrid Simulation Using Shake Tables and Dynamic Actuators," *Journal of Structural Engineering,* vol. 137, no. 7, pp. 748-760, 2011.

[2] O. S. Bursi, A. Gonzalez-Buelga, L. Vulcan, S. A. Neild and D. J. Wagg, "Novel Coupling Rosenbrockbased algorithm for real-time dynamic substructure testing," *Earthquake Engineering and Structural Dynamics,* vol. 37, no. 3, pp. 339-360, 2008.

[3] S. A. Mahin, P.-S. B. Shing, C. R. Thewalt and R. D. Hanson, “Pseudodynamic test method. Current status and future directions,” *Journal of Structural Engineering New York, N. Y,* vol. 115, no. 8, pp. 2113-2128, 1989.

[4] P. B. Shing, M. Nakashima and O. S. Bursi, “Application of pseudodynamic test method to structural research,” *Earthquake Spectra,* vol. 12, no. 1, pp. 26-56, 1996.

[5] M. Nakashima, H. Kato and E. Takaoka, "Development of real-time pseudo dynamic testing," *Earthquake Engineering and Structural Dynamics,* vol. 21, no. 1, pp. 79-92, 1992.

[6] M. Nakashima and N. Masaoka, "Real time on-line test for MDOF systems," *Earthquake Engineering and Structural Dynamics,* vol. 28, no. 4, pp. 393-420, 1999.

[7] T. L. Karavalis, J. M. Ricles, R. Sause and C. Chen, "Experimental evaluation of the seismic performance of steel MRFs with compressed elatsomer dampers using large-scale real-time hybrid simulation," *Engineering Structures,* vol. 33, no. 6, pp. 1859-1869, 2011.

[8] M. Ito, Y. Murata, K. Hoki and M. Nakashima, "Online Hybrid Test on Buildings with Stud-Type Damper Made of Slitted Steel Plates Stifferened by Wood Panels," *Procedia Engineering,* vol. 14, pp. 567-571, 2011.

[9] A. Jacobsen, T. Hitaka and M. Nakashima, "Online test of building frame with slit-wall dampers capable of condition assessment," *Journal of Constructional Steel Research,* vol. 66, no. 11, pp. 1320-1329, 2010.

[10] C. Chen, J. M. Ricles, T. L. Karavasillis, Y. Chae and R. Sause, "Evaluation of a real-time hybrid simulation system for performance evaluation of structures with rate dependent devices subjected to seimic loading," *Engineering Structures,* vol. 35, pp. 71-82, 2012.

[11] Y. Z. Lin and R. E. Christenson, "Comparison of Real-time Hybrid Testing with Shake Table Test for an MR Damper Controlled Structure," in *Americam Control Conference*, St. Louis, Missouri, USA, 2009.

[12] J. E. Carrion, B. F. Spencer and B. M. Phillips, "Real-Time Hybrid Testing of a Semi-Actively Controlled Structure with an MR Damper," in *American Control Conference*, St. Louis, Missouri, USA, 2009.

[13] M. S. Williams, "Real-time hybrid testing in structural dynamics," in *The 5th Australasian Congress on Applied Mechanics*, Brisbane, Australia, 2007.

[14] F. M. Jensen, B. G. Falzon, J. Ankersen and H. Stang, “Structural Testing and Numerical Simulation of a 34m Composite Wind Turbine Blade,” *Composite Structures,* vol. 76, no. 1-2, pp. 52 - 61, 2006.

[15] F. M. Jensen, “Ultimate Strength of a Large Wind Turbine Blade,” Department of Civil Engineering, Technical University of Denmark, Kgs. Lyngby, Denmark, 2008.

[16] J. H. Hoegh, J. P. Waldbjoern, J. Wittrup-Schmidt, H. Stang and C. Berggreen, "Quasi-static single-component hybrid testing of a composite structure with multi-axial control," *STRAIN,* vol. 51, pp. 459-473, 2015.

[17] J. P. Waldbjoern, J. H. Hoegh, J. Wittrup-schmidt, M. W. Nielsen, K. Branner, H. Stang and C. C. Berggreen, "Strain and displacement controls by fibre bragg grating and digital image correlation," *Strain,* vol. 50, no. 3, pp. 262-273, 2014.

[18] X. Fayolle, S. Calloch and F. Hild, "Controlling testing machines with digital image correlation," *Experimental techniques,* vol. 31, no. 3, pp. 57-63, 2007.

[19] R. L. Sierakowski, "Strain rate effects in composites," *American Society of Mechanical Engineers,* vol. 50, no. 11, pp. 741-761, 1997.

[20] T. Horiuchi, M. Nakagawa, M. Sugano and T. Konno, “Development of real-time hybrid experiment system with actuator delay compensation,” in *Proc. 11th World conference on Earthquake engineering* , Acapulco, 1996.

[21] S. J. Dyke, "Acceleration feedback control strategies for active and semi-active systems: modeling, alogrithm development and experimental verification," Ph.D. Dissertation, University of Notre Dame, IN, 1996.

[22] A. Maghareh, J. P. Waldbjoern, S. J. Dyke and A. Prakash, "Adaptive multi-rate interface: development and experimental verification of an interface for multi-rate real-time hybrid simulation," *Earthquake Engineering and Structural Dynamics,* Accepted for publication - december 2015.

[23] L. C. Overgaard, E. Lund and O. T. Thomsen, "Structural collapse of a wind turbine blade. part A: Static test and equivalent single layered models," *Composites: Part A,* vol. 41, pp. 257-270, 2010.

[24] J. H. Høgh, J. P. Waldbjørn, S. Andersen and C. Berggreen, "Compensation Methods in Real-Time Hybrid Simulation," *Strain,* Submitted for peer-review in 2016.

[25] S. Andersen and P. N. Poulsen, "Nonlinear Real-time Simulations Using a Taylor Basis," *International Journal for Numerical Methods in Engineering,* Submitted for peer-review in 2015.

[26] S. Andersen and P. N. Poulsen, "Reduction Method for Kinematic Nonlinear Real-time Simualtions," *International Journal for Numerical Methods in Engineering,* Submitted for peer-review in 2015.

[27] ASTM, "Standard Test Method for Tensile Properties of Polymer Matrix Composite Materials," ASTM International, West Conshohocken, Pennsylvania, United States of America, 2011.

[28] ASTM, "Standard Test Method for Shear Properties of Composite Materials by the V-Notched Beam Method," ASTM International, West Conshohocken, Pennsylnania, United States of America, 2014.

[29] R. D. Cook, D. S. Malkus, M. E. Plesha and R. J. Witt, Concepts and Applications of Finite Element Analysis, 4th edition, New York: John Wiley & Sons, 1974.

[30] A. K. Chopra, Dynamics of Structures: Theory and Application to Earthquake Engineering, Prentice-Hall, 1995.

[31] "http://www.ni.com/pdf/manuals/375874b.pdf," National Instruments, - 6 2014. [Online]. [Accessed 21 11 2014].

[32] "http://www.ni.com/pdf/manuals/373781e.pdf," National Instruments, - 8 2009. [Online]. [Accessed 12 11 2014].

[33] "http://www.ni.com/pdf/manuals/374188d.pdf," National Instruments, - 2 2008. [Online]. [Accessed 12 11 2014].

[34] J. P. Waldbjoern, A. Maghareh, G. Ou, S. J. Dyke and H. Stang, "Multi-rate Real Time Hybrid Simulation operated on a flexible LabVIEW real-time platform," *Smart Structures and Systems,* Submitted for peer review (2015).

[35] J. E. Carrion and B. F. Spencer, "Model-based Strategies for Real-time Hybrid Testing," Newmark Structural Engineering Laboratory, University of Illinois at Urbana-Champaign, Urbana-Champaign, Illinois, USA, 2007.

[36] P. A. Bonnet, "The development of multi-axis real-time substructure testing," University of Oxford, Oxford, United Kingdom, 2006.

[37] K. Takanashi and M. Nakaschiman, “Japanese Activities on ON-LINE Testing,” *Journal of Engineering Mechanics,* vol. 113, no. 7, pp. 1014-1032, 1987.

[38] S. A. Mahin, P.-S. B. Shing, C. R. Thewalt and R. D. Hanson, "Pseudodynamic test method. Current status and future directions," *Journal of Structural Engineering,* vol. 115, no. 8, pp. 2113-2128, 1989.

[39] P. B. Shing, M. Nakashima and O. S. Bursi, "Application of pseudodynamic test method to structural research," *Earthquake Spectra,* vol. 12, no. 1, pp. 29-56, 1996.

[40] R. Bitter, T. Mohiuddin and M. Nawrocki, *LabVIEW Advanced Programming Techniques,* Florida, USA: CRC Press, 2001.

[41] G. Ellis, Control system design guide, San Diego, CA: Academic Press, 2000.

[42] B. M. Phillips and B. F. Spencer, "Model-based servo-hydraulic control for real-time hybrid simulation," Newmark Structural Engineering Laboratory, University of Illinois at Urbana-Champaign, Urbana-Champaign, Illinois, USA, 2011.

[43] M. Nakashima, "Development, potential, and limitations of real-time online (pseudo-dynamic) testing," *Philosophical Transactions of the Royal Society A: Mathematical, Physical and Engineering Sciences,* vol. 373, no. 2035, pp. 1851-1867, 2001.

[44] A. Ashasi-Sorkhabi and O. Mercan, "Development, implementation and verification of a user configurable platform for real-time hybrid simulation," *Smart Structures and Systems,* vol. 14, no. 6, pp. 1151-1172, 8 2014.

[45] D. Ferry, A. Maghareh, G. Bunting, A. Prakash, K. Agrawal, C. Lu and S. Dyke, "On the performance of a highly parallelizable concurrency platform for real-time hybrid simulation," in *The 6'th World Conference on Structural Control and Monitoring*, Barcelona, Spain, 2014.

[46] J. P. Waldbjoern, J. H. Hoegh, H. Stang, C. C. Berggreen, J. Wittrup-Schmidt and K. Branner, "Hybrid Testing of Composite Structures with Single-Axis Control," in *The 19th International Conference on Composite Materials*, Montréal, 2013.

[47] A. Maghareh, S. J. Dyke, A. Prakash and J. F. Rhoads, "Establishing a Stability Switch Criterion for Effective RTHS Implementation," *Journal of smart Structures and Systems,* vol. 14, no. 6, pp. 1221-1245. doi:10.12989/sss.2014.14.6.1221, 2014.

[48] A. Maghareh, S. J. Dyke, A. Prakash and G. B. Bunting, "Establishing a predictive performance indicator for real-time hybrid simulation," *Earthquake Engineering & Structural Dynamics,* vol. 43, no. 15, pp. 2299-2318. doi:10.1002/eqe.2448, 2014.

[49] C. Chen and J. M. Ricles, "A General Approach for Analysis of Actuator Delay Compensation Methods for Real-time Testing," in *The 14th World Conference on Earthquake Engineering*, Beijing, China, 2008.

Hybrid testing is a cost efficient experimental method that can be used to test dynamically loaded structures. The method combines numerical simulation with experimental testing. However, due to a rapid increase in the computational time, only simple numerical models can be included in hybrid testing today. In the present thesis a number of mathematical methods that can help to increase the size and complexity of the numerical models are presented. One of the most significant elements presented are the so called modal derivatives, which are shown to reduce the computational time significantly.

DTU Civil Engineering
Technical University of Denmark

Brovej, Building 118
2800 Kongens Lyngby
Tlf. 4525 1700

http:www.byg.dtu.dk/english

ISBN 9788778774347
ISSN 1601-2917